Removal of Metal Ions from Synthetic and Galvanic Wastewater by Their Incorporation into Ferrites

Vom Promotionsausschuss der
Technischen Universität Hamburg-Harburg
zur Erlangung des akademischen Grades
Doktor-Ingenieurin
genehmigte Dissertation

von

Gumelar Pritosiwi
aus Jakarta
2012

1. Gutachter: Prof. Dr.-Ing. Wolfgang Calmano
2. Gutachter: Prof. Dr. Dr. h.c. Frerich Keil

Prüfungsausschussvorsitzender: Prof. Dr.-Ing. Rudolf Eggers

Tag der mündlichen Prüfung: 04.06.2012

urn:nbn:de:gbv:830-tubdok-11591

Acknowledgements

This work was carried out within the framework of German-Israeli cooperation in Water Technology Research. I am grateful for the financial support by the German Federal Ministry of Education and Research (BMBF) and the Israeli Ministry of Science, Culture and Sport (MOST).

I would like to express my sincere gratitude to my supervisor, Prof. Dr.-Ing. Wolfgang Calmano. Thank you for giving me the opportunity of carrying out this work, and for your guidance, steadfast support and valuable advice from start to finish. Your continuous encouragement drove me to finally get out my first full draft of this thesis.

I would also like to thank Prof. Dr. Dr. h.c. Frerich Keil, second examiner, and Prof. Dr.-Ing. Rudolf Eggers, chairman of the examining board, for the evaluation of this work and the willingness to take up the committee.

I am also immensely grateful to Dr. Joachim Gerth. Thank you for your mentorship, support, and all the valuable feedbacks provided during this work. I did enjoy your jokes and our unreserved discussion.

I am indebted to Prof. Ori Lahav from Technion Israel Institute of Technology for sharing the knowledge of ferrite process and making this research cooperation possible. My sincere gratitude also goes to Dr. Sivan Klas. I was lucky to have you as a research partner and learned many things from you. Thank you for your fruitful collaboration and valuable advice in my research.

I would like to thank Dr. Harald Prestel from WAFA Kunststofftechnik GmbH, Augsburg for giving the first-hand information about the galvanic wastewater and its treatment as well as for supplying the wastewater sample.

It is a great opportunity to thank all the colleagues at the Institute of Environmental Technology and Energy Economics for their support. Special thanks to Daniela Faika, for her kindness and friendship. It was wonderful to share an office room with you. Our chat on various topic used to be a relaxing time, after standing all day long in the laboratory. Many thanks also to Irene Richardt-Brauer for her help in the AAS measurement, and to Barbara Eckhardt and Petra Besdiak for their secretarial assistance. Grateful appreciation goes to the students that worked with me during my research.

I wish to express my deepest gratitude to my parents for their wholehearted support, unending understanding and unconditional love. I never would made it here without you and I am blessed to be your daughter. I would also like to thank my beloved brother, my sister-in-law and my nephew for their continous encouragement. Last but not least, I am greatly indebted to my husband. You have seen me through the ups and downs of the entire thesis and shared this amazing journey with me. You are always there to assist and help in any and every way. Thank you so much for your faithful love and endless help. Without you, this thesis wouldn't exist.

Abstract

The conventional chemical precipitation methods for the treatment of wastewater containing toxic metals generate voluminous, unstable, and non-reusable sludge. An alternative method, termed ferrite process, has been suggested in view of the fact that many non-iron metals can substitute iron atoms in the structure of mineral magnetite (Fe_3O_4). The product, called ferrite ($Me_xFe_{3\text{-}x}O_4$, Me is a non-iron metal), has a compact structure and can be magnetically separated, safely discarded or even reused. Ferrite process is originally carried out at a temperature above 65°C. The ambient temperature ferrite process (ATFP) seems to be a better option for a large scale application due to its lower energy consumption. The aim of this work is to further develop the ferrite process as a prospective alternative to the conventional techniques for the removal of metal ions from wastewater.

As a first step, magnetite synthesis from the solutions containing stoichiometric amount of Fe(II) and Fe(III) in a continuous system was examined. At ambient temperature, mixtures rather than a monophase product resulted unless the reaction conditions were carefully controlled. The results provided a basis for understanding the conditions under which ferrites are formed by the ATFP.

Further investigations focused on the formation of ferrite in synthetic wastewater. The establishment of the incorporation extent for various non-iron metals is important for the process application as it determines the external chemical demand. The incorporation of six non-iron metals into the ferrite produced by the partial oxidation of Fe(II) at 90°C was investigated. By employing multiple characterisation techniques, a comprehensive and reliable data set of the feasible incorporation extent of Zn^{2+}, Co^{2+}, Ni^{2+}, Cd^{2+}, Al^{3+}, and Cr^{3+} into the ferrite structure under the aforementioned conditions could be determined. The new data set was then used to propose the most probable mechanism that affects the incorporation extent of each examined metal ion.

The incorporation of non-iron metals into ferrite produced by the seeded ATFP was studied. Comparison between the ferrite produced by ATFP to those produced at elevated temperature allowed the quantification of the effect of temperature reduction on the incorporation extent and product characteristics. Considering this comparison, the incorporation mechanism involved in the ATFP was suggested. Following the investigation of single metal ion incorporation, the simultaneous incorporation of several non-iron metals into ferrite using the ATFP was explored. The influence of different synthesis conditions on the formation of multi-metal-substituted ferrite was evaluated. The optimised set of operational conditions leading to the formation of crystalline and stable ferrite using the ATFP could be then established.

In the last part of the work, the performance of ATFP for the purification of two types of galvanic wastewater (with and without chelating agents) was assessed. The ATFP was capable of completely and concurrently removing all toxic metals from the galvanic wastewater. The interference of other non-metal pollutants on the formation of ferrite, as well as some options to minimise it, was discussed. The knowledge obtained in this work is useful to estimate the application potential of ferrite process for treating other types of industrial wastewater.

Kurzzusammenfassung

Bei der herkömmlichen Behandlung von industriellen, metallhaltigen Abwässern mit chemischen Fällungsmethoden werden voluminöse, instabile und kaum wiederverwendbare Hydroxidniederschläge gebildet. Unter Berücksichtigung der Tatsache dass viele Schwermetalle die Eisenatome in der Struktur des Minerals Magnetit (Fe_3O_4) substituieren können, wurde mit dem “Ferrit-Prozess” eine alternative Methode vorgeschlagen. Das Fällungsprodukt Ferrit ($Me_xFe_{3\text{-}x}O_4$, Me ist das Nichteisen-Metall) hat eine kompakte Struktur und lässt sich magnetisch abtrennen, kann sicher entsorgt oder sogar wiederverwendet werden. Der Ferrit-Prozess wird in der Regel bei Temperaturen über 65 °C durchgeführt. Im großen Maßstab wäre jedoch wegen des niedrigeren Energieaufwands ein “Ambient Temperature Ferrite Process” (ATFP) die bessere Wahl. Das Ziel dieser Arbeit war es daher, den Ferrit-Prozess für die Entfernung von Metallionen aus Abwässern als potenzielle Alternative zu den herkömmlichen Verfahren weiter zu entwickeln.

Zunächst wurde die Bildung vom Magnetit aus stöchiometrisch zusammensetzten Fe(II)-Fe(III)-Lösungen in einem kontinuierlichen Reaktor-System untersucht. Im Unterschied zu höheren Temperaturen wurde bei Raumtemperatur ein Mischprodukt anstatt eines Monophasen-Produkts erhalten, sofern die Reaktionsbedingungen nicht sorgfältig kontrolliert wurden. Diese Erkenntnisse aus diesen Untersuchungen lieferten die Grundlagen zum Verständnis der Bedingungen unter denen Ferrite im ATFP gebildet wurden.

Die Untersuchungen wurden mit Versuchen zur Ferritbildung in synthetischen Abwässern fortgesetzt. Die Ermittlung des Einbaugrades von verschiedenen Schwermetallen in den Ferrit ist wichtig für die Anwendung des Verfahrens, denn er entscheidet über den Chemikalienbedarf. Zunächst wurde die Inkorporation von sechs Nichteisen-Metallen in den Ferrit, der durch partielle Oxidation einer Fe(II)-Lösung bei 90 °C hergestellt wurde, ermittelt. Mit Hilfe unterschiedlicher Analysenmethoden konnten umfangreiche und verlässliche Daten zu den Einbaugraden von Zn^{2+}, Co^{2+}, Ni^{2+}, Al^{3+}, Cd^{2+} und Cr^{3+} in den Ferrit erhalten werden. Hieraus ließen sich die unterschiedlichen Mechanismen ableiten, die den Einbaugrad jedes Nichteisen-Metalls steuern.

Danach wurde die Inkorporation der Schwermetalle in den Ferrit bei Raumtemperatur und in Gegenwart von Impfkristallen untersucht (ATFP). Ein Vergleich der im ATFP- mit denen im Hoch-Temperatur-Prozess hergestellten Ferrite ermöglichte die Bewertung des Einflusses der Temperatur auf Einbaugrad und die Produkteigenschaften. Aus den Ergebnissen der Experimente ließen sich die im ATFP wirksamen Einbaumechanismen ableiten. Nach der Untersuchung der Inkorporation einzelner Schwermetalle wurde die simultane Inkorporation von den mehreren Metallen in den Ferrit unter ATFP-Bedingungen ermittelt. Ebenso wurde der Einfluss unterschiedlicher Synthesebedingungen getestet, so dass schließlich die optimalen Betriebsbedingungen für die Bildung eines kristallinen und stabilen Ferrits festgelegt werden konnten.

Im letzten Teil der Arbeit wurde unter ATFP-Bedingungen die Behandlung von zwei galvanischen Abwässern (mit und ohne Chelatkomplexe) untersucht. Alle toxischen Metalle aus den galvanischen Abwässern konnten komplett und gleichzeitig abgetrennt werden. Es wurden Störungen durch organische Zusatzstoffe bei der Bildung von Ferrit festgestellt und Optionen zur deren Minimierung vorgeschlagen. Die erzielten Erkenntnisse erlauben die Beurteilung des Ferrit-Prozesses für die Behandlung anderer Arten von industriellen Abwässern.

Contents

List of Figures **xiii**

List of Tables **xvii**

List of Symbols **xix**

Abbreviations **xxiii**

1 Introduction **1**

1.1 Physico-chemical treatment methods for metal-contaminated wastewater . 1

1.2 Aim and outline of the thesis 4

2 General Overview **7**

2.1 Water and metal ions in aqueous solution 7

2.1.1 Properties of water 7

2.1.2 Hydration of ions 8

2.1.3 Water exchange on metal ions 8

2.1.4 Hydrolysis of metal ions 10

2.1.5 Metal speciation 12

2.2 Precipitation and dissolution processes 13

2.2.1 Solubility of solids 13

2.2.2 Precipitation process 15

2.2.3 Dissolution process 20

2.3 Structure and lattice energy of ferrites 24

2.3.1 Spinel structure 24

2.3.2 Cation radii in spinels 28

2.3.3 Lattice energy 29

2.4 Ferrite synthesis 32

2.5 Ferrite dissolution 32

3 Experimental Procedures and Methods **35**

3.1 Preparation of ferrites at elevated temperature 35

3.1.1 Experimental set-up 35

3.1.2 Experimental procedures 35
3.2 Preparation of ferrites at ambient temperature in the batch system 36
3.2.1 Experimental set-up 36
3.2.2 Experimental procedures 37
3.3 Preparation of ferrites at ambient temperature in the continuous system . . 39
3.4 Analyses 39
3.4.1 Chemical composition 40
3.4.2 X-ray diffraction (XRD) 41
3.4.3 Scanning electron microscopy (SEM) 44
3.4.4 Specific surface area 45
3.4.5 Fourier-transform infrared spectroscopy (FTIR) 46
3.4.6 Dissolution test 46
3.4.7 Leaching tests 47

4 Magnetite Synthesis at Ambient Temperatures 49
4.1 Previous works 49
4.1.1 Magnetite precipitation by oxidation method 49
4.1.2 Magnetite precipitation by stoichiometric method 52
4.2 Effect of operational parameters on magnetite formation 53
4.2.1 Effect of temperature 54
4.2.2 Effect of initial Fe^{2+}/Fe_T ratio and iron flux 56
4.2.3 Effect of pH 58
4.3 Conclusions 60

5 Incorporation of Metal Ions into Ferrites at Elevated Temperatures 61
5.1 Previous works 62
5.1.1 Extent of metal ion incorporation 62
5.1.2 Mechanism of metal ion incorporation 63
5.2 Determination of incorporation maxima of six metal ions into ferrites . . . 66
5.2.1 Chemical composition 66
5.2.2 Crystalline phases and unit cell sizes 68
5.2.3 Metal spatial distribution 70
5.2.4 Infrared spectra of the precipitates 72
5.3 Morphological characterisation of the ferrites 76
5.4 Predominant mechanisms determining the extent of metal ion incorporation into ferrites 80
5.5 Chemical stability of the ferrites 84
5.5.1 Dissolution stability 84
5.5.2 Leaching 89

5.6 Conclusions 90

6 Incorporation of Metal Ions into Ferrites at Ambient Temperatures 93

6.1 Previous works 94
  6.1.1 Ferrite precipitation by oxidation method 94
  6.1.2 Ferrite precipitation by stoichiometric method 95
6.2 Incorporation of single metal ions 95
  6.2.1 Chemical composition 95
    6.2.1.1 Zinc 95
    6.2.1.2 Nickel 97
    6.2.1.3 Cadmium 98
    6.2.1.4 Aluminium 99
    6.2.1.5 Copper 99
    6.2.1.6 Chromium 101
  6.2.2 Crystalline phases and unit cell sizes 102
  6.2.3 Metal spatial distribution 104
  6.2.4 Infrared spectra of the precipitates 105
  6.2.5 Morphological characterisation 108
  6.2.6 Chemical stability 112
6.3 Comparison of two ambient temperature ferrite synthesis methods 114
6.4 Comparison of ambient- and elevated-temperature ferrites 115
  6.4.1 Metal incorporation extent 116
  6.4.2 Morphology 117
  6.4.3 Chemical stability 118
6.5 Simultaneous incorporation of metal ions 119
  6.5.1 Chemical composition 120
  6.5.2 Crystalline phases and unit cell sizes 125
  6.5.3 Metal spatial distribution 126
  6.5.4 Infrared spectra of the precipitates 127
  6.5.5 Morphological characterisation 128
  6.5.6 Chemical stability 130
6.6 Incorporation of metal ions in the presence of Cr^{3+} ions 132
6.7 Conclusions 135

7 Treatment of Galvanic Wastewater by Ferrite Process 137

7.1 Characteristics of galvanic wastewater 137
7.2 Experiments performed on galvanic wastewater 138
  7.2.1 Treatment of galvanic wastewater with chelating agents 138
  7.2.2 Treatment of galvanic wastewater without chelating agents 139

7.3 Assessment of galvanic wastewater treatment by ATFP 145
7.4 Cost comparison of treatment technologies for galvanic wastewater 147
7.5 Conclusions 149

8 Concluding Summary and Outlook 151

References 153

List of Figures

2.1 Zn(II) speciation without solid precipitation at 25 °C in a system with 10^{-4} M $TOTZn$. 14
2.2 Log C–pH diagram of Zn(II) species in equilibrium with $Zn(OH)_2$(s). . . . 15
2.3 Log C–pH diagram of Fe species in equilibrium with $Fe(OH)_2$(s) and $Fe(OH)_3$(s). 16
2.4 Spinel structure. 25

3.1 Schematic diagram of batch experimental set-up at 90 °C. 36
3.2 Schematic diagram of batch experimental set-up at ambient temperature. . 37
3.3 Schematic diagram of continuous experimental set-up at ambient temperature. 39
3.4 An illustration of the principal components of an atomic absorption spectrophotometer. 41
3.5 Schematic of the X-ray diffraction method. 42
3.6 Schematic of the sealed X-ray tube. 42
3.7 Geometrical illustration of the Bragg's law. 43
3.8 Schematic of the basic components of the SEM. 44

4.1 Schematic diagram of magnetite formation. 50
4.2 Fe^{2+}/Fe_T ratios in the solid particles obtained at different temperatures and Fe^{2+}/Fe_{T_IN} ratios. 55
4.3 SEM images of the solid particles obtained at different temperatures. . . . 55
4.4 Fe^{2+}/Fe_T ratios in the solid particles obtained at different iron fluxes and pH values. 57
4.5 SEM images of the solid particles obtained at different iron fluxes. 57
4.6 Fe^{2+}/Fe_T ratios in the solid particles obtained at different pH values. . . . 59
4.7 SEM images of magnetite obtained at different pH values. 59

5.1 Me/Fe_T ratio in the particles synthesised at 90 °C as a function of Me/Fe_{T_IN}. 66
5.2 Ratio of divalent to trivalent metal ions in the particles synthesised at 90 °C. 67
5.3 Unit cell size of the spinel phase synthesised at 90 °C as a function of Me content in the product. 68

5.4 Plots of the fraction of Me versus Fe dissolved in 12.8% HCl solution for some representative solid particles produced at 90 °C. 71
5.5 FTIR spectra of different ferrites produced at 90 °C. 73
5.6 FTIR spectra of Ni ferrites produced at 90 °C. 74
5.7 FTIR spectra of Cr-associated ferrites produced at 90 °C and amorphous Cr hydroxide. 75
5.8 Changes in the crystallite size of ferrite produced at 90 °C as a function of Me content. 76
5.9 SEM images of Zn ferrites produced at 90 °C for different Zn^{2+}/Fe_{T_SP} ratios. 77
5.10 SEM images of Co ferrites produced at 90 °C for different Co^{2+}/Fe_{T_SP} ratios. 78
5.11 SEM images of Al ferrites produced at 90 °C for different Al^{3+}/Fe_{T_SP} ratios. 78
5.12 SEM images of Cd ferrites produced at 90 °C for different Cd^{2+}/Fe_{T_SP} ratios. 79
5.13 SEM images of Ni ferrites produced at 90 °C for different Ni^{2+}/Fe_{T_SP} ratios. 79
5.14 SEM images of Cr-associated ferrites produced at 90 °C for different Cr^{3+}/Fe_{T_SP} ratios. 80
5.15 Maximal attainable incorporation values of six investigated metals versus their k_{-w} values. 83
5.16 Dissolution profiles of Zn and Co ferrite for different Me/Fe_{T_SP} ratios. 85
5.17 Dissoluton profile and its cube rate law plot for Zn and Co ferrite. 86
5.18 Initial Fe dissolution rates (12.8% HCl solution, 23 ± 2 °C) of the investigated ferrites synthesised at 90 °C. 87
5.19 Correlation between the initial iron dissolution rates of ferrite against the water exchange rate and total electrostatic energy. 88
5.20 Weight percentages of non-iron metal leached from ferrites produced at 90 °C in leaching tests. 89

6.1 Zn^{2+}/Fe_T ratios in the ferrite produced at 30 °C. 96
6.2 Divalent to total metal ratio in Zn ferrite produced at 30 °C. 97
6.3 Ni^{2+}/Fe_T ratios in the ferrite produced at 30 °C. 97
6.4 Cd^{2+}/Fe_T ratios in the ferrite produced at 30 °C. 98
6.5 Cu^{2+}/Fe_T ratios in the solid particles produced at 30 °C. 100
6.6 Cr^{3+}/Fe_T ratios in the solid particles produced at 30 °C. 102
6.7 XRD patterns of Cd ferrites produced at 30 °C. 103
6.8 Unit cell size of the spinel phase produced at 30 °C as a function of Me content in the product. 103
6.9 Plots of the fraction of Me versus Fe dissolved in 12.8% HCl solution for some representative solid particles produced at 30 °C. 105

6.10 FTIR spectra of Zn ferrites produced by StFP at 30 °C. 106
6.11 FTIR spectra of Ni ferrites produced at 30 °C. 107
6.12 FTIR spectra of the solid particles obtained in the incorporation experiments at 30 °C with Cu^{2+} and Cr^{3+}. 107
6.13 SEM images of Zn and Ni ferrites produced at 30 °C. 109
6.14 Specific surface area of the solid particles obtained in the Me incorporation at 30 °C. 109
6.15 SEM images of Cd ferrites produced at 30 °C. 110
6.16 SEM images of the solid particles obtained in the incorporation of Cu^{2+} at 30 °C. 110
6.17 SEM images of the solid particles obtained in the incorporation of Cr^{3+} at 30 °C. 111
6.18 Crystallite size of the spinel phase produced at 30 °C as a function of Me/Fe_{T_SP}. 112
6.19 Initial Fe dissolution rates (12.8% HCl solution, 23 ± 2 °C) of the products synthesised at 30 °C. 112
6.20 Weight percentages non-iron metal leached from the products synthesised at 30 °C. 113
6.21 FTIR spectra of Co and Zn ferrites produced at ambient and elevated temperatures. 117
6.22 Initial Fe dissolution of ferrites produced at 30 °C and 90 °C as a function of Me/Fe_{T_SP}. 119
6.23 Me/Fe_T ratios in the ferrite produced from a solution containing several Me ions under different experimental conditions. 121
6.24 Me/Fe_T ratios in the ferrite produced under similar experimental conditions in the multi-metal and single-metal system a function of Me/Fe_{T_IN}. 122
6.25 Divalent to total metal ratios in the multi-metal-substituted ferrites. 124
6.26 Unit cell sizes of Zn ferrites and multi-metal-substituted ferrites as a function of total Me content. 126
6.27 Plots of fraction of Me versus Fe dissolved in 12.8% HCl solution for Zn-Ni and Zn-Ni-Co-Cd-Al ferrite. 126
6.28 FTIR spectra of multi-metal-substituted ferrites. 127
6.29 SEM images of multi-metal-substituted ferrites. 128
6.30 Specific surface area of the solid particles obtained in the simultaneous Me incorporation. 129
6.31 Crystallite size of ferrite obtained in the simultaneous Me incorporation. . 130
6.32 Initial Fe dissolution rates (12.8% HCl solution, 23 ± 2 °C) of multi-metal-substituted ferrites. 131

6.33 Weight percentages non-iron metal leached from multi-metal-substituted ferrites in the TCLP test. 131
6.34 Weight percentages non-iron metal leached from multi-metal-substituted ferrites in the BCR test. 132
6.35 Me/Fe_T ratios in the solid particles obtained in the Zn,Cr-experiment and Ni,Cu,Cr-experiment. 133
6.36 SEM images of the solid particles obtained in the Zn,Cr-experiment and Ni,Cu,Cr-experiment. 133
6.37 Plots of fraction of Me versus Fe dissolved in 12.8% HCl solution for the solid particles obtained in the Zn,Cr-experiment and Ni,Cu,Cr-experiment. 134

7.1 XRD patterns of the solids precipitated from galvanic wastewater in a continuous mode. 140
7.2 XRD patterns of the solids precipitated from galvanic wastewater in a single-cycle batch mode. 143
7.3 The extents of Ni incorporation into ferrite precipitated from galvanic wastewater without chelating agents in a single-cycle batch mode. 143
7.4 Weight percentages of Ni and Cu leached at pH 5 from the solid particles produced in the experiment without chelating agents. 144
7.5 Scheme of an integrated ATFP for wastewater laden with metal ions. . . . 146

List of Tables

2.1 Rate constant of water exchange. 9
2.2 Formulation of stability constant. 11
2.3 Stability constant for complexation of metals by OH^-. 11
2.4 Effective radii of some cations in tetrahedral (Tet) and octahedral (Oct) sites. 28
2.5 Lattice energy of ferrite end members. 31

4.1 Reported optimum operational parameters promoting magnetite formation at ambient temperatures. 53

5.1 Reported incorporation extents (IE) of non-iron metal (Me) into ferrites produced by Fe(II) oxidation with the important synthesis conditions. . . . 62
5.2 Known unit cell size (*a*) of some ferrites. 69
5.3 Some properties of the investigated metal ions and their corresponding ferrites. 81
5.4 Adsorption edges (pH range) of the investigated metal ions on several iron oxides. 83

6.1 Maximal incorporation extents of five metal ions into ferrites produced at ambient and elevated temperatures. 116
6.2 Operational conditions applied in multi-metal incorporation experiments. . 120
6.3 Me/Fe_{T_SP} ratios at steady state and Me incorporation efficiency obtained in the simultaneous Me incorporation experiments. 122

7.1 Metal concentrations in the investigated galvanic wastewater. 138
7.2 Maximum effluent discharge standards of Ni, Cu, and Cr in surface water. 138
7.3 Metal ion removal from galvanic wastewater with chelating agents. 139
7.4 Metal ion and COD removal from galvanic wastewater without chelating agents in the continuous experiment. 141
7.5 Operational conditions of batch experiments applied for treating galvanic wastewater without chelating agents. 141
7.6 Metal ion removal from galvanic wastewater without chelating agents in the batch experiments. 142

7.7 Operational costs of different treatment techniques for metal containing wastewater. 148

List of Symbols

ΔG_f^0	[kJ/mol]	free energy of formation
a	[Å]	unit cell size
k_{-w}	[s^{-1}]	rate constants for water exchange
k_{sp}	[ ]	stability constants for solid hydroxides
$^*K_1$	[ ]	first hydrolysis constant
Al^{3+}/Fe_{T_IN}	[molar/molar]	molar ratio of aluminium(III) to total iron in the initial solution
Al^{3+}/Fe_{T_SP}	[molar/molar]	molar ratio of aluminium(III) to total iron in the solid particles
Cd^{2+}/Fe_{T_IN}	[molar/molar]	molar ratio of cadmium(II) to total iron in the initial solution
Cd^{2+}/Fe_{T_SP}	[molar/molar]	molar ratio of cadmium(II) to total iron in the solid particles
Co^{2+}/Fe_{T_IN}	[molar/molar]	molar ratio of cobalt(II) to total iron in the initial solution
Co^{2+}/Fe_{T_SP}	[molar/molar]	molar ratio of cobalt(II) to total iron in the solid particles
Cr^{3+}/Fe_{T_IN}	[molar/molar]	molar ratio of chromium(III) to total iron in the initial solution
Cr^{3+}/Fe_{T_SP}	[molar/molar]	molar ratio of chromium(III) to total iron in the solid particles

Cu^{2+}/Fe_{T_IN}	[molar/molar]	molar ratio of copper(II) to total iron in the initial solution
Cu^{2+}/Fe_{T_SP}	[molar/molar]	molar ratio of copper(II) to total iron in the solid particles
Fe^{2+}/Fe_{T_IN}	[molar/molar]	molar ratio of ferrous to total iron in the initial solution
Fe^{2+}/Fe_{T_SP}	[molar/molar]	molar ratio of ferrous to total iron in the solid particles
Fe^{2+}/Fe^{3+}	[molar/molar]	molar ratio of ferrous to ferric
Fe_T	[molar]	total iron
Fe_f	[mg l^{-1} min^{-1}]	total iron flux
M^{2+}	[molar]	total divalent metals
M^{2+}/M^{3+}_{SP}	[molar/molar]	molar ratio of divalent to trivalent metals in the solid particles
M^{2+}/M_{T_SP}	[molar/molar]	molar ratio of divalent to total metals in the solid particles
M^{3+}	[molar]	total trivalent metals
M_T	[molar]	total metals
Me_T	[molar]	total non-iron metals
Me_T/Fe_{T_IN}	[molar/molar]	molar ratio of total non-iron metals to total iron in the initial solution
Me_T/Fe_{T_SP}	[molar/molar]	molar ratio of total non-iron metals to total iron in the solid particles
Ni^{2+}/Fe_{T_IN}	[molar/molar]	molar ratio of nickel(II) to total iron in the initial solution
Ni^{2+}/Fe_{T_SP}	[molar/molar]	molar ratio of nickel(II) to total iron in the solid particles

Me/Fe_{T_IN}	[molar/molar]	molar ratio of non-iron metal to total iron in the initial solution
Me/Fe_{T_SP}	[molar/molar]	molar ratio of non-iron metal to total iron in the solid particles
r_{oct}	[Å]	ionic radius in octahedral site
r_{tet}	[Å]	ionic radius in tetrahedral site
Zn^{2+}/Fe_{T_IN}	[molar/molar]	molar ratio of zinc(II) to total iron in the initial solution
Zn^{2+}/Fe_{T_SP}	[molar/molar]	molar ratio of zinc(II) to total iron in the solid particles

Abbreviations

AAS	atomic absorption spectroscopy
AMD	acid mine drainage
ATFP	ambient temperature ferrite process
BCR	Bureau Communautaire de Référence
CFAE	crystal field activation energy
CFSE	crystal field stabilisation energy
COD	chemical oxygen demand
DRC	dark red complex
EDTA	ethylenediaminetetraacetic acid
EN	electronegativity
FI	ferrous intermediate
FTIR	Fourier-transform infrared spectroscopy
FWHM	full width at half maximum
GC	green complexes
GR	green rust
GR-I	green rust formed in chloride solution
GR-II	green rust formed in sulphate solution
HCO	hydrous chromium oxide
HFO	hydrous ferric oxide

JCPDS	Joint Committee on Powder Diffraction Standards
LFSE	ligand field stabilisation energy
OxFP	oxidation ferrite process
SE	structural energy
SEM	scanning electron microscopy
StFP	stoichiometric ferrite process
TCLP	toxicity characteristic leaching procedure
US EPA	United States Environmental Protection Agency
XPS	X-ray photoelectron spectroscopy
XRD	X-ray diffraction

Chapter 1

Introduction

Metals have been evolved in all life by playing at once beneficial and detrimental roles [1]. Some metals are essential elements (e.g. zinc, copper) for living organisms, and their deficiency results in impairment of biological functions [2]. The use of metals has also been critical to different industrial processes such as electroplating, dyeing, battery manufacturing, mining operations, chemical manufacturing, tanneries, glass and pharmaceutical manufactures [3]. On the contrary, metals are often associated with contaminant and potential toxicity. Some metals are recognised as major toxic metals, e.g. cadmium and lead. Even, essential metals can cause serious health disorders with increasing exposure. The excessive presence of metals in living organisms can results in carcinogenic, mutagenic, teratogenic and other toxic effects on them [4, 5]. Furthermore, metals are also known to be persistent in the environment and, in essence, non-biodegradable.

With the extensive utilisation of metals in various industries, the treatment of industrial wastewater contaminated by toxic metals becomes a global environmental issue. With regard to metal plating industries, it was reported that around 60,000–80,000 tons/year of galvanic sludges are generated in Germany by approximately 3,000 industrial units during the precipitation process of the galvanic wastewater [6]. In Portugal, about 4,000 tons of galvanic sludge are produced annually [7]. Another study in Austria calculated the production of about 4,500 tons of the corresponding sludge in 1998 [8]. The mining industries have also faced with a major challenge regarding the production of acid mine drainage (AMD). McKinnon et al. [9] reported that a typical mine site would treat about 3 million cubic meter of AMD yearly. In Canada, the reclamation cost of non ferrous mines sites is estimated about US $3.5 billion over the next 20 years [10].

1.1 Physico-chemical treatment methods for metal-contaminated wastewater

In order to minimise the impact of these pollutants, it is necessary to design an adequate treatment for metal removal and disposal at their source [11]. Different treatment methods for wastewater laden with metals have been developed in recent years to improve not only the quality of the treated effluent but also the technical applicability and cost-effectiveness of the methods. Various treatments for metal-contaminated wastewater, which have been extensively investigated, include chemical precipitation, coagulation-flocculation, flotation, ion exchange, and membrane filtration. Short descriptions of these methods are presented in the following and summarised from Kurniawan et al. [12], who reviewed about 124 published studies of the respective methods.

Chemical precipitation

This method is widely used for metal removal from inorganic effluent. After pH adjustment to basic conditions (around pH 11), the dissolved metal ions are converted to an insoluble solid phase. Typically, the metal precipitated from the solution is in the form of hydroxide. The conceptual mechanism of metal removal by chemical precipitation is presented in Equation 1.1,

$$\mathrm{M^{2+}} + 2\,\mathrm{OH^-} \longrightarrow \mathrm{M(OH)_2} \tag{1.1}$$

where M^{2+} and OH^- represent the dissolved metal ions and the precipitant, respectively and $M(OH)_2$ is the insoluble metal hydroxide. Because of its availability in most countries, lime or calcium hydroxide is the most commonly employed precipitant agent. Some advantages of lime precipitation include the simplicity of the process, inexpensive equipment requirement, and convenient and safe operations, making it a popular method for metal removal from contaminated wastewater. In spite of its advantages, chemical precipitation needs a large amount of chemicals to reduce metals to an acceptable level. Other drawbacks are its excessive sludge production, the increasing cost of sludge disposal, slow metal precipitation, poor settling and dewatering properties, and the long term impacts of sludge disposal.

Coagulation-flocculation

Principally, the coagulation process destabilises colloidal particles by adding a coagulant and results in sedimentation. To increase the particle size, coagulation is followed by the flocculation of the unstable particles into bulky flocs. The general approach for this method includes pH adjustment and addition of ferric/aluminium salts as the coagulant to overcome the repulsive forces between particles. Like chemical precipitation, pH 11.0 to 11.5 has been found to be optimum for this process. Compared to chemical precipitation, lime-based coagulation has several advantages such as improved sludge settling and dewatering characteristics and bacterial inactivation capability. However, coagulation-flocculation has limitations such as high operational cost due to chemical consumption and increased sludge volume. Electrocoagulation maybe a better alternative than the conventional coagulation as it can remove the smallest colloidal particles and produce just a small amount of sludge. Nevertheless, this method also creates flocs of metallic hydroxides, which requires further purification, making the recovery of valuable metals uneconomically.

Flotation

Flotation is based on the separation of solids or dispersed liquids from a liquid phase using bubble attachment. Adsorptive particulate is employed to separate the metal impurities by foam formation. The target floated substances are separated from bulk water in a foaming phase. Some advantages of this technique are low cost materials and shorter hydraulic retention time. However, subsequent treatment is required to improve the removal efficiency of metals.

Membrane filtration

Membrane filtration can be used not only to separate suspended solids and organic compounds but also inorganic contaminants such as metal ions. Depending on the size of the particle that can be retained, various types of membrane filtration such as ultrafiltration, nanofiltration, and reverse osmosis can be applied for metal removal. However, membrane filtration in general has two main drawbacks, i.e. high operational cost and its susceptibility to membrane fouling.

Ion exchange

Ion exchange process is based on a reversible interchange of ions between the solid and liquid phase where an insoluble substance (resin) removes ions from an electrolytic solution and releases other ions of similar charge in a chemically equivalent amount without any structural change of the resin. Unlike chemical precipitation, ion exchange does not present any sludge disposal problems, thus lowering the operational costs for the disposal of the residual metal sludge. However, ion exchange has some limitations in its application for wastewater laden with toxic metals. Appropriate pre-treatment systems for secondary effluent such as the removal of suspended solid from wastewater are required and only wastewater containing low concentration of metal ions can be treated. In addition, not all ion exchange resin is suitable for all metals and the capital and operational cost is high.

Based on the above description, it can be deduced that no individual treatment is universally effective and applicable for toxic metal removal. As their benefits often are outweighed by a number of drawbacks, a search for alternatives to the above described methods has been an area of interest for scientists.

An alternative method for the removal of toxic metals from aqueous solution, termed ferrite process, was introduced in the late 1970's in Japan for the treatment of laboratory wastewater [13, 14]. This method is based on the fact that several non-iron metals can substitute iron atoms in the structure of magnetite (Fe_3O_4) during its precipitation at temperature above 65 °C, forming "substituted magnetite" or also known as ferrite ($Me_xFe_{3\text{-}x}O_4$, Me is a non-iron metal). Compared to the conventional chemical precipitation, ferrite process has several advantages, i.e. (a) simultaneous treatment of several metal ions is possible; (b) ferrite precipitates are chemically stable; (c) solid and liquid separation can be easily conducted by magnetic separation; (d) ferrite precipitates can be reused in numerous applications [15]. Although this process can be used extensively, its application is limited by its high cost associated with heating requirement.

As an attempt to extend the application of ferrite process on a larger scale, modifications of the process allowing its operation at ambient temperature, termed ambient temperature ferrite process (ATFP), have been suggested [9, 16–18]. However, the research in this area has only been scantily performed considering the number of operational parameters affecting the process and different types and/or combination of metals contained in the wastewater. A comprehensive understanding of the process is required for its optimisation and eventually for its application in the treatment of industrial wastewater.

1.2 Aim and outline of the thesis

The main aim of this thesis is to further develop the ferrite process as a viable alternative to the conventional techniques for the treatment of metal-containing wastewater. The fundamental questions addressed in this work are as follows:

- What are the differences between ATFP and ferrite process at elevated temperature (60–100 °C) in terms of process mechanism and product characteristics?
- What are the optimum operational conditions for ferrite synthesis at ambient temperature considering the extent of non-iron metal incorporation and chemical stability of the product?
- How is the feasibility of ATFP for the treatment of galvanic wastewater?

Accordingly, this work is organised into eight chapters, whose contents are described as follows.

Chapter 2 presents a general overview of the metal ion chemistry in the aqueous and the solid phase. This includes the behaviour of water and metal ion in aqueous solution and the precipitation and dissolution processes of solids. Getting more specific, different aspects of crystal ferrite such as crystal structure, properties, lattice energy are presented. A short introduction about the ferrite synthesis is also given followed by a review about the ferrite dissolution.

Chapter 3 describes the experimental procedures and setups employed in this study. Different analysis techniques to characterise the produced ferrites are also explained.

Chapter 4 examines the magnetite formation at ambient temperature, which is considered as the fundamental process for the ATFP. The literature relevant to this subject are firstly reviewed. The effects of different operational parameters on the formation of magnetite at ambient temperature are then discussed.

Chapter 5 focuses on the incorporation of non-iron metals into the ferrite structure at elevated temperature. The establishment of the maximal attainable incorporation extent of different non-iron metals is presented. The mechanisms affecting the incorporation of non-iron metal into the ferrite structure are discussed. The effects of metal incorporation on the ferrite stability are also assessed.

Chapter 6 discusses the incorporation of non-iron metals into the ferrite structure at ambient temperature. Two methods of seed-promoted ATFP are compared. The results obtained at ambient temperature are then compared to those found at elevated temperature in order to determine the differences between these two processes. Simultaneous incorporation of several non-iron metals into the ferrite structure using the ATFP at different conditions is discussed as well.

Chapter 7 presents the application of the ATFP for treating galvanic wastewater. The feasibility of the ATFP is evaluated and some options to improve the process performance are given. Comparison of the overall cost of different treatment methods for wastewater laden toxic metal is also presented.

Chapter 8 summarises the main conclusions of this work and provides the outlook for further works.

Chapter 2

General Overview

Ferrite materials have been receiving a growing interest for both technological and theoretical reasons. The formation and/or transformation of this crystalline and magnetic solid phase from soluble phase involve various stages making this indeed a complicated process. The fundamental principles of the metal ion chemistry in aqueous medium, which provide a basic concept for these transformation processes, are first presented. A better insight into the mechanisms of the individual steps in the formation of the solid phase would be a great help in explaining the transformation of ferrite precipitates. Valuable reviews are available on the principles of precipitation and crystal growth [19, 20]. Only the important and relevant steps of the precipitation process of metal ion are described in this chapter in order to illustrate the complex mechanisms of solid precipitation from the aqueous phase. Dissolution process can be considered as the reverse of precipitation, although the phenomena involved in these two processes are not exactly the same [21]. The crystal structure and different properties of ferrite are also illustrated in this chapter. In the last section, the methods for the preparation of ferrites are shortly introduced, followed by a literature review regarding the dissolution of ferrite in an acidic solution.

2.1 Water and metal ions in aqueous solution

2.1.1 Properties of water

Water is non-toxic, the most abundant and cheapest solvent. It has unique properties, which stem from its electronic structure, i.e. high polarity ($\mu = 1.84$ debye) and high dielectric constant ($\varepsilon = 78.5$ at $25\,^{\circ}\mathrm{C}$) [22]. The high polarity of water molecule, which explains its good solvation power, is due to the electronegativity difference between oxygen and hydrogen. Oxygen has a much higher affinity for electrons than hydrogen, resulting in a highly polarised bond between O and H. In fact, the oxygen atoms in water are partially negatively charged, and the hydrogen atoms are partially positively charged. As a result, both atoms have the ability to form weak chemical bonds in water, called hydrogen bonds, with more than two hydrogen atoms. The high dielectric constant makes water a dissociating medium because the decrease in the attractive force between pairs of solvated anions and cations allows their easy solubilisation in water [23]. Water has also a Lewis base (electron donor) character, which explains its ionising properties and its aptitude to coordinate Lewis acids (complexing properties) such as metal ions.

2.1.2 Hydration of ions

Given that water is a very polar molecule, there are strong favourable interactions between the metal ion and solvent water. Once dissolved, the metal ion becomes hydrated. The number of water molecules involved in the hydration of a metal ion increases with its polarising strength, i.e. as the metal ion charge z increases and its radius r decreases. The attraction and organisation of water molecules around cation can be distinguished in four solvent regions [24]:

1. A primary hydration sphere in which the water molecules are chemically bound to the ion. Small size and high charge cations develop stronger electrostatic interactions with water and have strong hydration energy. All divalent and trivalent ions from the first transitions series are hexacoordinated in an octahedral symmetry, i.e. $[M(OH_2)_6]^{2+}$ (M = Zn, Ni, Co, Cd, etc) and $[M(OH_2)_6]^{3+}$ (M = Fe, Al, Cr, etc), respectively. This chemical symbolism is in fact the more reasonable representation for the hydrated metal ion, which is frequently abbreviated as M^{2+} and M^{3+} for divalent and trivalent ions, respectively.
2. A secondary hydration sphere in which the water molecules are ordered by the electrostatic influence of the ion. As the primary hydration sphere, the volume of this sphere depends on the nature of the cation (charge of the ion and its size).
3. A transition region separating the hydrated metal ion from the bulk solution. In this region, the water molecules are less ordered than either the solvation shell or the bulk solution.
4. The bulk solvent where the presence of metal ion can be ignored.

The primary and secondary spheres have an intimate role to play in water ligand exchange dynamics.

2.1.3 Water exchange on metal ions

A variety of other molecules can replace the water molecules in the hydration spheres. All such molecules that bind metals are called ligands, and the entire cluster is called a metal-ligand complex or simply a complex. Every complexation reaction in water is basically a ligand exchange reaction, which is partly dependent on the rate at which water leaves and enters the hydration sphere of the ion because in order to form an inner-sphere complex, at least one of the water molecules coordinated to the metal ion have to be dissociated or displaced [24, 25], as described in Equation 2.1 [26]. The replacement of a water molecule from the first hydration shell is an important step not only in complex formation reaction but also in many redox processes [26, 27]. It is also a critical reaction of cation adsorption [25] and of crystal growth [19].

$$[\mathrm{M(H_2O)_n}]^{z+} + \mathrm{nH_2O^*} \longleftrightarrow [\mathrm{M(H_2O^*)_n}]^{z+} + \mathrm{nH_2O} \tag{2.1}$$

The water exchange rate, also termed the water loss rate and denoted k_{-w}, is characteristic of the metal ion. Rates of water exchange at metal ions vary enormously with the nature of the cation. The range of k_{-w} values is from almost 10^9 sec^{-1} for Cu^{2+} right down to less than 10^{-7} sec^{-1} for Rh^{3+} (Table 2.1). Cation charge and size are important in determining rates of water exchange of metal cations, but another factor is also operative, one of comparable importance particularly for transition metals. This additional factor is crystal field stabilisation energy (CFSE). The particular inertness of some metals such as Cr^{3+}, Rh^{3+}, and Ni^{2+} relative to other metals has been ascribed to unfavourable changes in the CFSE during complex formation [24]. The CFSE is related to the electronic configurations of metals and electronic interactions in metal complexes.

Table 2.1: Rate constant of water exchange [24].

Metal	k_{-w}	Metal	k_{-w}
Pb^{2+}	7×10^9	Co^{2+}	2×10^6
Hg^{2+}	2×10^9	Mg^{2+}	3×10^5
Cu^{2+}	1×10^9	Ni^{2+}	3×10^4
Ca^{2+}	6×10^8	Fe^{3+}	2×10^2
Cd^{2+}	3×10^8	Ga^{3+}	8×10^2
Zn^{2+}	7×10^7	Al^{3+}	1
Mn^{2+}	3×10^7	Cr^{3+}	5×10^{-7}
Fe^{2+}	4×10^6	Rh^{3+}	3×10^{-8}

The electronic configuration of metallic elements, i.e. the occupancy of their electron orbitals (designated as s, p, d, f orbitals) determines their chemical and physical properties. In the context of this thesis, the main concerns are the d orbitals. There are five available d orbitals, each with a different orientation in space. The first set consists of the d_{xy}, d_{yz}, and d_{xz} orbitals which have four lobes each directed between the coordinate axes of the nucleus. The second set consists of the d_{x^2} and $d_{x^2-y^2}$ orbitals which have their lobes (where electron density is a maximum) directed along the axes [28]. In an isolated atom, these five orbitals are equal in energy. In the presence of ligand, the atomic orbitals of the metal, specifically the d orbitals, are perturbed by the electrostatic effect of the ligand. This specific influence of the ligands on transition metal is modelled by the crystal field theory. In the crystal field model, the bonding between metal ion and donor atoms is considered to be largely electrostatic. The energy of the metal ion plus coordinated ligands is lower than that of the separated metal ion plus ligands because of the electrostatic attraction. At the same time, the repulsive interaction between the metal electrons and the electrons of the ligands give rise to the splitting of the metal d orbital energies [29]. The magnitude of the energy difference between t_{2g} (d_{xy}, d_{yz}, d_{xz}) and e_g (d_{x^2} and $d_{x^2-y^2}$) sets of orbitals is referred as the crystal field stabilisation energy (labelled as Δ). For octahedral complexes, the energy of e_g is increased and the energy of t_{2g} is decreased. Strong field ligands produce a large energy gap (Δ) and favour the low spin configuration (two of the four electrons in the t_{2g} orbitals must have opposite spin). In contrast, weak field ligands produce only a small Δ and favour the high spin configuration (four electrons of the t_{2g} orbitals have the same spin). The electronic configurations with the large CFSE energies are d^3, d^6 (low spin), and d^8. Water exchange rates, which are relatively very slow, have been established for cations with such configurations, e.g. Cr^{3+} (d^3) and Ni^{2+} (d^8) [27]. However, these rates can be significantly accelerated by metal hydrolysis [24].

2.1.4 Hydrolysis of metal ions

Hydrolysis literally means 'breakdown by water' [30]. In the context of aqueous metal ions, hydrolysis occurs when the acidity of the protons on water molecules reaches a level when a free water molecule itself can effectively remove a proton forming a hydroxyl metal species and $\mathrm{H_3O^+}$ (or shortly written as $\mathrm{H^+}$). The following equations are normally used to express the various equilibriums involved.

$$\mathrm{M^{n+} + H_2O \longleftrightarrow MeOH^{n-1} + H^+} \qquad {}^*K_i \tag{2.2}$$

$$\mathrm{M^{n+} + OH^- \longleftrightarrow MeOH^{n-1}} \qquad K_i \tag{2.3}$$

$$\mathrm{H_2O \longleftrightarrow H^+ + OH^-} \qquad K_w \tag{2.4}$$

As inferred from the above equations, K_i and ${}^*K_i$ are related by the ionic product of water, K_w ($= {}^*K_i/K_i$) which is $\approx 10^{-14}$.

One can also view the hydrolysis reaction as a complex formation reaction because the net effect of the above reaction (Equation 2.2) is the replacement of a water molecule by a hydroxide ion as one of the ligands in the inner hydration sphere. Hence, in a more general form, the equilibrium constants, K_i and ${}^*K_i$ are the stability constants for the formation of hydroxide complexes. When different protonated forms of a metal-ligand complex exist in equilibrium, another equilibrium constant, called overall stability constant, β_n is relevant. In Table 2.2 the notations commonly used for the equilibrium constants of different formation or dissociation reactions are presented. Some relevant values of the stability constant for hydroxide complexes are given in Table 2.3.

Table 2.2: Formulation of stability constant [24].

Addition of ligand

$$\mathrm{M} \xrightarrow[K_1]{\mathrm{L}} \mathrm{ML} \xrightarrow[K_2]{\mathrm{L}} \mathrm{ML}_2 \ldots\ldots \xrightarrow[K_i]{\mathrm{L}} \mathrm{ML}_i \ldots\ldots \xrightarrow[K_n]{\mathrm{L}} \mathrm{ML}_n$$

$$\text{———} \ \beta_2 \longrightarrow$$

$$\text{———} \ \beta_i \xrightarrow{\hspace{6em}}$$

$$\text{———} \ \beta_n \xrightarrow{\hspace{12em}}$$

$$K_i = \frac{[\mathrm{ML}_i]}{[\mathrm{ML}_{(i-1)}][\mathrm{L}]}$$

$$\beta_i = \frac{[\mathrm{ML}_i]}{[\mathrm{M}][\mathrm{L}]^i}$$

Addition of protonated ligand

$$\mathrm{M} \xrightarrow[{}^*K_1]{\mathrm{HL}} \mathrm{ML} \xrightarrow[{}^*K_2]{\mathrm{HL}} \mathrm{ML}_2 \ldots\ldots \xrightarrow[{}^*K_i]{\mathrm{HL}} \mathrm{ML}_i \ldots\ldots \xrightarrow[{}^*K_n]{\mathrm{HL}} \mathrm{ML}_n$$

$$\text{———} \ {}^*\beta_2 \longrightarrow$$

$$\text{———} \ {}^*\beta_i \xrightarrow{\hspace{6em}}$$

$$\text{———} \ {}^*\beta_n \xrightarrow{\hspace{12em}}$$

$${}^*K_i = \frac{[\mathrm{ML}_i][\mathrm{H}^+]}{[\mathrm{ML}_{(i-1)}][\mathrm{HL}]}$$

$${}^*\beta_i = \frac{[\mathrm{ML}_i][\mathrm{H}^+]}{[\mathrm{M}][\mathrm{HL}]^i}$$

Table 2.3: Stability constant for complexation of metals by OH^- [31].

Metal	i	log K_i	log ${}^*K_i$	Metal	i	log K_i	log ${}^*K_i$
Al^{3+}	1	9.01	−4.99	Fe^{2+}	1	4.50	−9.50
	2	8.89	−5.11		2	2.93	−11.07
	3	8.10	−5.90		3	3.57	−10.43
	4	7.00	−7.00				

Continued on next page . . .

Metal	i	log K_i	log $^*K_i$	Metal	i	log K_i	log $^*K_i$
Cd^{2+}	1	3.92	−10.08	Fe^{3+}	1	11.81	−2.19
	2	3.73	−10.27		2	10.52	−3.48
	3	1.05	−12.95		3	6.07	−7.93
	4	−0.05	−14.05		4	6.00	−8.00
Co^{2+}	1	4.80	−9.20	Ni^{2+}	1	4.14	−9.86
	2	4.90	−9.10		2	4.86	−9.14
	3	1.10	−12.90		3	3.00	−11.00
Cr^{3+}	1	10.00	−4.00	Zn^{3+}	1	5.04	−8.96
	2	8.38	−5.62		2	6.06	−7.94
	3	6.87	−7.13		3	2.50	−11.50
	4	2.98	−11.02		4	1.20	−12.80

2.1.5 Metal speciation

The stability constants of metal-ligand complexes explained previously are critical in determining the distribution of various distinct chemical species in solution including uncomplexed and complexed forms (i.e. chemical speciation). An approach to visualise species concentration at equilibrium is by using a log concentration–pH (log C–pH) diagram showing at one glance how a complicated equilibrium is shifted on varying pH, which species predominate and which are negligible. For systems with many species, computer methods can be used to set up and solve chemical equilibrium systems quickly. A number of software packages have been developed for this purpose.

In a system containing total Zn concentration (TOTZn) of 10^{-4} M, the following equilibrium reactions are relevant.

$$\mathrm{Zn^{2+} + OH^- \longleftrightarrow ZnOH^+} \qquad \log\ {}^*K_1 = -8.96 \tag{2.5}$$

$$\mathrm{ZnOH^+ + OH^- \longleftrightarrow Zn(OH)_2^0} \qquad \log\ {}^*K_2 = -7.94 \tag{2.6}$$

$$\mathrm{Zn(OH)_2^0 + OH^- \longleftrightarrow Zn(OH)_3^-} \qquad \log\ {}^*K_3 = -11.50 \tag{2.7}$$

$$\mathrm{Zn(OH)_3^- + OH^- \longleftrightarrow Zn(OH)_4^{2-}} \qquad \log\ {}^*K_4 = -12.80 \tag{2.8}$$

The fraction of the total dissolved metal that is present as a given species is designated by α. Thus, in the Zn system, $\alpha_{Zn^{2+}}$ is defined according to Equation 2.9.

$$\alpha_{Zn^{2+}} = \frac{[Zn^{2+}]}{TOTZn} \tag{2.9}$$

Assuming that the solutes behave ideally (each species concentration equals its activity), the total dissolved Zn concentration can be written in terms of the concentration of free Zn^{2+}, the stability constants for formation of the complexes, and the hydroxide ion concentration, as follows:

$$TOTZn = [Zn^{2+}] + [ZnOH^{+}] + [Zn(OH)_2^0] + [Zn(OH)_3^-] + [Zn(OH)_4^{2-}] \tag{2.10}$$

$$\begin{aligned} &= [Zn^{2+}]\Bigg[1 + \frac{[ZnOH^{+}]}{[Zn^{2+}]} + \frac{[Zn(OH)_2^0]}{[Zn^{2+}]} \\ &\quad + \frac{[Zn(OH)_3^-]}{[Zn^{2+}]} + \frac{[Zn(OH)_4^{2-}]}{[Zn^{2+}]}\Bigg] \end{aligned} \tag{2.11}$$

$$= [Zn^{2+}](1 + K_1[OH^-]^1 + \beta_2[OH^-]^2 + \beta_3[OH^-]^3 + \beta_4[OH^-]^4) \tag{2.12}$$

$$= [Zn^{2+}]\left(1 + \sum_{i=1}^{4} \beta_i (OH^-)^i\right) = [Zn^{2+}]\left(1 + \sum_{i=1}^{4} \frac{{}^*\beta_i}{(H^+)^i}\right) \tag{2.13}$$

Based on Equation 2.13 the concentration of free Zn^{2+} can be calculated. The concentration of other Zn species is obtained using the similar derivation. The log C–pH diagrams prepared by ChemEQL software for Zn(II) speciation are presented in Figure 2.1.

2.2 Precipitation and dissolution processes

Precipitation and dissolution processes form a dynamic equilibrium. Whenever a supersaturated solution forms, the equilibrium will sooner or later be achieved by precipitation of solid. Whenever an unsaturated solution is present in contact with a solid, the equilibrium will be reached by dissolution of all or part of the solid. As equilibrium reactions, two parameters considered during precipitation and dissolution processes are a static one, the solubility, and a kinetic one, the reaction rates [32].

2.2.1 Solubility of solids

The solubility of a solid is determined by the free energy of dissolution, i.e. the difference between the lattice energy of the solid and the hydration energy of its ions. When the lattice energy is much greater than the hydration energy, the solubility of the solid is low [28]. The extent to which a sparingly soluble solid dissolves is expressed by the solubility product. This describes the equilibrium established between the solid and the concentration of its ions in a saturated solution. Consider, for example, the dissolution of a metal hydroxide solid:

$$\mathrm{M(OH)_n(s) \longleftrightarrow M^{n+} + nOH^-} \tag{2.14}$$

Assigning a value of 1.0 to the activity of the solid, the equilibrium constant for the

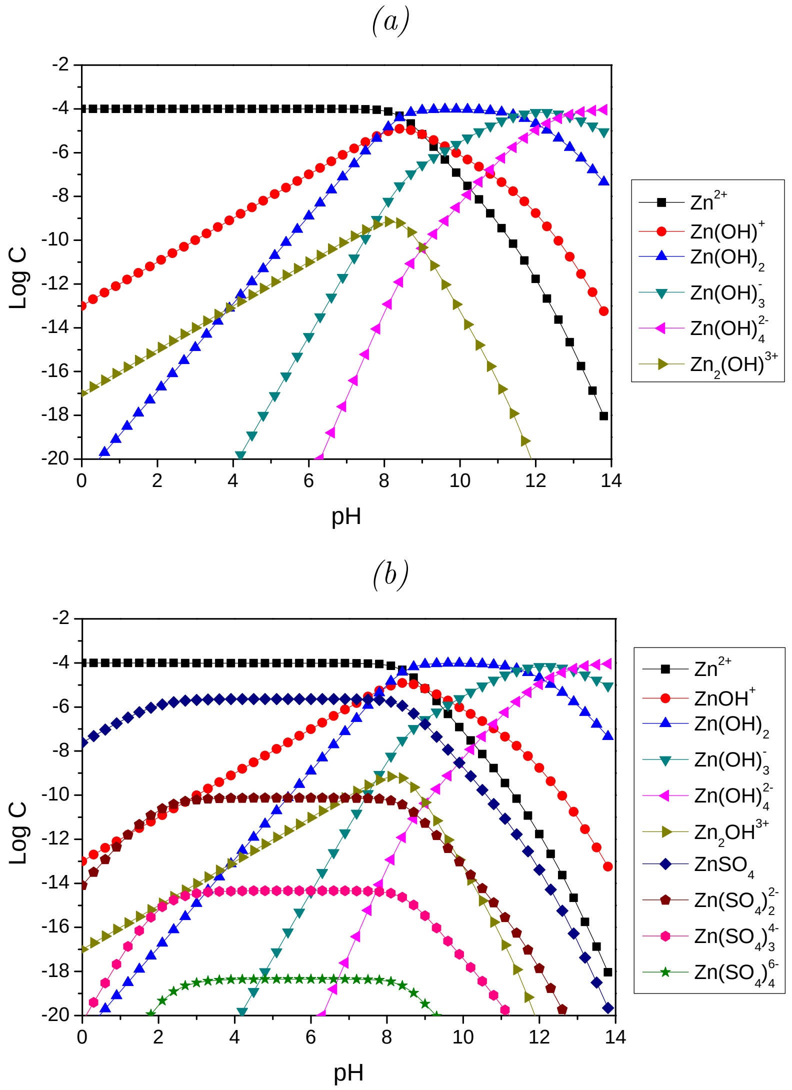

Figure 2.1: Zn(II) speciation without solid precipitation at 25°C in a system with 10^{-4} M TOTZn: (a) Log C–pH diagram with hydroxide and (b) Log C–pH diagram with hydroxide and sulphate.

above reaction is as follows:

$$K_{sp} = \frac{\{M^{n+}\}\{OH^-\}^n}{\{M(OH)_n\}(s)} = \{M^{n+}\}\{OH^-\}^n \tag{2.15}$$

The solubility product K_{sp} is the constant that applies if the system is at equilibrium, whereas Q_{sp} equals the product $\{M^{n+}\}\{OH^-\}^n$ under any conditions (equilibrium or non-equilibrium). The constant Q_{sp} is often represented as ion activity product. Solutions in which $Q_{sp}<K_{sp}$ are undersaturated with respect to the solid; in such solutions, if the solid is present, it will dissolve as the system equilibrates and if no solid is present none will form. Correspondingly, solutions in which $Q_{sp}>K_{sp}$ are supersaturated with respect to the solid, and in such solutions the solid will tend to precipitate.

As with other equilibria that involve H^+ or OH^- ions and are therefore sensitive to pH, a great deal of information about the solubility of $M(OH)_n(s)$ solids can be displayed on log C–pH diagrams. The derivation of equations for such diagram is subjected to the criterion that all the equations are consistent with the equilibrium expression for solubility [31]. For a system in equilibrium with solid $Zn(OH)_2(s)$, Equation 2.16 indicates the total dissolved Zn concentration that must be present at any given pH and that contains hydroxide ions as the only complex-forming ligands.

$$TOT\text{Zn}_{\text{diss}} = \frac{K_{sp}}{\{OH^-\}^2}\left(1+\sum_{i=1}^{4}\beta_i\{OH^-\}^i\right) = {}^*K_{sp}\{H^+\}^2\left(1+\sum_{i=1}^{4}\frac{{}^*\beta_i}{\{H^+\}^i}\right) \qquad (2.16)$$

The log C–pH diagram for such system prepared by ChemEQL software is shown in Figure 2.2. Because the concentration of $Zn(OH)_3^-$ and $Zn(OH)_4^{2-}$ increases with pH, the curve representing $TOT\text{Zn}_{\text{diss}}$ is bowl-shaped and at pH 8.5–11 the total solubility of $Zn(OH)_2$ passes through a minimum. Such a minimum is a common feature of the solubility diagram for many metals including Fe^{2+} and Fe^{3+} (Figure 2.3) and is very useful to describe the range of pH where metal ions can be removed effectively from the solution by chemical precipitation.

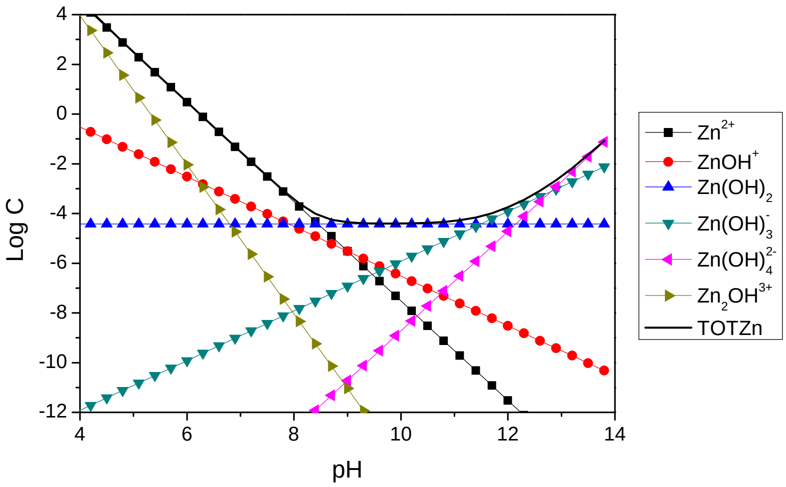

Figure 2.2: Log C–pH diagram of Zn(II) species in equilibrium with $Zn(OH)_2(s)$.

2.2.2 Precipitation process

Precipitation of cation is often considered a simple phenomenon because it is so common. However, the transition of the ion in solution to the solid comprises complex phenomena from chemical and structural standpoints because it involves a set of chemical processes. The experimental conditions such as concentration, acidity, temperature, nature of cations and anions, etc, also have a strong influence on the chemical, structural, and morphological

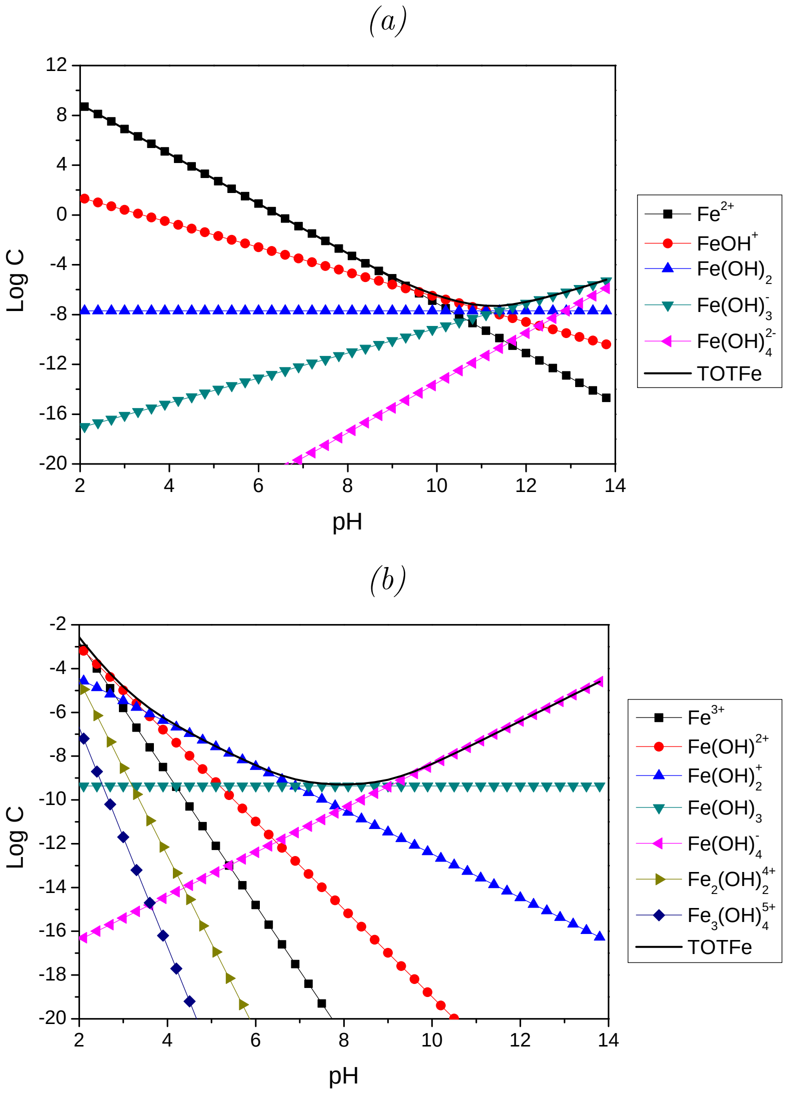

Figure 2.3: Log C–pH diagram of Fe(II) species in equilibrium with (a) $Fe(OH)_2(s)$ and Fe(III) species with (b) $Fe(OH)_3(s)$.

characteristics of the resulting solid [22]. Precipitation process can result either in the formation of solid with a less/non defined structure (amorphous solid) or solid with a rigid arrangement of internal structure (i.e. crystal). In the latter case, the precipitation process is considered as crystallisation process.

The formation of solids includes some basic steps, i.e. formation of precursors, creation of nuclei, growth of nuclei, and ageing of the particles. These steps are described below and summarised from Jolivet et al. [22], unless otherwise stated.

Formation of zero-charge precursors

The formation of solid requires the presence of zero-charge complexes as precursors such as $[M(OH)_z(OH_2)_{N-z}]^0$ (z and N are the cation charge and coordination number, respectively). Hydroxylation of the metal cation obtained through an acid-base reaction or an oxidation-reduction reaction leads to the formation of such a complex. The speed of this reaction is very variable depending on, for example, whether the reaction starting from cationic or anionic complexes, thermohydrolysis (by heating the solution) or by themal decomposition of the base.

Nucleation

Nuclei are created through condensation of zero-charge precursors. Condensation involves a substitution mechanism induced by the nucleophilic character of the hydroxo ligand in the precursor via two basic mechanisms depending on the nature of the coordination sphere of the cation [33, 34]. With aquohydroxo complexes, condensation proceeds by elimination of water molecules and formation of hydroxo bridges (olation mechanism) described in Equation 2.17.

$$\mathrm{M{-}OH} + \mathrm{M{-}OH_2} \longrightarrow \mathrm{M{-}OH{-}M} + \mathrm{H_2O} \tag{2.17}$$

With hydroxo or oxohydroxo complexes in which the coordination spheres do not include water molecules, there is no leaving group and condensation may proceed via a two step mechanism allowing formation of a water molecule as a leaving group and leading to an oxo bridge (oxolation mechanim) (Equation 2.18).

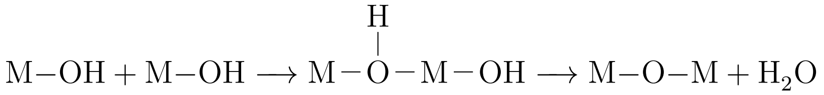

$$\mathrm{M{-}OH} + \mathrm{M{-}OH} \longrightarrow \mathrm{M{-}\overset{\displaystyle H}{\overset{|}{O}}{-}M{-}OH} \longrightarrow \mathrm{M{-}O{-}M} + \mathrm{H_2O} \tag{2.18}$$

The condensation rate is a function of the precursor concentration and the rate is almost zero at the onset of cation hydroxylation. Beyond a critical concentration C_{min}, the condensation rate increases abruptly and polynuclear entities, the nuclei, are formed in an explosive manner throughout the solution. If the rate of precursor generation is much smaller than the condensation rate, nucleation sharply reduces the precursor concentration and the condensation rate decreases equally. When the precursor condensation is again close to C_{min}, formation of new nuclei is no longer possible.

Homogenous nucleation arises mainly in pure solutions when the supersaturation is rather high [35]. In the homogenous nucleation, the chemical nature of the condensed and the remaining non-condensed one being chemically identical, with only new bonds being formed and boundary surfaces being created [19]. The formation of nuclei requires passage through a maximum activation energy barrier (ΔG^*). The value of ΔG^* for spherical nuclei is

$$\Delta G^* = \frac{16\pi\gamma^3\nu^2}{3(kT\ln S)^2} \tag{2.19}$$

where γ is the interfacial energy between nucleus and solution, ν is molecular volume of the precursor, k is the Boltzmann constant, T is the temperature, and S is the supersaturation ratio of the solution. The latter term is defined as the ratio of the precursor concentration in the solution and the solubility of the solid phase. Equation 2.19 shows that the activation energy barrier of nucleation process decreases with increasing saturation ratio and temperature, and with decreasing interfacial energy.

A small solid cluster whose free energy formation equals ΔG^* is known as a critical nucleus [20]. The radius of the critical nucleus is given in Equation 2.20 [22].

$$r^* = \frac{2\gamma\nu}{kT\ln S} \tag{2.20}$$

The critical size r^* represents the minimum size of a stable nucleus. It is smaller for higher supersaturation and smaller surface tension. The critical nuclei are in metastable equilibrium with the solution. Thus, a small change in their size leads to either dissolution or growth because only in this way the particles can achieve a reduction in their free energy. Indeed, the probability of growth of nuclei is higher than that of dissolution and precipitation is spontaneous.

Nucleation can be sharply accelerated in the presence of crystal solid in the precipitation medium. This is a typical catalytic effect due to a decrease in the activation energy barrier. When the surface of the foreign solid is compatible with that of the precipitating solid surface because of the presence of adsorption sites or structural similarities, the solid-solid surface tension γ' is smaller than the solid-solution tension γ. Nucleation on the surface of foreign solid occurs more easily. In this case the nucleation is termed heterogeneous and it is used in the seeding process, in which crystals of the desired solid are placed in the solution. The small energy barrier allows nucleation to occur at low supersaturation level.

From a kinetic standpoint, the nucleation rate J represents the number of nuclei formed per unit time and unit volume. Schematically, J maybe written as

$$J = J_0 \exp\left(\frac{-\Delta G_N}{kT}\right) \tag{2.21}$$

where J_0 is the frequency of collisions between precursor molecules and ΔG_N is total nucleation activation energy, which includes two major contributions [22]. The first is the activation energy barrier ΔG^* (Equation 2.19) and the second component is ΔG^R, which is related to the type of chemical reaction (olation and/or oxolation) involved in the process. Taking into account these two components, the nucleation rate may be written as

$$J = J_0' \exp\left[\frac{16\pi\gamma^3\nu^2}{3(kT)^3(\ln S)^2}\right] \tag{2.22}$$

with $J_0' = J_0 \exp(-\Delta G^R/kT)$.

Equation 2.21 suggests that a critical parameter determining the nucleation rate of solid is its interfacial energy with respect to solution. Amorphous and poorly crystalline solids are characterised by low interfacial energies and thus will nucleate easily once the solution composition exceeds their solubility. Conversely, high crystalline solids having relatively large interfacial energies nucleate slowly, even in the presence of favourable substrates. In general, it can be concluded that substances with low interfacial energies tend to be less crystalline and have higher solubilities than their more stable analogues [20].

Growth

The unstable nature of critical-size nuclei formed during the nucleation stage leads to their growth through incorporation of the precursor molecules which continue to be generated after nucleation. The average size of the final particles depends on the number of nuclei and the amount of matter available during the synthesis. The widely accepted classification of growth mechanisms is set forth according to the rate determining mechanisms [19]: (1) diffusion or transport followed by adsorption at the crystal face (a linear function of the supersaturation degree), (2) surface reaction (a parabolic function), (3) surface nucleation (an exponential function). Crystal growth theories are mostly presented from the viewpoint of physical phenomena. The molecular processes and chemical changes are hardly in the focus of attention. On entering into a crystal structure the ions release some, or all, of their hydration water, which is quantitatively expressed in terms of dehydration frequency (previously described as water exchange rate). Mathematical expressions of the growth rate as a function of the dehydration frequency are given in the text of Sarig [19]. Detailed discussions regarding the crystal growth mechanisms can be found in the literature [36–38].

For many industrial applications, monodispersed particles (i.e. particles uniform in size, shape, and composition) are highly desirable. Such particles can be obtained by preventing as far as possible simultaneous occurrence of the nucleation and growth steps. In this case, the precursor concentration (supersaturation level) must be maintained closed to C_{min} to ensure that the nucleation rate is much greater than the rate at which the precursor generated. If the precursor concentration remains higher than C_{min} throughout the reaction the nucleation rate is not high enough compared with the precursor generation rate, hence nucleation and growth occurs simultaneously. Other conditions leading to the formation of monodispersed particles are extensively discussed by Sugimoto [39].

Aging

The particles formed in the nucleation and growth steps are not necessarily thermodynamically stable. Aging of the suspensions, which may take place over large time scale (hours, days or months), allows the system to tend towards or reach stability. This is the reason for the modifications of some physical or chemical characteristics of the particles observed during aging described below.

(a) Change in crystallinity

When a solid can exist as both a crystalline and a poorly ordered (or amorphous) phase, according to Stranski rule (also called Ostwald's step rule), the less ordered, more soluble (less stable, less supersaturated) phase usually precipitates first because the interfacial energy requirements are less stringent [40]. When growth proceeds, the solute concentration decreases until it reaches equilibrium with respect to the first phase. At this moment the solution is supersaturated only with respect to the second, less soluble phase. If no crystals of this latter phase form, then the first precipitated phase remains in a metastable state. When the crystals form, the solute concentration decreases once more and the first phase becomes unstable. It dissolves more or less rapidly, the generated solute molecules contribute to the growth of the stable phase [35]. It is often that the growth rate of the more stable phase is governed by the dissolution rate of the less stable phase [40].

(b) Change in morphology

The morphology of particles formed by precipitation is connected to the synthesis conditions. Recrystallisation of a solid in suspension into a more thermodynamically stable phase according to the Stranski rule can also be associated with a change in the shape of the particles.

(c) Increase in particle size

In the condition of positive liquid-solid interfacial tension, true thermodynamic equilibrium is reached when all precipitated matter is gathered in a single particle (surface area of the solid is at minimum). This precipitate will be shaped according to the principle of minimum total surface free energy. The processes prompted by the momentum towards equilibrium are also called ripening. There are two main routes by which a system of many smaller particles can be transformed into a more advanced system of larger particles in smaller number: one by which the smaller particles are dissolved and the larger ones grow (Ostwald ripening), and the other by which the particles combine by coagulation or agglomeration (contact-recrystallisation) [19].

2.2.3 Dissolution process

As noted previously, the driving force for the dissolution process is the extent of undersaturation with respect to the solid phase, as opposed to the supersaturation for the precipitation process. The dissolution process involves six successive elementary steps: (1) mass transport of dissolved reactants from bulk solution to the solid surface, (2) adsorption of solutes, (3) transfer of reacting species, (4) chemical reactions, (5) detachment of reactants from the surface, (6) mass transport into the bulk of the solution [25].

Essentially, two main mechanisms of dissolution process can be distinguished, i.e. transport (diffusion)-controlled and surface-controlled mechanisms [24, 41, 42].

Dissolution mechanisms

The distinction of two dissolution mechanisms is merely based on the rate determining step (the slowest step) of the dissolution process which may be either mass transport (diffusion) of reactants and products in the solid phase, or reactions controlled by a surface process and the related detachment process of reactants.

(a) Transport-controlled dissolution

In the transport-controlled dissolution, the solute concentration near the solid surface varies from the equilibrium value C_e at the surface to the bulk concentration far from the surface C, creating a concentration gradient in a fluid layer adjacent to the solid (diffusion boundary layer). Dissolution is limited by the reactant supply to the solid surface and the rate at which dissolved solution products are transported to the bulk of the solution through the boundary layer. The increase of flow velocities or stirring can result in a faster dissolution process because it reduces the thickness of the boundary layer. The rate equation corresponding to a transport-controlled reaction is known as the parabolic rate law, i.e.

$$r = \frac{dC}{dt} = k_p t^{1/2} \tag{2.23}$$

where k_p is the reaction rate constant [25]. By integration the concentration C increases with the square root of time:

$$C = C_e + 2k_p t^{1/2} \tag{2.24}$$

Many important dissolution reactions are, however, surface-controlled [25, 41].

(b) Surface-controlled dissolution

When the chemical reactions at the surface are slow in comparison with the diffusion processes, the dissolution kinetics are controlled by the chemical surface processes, and thus transport of the reactants from the bulk solution to the surface and of products from the surface into the solution can be neglected [43]. In this case, the concentration of solute adjacent to the surface will be the same as in the bulk solution. The surface-controlled dissolution is considered to occur in a two-step process. The first step involves a rapid, reversible sorption of reactive chemical species such as protons, ligands, or reductants, from solution to the surface sites which polarise, weaken, and tend to break the metal-oxygen bonds in the solid surface. The second step results in the detachment of a metal from the solid surface [24]. Although both of these steps consist of a series of smaller reaction steps, the rate law of surface-controlled dissolution is based on the assumption that the first step is fast and the second step is rate limiting. These are schematically described in Equation 2.25 and 2.26

$$\text{surface sites} + \text{reactants}(\text{H}^+,\text{OH}^-,\text{or ligands}) \xrightarrow{\text{fast}} \text{surface species} \tag{2.25}$$

$$\text{surface species} \xrightarrow[\text{detachment of M}]{\text{slow}} \text{M(aq)} \tag{2.26}$$

where M stands for metal [41]. When the initial surface sites are regenerated completely after the detachment step and provided that the concentrations of the reactants are kept constant, steady state conditions with regard to the surface species are established. This is valid under conditions that are far from dissolution equilibrium so that back reactions can be neglected and constant dissolution rates occur.

Dissolution pathways

Based on the reactants participating in the dissolution process, the dissolution process can be differentiated into several pathways, i.e. proton-promoted, ligand-promoted, and reduction dissolutions.

(a) Proton-promoted dissolution

Many dissolution processes were conducted under low pH. In this dissolution pathway, protons get bound to the surface hydroxyl groups or to the oxide ions closed to the surface of the solid. At this position, the protons polarise the critical bonds between the oxide and metal ions, thus the detachment of the metal ion from the bulk solid is promoted. The adsorption of protons at the surface is significantly faster than the detachment of the metal ion, thus the proton concentration at the surface is in equilibrium with the solution [41]. The similar principle may hold for anion accompanying the proton, i.e. the anion replaces surface OH groups and thereby assists in the release of metal ion. One example is chloride ions, which have a strong dissolution promoting effect. The effect of chloride can be explained as follows; its adsorption lowers the positive surface charge thus facilitates protonation. In addition, the surface metal-chloride complex causes weakening of the bond between metal and neighbouring ions in the bulk oxide.

(b) Ligand-promoted dissolution

As already shown for chloride ions, organic and inorganic ligands can substantially increase the dissolution process [28]. Ligands form inner-sphere complexes by ligand exchange with surface functional groups. These ligands bring negative charge into the coordination sphere of the metal ion at the surface and may labilise the critical metal-oxygen bonds, thus facilitating the detachment of the metal ion from the surface [43]. Ligands which promote dissolution are considered to form mononuclear surface complexes. Other ligands forming binuclear (or even trinuclear) surface complexes can, however, inhibit the dissolution process [28].

(c) Reduction
Reductive dissolution may be more complex than the previous pathways in that it involves electron transfer processes [28]. A plausible mechanism assumes that prior to the detachment step, the reduction of the metal ion and the protonation of the nearest-neighbour oxide or hydroxide ions must take place. After it has been transferred to the solid surface, the electron will move to the metal ion which then becomes the centre of the detachable group. After reduction of the central metal ion, the existing coordination sphere of the metal centre will be labilised and detached from the bulk solid.

Dissolution models

The composition of the solution in which dissolution takes places (e.g. pH, acid concentration, reductants, and complexing agents) influences the dissolution behaviour of the solid. Other factors which can also affect the dissolution rate of solid include the properties of the overall system (e.g. temperature, UV light) and the properties of the solid (e.g. specific surface area, chemical composition of the solid, presence of defects) [28]. By taking one or more factors into account, many dissolution models have been developed to describe the dissolution reaction and its kinetics. Models which consider all of the above factors are not available.

A list of different rate equations applicable to dissolution reactions can be found in [28]. Two equations that are used quite frequently are the cube rate law which takes the geometry of the dissolving particle into account, and the Avrami-Erofejev law which applies to sigmoidal dissolution curves.

The cube rate law, also termed the shrinking core model, is expressed in Equation 2.27,

$$1 - (1 - \alpha)^{1/3} = kt \tag{2.27}$$

where α is the fraction of solid dissolved. A plot of the left side of Equation 2.27 against t should results in a straight line having a slope k (s^{-1}). This rate equation applies to a situation in which the reaction interface moves inwards at a constant rate and implies isotropic dissolution, i.e. that the particle shape is maintained during dissolution process [28]. It can describe a surface-controlled dissolution [44, 45], although a similar rate law has also been found if the rate-limiting step was diffusion [46]. In the latter case, it is not possible from the kinetics alone to determine if k contains a constant rate for a surface reaction or includes diffusion through the boundary layer. The effect of temperature must be measured to distinguish between the two [46].

The Avrami-Erofejev law, i.e.

$$(\ln(1 - \alpha))^{1/2} = kt \tag{2.28}$$

indicates that the reaction is surface rather than diffusion-controlled [45]. Another equation that has been applied to reactions with sigmoidal kinetics is the Kabai equation,

$$1 - \alpha = e^{-(kt)^a} \tag{2.29}$$

where a is a phase-specific constant [47, 48]. A linear form of this equation can be written:

$$\ln \ln(1 - \alpha) = \alpha \ln k + \alpha \ln t \tag{2.30}$$

A plot of the left side of Equation 2.30 against $\ln k$ results in a straight line from which k and a can be calculated. When dissolution of two distinct phases is occurring, this plot commonly exhibit two linear portions that can be allocated to the two phases.

2.3 Structure and lattice energy of ferrites

Ferrites ($Me_xFe_{3\text{-}x}O_4$) are a class of spinel which consist of an interlocking network of positively charged metal ions and negatively charged divalent oxygen ions. The spinel structure is derived from the mineral spinel ($MgAl_2O_4$) whose structure was first determined in 1915 by Bragg and Nishikawa. The group contains more than 200 investigated species [49]. Some of these species are among the most studied substances in solid state science because of their industrial application and wide occurrence in nature. Spinel ferrites have been used for many years in different areas such as magnetic devices, switching devices, recording tapes, permanent magnets, hard disc recording media, flexible recording, read-write heads, active components of ferrofluids, colour imaging, magnetic refrigeration, detoxification of biological fluids, magnetically controlled transport of anti-cancer drugs, magnetic resonance imaging contrast enhancement, magnetic cell separation, etc [50]. They are also the main ores yielding several elements and responsible for most magnetism in rocks. The widespread occurrence of spinels is in part a result of the very large number of cations of different valences that the structure can accommodate [51].

2.3.1 Spinel structure

Spinels having the general formula AB_2X_4 (A and B are cations; X is anion) are made up by a dense cubic packing of 32 anions as the smallest unit of the crystal structure (i.e. unit cell). Each unit cell contains eight formula units, e.g. $Mg_8Al_{16}O_{32}$ for $MgAl_2O_4$ spinel. Oxygen ions are the most common anions found in the spinels, although F, S, Se, Te ions are also observed [52]. Between the anion layers, there are interstices where small interstitial atoms or ions like Fe or other metal ions may be situated. There are two types of interstices, called octahedral and tetrahedral sites. In a tetrahedral site, three anions in one layer and one anion in the layer above surround or co-ordinate an interstice in the shape of a tetrahedron. On the other hand, in an octahedral site , three anions in one layer and three anions in the layer above surround an interstice in the form of an octahedron (see Figure 2.4). In the unit cell of spinel, there are 64 tetrahedral sites and 32 octahedral sites. However, only 8 tetrahedral sites and 16 octahedral sites are occupied by cations [53].

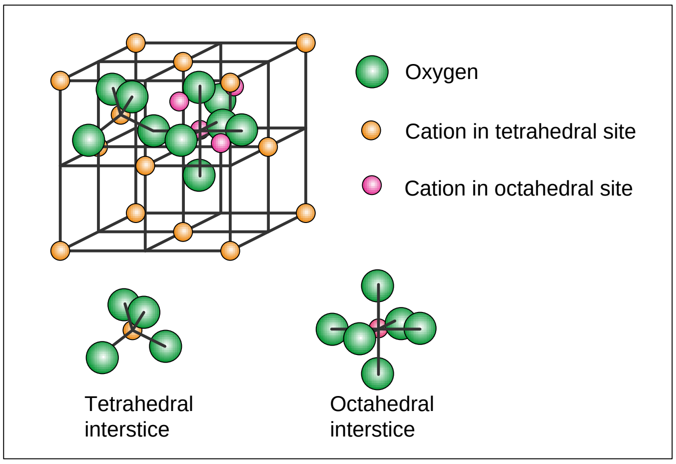

Figure 2.4: Spinel structure. Oxygen ions are shown in only two octants within the unit cell [54].

The structure of spinel is defined by the tetrahedral cation–oxygen (TO) and octahedral cation–oxygen (MO) distances, which are related to the lattice parameter a (i.e. unit cell size) and the anion parameter u by the following equations:

$$a = \frac{8}{11\sqrt{3}}\left[5(TO) + \sqrt{33(MO)^2 - 8(TO)^2}\right] \tag{2.31}$$

$$u = \frac{0.75R^2 - 2 + \sqrt{\frac{33}{16}R^2 - 0.5}}{6(R^2 - 1)} \tag{2.32}$$

where R = (MO)/(TO) [55, 56]. The parameter u reflects the adjustment of the crystal structure to accommodate differences in the cation sizes in the tetrahedral and octahedral sites. When u equals to 0.25, the anions form an exactly cubic close packed array. However, this particular situation is rarely occurred. The u value of most spinels lies in the range of 0.25 to 0.27 [49]. As u increases from its ideal value (0.25), the oxygen ions move away from the nearest tetrahedral cation in a [111] direction, which increases the volume of each tetrahedral-site interstice, while the octahedral site becomes correspondingly smaller. The oxygen framework expands or contract by varying u until the tetrahedral- and octahedral-site volumes match the radii of the constituent cations.

The cations A and B in the spinel must have the formal charges required by the condition for electrical neutrality:

$$Q_A + 2Q_B + 4Q_O = 0 \tag{2.33}$$

where Q_A and Q_B are the charges on the A and B cations, and Q_O that on anions (i.e. -2 for oxide spinels). When $Q_A = 2$ (divalent cation) and $Q_B = 3$ (trivalent cation), it is defined as 2-3 spinel, and it is 4-2 spinel when $Q_A = 4$ (tetravalent cation) and $Q_B = 2$ (divalent cation).

Based on the configuration of cations in the structure, spinel can be designated as normal and inverse spinel. A perfectly normal spinel is one in which the single A cation of the formula unit occupies the tetrahedral site and the two B cations the two equivalent octahedral sites. If the parentheses ( ) and [ ] denote tetrahedral and octahedral sites, respectively, then this distribution can be written $(A)[B_2]O_4$. On the other hand, the arrangement of a perfectly inverse spinel is represented as $(B)[AB]O_4$. In this spinel, A cations occupy octahedral sites, while B cations are equally distributed between the tetrahedral and the octahedral sites. Between these two extreme distributions, an intermediate distribution may be realised. To describe this distribution, it is convenient to define an additional parameter, i.e. the inversion degree x. This parameter is defined as the fraction of B cations occupies the tetrahedral sites [57]. Hence, the formula of the intermediate distribution of spinel (mixed spinel) is $(A_{1\text{-}x}B_x)[A_xB_{2\text{-}x}]O_4$. The value of x tends toward 0 for perfectly normal spinel and toward 1 for inverse spinel. Both values correspond to a low-entropy, completely ordered state. When x is closed to 2/3, a fully disordered state corresponding to maximum entropy and random distribution of cations is achieved [57]. With thermal treatment, the inversion value of normal or inverse spinel tends toward 2/3 [57–59].

Based on different research works, Sickafus et al. [58] summarised four primary factors influencing the inversion parameter in spinel, i.e. (i) temperature, (ii) electrostatic contribution to the lattice energy, (iii) cationic radii, (iv) cationic charge, and (v) crystal field effects. Thermally induced cation disorder has been briefly mentioned before. Effects (ii)–(v) are shortly described below.

The contribution of electrostatic energy is evident upon consideration of the Madelung constant (Section 2.3.3) for different cation arrangement. It was proposed that the most stable arrangement is the structure with a greater electrostatic potential [58, 60]. The 2-3 spinel is often found in the normal arrangement (more stable), while the opposite tendency is observed for the 4-2 spinel.

Cationic radii in the spinel structure will not vary over a very wide range because the spinel structure is stable only if the cations are rather medium sized and the radii of the different ionic species in the same compound do not differ too much [60]. The effect of cationic charge on the cation arrangement is closely related to two previous factors (electrostatic consideration and cationic radii). The stable arrangement of 2-3 and 4-2 spinels explained above can also roughly be explained on the basis of the Verwey-Heilmann principle of maximal charge neutralisation, i.e. cations of high charges occupy interstices with the highest coordination number so they can be neutralised efficiently by numerous anions in the first coordination shell. However, the 2-3 spinels with inverse arrangement defy this principle. From a geometrical point of view, the arrangement based on the electrostatic rule where the comparatively larger divalent cations go into the smallest interstices is not the most favourable one. Hence, Pauling's first rule which is based on the geometric stability of packing of ions of different sizes should also be considered. According to this rule, high valence cation which generally possesses small ionic radius is a better fit for a small interstice (small coordination number) [61]. The propensity of cation arrangement in spinel is, in part, a consequence of the competition between these cross-purposes [58].

Crystal field theory has often been used to understand cation distribution in spinel. The effects of the crystal field in the spinels are summarised as follows [58]. If one of the constituents of a spinel compound is a transition-metal ion, and this ion has a relatively large CFSE, then this ion will compete for octahedral-site occupancy, even at the expense of increased electrostatic energy or other structural factors. Since oxygen ions are weak field ligands, almost all transition metal ions in spinel adopt high spin configurations (see Section 2.1.3). Some transition metal ions such as Mn^{2+}, Fe^{3+}, Zn^{2+}, and Cd^{2+} in their high spin configurations exhibit no CFSE and, thus, have no crystal-field-induced preference for octahedral sites. Among the transition metal ions, the Cr^{3+} and Ni^{2+} ions have the largest CFSEs. Of these ions, the Cr^{3+} ion exhibits the maximum tendency for octahedral-site occupancy. The 2-3 spinel chromite has a normal cation arrangement and may be written as $(Fe^{2+})[Cr^{3+}Cr^{3+}]O_4$. In chromite, the Fe^{2+} ion is relegated to the tetrahedral site, even though it possesses a respectable CFSE. The tendency of chromite forming a normal spinel can also be explained by the Verwey-Heilmann principle. In the 2-3 spinel magnetite, the Fe^{2+} ion successfully occupies the octahedral site, and this spinel is an inverse spinel. In this case, the Fe^{3+} ion, with no CFSE, relinquishes half of the octahedral sites to the Fe^{2+} ion. A similar trend is also observed for nickel ferrite $NiFe_2O_4$ as the Ni^{2+} ion has a high tendency to occupy the octahedral site (due to its large CFSE) [62]. However, in the 2-3 iron aluminate spinel hercynite, the Fe^{2+} ion again concedes the battle for the octahedral site. Hercynite is a normal spinel with a structure given by $(Fe^{2+})[Al^{3+}Al^{3+}]O_4$. Despite possessing no CFSE, the Al^{3+} ion in hercynite shows a remarkable Verwey-Heilmann preference for the octahedral site. The opposite trend is observed for the divalent cations such as Zn^{2+} and Cd^{2+} having no CFSE. These cations have a high preference for occupying the tetrahedral site allowing the Fe^{3+} ion to occupy the octahedral site and leading to the formation of a normal spinel structure.

2.3.2 Cation radii in spinels

The importance of accurate values of cationic radii becomes apparent from the preceding section. One complete compilation of ionic radii was published by Shannon and Prewitt [63] and later revised by Shannon [64]. They derived the radii from approximately 1000 interatomic distances by using the principle of additivity (i.e. $r_c + r_a$, where r_c is the cation radius and r_a is the anion radius). The term 'effective' ionic radius is used to emphasise that these radii are empirical and include effects of covalence in specific metal-oxygen or metal-fluorine bonds. O'Neill and Navrotsky [65] refined Shannon's radii specifically for the spinel structure. Their results together with Shannon's radii are listed in Table 2.4.

Table 2.4: Effective radii of some cations in tetrahedral (Tet) and octahedral (Oct) sites.

Cation	O'Neill and Navrotsky [65]		Shannon [64]	
	Tet (Å)	Oct (Å)	Tet (Å)	Oct (Å)
Al^{3+}	0.39	0.53	0.39	0.535
As^{3+}	-	-	-	0.58
Ba^{2+}	-	-	-	1.35
Be^{2+}	-	-	0.27	0.45
Ca^{2+}	-	-	-	1.00
Cd^{2+}	0.78	-	0.78	0.95
Co^{2+}	0.58	0.72	0.58	0.745
Co^{3+}	0.45	0.53	-	0.545
Cr^{3+}	-	0.615	-	0.615
Cu^{2+}	-	-	0.57	0.73
Fe^{2+}	0.615	0.74	0.63	0.78
Fe^{3+}	0.485	0.645	0.49	0.645
Hg^{2+}	-	-	0.96	1.02
Mg^{2+}	0.585	0.715	0.57	0.72
Mn^{2+}	0.655	0.80	0.66	0.83
Mo^{3+}	-	-	-	0.69
Ni^{2+}	0.565	0.69	0.55	0.69
Pb^{2+}	-	-	0.98	1.19
Pb^{4+}	-	-	0.65	0.775
Sb^{3+}	-	-	0.76	0.76
Sn^{4+}	-	-	0.55	0.69
Zn^{2+}	0.58	0.73	0.60	0.74

2.3.3 Lattice energy

The energy of the lattice is related to the stability of a given ionic structure and directly or indirectly determines some critical properties such as melting temperatures, thermal expansion, stiffness, and others [66]. In the ionically bonded solid, the lattice energy is defined as the energy change that accompanies the process in which the isolated gaseous ions of a compound come together to form 1 mole of the ionic solid [62]. It is the net potential energy of the arrangement of ions that forms the structure [61]. Two principal kinds of forces are involved in the calculation of the lattice energy: (i) the electrostatic forces of attraction and repulsion between ions and (ii) short range repulsive forces which are important when atoms or ions are so close together that their electron clouds begin to overlap.

The calculation of lattice energy in spinel proposed by several authors [51, 65, 67] is largely based on the similar approach as for the ionic solid mentioned above. It composed of a coulombic attractive term and a short range repulsion term, given by Equation 2.34. The term U_E is the electrostatic energy (coulombic term) that accompanies the movement of the constituent ions of the crystal from an infinite separation to their observed positions in the crystal lattice and depends only on the geometry of the lattice. The other term U_R is non-coulombic terms or a repulsion term which is typically about 10–20% of U_E.

$$U_L = U_E + U_R \tag{2.34}$$

The electrostatic energy considered to be the largest component of the lattice energy can be approached as follows:

$$U_E = 1389\,\frac{M}{a} \quad kJmol^{-1} \tag{2.35}$$

where a is the lattice parameter and M is the Madelung constant [65]. The latter term is a simple numerical quantity, which depends upon the geometrical arrangement of the ionic charges and their supposed valence states [68]. It is a function of the charges of each ion and also of the oxygen parameter u, given by following equation:

$$M = \alpha_1 Z_O^2 + \alpha_2 Z_O Z_T + \alpha_3 Z_T^2 + \alpha_4 Z_O Z_{AN} + \alpha_5 Z_{AN}^2 + \alpha_6 Z_T Z_{AN} \tag{2.36}$$

where Z_O, Z_T, and Z_{AN} are the average charges on the octahedral, tetrahedral and anion sites, respectively. The first three coefficients are constant terms evaluated by Thompson and Grimes as follows [68]:

$$\alpha_1 = -0.079 \tag{2.37}$$

$$\alpha_2 = -3.076 \tag{2.38}$$

$$\alpha_3 = 1.0905 \tag{2.39}$$

The remaining terms are functions of the oxygen parameter u and, as proposed by Ottonello [67], are expressed as:

$$u'' = u - 0.25 \tag{2.40}$$

$$\alpha_4 = -21.31269 - 151.17688 \cdot u'' \tag{2.41}$$

$$\alpha_5 = -7.306 - 2230 \cdot u''^2 \tag{2.42}$$

$$\alpha_6 = -19033.6378 \cdot u''^3 - 724.91421 \cdot u''^2 + 132.08668 \cdot u'' - 11.23988 \tag{2.43}$$

The short range repulsion energy estimated based on the Born-Mayer exponential form was proposed by Ottonello [67] according to the following equation:

$$\begin{aligned} U_R &= 4\, N_o c'_{tet} \exp\left(\frac{-\bar{R}_{tet}}{\rho}\right) + 12\, N_o c'_{oct} \exp\left(\frac{-\bar{R}_{oct}}{\rho}\right) \\ &= +4\, N_o exp\left(\frac{-\bar{R}_{tet}}{\rho}\right) \sum_i X_{tet} b_{tet} \exp\left(\frac{r_{tet} + r_{ox}}{\rho}\right) \\ &= +12\, N_o exp\left(\frac{-\bar{R}_{oct}}{\rho}\right) \sum_j X_{oct} b_{oct} \exp\left(\frac{r_{oct} + r_{ox}}{\rho}\right) \end{aligned} \tag{2.44}$$

where:
N_o = Avogradro's number
$c'_{tet} = 2.4004 \cdot 10^{-16}$
$c'_{oct} = 6.4393 \cdot 10^{-17}$
$b_{tet} = 8.4567 \cdot 10^{-18}$
$b_{oct} = -3.7944 \cdot 10^{-18}$
r_{tet}, r_{oct} = tetrahedral and octahedral ionic radii
r_{ox} = oxygen ionic radii
X_{tet} , X_{oct} = ionic fraction in tetrahedral and octahedral sites
$\bar{R}_{tet}$ = average tetrahedral bond length
$\bar{R}_{oct}$ = average octahedral bond length

The average tetrahedral ($\bar{R}_{tet}$) and octahedral ($\bar{R}_{oct}$) bond lenghts in spinels containing A and B cation are approximated by [65]:

$$\bar{R}_{tet} = r_{tet,A}(1 - x) + r_{tet,B}(x) \tag{2.45}$$

$$\bar{R}_{oct} = r_{oct,A}(0.5x) + r_{oct,B}(1 - 0.5)(x) \tag{2.46}$$

where:
$r_{tet,A}$, $r_{tet,B}$ = tetrahedral ionic radii of A and B

$r_{oct,A}$, $r_{oct,B}$ = octahedral ionic radii of A and B

Grimes et al. [54] proposed another method for calculating the lattice energy of spinels based on normalised ion energy. They considered the charge density resulting from the redistribution or delocalisation of charge as a bond forms. However, they used a single average lattice parameter of 8.40 Å and a constant u parameter (0.25) for all studied spinel compounds.

The lattice energy of different metal ferrites are calculated based on the Equation 2.34 to 2.44. The results are presented in Table 2.5 together with the total structure energy calculated by Grimes et al. [54].

The values obtained by these two different approaches are of different magnitude and trends. This result suggests that an accurate estimation of lattice energy in spinel is difficult to acquire. Indeed, O'Neill and Navrotsky [65] stated that the calculated lattice energy considerably overestimates the magnitude the actual energy. Hence, it may only be used to predict the relative stability of cation distribution.

Table 2.5: Lattice energy of ferrite end members.

Spinel	Type[a]	Cation distribution (tet, oct, oct)	M	u_{cal}[b]	a_{cal}[b]	UE_{cal}[b]	U_L	Total structure energy[c]
Fe_3O_4	I	$Fe^{3+}Fe^{2+}Fe^{3+}$	130.9	0.253	8.397	−21647	−17906	−65986
$ZnFe_2O_4$	N	$Zn^{2+}Fe^{3+}Fe^{3+}$	131.9	0.260	8.409	−21795	−18509	−74794
$NiFe_2O_4$	I	$Fe^{3+}Ni^{2+}Fe^{3+}$	130.8	0.254	8.330	−21811	−17983	−68929
$CdFe_2O_4$	N	$Cd^{2+}Fe^{3+}Fe^{3+}$	134.2	0.268	8.691	−21452	−19034	-
$CoFe_2O_4$	I	$Fe^{3+}Co^{2+}Fe^{3+}$	130.8	0.254	8.370	−21713	−17937	−67276
$CuFe_2O_4$	I	$Fe^{3+}Cu^{2+}Fe^{3+}$	130.9	0.253	8.384	−21680	−17921	−71286
$FeCr_2O_4$	N	$Fe^{2+}Cr^{3+}Cr^{3+}$	132.7	0.262	8.392	−21961	−18746	−61581
$CrFe_2O_4$	I	$Fe^{3+}Cr^{3+}Fe^{2+}$	130.8	0.254	8.357	−21745	−17953	−63843
$AlFe_2O_4$	I	$Al^{3+}Fe^{3+}Fe^{2+}$	131.1	0.249	8.252	−22062	−17497	−61608
$FeAl_2O_4$	N	$Fe^{2+}Al^{3+}Al^{3+}$	133.8	0.267	8.140	−22826	−19211	−57019

[a] I = Inverse spinel and N = Normal spinel

[b] cal = calculated

[c] Grimes [54]

2.4 Ferrite synthesis

Ferrite is traditionally prepared by a ceramic method which involves reacting oxides, carbonates or other compounds of component metals by repeated grinding and heating [69]. This method involves a direct reaction, in the solid-state, of a mixture of solid starting materials. Solids do not usually react together at room temperature over normal time scales and it is necessary to heat them to much higher temperatures, often 1000 to 1500 °C, in order for the reaction to occur at an appreciable rate [61]. The reaction rate depends to a large degree on the particle size of the reactants, the degree of homogenisation achieved on mixing and the intensity of contact between the grains, as well as the obvious effect of temperature. The particles obtained by this method are rather large and non-uniform in size. These non-uniform particles result in the formation of voids or low density [70].

In order to overcome the above difficulties and obtain materials with tailor made properties to suit specific applications, chemical methods are adopted. One of the chemical methods widely studied is ferrite precipitation from aqueous solution. This method has been the subject of many investigations because it can produce smaller and more uniform particles with good chemical homogeneity, high purity, and unique properties [71–75]. It is also considered as an easy and cheap route for synthesis of ferrite and other metal oxide particles [22]. The importance of this precipitation process in the field of corrosion prevention has also been investigated by several researchers [76, 77]. More importantly, as mentioned in Chapter 1, it has been suggested that this process can be applied for the removal of metals from the aqueous solution such as wastewater. Reviews of the published studies regarding magnetite and ferrite precipitation are given in the subsequent chapters.

2.5 Ferrite dissolution

Dissolution process has a variety of application such as hydrometallurgic process, weathering of minerals, metal corrosion, and mobilisation of metal ions in the environment [42]. The latter is particularly important in the context of this work because it is closely related to the stability of ferrite.

Dissolution of metal oxides in acidic aqueous solutions is, in principle, one of the simplest groups of heterogeneous inorganic reactions. Dissolution always involves protonation of oxo group of the solid, rupture of metal-oxygen bonds and phase transfer of the metal [78]. Even though the basic principles are the same in many cases of dissolution, it is noted that many differences found in the literature arise from the very diverse nature of the materials being studied [79]. Some relevant published works on ferrite dissolution are summarised below.

Blesa and Maroto [80] indicated that there are very large differences (many orders of magnitude) in the rates of dissolution of various oxides such as ferrite in mineral acids that can be attributed to structural factors. In general, rates of dissolution (as well as thermodynamic solubility and ionic character of the metal-oxygen bonds) decrease as the charge of the cation increases and its radius decreases. In non-redox dissolutions, increasing covalent character of the metal-oxygen bond renders the solubility of the oxides.

Magnetite usually dissolves faster than the pure Fe(III) oxides due both to its Fe^{2+} content and also because Fe^{3+} occurs in octahedral and tetrahedral positions [28]. Bruyere and Blesa [81] have reviewed dissolution studies of magnetite in mineral acids. The overall rate of dissolution was found to be governed by the rate of release of less labile species (Fe^{3+}). Baumgartner et al. [82] found that the dissolution of magnetite in acidic solutions containing complexing ions (i.e. thioglycolic acid) was linearly related to surface area of solid and was at a maximum at pH 4–5. The overall dissolution of magnetite appears to be shape preserving, at least to the extent that dissolution can be modelled with the cube root law (up to a dissolved iron fraction of 0.7). The probable reaction mechanism was complexation of both Fe^{2+} and Fe^{3+} ions by thioglycolic acid and further reduction of the later ion by intramolecular electron transfer. Borghi et al. [83] indicated that the dissolution rate of magnetite particles in ethylenediaminetetraacetic acid (EDTA) solution alone was very slow due to the formation of stable EDTA-Fe surface complexes which hindered detachment of structural Fe. In the presence of dissolved Fe^{2+}, dissolution was accelerated significantly because the rate determining electron transfer from an Fe(II)-EDTA complex to an Fe(III)-EDTA surface complex is facilitated by the higher stability of the Fe(III) complex over the Fe(II) complex. Based on their experimental evidences, Borghi et al. [83] proposed that the dissolution mechanism should be visualised as involving not only ion-by-ion removal process but also larger discrete units which can be transferred to the solution through the breaking of adequate bonds. The acceleration of dissolution rate was also observed in oxalic acid-Fe(II) solution [84, 85].

Blesa et al. [80] investigated the dissolution of cobalt ferrite $Co_xFe_{3\text{-}x}O_4$ by thioglycolic acid. The reaction involved the chemisorptions of thioglycolate anion onto Fe^{3+} ions of the solid, followed by an electron transfer from the ligand to the metal ion and subsequent release of Fe^{2+}. Substitution of Co^{2+} for Fe^{2+} did not bring about any noticeable change in the kinetics up to $x = 0.5$ but lowered the rate at $x = 0.69$. It was suggested that electron hopping between Fe^{2+} and Fe^{3+} ions within the octahedral cationic sublattice is responsible for the decrease in the dissolution rates of substituted magnetite. As the Fe^{2+} ions in the lattice were progressively substituted by the Co^{2+} ions, the intervalence transfer became less significant which resulted in the deceleration of the dissolution process. This hypothesis was confirmed by the same research group in their recent publication for the dissolution of cobalt ferrite in 0.1 M oxalic acid [86].

To investigate the effect of divalent cation on the dissolution kinetics, Sellers and Williams [87] studied the ability of oxalic acid (at pH 2.5 and 140 °C) to dissolve four different ferrites ($MeFe_2O_4$ where M = Co, Fe, Mn, Ni) obtained by calcinations at 1400 °C.

They observed a marked dependence of the dissolution rate on the nature of the divalent cation; the reactivity decreased in the order Fe > Mn > Co > Ni. The large dissolution rate of magnetite reflected the strong influence of structural Fe^{2+}, as indicated by Blesa et al. [80]. Sellers and Williams [87] proposed several possible explanations for the larger passivity of nickel ferrite compared to that of manganese or cobalt ferrites: (1) inhibition of reductive dissolution by surface complexation of metal by oxalate (nickel(II) forms the most stable oxalato complexes in solution); (2) differences in the solubilities of MC_2O_4; (3) solid state factors reflecting the history of each sample (defect density and surface morphology); and (4) crystal chemistry effects (size distribution of M^{2+} and Fe^{3+}). A slower dissolution of nickel ferrite than magnetite was also observed by Segal and Sellers [88] during their dissolution by $V(pic)_3^-$.

Rodenas et al. [78] studied the dissolution rates of metal ferrites ($NiFe_2O_4$, $CoFe_2O_4$, $ZnFe_2O_4$) in 1 M oxalic acid at pH 3.5 and 70 °C. They found that the reactivity order for these ferrites towards dissolution was $ZnFe_2O_4 > CoFe_2O_4 \gg NiFe_2O_4$. This trend corresponded well with the results obtained by Sellers and Williams [87] described above, even though the dissolution conditions applied in these two studies were different. It was suggested that the most important factor determining the rates of dissolution of ferrites is the lability of metal-oxygen bonds which is in turn defined by the electronic structure of the metal ion and its charge/radius ratio.

Lu and Muir [89] investigated the dissolution of magnetite, hematite, copper, zinc, and nickel ferrites prepared by calcinations at temperature up to 1200 °C. They found that the dissolution rates of the investigated iron oxides and metal ferrites in 1 M HCl at 25 °C were in the order $Fe_3O_4 \gg ZnFe_2O_4 > CuFe_2O_4 > Fe_2O_3 > NiFe_2O_4$. The dissolution was enhanced in the presence of 0.01 M Cu(I). Under this condition, zinc and copper ferrites was found to dissolve faster than magnetite.

Kishi and Nagai [90] applied electrochemical method to investigate the dissolution of $Ni_xFe_{3\text{-}x}O_4$ prepared by sintering at 1300 °C. The experiments were conducted under cathodic polarisation in HCl solution (pH 0). They found that the dissolution rate decreased almost linearly with the increasing value of x. This dissolution phenomenon was due to the stabilisation of the oxygen ion on the ferrite surface at increasing x. The decrease of the dissolution rate with x was also correlated with the observation that iron component dissolved faster than nickel component. This behaviour was related to the larger water exchange rate constant of the Fe^{2+} ions compared to that of the Ni^{2+} ions (Table 2.1).

In another study Kishi et al. [91] investigated the dissolution of $Co_xFe_{3\text{-}x}O_4$ and $Ni_xFe_{3\text{-}x}O_4$ sintered at 1300 °C under anodic polarisation at pH 2. They observed a decrease in the dissolution rates of both ferrites as the parameter x increased. However, cobalt ferrite dissolved faster than nickel ferrites. This result was suggested due partly to a much larger value of water exchange rate of Co^{2+} relative to that of Ni^{2+} (Table 2.1).

Chapter 3

Experimental Procedures and Methods

In this chapter, the experimental procedures and methods employed in this study are presented. These include experimental set-up, procedures for the preparation of ferrites at elevated and ambient temperature as well as product analyses.

3.1 Preparation of ferrites at elevated temperature

3.1.1 Experimental set-up

The experiments were carried out in a 1.5 l covered glass vessel. Temperature of the system was automatically controlled and a pH monitor was used. Nitrogen gas was bubbled into the reactor through a fritted glass dispersion tube to prevent oxidation by air. The alkaline-oxidising $KOH{-}KNO_3$ solution was added dropwise using a peristaltic pump (Ismatec IPC). The experimental set-up is illustrated in Figure 3.1.

3.1.2 Experimental procedures

The ferrite preparation procedure was that of Sidhu et al. [92] and Regazzoni et al. [93]. About 655 ml of distilled water was heated to $90 \pm 5\,^{\circ}\mathrm{C}$ and simultaneously deoxygenated using N_2 gas. Ferrous sulphate salt and Me salt (metal sulphate salts > 98%, except of $CrCl_3$ > 98%) were added in amounts designated to attain x (as in $\mathrm{Me}_x\mathrm{Fe}_{3\text{-}x}\mathrm{O}_4$) values between 0.0 and 1.0 (2.0 for chromium) and total metals of 196 mmol. A basic oxidising solution, prepared by dissolving 52 g KOH, 7.65 g KNO_3, and 21 mg hydrazine sulphate in 281 ml distilled water, was added dropwise for about 20 min. The solution was then aged for 1 h under the same conditions (or several hours if black precipitates had not been obtained after 1 h). The precipitates were washed twice with 5 l distilled water after settling for 1 h. A third wash with distilled water at pH 2.0 ("pH 2 solution", adjusted with 98% H_2SO_4) was employed to remove approximately 97% (assuming the volume of the precipitates was less than 0.3 l out of the 5 l pH 2 solution) of any adsorbed or hydroxide metal species. The rinsing pH was selected based on preliminary experiments

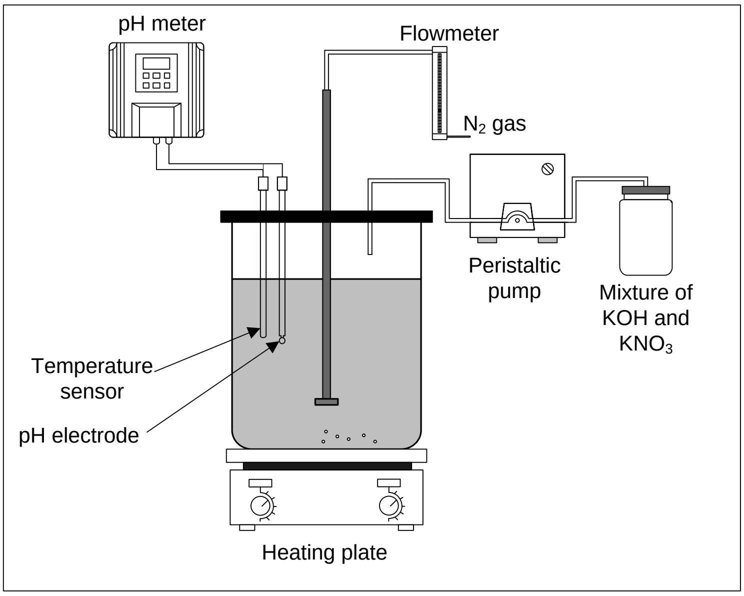

Figure 3.1: Schematic diagram of batch experimental set-up at 90 °C.

and on the reported adsorption behaviour of some Me on iron oxides [28, 94–96]. A final volume of 1000 ml was prepared by adding distilled water and pH value was adjusted to 8.0–9.0 using 5 M NaOH solution. This final solution is referred as the "ferrite sample" and its solid phase is named "ferrite particles". To determine the chemical composition of the ferrite particles, about 4 ml of ferrite sample was filtered (0.7 μm glass microfibre filter) and then the filter with the filtered solid was transferred to 10 ml 32% HCl solution for solid dissolution. The metal concentration in this solution was determined according to the methods described in section 3.4.1.

3.2 Preparation of ferrites at ambient temperature in the batch system

The procedure of ferrite preparation at ambient temperature is based on the seeded ATFP methods described by McKinnon et al. [9] and Morgan et al. [18]. These methods are termed in this work oxidation ferrite process (OxFP) and stoichiometric ferrite process (StFP), respectively. In the OxFP, ferrite is synthesised via oxidation of Fe(II), while the StFP is based on the ferrite synthesis from the solution containing Fe(II)-Fe(III).

3.2.1 Experimental set-up

The experiments were carried out in a 3 l reactor provided with a removable lid with openings for addition of influent, sampling, and mixing. Temperature of the reactor was controlled by means of a water bath and the contents were mixed during the reaction time with a stirrer operated at 100 rpm. A 5 M NaOH solution was used for pH adjustment by means of pH controller (Prominent, Dulcometer D1CA) and dosing pump (Prominent, GALA Gamma/L). The experimental set-up used for the preparation of ferrites at ambient temperature is presented in Figure 3.2.

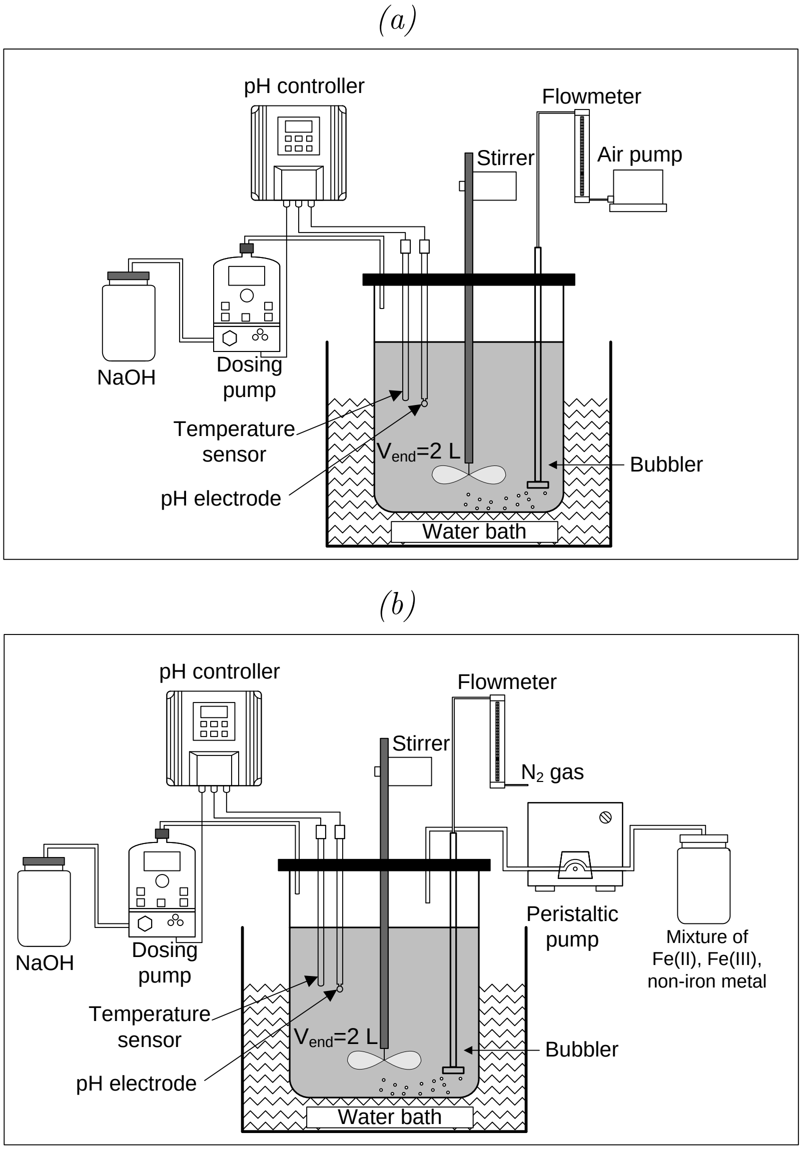

Figure 3.2: Schematic diagram of batch experimental set-up at ambient temperature: (a) Oxidation ferrite process (OxFP) and (b) Stoichiometric ferrite process (StFP).

3.2.2 Experimental procedures

Each batch experiment consisted of a sequence of repeating batch cycle. The overall volume of the mixed solution was about 2 l. The reactor solution was initially bubbled with N_2 gas to remove any dissolved oxygen. Magnetite, prepared according to Regazzoni et al. [93], was used as the initial seed. The intrinsic ferrite, formed by the process, was then served as the seed in each batch cycle and its concentration was maintained at approximately 20 ± 2 g/l as Fe. About 35 to 40 cycles (equivalent to about 1.5 to 2 months) were conducted in each batch experiment to make sure the system reached steady state conditions, i.e. when the incorporation extent reached a plateau, indicating that all of the original solids had been replaced by the new forming ferrite. Afterwards, the solid samples were rinsed according to the procedure described in section 3.1.2.

OxFP procedure

Before each experimental cycle, the concentration of ferrous intermediate species (FI) in the reactor was determined according to the following procedure. Two ml sample was taken from the reactor, immersed in 100 ml acidified distilled water (pH 2) for 15 min, and then filtered. The Fe(II) concentration in the filtrate was measured.

About 400 ml influent solution was prepared by the addition of divalent metal sulphate salts at required molar ratios. The amount of ferrous salt added to the solution was adjusted to establish FI concentration of ca. 3000 mg Fe^{2+}/l in the reactor. The influent solution was then added to the reactor over about 1 min and pH was manually corrected by adding 5 M NaOH. Subsequently, N_2 gas purging was replaced by air, adjusted at a certain flow rate in order to reduce FI concentration to ca. 1500 mg Fe^{2+}/l in about 2.5 h reaction time [97]. At the end of each cycle, the 2-ml sample taken from the reactor was prepared according to the FI determination procedure. The determination of the metal concentration was conducted after solid (retained in the filter) dissolution in 10 ml 32% HCl solution. Finally, a certain amount of mixed solution (approximately 150 ml) was removed to maintain the seed concentration constant. Subsequently, mixing was stopped and the precipitates were left to age overnight. Before the next cycle was commenced, an appropriate volume of clear supernatant was removed from the reactor to allow for the addition of a new metal solution. The supernatant taken from the reactor represents the process effluent.

StFP procedure

About 400 ml metal solution was prepared using $FeCl_3$ solution, ferrous and non-iron metal sulphate salts. The ratio of Fe^{2+}/Fe^{3+} in the initial solution was 0.5, unless otherwise stated. The metal solution was then added within about 2.5 h using a peristaltic pump (Ismatec IPC) to maintain the same reaction time as applied in the OxFP procedure, except for the simultaneous incorporation of Zn^{2+} and Ni^{2+} (see Table 6.2). The subsequent steps were as described for the OxFP procedure.

Experiments without seed were carried out in an identical fashion to that described above, the only differences being that no seed was present in the initial solution and no recycling was performed. In other words, the experiments without seed are operated in a single-cycle batch mode, while the experiments with seed in a repeated-cycle batch mode.

3.3 Preparation of ferrites at ambient temperature in the continuous system

The continuous experimental set-up, illustrated in Figure 3.3 was operated based on the StFP procedure. A relatively high solid recycle flow rate was employed in the system in order to prevent clogging in the tubing. This resulted in a relatively short retention time of the ferrite solids in the settler. Approximately 1 l of excess solid was removed once a day from the settler to maintain a constant seed concentration (20 ± 2 g/l as Fe) in the reactor. Unless otherwise stated, the ratio of Fe^{2+}/Fe^{3+} in the initial solution was maintained at 0.57, while the total metal concentration in the inflow was 50 mM. The resulting total metal flux per reactor volume was thus approximately 18 mg $l^{-1}min^{-1}$. At the end of each experiment (when the system reached steady state), the precipitates were taken from the reactor and rinsed according to the method described in section 3.1.2. It should be noted that magnetite was also prepared according this procedure. The operational conditions employed in the experiments are given in Chapter 4.

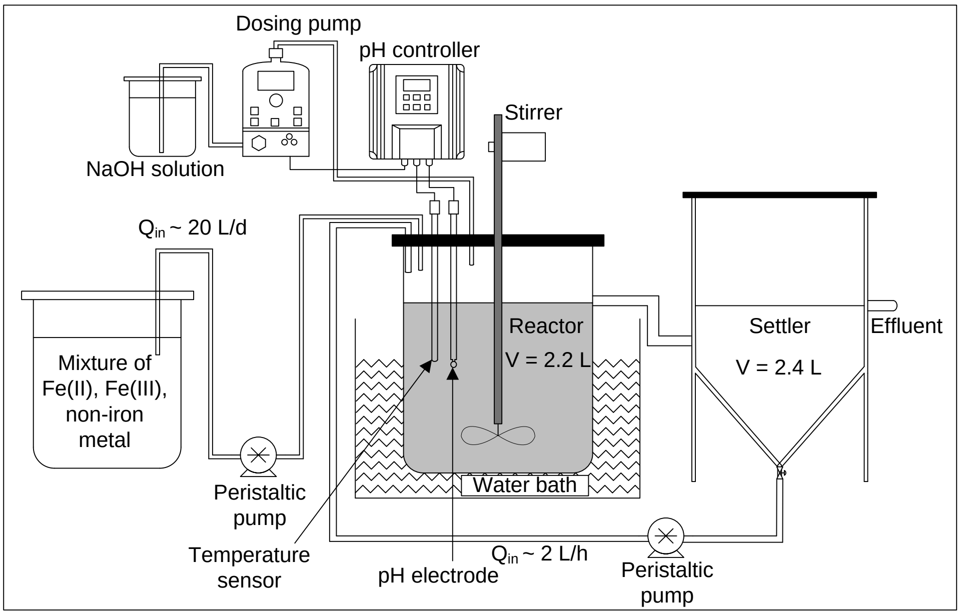

Figure 3.3: Schematic diagram of continuous experimental set-up at ambient temperature.

3.4 Analyses

This section presents various methods used in the current work to characterise the samples. The basic principles of each method are also given.

3.4.1 Chemical composition

The chemical composition of ferrite particles was determined by the following methods.

Determination of iron

For the determination of iron concentration, spectrophotometric methods are preferred as they offer a number of advantages such as simplicity, speed, and sensitivity over other methods (e.g. titrametric analyses) [98]. This technique is based on the principle of the reaction of a chemical interest in solution with a colorimetric reagent. The reagent gives a colour in proportion to the amount of chemical interest. The intensity of the colour (the absorbance) is measured in the ultraviolet-visible range of the spectrum using a spectrophotometer. This is compared with a set of standards with colour developed with known concentrations to give a linear plot of absorbance vs. concentration, according to the Beer-Lambert's law [99]. This law states that

$$A = \epsilon \; b \; c \tag{3.1}$$

where A is absorbance; ϵ, molar absorptivity; b, path length (cm); and c, the concentration of chemical in solution. Since ϵ and b are constants, A is directly proportional to c and a linear plot is obtained.

The commonly used method for determining dissolved ferrous concentration is the phenanthroline method. This method is based upon the colour (orange-red) developed by Fe(II) reacting with 1,10-phenanthroline [100]. However, an accurate Fe(II) measurement in the presence of a high concentration of soluble Fe(III) species was difficult to attain [101]. The interference in the method apparently emanates from the formation of colour due to a reaction between Fe(III) species and the phenanthroline reagent [98] which can result in overestimation of the Fe(II) concentration. To overcome this problem, Herrera et al. [98] suggested the addition of sodium fluoride (NaF) solution as part of the analytical procedure. Fluoride forms a colourless complex with Fe(III) minimising the Fe(III) concentration available for reaction with the phenanthroline reagent. They found that this modified method was accurate as long as the $\mathrm{Fe^{2+}/Fe_T}$ ratio is higher than around 5%. Considering the relatively high concentration of ferrous in the dissolved ferrite particle (high $\mathrm{Fe^{2+}/Fe_T}$ ratio), the modified phenanthroline method proposed by Herrera et al. [98] was adopted in this study. With regard to the determination of dissolved ferric ion in the sample solution, a relatively simple method was employed. It was based on the reaction of ferric ion in an acidic solution with sulfosalicylic acid (SSA) to yield a violet-coloured complex [102, 103]. The absorbance of the ferrous-phenanthroline and ferric-SSA complexes was measured using UV-VIS spectrophotometer at a wavelength of 510 nm (Hach Lange DR2800).

Determination of non-iron metals

The non-iron metal concentration was measured using atomic absorption spectroscopy (AAS) (contraAA 700, Analytik Jena). This technique is widely used for the chemical analysis of metals because its versatility for the measurement of traced quantities of most elements in water [104]. The principle of Beer-Lambert's law applies and the basis of this technique is outlined in Figure 3.4.

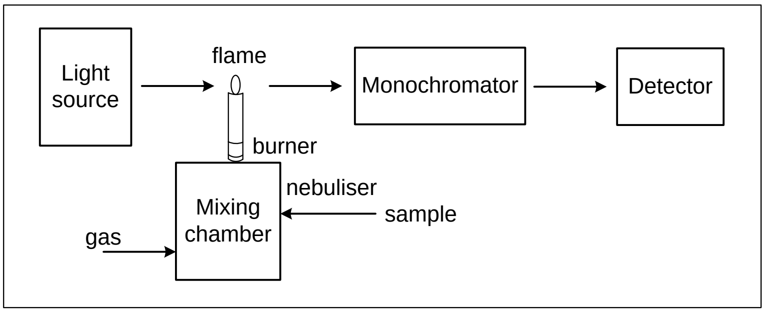

Figure 3.4: An illustration of the principal components of an atomic absorption spectrophotometer [99].

As shown in Figure 3.4, the sample solution is drawn through a nebuliser into a mixing chamber. Here the sample is mixed with the combustion gas before being burnt in a high temperature flame (e.g. air-acetylene at 1700–2000 °C). The flame absorbs radiation from the light source which emits the unique spectrum of the specific metal (the critical lamp components are deliberately constructed from that metal). The transmitted radiation is measured using a monochromator adjusted to a unique wavelength emitted from the lamp and a detector. The metal concentration is proportional to the light absorbed.

3.4.2 X-ray diffraction (XRD)

X-ray diffraction (XRD) is by far the most widely used diffraction technique for the fingerprint characterisation of crystalline materials and for determination of their structure [105]. It involves interaction of electromagnetic radiation with a wavelength (λ) of around 0.1 nm, with the atoms in the solid.

When reduced to the basic essentials, the X-ray diffraction method, schematically shown in Figure 3.5, requires an X-ray source, the sample under investigation, and a detector to pick up the diffracted X-rays. The X-ray source commonly used is the sealed X-ray tube as depicted in Figure 3.6. In the X-ray tube, electrons are emitted by the cathode, usually electrically heated tungsten filament and they are accelerated toward the anode by a high electrostatic potential (30–60 kV) maintained between the cathode and the anode. The typical current in a sealed tube is between 10 and 50 mA. The X-rays are generated by the impacts of high energy electrons with the metal target of water cooled-anode. The anode is usually made of high purity copper (Cu), which may be coated with a layer of a different metal such as Co, Cr, Fe, Mo, etc., to produce a target other than Cu. The X-rays leave the tube through beryllium (Be) windows (see Figure 3.6). The detector is an integral part of any diffraction analysis system and its major role is to measure the intensity. The detection is based on the ability of X-rays to interact with matter and to produce certain effects or signals. In other words, each photon entering the detector generates a specific event or a series of events that can be recognised and from which the total photon count (intensity) can be determined. The detectors must be sensitive to X-rays and should have an extended dynamic range and low background noise [106]. An extended discussion of the X-ray detectors can be found in the literature [106, 107]. Depending on the form of sample investigated, X-ray diffraction method can be divided into single crystal and powder method. The latter is largely used in many research works including this work.

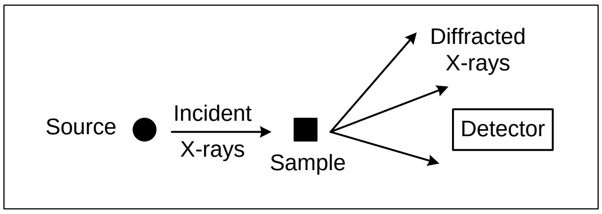

Figure 3.5: Schematic of the X-ray diffraction method [105].

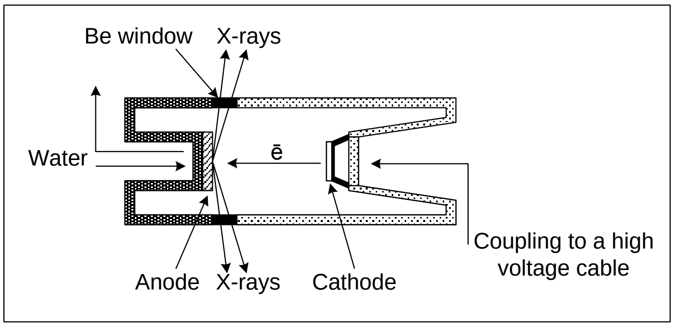

Figure 3.6: Schematic of the sealed X-ray tube [106].

The most useful equation in the powder diffraction is the Bragg equation which describes the principle of X-ray diffraction in terms of a reflection of X-rays by sets of lattice planes. Lattice planes are crystallographic planes, characterised by the index triplet hkl, the so-called Miller indices [108]. Parallel planes have the same indices and are equally spaced, separated by the distance d_{hkl}. According to Bragg's analysis, diffraction from a crystalline sample can be explained and visualised by using a simple notion of mirror reflection of the incident X-ray beam from a series lattice planes. Consider an incident front of waves with parallel propagation vectors, which form an angle θ with the planes (hkl) described in Figure 3.7. In a mirror reflection, the reflected wave front will also consist of parallel waves, which form the same angle θ with all planes. The path differences between a pair of waves, both before and after they are reflected by the neighbouring planes, Δ, are determined by the interplanar distance as $\Delta = d_{hkl}\ sin\theta$. The total path difference is 2θ and the constructive interference is observed when $2\Delta = n\lambda$, where n is integer and λ is the wavelength of the incident wave front [106]. This simple geometrical analysis results in the Bragg's equation:

$$2\ d_{hkl}\ sin\theta_{hkl} = n\lambda \tag{3.2}$$

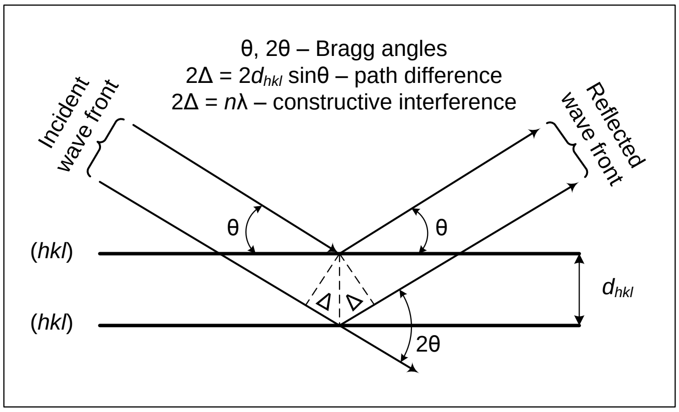

Figure 3.7: Geometrical illustration of the Bragg's law [106].

The X-ray pattern of a powder sample is a plot of the observed diffraction intensity against the Bragg angle. Depending on the interference conditions each atom plane produces a series of n reflections. From these patterns the d_{hkl} values are calculated using the Bragg equation (Equation 3.2). Each compound has its own characteristic set of d_{hkl} values and intensities which can be used for identification. From the line positions, widths, and intensities of the X-ray diffraction pattern, information about the nature of the sample, its quantity (in a mixture), its unit cell parameters, and its crystallinity is obtained.

The rinsed ferrite samples were dried at 40 °C and ground before analysis by XRD (Siemens D500) using Cu Kα radiation at 30 mA and 40 kV. The scanning was done in the 2θ range from 10° to 70° at a rate of 0.3°/min (step size 0.02° 2θ and counting time 4 s). The XRD patterns were evaluated using the Bruker EVA software. The exact peak positions were taken at half height after position correction using lead nitrate as internal standard. The values of the unit cell size (a) were obtained by fitting the diffraction peaks with *hkl* 111, 220, 311, 222, 400, 422, 511, and 440 using least square methods.

Crystallite size of the powdered sample may vary considerably. It reflects growth conditions and determines the surface area of the particle [28]. Crystallite usually means a tiny single crystal. Each particle in a polycrystalline material usually consists of multiple crystallites that join together in different orientation. A small powder particle can be a single crystallite as well [106]. From XRD line broadening, an average crystallite size is calculated using the Scherrer formula

$$D_c = \frac{k\lambda}{\beta \cos\theta} \tag{3.3}$$

where β is the full width at half maximum (FWHM) in 2θ, k is the shape factor or Scherrer constant which is about 0.85, and λ is the wavelength of the X-ray source used in the XRD. In this work, the D_c value was calculated in the direction perpendicular to the main line of XRD pattern of ferrite (311).

3.4.3 Scanning electron microscopy (SEM)

The scanning electron microscopy (SEM) is an extremely versatile technique capable of providing structural information over a wide range of magnification [61]. Its popularity stems from its capability of obtaining three-dimensional-like images of the surfaces of a very wide range of materials [109]. The basic components of the SEM consist of the lens system, the electron gun, the electron collector, the visual and photorecording cathode ray tubes (CRTs), and the associated electronics (see Figure 3.8).

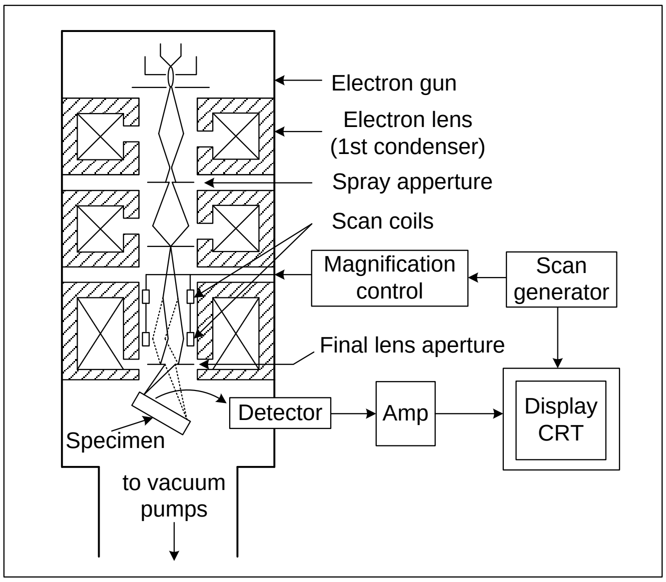

Figure 3.8: Schematic of the basic components of the SEM [109].

In the SEM, the area to be examined or the microvolume to be analysed is irradiated with a finely focused electron beam which may be swept in a raster across the surface of the specimen to form images or may be static to obtain an analysis at one position. The types of signals produced from the interaction of the electron beam with the sample include secondary electrons, backscattered electrons, characteristic X-rays, and other photons of various energies [109]. These signals are obtained from specific emission volumes within the sample and used to examine many characteristics of the sample (surface topography, crystallography, composition, etc.). Among the imaging signals, the secondary and backscattered electrons are of the greatest interest because these vary primarily due to the differences in the surface topography. The analysis of the X-ray radiation also emitted from samples can yield both qualitative identification and quantitative elemental information from a certain region of a specimen.

In this work, SEM (LEO Zeiss 1530) was mainly used to study the surface topography (morphology) of the ferrite particle. A rough determination of the particle size distribution was also deduced from the SEM images. To prepare the specimen for SEM observation, the following procedure was conducted. First, a certain amount of dried ferrite powder (about 16 mg) was dispersed in 2 ml ethanol and then treated by ultrasound for 10 min. The suspension was then dripped onto an aluminium plate and dried at 60 °C for 24 h. To increase conductivity, the sample was coated with gold.

3.4.4 Specific surface area

The specific surface area of a solid is the surface area of a unit mass of material, usually expressed as m^2/g. Surface areas of iron oxides are commonly measured by the Brunauer, Emmett, and Teller (BET) method [110] using N_2 gas as the adsorbate. In this work, the measurement was done with the surface area analyser Nova 3200e (Quantachrome Instruments). Before performing gas sorption measurement, the solid surface must be freed from contaminants such as adsorbed water. Surface cleaning (degassing) was carried out by placing about 1 g solid sample in a glass cell and heating it under vacuum. Once clean, the sample was brought to a constant temperature by means of an external bath. Then, small amounts of N_2 gas were admitted in steps into the evacuated sample chamber. Gas molecules that stick to the surface of the solid (adsorbent) were adsorbed and tended to form a thin layer that covered the entire adsorbent surface (monolayer).

Based on BET theory, the extent of N_2 adsorption at 77 K (i.e. the boiling temperature of liquid N_2) on the outgassed solid is a function of the relative pressure, p/p_0, i.e. the adsorption isotherm; p is the partial pressure of the adsorbate and p_0 is its equilibrium vapour pressure [28]. The linear relationship between the amount N_2 adsorbed, ν (cm^3/g) and the relative vapour pressure p/p_0 is described by the following equation:

$$\frac{p/p_0}{\nu(1-p/p_0)} = \frac{1}{\nu(p_0/p-1)} = \frac{1}{\nu_m c} + \frac{c-1}{\nu_m c} \times \frac{p}{p_0} \tag{3.4}$$

where ν_m is the monolayer capacity of adsorption and c the so-called BET constant. The values of c and ν_m are obtained from the slope of the plot, s, and the intercept, i, on the ordinate, i.e. $\nu_m = (s+i)^{-1}$ and $c = \frac{s}{i} + 1$. The surface area is then calculated from ν_m and the area occupied by one molecule of the adsorbate, i.e. $0.162\,nm^2$/molecule for

N_2. Further detailed discussion regarding the BET method can be found in the literature [110–112].

3.4.5 Fourier-transform infrared spectroscopy (FTIR)

Spectroscopic methods can provide useful information for the identification and characterisation of iron oxides and complement well the results obtained from diffraction. The latter techniques concern primarily with the long-range structures of crystals. Because this results in an average picture of the local structure, information on defects, impurities, and subtle variations in local structure may be lost [105]. On the contrary, the former techniques may give information on local structure such as the nature of adsorbed molecule and surface complexes, the degree of impurities and imperfections [105]. The amorphous materials can be studied as easily as the crystalline materials with these techniques. One technique widely applied to characterise iron oxides is infrared (IR) spectroscopy.

Infrared spectroscopy produces spectra which arise as a result of interactions of iron oxides with electromagnetic radiation (photons) in the wavelength range 1–300 μm (i.e. wavenumbers of 10000–33 nm^{-1}). These interactions involve excitation of vibrations or rotation of molecules in their ground electronic state and are associated with stretching deformations of the interatomic bonds and bending deformations of the interbond angles [28]. An infrared spectrum is a plot of percent radiation absorbed vs. the frequency of the incident radiation usually given in wavenumbers (cm^{-1}). Compared with conventional IR spectroscopy, Fourier-transform infrared spectroscopy (FTIR) has a better resolution because it averages a large number of spectra and it gives an improved signal to noise ratio resulting in an increased sensitivity. It also permits a more rapid data collection [28].

In this work, FTIR spectra were recorded in the 4000–400 cm^{-1} range at room temperature using Alpha spectrometer (Bruker Optics). The FTIR spectrometer was coupled with a personal computer loaded with Opus program (Bruker) to process the recorded spectra. For FTIR analysis, KBr pellet of each solid sample was prepared by the following procedure. A mixture of 3 mg of dried ferrite sample and 297 mg of KBr was ground in an agate mortar. About 100 mg of this finely powdered mixture was pressed to form disks of ~0.2 mm thickness and 7 mm diameter for FTIR spectrum observation.

3.4.6 Dissolution test

Dissolution test was conducted to study the chemical stability of ferrite towards dissolution in an acidic solution and to determine the dissolution congruency of metals in the ferrite structure. It was performed by adding 2 ml of ferrite sample to a 1 l of 12.8% HCl solution and stirred continuously at room temperature (23 ± 2 °C). Suspension aliquots (5 ml) were withdrawn at predetermined time intervals and filtered immediately through 0.22 μm membrane filters. Dissolved metal concentrations were determined by AAS.

3.4.7 Leaching tests

To analyse the metal release under acidic environmental conditions, two standardised leaching tests were performed, i.e. toxicity characteristic leaching procedure (TCLP) and Bureau Communautaire de Référence (BCR) (or Community Bureau of Reference in English) extraction procedure (step 2). To determine the amount of extract fluid to be used in the leaching tests, the amount of dry solid in the ferrite sample was measured first. About 30 ml of rinsed ferrite sample was extracted, weighted (A) and filtered with a pre-weighted filter (B). The filter containing the solid was then dried at 40 °C until the weight was constant (C). The content of dry solid (D, in %) was calculated according to Equation 3.5.

$$D = \frac{(C - B) \times 100}{A} \tag{3.5}$$

Toxicity characteristic leaching procedure (TCLP)

TCLP test was carried out to analyse the metal leaching under relatively mild acidic condition according to United States Environmental Protection Agency (US EPA) Test method 1311 [113]. The extraction fluid was prepared by adding 5.7 ml of glacial acetic acid and 64.3 ml of 1 M NaOH to a 1 l volumetric flask that contained 500 ml distilled water. The solution was then diluted to 1 l by adding distilled water. The pH of the extraction fluid was 4.93 ± 0.05 and it was always checked prior to use. For the solid extraction, about 50 ml of rinsed ferrite sample was weighted (F) and filtered. The filter with the solid on it was then placed in a 50 ml extraction bottle. The amount of extraction fluid added to the extraction bottle was determined according to Equation 3.6.

$$Weight\, of\, TCLP\, extraction\, fluid\, (ml) = \frac{D \times F \times 20}{100} \tag{3.6}$$

The extraction bottle was placed on the rotary agitation device and the bottle rotated at 30 ± 2 rpm for 18 ± 2 h at room temperature (23 ± 2 °C). Following this procedure, the concentration of the metals in the extraction liquid was measured using AAS.

BCR extraction procedure (step 2)

To assess the leachability of metals under combined acidic and reducing conditions, step 2 of the revised extraction procedure proposed by the BCR (now superseded by the Standards, Measurement and Testing Programme) was performed. The extraction fluid employed in this procedure was 0.5 M hydroxylammonium chloride at pH 1.5 (by adding

0.05 M nitric acid) [114–116]. About 25 ml of the rinsed ferrite sample was weighted (G) and filtered. The amount of extraction fluid used was according to Equation 3.7. The following extraction procedure is similar to the TCLP test, except that it was run for a shorter period of time (16 h).

$$Weight\,of\,BCR\,(step\,2)\,extraction\,fluid\,(ml) = \frac{D \times G \times 40}{100} \tag{3.7}$$

Chapter 4

Magnetite Synthesis at Ambient Temperatures

Magnetite has been the subject of investigations from different standpoints for many years due to its widely and important applications (such as magnetic tapes, magnetic memories, wave-guides, transformers, etc.) [117]. In essence, magnetite can be synthesised either via Fe(II) oxidation or from the solution containing Fe(II)-Fe(III), shortly here named as oxidation and stoichiometric method, respectively. Although much is known about the favourable conditions for the synthesis of magnetite at ambient temperatures by the former method, such knowledge is limited for the latter method. The experimental works, discussed below, focus on this issue with the main aim of identifying the influence of different operational parameters on the solid characteristics and the process performance. As a basis, a review of the current knowledge concerning two methods of magnetite synthesis is firstly given. The review also includes the literature dealing with the corresponding methods at elevated temperatures which are widely known as the conventional synthesis route for the crystal magnetite.

4.1 Previous works

Besides investigating the optimum conditions to precipitate magnetite from the aqueous solution, several works tried to elucidate the mechanisms governing a particular synthesis method. It has been widely suggested that magnetite is formed through a series of transformation reactions involving a variety of intermediate species, as described in the following two sections.

4.1.1 Magnetite precipitation by oxidation method

Feitknecht [118] firstly reported that magnetite is formed by air oxidation of $Fe(OH)_2$ suspensions. Misawa et al. [119] subsequently suggested that the formation of magnetite at room temperature occurs through slow aerial oxidation of $Fe(OH)_2$ or $FeOH^+$, while rapid oxidation can result in the formation of other ferric oxyhydroxides, such as lepidocrocite (γ-FeOOH) (Figure 4.1). The synthesis reactions of magnetite involve the formation of intermediates, i.e. green rust (GR) and green complexes (GC). The GR-I is formed in the chloride solution, while the GR-II in the sulphate solution. The configuration of both GR and GC were considered similar, consisting of stacking of hexagonal and cubic layers of close-packed oxygen.

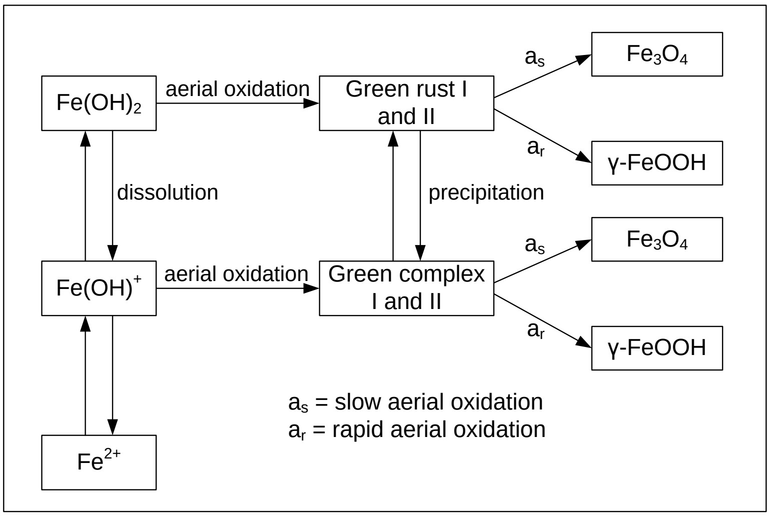

Figure 4.1: Schematic diagram of magnetite formation proposed by Misawa et al. [119].

The formation of magnetite by air oxidation of $Fe(OH)_2$ was further investigated by Kiyama [120] at various temperatures. This author found that magnetite was formed only when the mol ratio of NaOH to $FeSO_4$ (R) was 2 and at temperatures above 50 °C. The temperature of formation was lowered as R approached 1.0. In neutral suspensions ($R < 1$), Fe_3O_4 was formed via GR-II or a mixture of GR-II and $Fe(OH)_2$, while in alkaline suspensions ($R > 1$), Fe_3O_4 was formed directly. It was suggested that the Fe_3O_4 particles are formed near the surface of the particles of $Fe(OH)_2$ and GR-II by the coprecipitation of $FeOH^+$ with ferric hydroxo-complexes.

Tamaura et al. [121] reported that GR can be transformed into Fe_3O_4 not only by oxidation but also spontaneously without oxidant (under a nitrogen atmosphere and at 50–75 °C). The spontaneous transformation proceeds through the dissolution process of GR followed by the precipitation of Fe_3O_4 (dissolution-reprecipitation process), where the former step is the rate determining step of the reaction. In the presence of Fe^{2+} ions, Tamaura et al. [122] found that γ-FeOOH transforms into magnetite in an alkaline solution. The transformation taking place at room temperature is stoichiometric, i.e.

$$2\,\mathrm{FeOOH} + \mathrm{Fe}^{2+} \longrightarrow \mathrm{Fe_3O_4} + 2\,\mathrm{H}^+ \tag{4.1}$$

Neutralisation of H^+ promotes the reaction and keeps the system supersatured with respect to magnetite. The laths of lepidocrocite gradually transform into numerous, much smaller cubic crystals of magnetite involving the dissolution-reprecipitation process. The mechanism was thought to involve adsorption of Fe^{2+} species on and interaction with surface groups of the γ-FeOOH to form magnetite directly or via GR hydroxo species, either on the surface or in the water layer adjacent to the surface.

The formation of magnetite under ambient condition requires that certain reaction conditions should be carefully controlled to obtain a monophase product. In agreement with the earlier publication of Misawa et al. [119], several recent publications suggested that a slow oxidation rate is imperative for the formation of magnetite [18, 123–125]. The reason for this requirement is because complete dehydroxylation of the precursor prior to oxidation is only possible if sufficient time is available [28]. Thus, dehydroxylation and oxidation appear to be competing reaction steps. Perales-Perez and Umetsu [124] suggested that an extremely fast oxidation rate can destroy the incipient ferrous-ferric frameworks by consuming all ferrous iron (overoxidation) and promoting the generation of ferric-rich precipitates of an amorphous, voluminous, and non-magnetic nature. According to Blesa and Matijević [40], in a condition of rapid oxidation rate, the nucleation rate of magnetite is equal to the oxidation rate of neighbouring Fe^{2+} ions, leading to the nucleation of only ferric (hydrous) oxides.

At elevated temperatures, magnetite can be synthesised in a wider range of pH (7–13) than at ambient temperatures. Perales-Perez et al. [124] suggested that the higher the temperature the lower the pH required for the formation of precipitates as hydrolysis and dehydration reactions occur at a lower pH value when the temperature is increased. Under ambient condition, several authors proposed that Fe_3O_4 is formed preferentially at pH 9–11 [123, 125, 126]. The presence of excess OH^- can promote the reducing conditions required for the exclusive establishment of magnetite frameworks. At low pH values, the formation of magnetite is retarded. On the other hand, in the strongly alkaline solution goethite is preferentially formed as $Fe(OH)_2$ exist in the form of $Fe(OH)_3^-$. The latter soluble species is easily oxidised to electroneutral $Fe(OH)_3$ and then converted rapidly into α-FeOOH.

Morgan et al. [18] introduced the term ferrous intermediate (FI) to present the metastable, amorphous solid ferrous species, as distinct from stable crystallised products. They proposed that FI concentration in the oxidation reactor should be maintained above 500 mg/l to synthesise magnetite under ambient temperature conditions. This level must be increased to at least 1200 mg/l in the presence of inhibitors such as Ca^{2+} ions [127]. Thus, it seems that the formation of magnetite requires that the available Fe^{2+} behaves as a scavenger for Fe^{3+} ions, preventing the formation of solids containing ferric ions only [40]. It is noted that the term FI is also used in this study whose determination is described in Chapter 3.2.2.

The presence of magnetite seed is able to facilitate the formation of high quality magnetite at ambient temperatures. McKinnon et al. [9] suggested that the presence of seeds reduces the activation energy required for magnetite formation. Morgan et al. [18] proposed that seed alters the reaction pathway probably involving a ferrous species-magnetite complex which directs the reaction towards the formation of magnetite. Interestingly, they observed a similar FI concentration at the end of batch cycles, despite the different initial ferrous concentrations applied. They explained that this observation might be related to either substrate/substrate-seed effects or final product dissolution. With regard to the latter explanation, selective release of ferrous from magnetite is of concern due to the complex behaviour of magnetite at low pH, as described by Jolivet and Tronc [128]. By supplying a large surface area of nucleation sites, seeds can assist in overcoming unfavourable conditions for magnetite formation, such as low temperatures and relatively high oxidation kinetics [97].

Increasing aging time can also promote the formation of magnetite under unfavourable conditions [123, 126]. Wang et al. [126] suggested that the activation energy of Fe_3O_4 formation is decreased during aging. However, a large uncertainty regarding the optimum conditions for aging still exists.

4.1.2 Magnetite precipitation by stoichiometric method

Welo and Baudisch [129] firstly reported that magnetite can also be formed by bringing a solution with $Fe^{3+}/Fe^{2+} \cong 2$, i.e. the mol ratio of magnetite, up to pH 9–10. Misawa et al. [119] suggested that the reaction involved the formation of dark red complex (DRC) cation, according to Equation 4.2.

$$\mathrm{mFe(II)} + 2\,\mathrm{mFe(III)} + 6\,\mathrm{mOH^-} \longrightarrow [\mathrm{Fe(II)_1Fe(III)_2O_x(OH)_{2(3-x)}}]_\mathrm{m}^{2\mathrm{m}+} + \mathrm{mxH_2O} \tag{4.2}$$

When pH was about 7.2, further addition of OH^- to the DRC solution resulted in the rapid precipitation of fine-black particles according to Equation 4.3.

$$[\mathrm{Fe(II)_1Fe(III)_2O_x(OH)_{2(3-x)}}]_\mathrm{m}^{2\mathrm{m}+} + 2\,\mathrm{mOH^-} \longrightarrow \mathrm{mFe_3O_4} + (4-\mathrm{x})\mathrm{mH_2O} \tag{4.3}$$

They identified the particles as incompletely deprotonated or dehydrated Fe_3O_4 with smaller unit cell size (a) than that of usually found in magnetite (8.37 Å compared to 8.396 Å in magnetite). This was explained due to the presence of iron vacancies and some extent of OH^- or coordinated water in the crystal structure. The configuration of the DRC was assumed to be analogous to that of Fe_3O_4 and can be converted easily to magnetite by addition of OH^-.

Other authors suggested that magnetite formation involved interaction of Fe^{2+} with some ferrihydrite that had precipitated initially [40, 130]. Jolivet et al. [33, 131, 132] suggested that the transformation of the Fe^{2+}-ferrihydrite precursor into spinel occurs by two simultaneous competing pathways:

(i) solid state reaction with dehydration and spinel ordering at short range without particle size variation;

(ii) dissolution of Fe^{2+}-Fe^{3+} complexes from the surface followed by crystallisation of spinel oxide (dissolution-reprecipitation) with particle growth.

Electron mobility between Fe^{2+}-Fe^{3+} ions in the precursor drives a local cubic close-packed ordering. This local ordering gradually extends to the whole fine particles (process (i)) and to the growing particles by process (ii).

It is interesting to note that GR phase can also be formed as an intermediate product during coprecipitation of ferric and ferrous ions, as reported by several authors [133, 134]. This phase forms following a heterogeneous crystallisation process because these ions precipitate successively [134, 135].

4.2 Effect of operational parameters on magnetite formation

Table 4.1 summarises the optimum operational parameters promoting the formation of magnetite as a single product at ambient temperatures by the oxidation method, reported in the literature.

Table 4.1: Reported optimum operational parameters promoting magnetite formation at ambient temperatures.

Parameter	Optimum values	References
Air flow rate	0.05–0.1 l/min	[124]
	0.05–0.6 l/min	[125]
pH	> 10.5	[136]
	9–10.5	[125]
	9–11	[126]
Ferrous intermediate (FI)	$\sim$ 500 mg Fe/l	[127]
	$\sim$ 1200–2000 mg Fe/l [a]	[127, 137]
Aging time	24 h	[123, 124]
	18 h	[137]
Seed concentration	4.8–8.4 g Fe/l	[125]
	20 g Fe/l	[127]

[a] In the presence of inhibitors

In the current work, the experiments of magnetite formation by the stoichiometric and oxidation method without seed (in a single-cycle batch mode) were firstly carried out at a temperature of 30 °C, a pH value of 10.5, and a reaction time of 150 min. The solid formed under these conditions was magnetite, as confirmed by the XRD analysis, but the crystallinity degree of the solids was relatively low. The molar ratio of ferrous to total iron in the solid particles (Fe^{2+}/Fe_{T_SP}) was 0.16 and 0.18 for the stoichiometric and oxidation method, respectively. These values are significantly lower than the Fe^{2+}/Fe_{T_SP} ratio of an ideal magnetite (i.e. 0.33). Thus, it can be deduced that crystallisation of magnetite was actually quasi-immediate at ambient temperatures, in agreement with the statement of Jolivet et al. [33, 131]. Nevertheless, the magnetite produced was non-stoichiometric and its crystallinity degree was low.

As an attempt to improve the quality of the magnetite prepared at ambient temperatures, further experiments were conducted in the presence of magnetite seed with a concentration of about 20 g Fe/l. The effects of four important process parameters, i.e. temperature, molar ratio of ferrous (Fe^{2+}) to total iron (Fe_T) in the initial solution (Fe^{2+}/Fe_{T_IN}), iron flux (Fe_f) and pH, on the formation of magnetite under ambient condition were investigated using the stoichiometric method in a continuous system (Chapter 3.3). The continuous reactors were operated for several days to ensure the that the system reached steady state conditions (i.e. when nearly all of the original magnetite seed had been replaced by new ones).

4.2.1 Effect of temperature

The experiments were firstly conducted at two different temperatures (i.e. 23 ± 2 and 30 ± 2 °C), pH value of 10.5, Fe_f of 9.8 mg $l^{-1}min^{-1}$, Fe^{2+}/Fe_{T_IN} of 0.364, followed by other experiments at the Fe^{2+}/Fe_{T_IN} ratio of 0.5. The Fe^{2+}/Fe_T ratios in the solid particles (Fe^{2+}/Fe_{T_SP}) obtained in these experiments are plotted in Figure 4.2. For the experiment at 23 °C and Fe^{2+}/Fe_{T_IN} ratio of 0.364, a rapid decrease in the Fe^{2+}/Fe_{T_SP} ratio was observed, reaching a value of about 0.08 at steady state. When the temperature was increased to 30 °C, a higher Fe^{2+}/Fe_{T_SP} ratio was obtained, i.e. around 0.18 at steady state. The experiment at 23 °C and Fe^{2+}/Fe_{T_IN} ratio of 0.5 showed that at steady state the Fe^{2+}/Fe_{T_SP} ratio was around 0.14. Increasing the temperature to 30 °C resulted in the increased Fe^{2+}/Fe_{T_SP} ratio (i.e. 0.24), in accordance to the previous experiment. The effects of different Fe^{2+}/Fe_{T_IN} ratios are further described in Section 4.2.2.

The XRD patterns of the solid particles produced at 23 °C indicated the coexistence of two distinct iron oxide species, i.e. magnetite and goethite. These result were corroborated by SEM observation showing the presence of needles which is typical for goethite particles, together with spherical magnetite crystals (Figure 4.3a). On the other hand, the solid particles synthesised at 30 °C consisted only of magnetite particles as confirmed by XRD

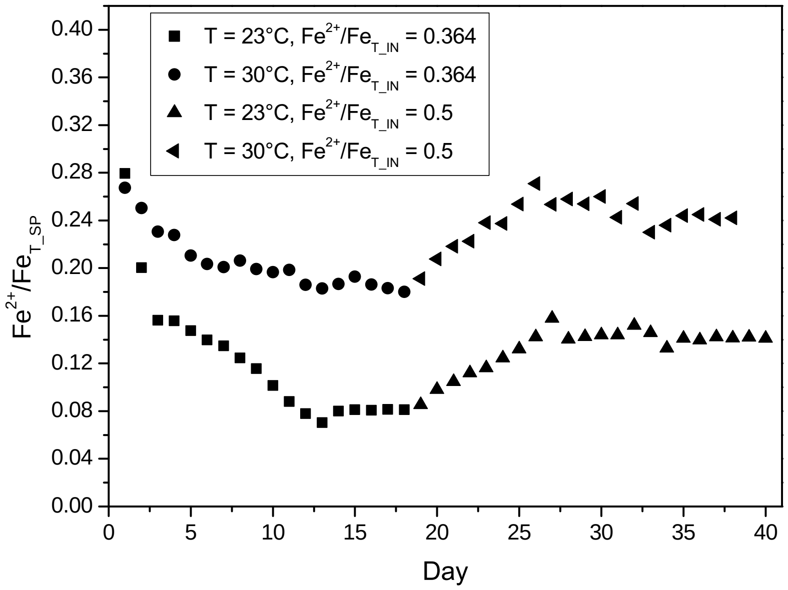

Figure 4.2: Fe^{2+}/Fe_T ratios in the solid particles obtained at two different temperatures and Fe^{2+}/Fe_{T_IN} ratios.

analysis. Solid particle characterisation by SEM indicated disappearance of goethite and the existence of spherical particles of about 30–50 nm across (Figure 4.3b). Although magnetite was the only constituent found in the experiments at 30 °C, it had a lower $\mathrm{Fe}^{2+}/\mathrm{Fe}_\mathrm{T}$ ratio than the stoichiometric magnetite (i.e. $\mathrm{Fe}^{2+}/\mathrm{Fe}_\mathrm{T} = 0.33$ or $\mathrm{Fe}^{2+}/\mathrm{Fe}^{3+} = 0.5$). So, it can be deduced that the magnetite formed in the system had Fe^{2+} deficiency indicating its non-stoichiometric (oxidised) structure.

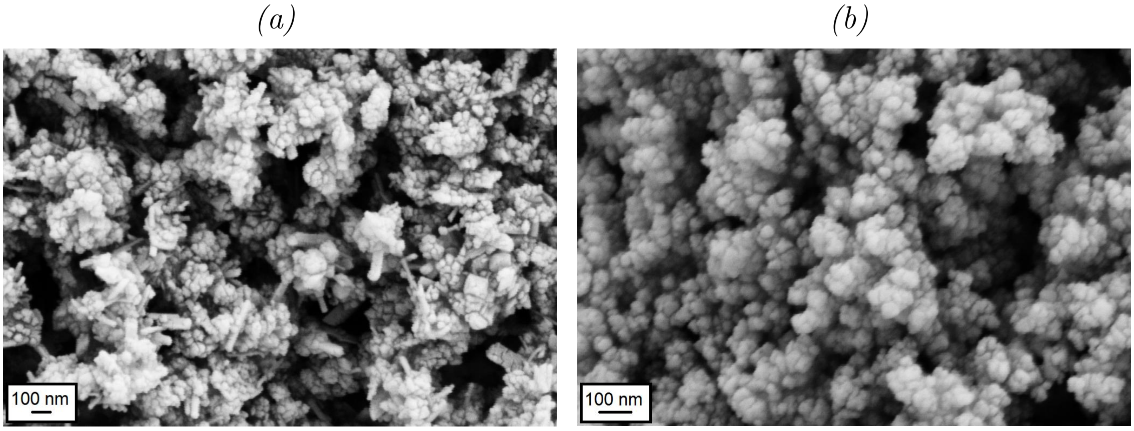
(a) *(b)*

Figure 4.3: SEM images of the solid particles obtained at $Fe^{2+}/Fe_{T\_IN} = 0.5$ and temperature of (a) 23°C *and (b) 30*°C.

The appearance of goethite together with magnetite in the product of the experiment at 23 °C indicates that under such condition the nucleation of goethite was competitive with that of magnetite, hence transformation process to goethite was promoted. The formation of these two different iron oxides involves a dissolution-reprecipitation mechanism [28, 75, 138]. Apparently, goethite was generated from the dissolved amorphous ferric hydroxide or hydrous ferric oxide (HFO) or probably ferrihydrite. The increase of oxygen solubility in the aqueous solution due to temperature decrease can enhance the formation of these solid precursors. In every experiment, no specific measure was taken to minimise the amount of oxygen dissolved in the solution, e.g. by nitrogen bubbling, unintentionally creating a suitable environment for the precipitation of goethite. Under oxic condition, goethite is considered as one of the most stable compounds in the system; thus, it is the end member of many transformation routes [28]. The inhibition of hydrolysis reaction due to temperature decrease, as suggested by several authors [124, 126], probably affected the process to a lesser degree as in high alkaline condition the hydrolysis reaction is very fast [139]. The formation of goethite observed in this experiment is considered to be due to the combined effect of different operational parameters, i.e. temperature, Fe^{2+}/Fe_{T_IN}, and Fe_f. The latter two parameters determine the FI concentration in the system, as discussed below.

4.2.2 Effect of initial Fe^{2+}/Fe_T ratio and iron flux

Increasing initial Fe^{2+}/Fe_T ratio (Fe^{2+}/Fe_{T_IN}) resulted in the increased Fe^{2+}/Fe_{T_SP} ratio, as described in Figure 4.2. The relatively low Fe^{2+}/Fe_{T_SP} ratio obtained in the experiment at 23 °C can be related not only to the presence of goethite in the solid and but also to the Fe^{2+} deficiency in the magnetite structure. In case of the experiment at 30 °C, only the latter explanation is important as no goethite was found in the solid particles. In this experiment, about 48% of the influent Fe^{2+} was found in the magnetite structure.

To investigate the possibility of increasing Fe^{2+} incorporation efficiency and suppressing goethite formation, further experiments were conducted at a similar Fe^{2+}/Fe_{T_IN} ratio (0.364) but different iron flux (Fe_f) values. The Fe^{2+}/Fe_{T_SP} ratios found in these experiments at pH 10.5 and 9.5 are presented in Figure 4.4. Increasing Fe_f appeared to result in a significant increase of the Fe^{2+}/Fe_{T_SP} ratio (Figure 4.4a and 4.4b). For the experiment at Fe_f of 17.6 mg $l^{-1}min^{-1}$ and pH 10.5, the Fe^{2+}/Fe_{T_SP} ratio was found to be around 0.22 resulting in the Fe^{2+} incorporation efficiency of about 60%. On the other hand, the experiment at Fe_f of 8.8 mg $l^{-1}min^{-1}$ under a similar pH condition resulted in a significantly lower Fe^{2+}/Fe_{T_SP} ratio and the formation of some goethite particles, as observed by SEM (Figure 4.5a). A similar behaviour was also observed in the experiments at pH 9.5. It seems that under low Fe_f value the formation of goethite was enhanced even at 30 °C, suggesting that in the current system Fe_f had a more significant role than temperature in promoting the formation of magnetite.

The above findings reveal that a high value of Fe_f combined with a Fe^{2+}/Fe_{T_IN} ratio

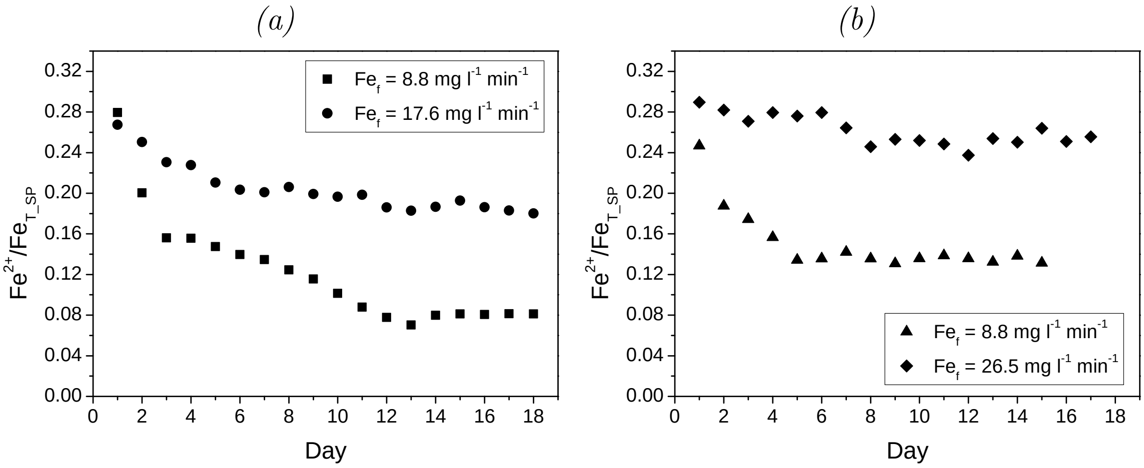

Figure 4.4: Fe^{2+}/Fe_T *ratios in the solid particles obtained at 30* °C, *different iron fluxes, pH (a) 10.5 and (b) 9.5.*

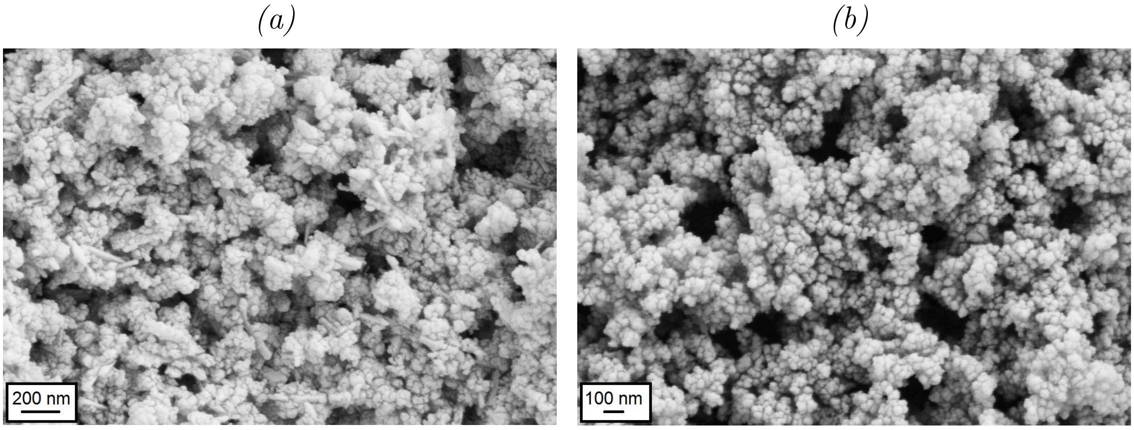

Figure 4.5: SEM images of the solid particles obtained at 30 °C, *pH 10.5,* $Fe^{2+}/Fe_{T\_IN} = 0.364$, *iron flux of (a) 8.8 mg* $l^{-1}min^{-1}$ *and (b) 17.6 mg* $l^{-1}min^{-1}$.

above 0.33 are favourable for the formation of magnetite under the current experimental conditions. As this condition resulted in a high ferrous intermediate (FI) concentration in the reactor, it can be deduced that a certain level of FI is required to ensure the formation of magnetite only. It was found that the minimum FI concentration in the reactor required for the magnetite synthesis at 30 °C by the stoichiometric method was around 500 mg/l, which is similar to the value found in the synthesis by the oxidation method reported in the literature [127]. This result suggests a similar threshold of FI concentration, despite the different synthesis procedures. However, a higher FI threshold is required for the synthesis at a lower temperature (< 30 °C).

The requirement of high Fe(II) background concentration in the system is related to the fundamental role of electron transfer between Fe^{2+} and Fe^{3+} ions to bring local structure arrangement and drive spinel ordering during magnetite precipitation (Section 4.1.2). The Fe^{2+}-Fe^{3+} electron mobility ensures the transformation of solid precursors into spinel. Increasing Fe(II) level in the system accelerates spinel ordering; soluble complexes contain too much Fe(II) for goethite to precipitate and only magnetite crystallises [140].

The favourable effect of a high Fe_f value obtained in this study implicates that the synthesis of magnetite by the stoichiometric method can proceed at a higher reaction rate. This might be important for the process application as a smaller reactor can be employed for the synthesis. In case of the oxidation method, the reaction rate is limited by the ferrous oxidation rate, which was found by Morgan et al. [18] to be about $12.8\,\mathrm{mg\,l^{-1}min^{-1}}$. In this respect, the stoichiometric method seems to have an advantage over the oxidation method.

The non-stoichiometric character of magnetite obtained in every experiment suggests that this iron oxide is sensitive to the oxidation process, as indicated by several authors [28, 33, 128]. The high reactivity of magnetite toward oxidation is obviously due to the relatively small particle size (high surface-to-volume ratio) and high electron mobility in the bulk of magnetite [33]. Kiyama [120] suggested that the Fe^{2+} ions should diffuse toward the surface of Fe_3O_4 particles in order for the oxidation reaction to take place. Because the oxidation of Fe_3O_4 particles occurs topotaxially and its rate depends on the surface area, the Fe^{2+} content in each Fe_3O_4 particle is also determined by its particle size.

4.2.3 Effect of pH

To investigate the effect of pH, experiments were conducted at two different pH values (i.e. pH 10.5 and 9.5), while keeping the other experimental conditions the same. The results are given in Figure 4.6. It can be seen that the Fe^{2+}/Fe_{T_SP} ratio obtained at pH 9.5 was slightly larger than that obtained at pH 10.5 (0.26 vs. 0.23 for the experiment at pH 9.5 and 10.5, respectively). It is also noticed that a reduction in the Fe^{2+}/Fe_{T_IN} ratio from 0.373 to 0.364 at pH 9.5 resulted in the decreased Fe^{2+} content in the particles (Figure 4.6), indicating a similar trend as observed in the experiments at pH 10.5 (see Figure 4.2).

The XRD patterns of solid samples were typical of spinel and no other phase was identified. SEM observation showed that the particles synthesised at pH 9.5 consisted of a mixture of spherical and octahedral particles with a size around 50–200 nm across (Figure 4.7a). On the other hand, spherical particles with a more homogeneous size of about 40–50 nm were found in the experiment at pH 10.5 (Figure 4.7b). This result indicates a decrease in the particle size with increasing synthesis pH.

It has been suggested by several authors [28, 37] that the dominant system parameter governing the shapes and sizes of crystalline solid is the supersaturation degree (see Chap-

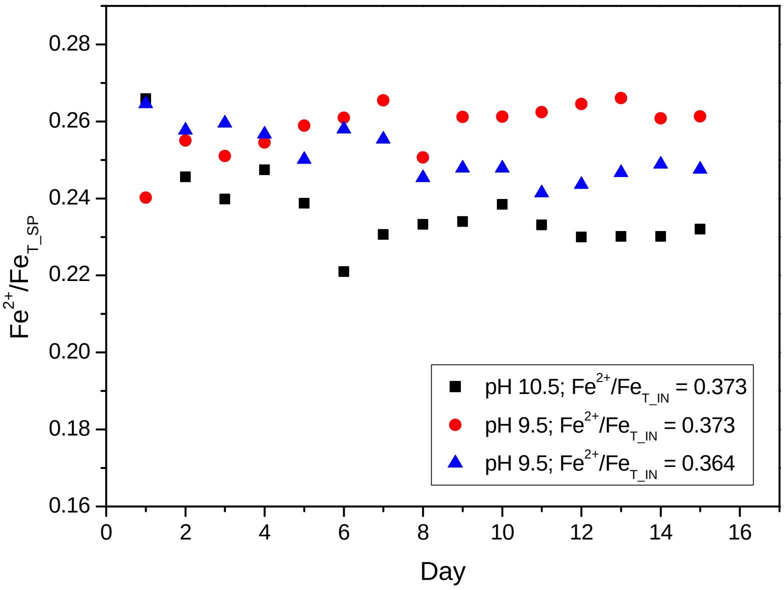

Figure 4.6: Fe^{2+}/Fe_T ratios in the solid particles obtained at 30°C, $Fe_f = 17.6\,mg\,l^{-1} min^{-1}$, and two different pH values.

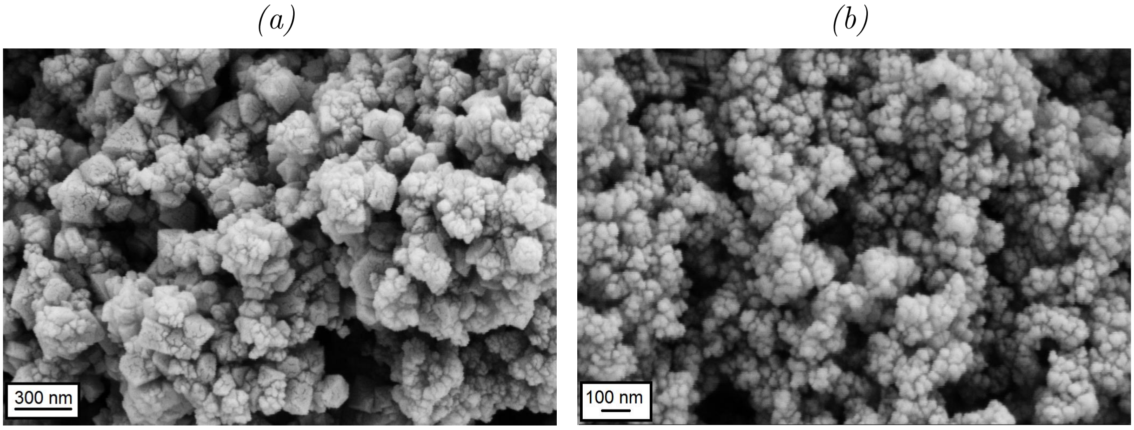
(a) *(b)*

Figure 4.7: SEM images of magnetite obtained at 30°C, $Fe_f = 17.6\ mg\ l^{-1} min^{-1}$, $Fe^{2+}/Fe_{T\_IN} = 0.373$, pH (a) 9.5 and (b) 10.5.

ter 2.2.2). Under high supersaturation, nucleation rate is high leading to the production of a large number of small particles which eventually aggregate to give larger ones. Under low supersaturation, nucleation rate is low and particles tend to grow in size resulting in a relatively small number of larger size particles [126, 141]. A slightly bigger particle size obtained in the experiment at Fe_f of 17.6 mg l^{-1}min^{-1} compared to that found at Fe_f of 26.5 mg l^{-1}min^{-1} under the same precipitation pH (9.5) indicates the influence of such kinetic aspect on the particle size. However, this difference was relatively small in comparison with the particle size difference obtained at different pH values described above. Apparently, kinetic is not the only limiting factor governing the particle size.

The variation in the particle size obtained at different pH values may reflect the role of the thermodynamic aspect on the particle size control. This aspect is rarely considered but it has been suggested by Jolivet and coworkers [132, 142, 143]. They observed an increase in the particle size with the decrease of pH value from 12 to 9.5 and suggested the following explanation. The increase of particle size often involves the Ostwald ripening process (see Chapter 2.2.2). Due to kinetic restrictions, this process stops at a more or less advanced stage [142]. However, in response to a change in at least one of the suspension conditions, such as pH, the particle size is modified. When the pH of the solution is increased, the surface electrical charge will be increased inducing a decrease in the interfacial tension. At last the contribution of the surface energy on the free enthalpy of particle formation is lowered, allowing the formation of small particles with large surface area [142, 143].

4.3 Conclusions

Precipitation of magnetite under ambient condition requires a careful control of synthesis conditions. A small increase in the synthesis temperature could increase the Fe^{2+} content in the magnetite. A similar effect was also observed when the Fe^{2+}/Fe_{T_IN} ratio was increased. The value of iron flux employed in the system seemed to be a critical parameter affecting the composition of the end-product. A large excess of Fe(II) in the system, which was obtained by maintaining a high value of iron flux in combination with a Fe^{2+}/Fe_{T_IN} ratio close to or above 0.33, leads the exclusive establishment of magnetite structure at ambient temperatures. Electron transfer between Fe^{2+} and Fe^{3+} ions is thus essential for spinel ordering and its presence implies that structural rearrangement have occurred. The particle size of magnetite was found to decrease with the slight increase in the synthesis pH value. Such a correlation is more relevant to thermodynamics rather than kinetics.

Chapter 5

Incorporation of Metal Ions into Ferrites at Elevated Temperatures

The incorporation extent of non-iron metal (Me) into the ferrite structure is an essential parameter for the application of ferrite process as it determines the external iron addition demand. The latter has a significant effect on the whole chemical cost, especially when the process is going to be applied for wastewater with low iron content.

Full Me incorporation into the ferrite structure, i.e. x in the ferrite formula $Me_xFe_{3\text{-}x}O_4$ equals to 1.0 or 2.0 for divalent or trivalent Me, respectively, is frequently obtained when synthesis is carried out via high temperature solid-state reactions [49, 53, 54]. In the ferrite synthesised by coprecipitation of divalent Me with Fe(III) (i.e. without oxidation) at moderate temperatures (60–100 °C), full incorporation was also reported by several authors [138, 144, 145]. However, when ferrite is precipitated via Fe(II)-oxidation method, the incorporation of certain Me was reported to be limited . A comprehensive and reliable data set of maximal incorporation extent of different non-iron metals into ferrite under these conditions seems to be lacking. Furthermore, the reasons responsible for the limited incorporation extent of some non-iron metals, as compared to others, still cannot be fully understood.

Accordingly, the current work attempts to comprehensively investigate the ferrite formation involving Fe(II)-oxidation methods at elevated temperatures. The maximal attainable incorporation extent of six non-iron metals, i.e. Zn^{2+}, Co^{2+}, Ni^{2+}, Cd^{2+}, Cr^{3+}, and Al^{3+} into the ferrite is reevaluated by employing multiple characterisation techniques. The new data set is then used to propose the most probable mechanism governing the incorporation extent of each examined metal ion. The results of the investigation are presented in the following sections and have been published in [146].

The chemical stability of ferrite is also essential to assess as the toxic metals may be released back to the environment and become bio-available. The release of metals is thus investigated under different acidic conditions aimed at evaluating the effect of metal incorporation on the dissolution stability and the pollution potential of the produced ferrites.

5.1 Previous works

To address the issue of the extent and mechanism of metal incorporation into the ferrite structure, a comprehensive literature survey was firstly carried out. The results are presented in this section. A review of the literatures on ferrite dissolution stability is presented in Chapter 2.5.

5.1.1 Extent of metal ion incorporation

Table 5.1 summaries the maximal incorporation extent of six non-iron metals into the ferrite reported by different studies together with the relevant experimental conditions. It can be seen that there is a reasonable agreement regarding the incorporation extent of Zn^{2+}, Co^{2+}, Cd^{2+}, and Al^{3+}, despite the significant differences in the synthesis procedure. However, the reported incorporation extents of Ni^{2+} and Cr^{3+} are significantly different.

Table 5.1: Reported incorporation extents (IE) of non-iron metal (Me) into ferrites produced by Fe(II) oxidation with the important synthesis conditions [146].

Me	Initial Me/Fe_T	IE Me/Fe_T	IE x	Oxidant	Reaction T(°C)	Reaction pH	Product rinsing pH	Ref.
Zn^{2+}	0.5	0.5	1.0	O_2	65	10	4.0	[147]
	0.5	0.5	1.0	NO_3^-	90	St	H	[148]
	0.5	0.5	1.0	NO_3^-	90	3.5→13	2.0	TW
Co^{2+}	0.5	0.5	1.0	O_2	70	10.5	H	[149]
	0.5	0.5	1.0	NO_3^-	90	St	-	[86]
	0.5	0.49	0.98	NO_3^-	90	8→4	-	[150]
	0.50	0.47	0.96	NO_3^-	90	3.5→13	2.0	TW
Ni^{2+}	0.25	0.21	0.52	O_2	65	10	4.0	[151]
	0.33	0.28	0.65	O_2	60	10	-	[152]
	1.0	0.35	0.78	NO_3^-	90	St	~0.75	[76]
	NI	0.28	0.66	NO_3^-	90	St	~0.75	[153]
	NI	0.5	1.0	NO_3^-	100	St	-	[154]
	0.43	0.28	0.66	NO_3^-	90	9–11	H	[155]
	0.5	0.07	~0.2	NO_3^-	90	3.5→13	2.0	TW

Continued on next page ...

Me	Initial Me/Fe_T	IE Me/Fe_T	IE x	Oxidant	Reaction T(°C)	Reaction pH	Product rinsing pH	Ref.
Al^{3+}	0.2	0.08	0.23	O_2	65	10.5	11.4	[156]
	0.23	0.14	0.37	O_2	80	11.7	H	[157]
	0.5	0.2	0.49	NO_3^-	90	2.5→12	2.0	TW
Cd^{2+}	>0.2	0.13	0.35	O_2	65	9.0	5.0	[158]
	>0.33	0.09	0.25	NO_3^-	90	3.5→13	2.0	TW
Cr^{3+}	NI	0.16	0.42	NO_3^-	80	7.0	1.2	[159]
	NI	0.5	1.0	NO_3^-	100	St	-	[154]
	S	0.0	0.0	NO_3^-	75–95	S	NI	[160]
	0.067	0.07	0.19	O_2	50	9.0	-	[161]
	0.333	0.24	0.59	O_2	60	10.0	-	[162]
	0.081	0.07	0.19	NO_3^-	90	9–11	H	[155]
	1.0	0.0	0	NO_3^-	90	2.5→12	2.0	TW

Note:
x in $Me_xFe_{3\text{-}x}O_4$;
NI = not indicated;
S = several;
St = stoichiometric OH^- addition ($[OH^-] = 2[Me(II)]$, initial pH is around 9–10 and final pH can be as low as 2.5 [120]);
H = rinsing with distilled water, usually followed by subsequent rinsing with acetone;
TW = this work

5.1.2 Mechanism of metal ion incorporation

Formation of ferrite is believed to progress mainly through a dissolution-reprecipitation process [33, 131, 132]. Tamaura et al. [14] suggested two pathways by which ferrite precipitates from the solution at temperatures above 65 °C: (1) the green rust (GR) pathway at pH 7–10 and (2) the γ-FeOOH pathway at pH 10.5–11. In the first pathway, GR-II is formed in the course of oxidation reaction. The Me ions in the GR-II are transferred into the lattice site of the spinel structure by further oxidation of the GR-II. However, Tamaura et al. [163] found that Me-bearing GR-II could also be transformed spontaneously to Me-bearing ferrite. When the reaction pH is over 10.5, the ferrites are formed not from the GR-II, but from the γ-FeOOH phase. In the course of the crystal growth of the ferrite, the adsorption of the Fe^{2+} and Me ions, and the oxidation of the adsorbed Fe^{2+} ion takes place on the surface of the ferrite particles. The γ-FeOOH phase, which is formed by oxidation of the adsorbed Fe^{2+} ions, is transformed into a ferrite layer by the adsorption of the Fe^{2+} and Me ions. At 25 °C, γ-FeOOH was not directly transformed into the ferrite but gave rise to the metastable intermediate product, i.e. GR-II [164]. Since the particle shapes of γ-FeOOH (rod type) and GR-II (hexagonal plate type) are different, it was assumed that the intermediate is formed from γ-FeOOH by a dissolution-reprecipitation process. Several authors [138, 165] also found that the interaction of soluble Me^{2+} species with ferrihydrite at 70 °C could lead to the formation of spinel phase. It was considered that the spinel phase nucleates in the water layer adsorbed on or adjacent to the surfaces of the ferrihydrite particles. These nuclei grow by addition of soluble Me-Fe-hydroxo complexes released by the dissolution of Me-ferrihydrite co-precipitate.

Different parameters have been suggested to control the incorporation extent of different Me ions. No general agreement was, however, found in the literatures regarding the dominant parameter, as reflected by the following literature review.

Cornell and Schwertmann [28] proposed some parameters influencing the incorporation extent of cations into iron oxides, i.e. similarity of the valences and the ionic radii of the cations (about 18% difference can be tolerated for the substitution of Fe^{3+} with Me^{3+} in octahedral coordination), structural strain development, changes in lattice energy and crystal field stabilisation energy (CFSE), structural defects, synthesis conditions (such as pH, temperature, ratio of Me to Fe), nucleation and growth rates of metal precursors. In the case of isomorphous Me substitution in goethite, it was reported to be determined by the degree of congruency of dissolution of the precursors. Non-iron metals, which were released more rapidly than Fe, were only adsorbed on the surface of the goethite and were not structurally incorporated [138].

Schwertmann and Murad [157] reported that the development of structural strain with the increasing Al^{3+} substitution in the ferrite synthesised at ambient temperatures limited the capacity of the magnetite structure to incorporate Al^{3+}. At higher Al^{3+} concentration, goethite was found to replace magnetite due to the higher capacity of its structure to tolerate more Al^{3+}.

To explain the incorporation behaviour of small amount of metals ($< 1\%$), Sidhu et al. [92] referred to two factors. The first is the ionic radius. It was stated that if the properties of two elements are similar, the element with the smaller ionic radius is preferentially incorporated into the mineral (Goldschmidt rule). This principle alone, however, could not explain the incorporation behaviour of several divalent Me ions which have very similar ionic radii to that of Fe^{2+}. Thus, it was suggested that when the ionic radii of two elements are similar and electronegativities differ by more than 0.1, the element with the smaller electronegativity is preferentially incorporated into the structure because it forms a more ionic bond with oxygen.

Tang et al. [145] proposed that the incorporation of Mg^{2+}, Mn^{2+}, Ni^{2+}, and Co^{2+} was directed by the minimum pH values (pH_{min}) at which the corresponding metal hydroxides precipitate. The closer the $\mathrm{pH_{min}}$ of Me to that of Fe^{2+}, the easier they could precipitate simultaneously.

Yang et al. [155] deduced that the capability of Zn^{2+}, Ni^{2+}, and Cr^{3+} entering the ferrite structure might have some relation with the solubility product constant of their corresponding hydroxides. Metal with a relatively high hydroxide solubility product might enter the spinel lattice more easily.

Tamaura [163] suggested that the incorporation extent of Zn^{2+}, Ni^{2+}, and Fe^{2+} into the ferrite structure during its spontaneous transformation reaction from GR-II was related to the ease of hydrolysis of those metal ions. Because hydrolysed species (MOH^{+}) are preferentially incorporated into the ferrite, they hypothesised that the first hydrolysis constant ($^{*}K_1$) of metal directs the ease of incorporation. The Me ion with a higher hydrolysis constant can be more readily incorporated into the ferrites. Because the differences in the ligand field stabilisation energy (LFSE) of these metal ions between GR-II and ferrites were zero, they concluded that LFSE could not satisfactorily explain the incorporation behaviour of metal ions into the spinel structure.

Tamaura and Abe [166] suggested that the incorporation of Me ions proceeds through the adsorption-incorporation mechanism which is similar to the γ-FeOOH pathway [14] described above. They concluded that the Me content in the ferrite is determined by the adsorption equilibrium of the Me ion and Fe^{2+} ion on the surface of γ-FeOOH. Thus, the lower the pH of the adsorption edges of the Me ions, the higher the Me content in the ferrites.

Regazzoni and Matijević [76] suggested the following phase transformation of Ni ferrite formation. First, divalent metal hydroxides gels changed into GR by oxidation. On further oxidative aging, finely dispersed primary particles aggregated to give colloidal spheres of Ni ferrite. The free energy formation change (ΔG_f^0) of $MeFe_2O_4$ (where Me = Co^{2+}, Ni^{2+}, or Mg^{2+}) was suggested as the main factor controlling the relative enrichment of the three Me ions in the ferrite. By applying a similar approach, they were also able to explain the higher incorporation extent of Co^{2+} compared to that of Ni^{2+} in the mixed Co-Ni ferrite particles [77].

Huang and Matijević [74] argued that the approximation of free energy changes did not take into account the surface energy of small particles. Thus, it was not the key factor for the limited incorporation of certain Me ion, such as Ni^{2+}. Other factors, i.e. solubility of metal hydroxides, radii of metal ions, and crystal distortion were also considered insignificant for controlling the formation of Ni ferrite. Instead, they suggested the crystal field activation energy (CFAE) as an important factor for the formation of Ni ferrite. The CFAE of Ni^{2+} complex formation was lower than that of most other first transition metal divalent cations. Therefore, the release of Ni^{2+} from $Ni(OH)_2$ precursor and their adsorption onto $Fe(OH)_3$ was slower, resulting in a lower rate formation of Ni ferrite.

5.2 Determination of incorporation maxima of six metal ions into ferrites

The incorporation extent of Me into the ferrite structure was evaluated based on the three different properties of the obtained products: (1) chemical composition, determined after complete dissolution, (2) crystalline phases and unit cell sizes, determined through XRD analysis, (3) metal distributions along the particle depth based on the dissolution congruency test. Complementarily, the infrared spectra of the solids were examined.

5.2.1 Chemical composition

Based on the chemical analysis of the solid particles, the molar ratio of non-iron metal (Me) to total iron (Fe_T) in the particles (i.e. Me/Fe_{T_SP}) can be determined. This result is depicted in Figure 5.1 as a function of the corresponding ratio in the initial solution (Me/Fe_{T_IN}). As can be seen, only Zn^{2+} and Co^{2+} could attain the designated Me/Fe_{T_SP} ratio, suggesting a complete incorporation for these ions. It is noted that, although the Cr^{3+}/Fe_{T_SP} ratio was not similar to the Cr^{3+}/Fe_{T_IN} ratio in the range of 0.09–0.5, the opposite was true in range of 0.7–2.0 (data not shown).

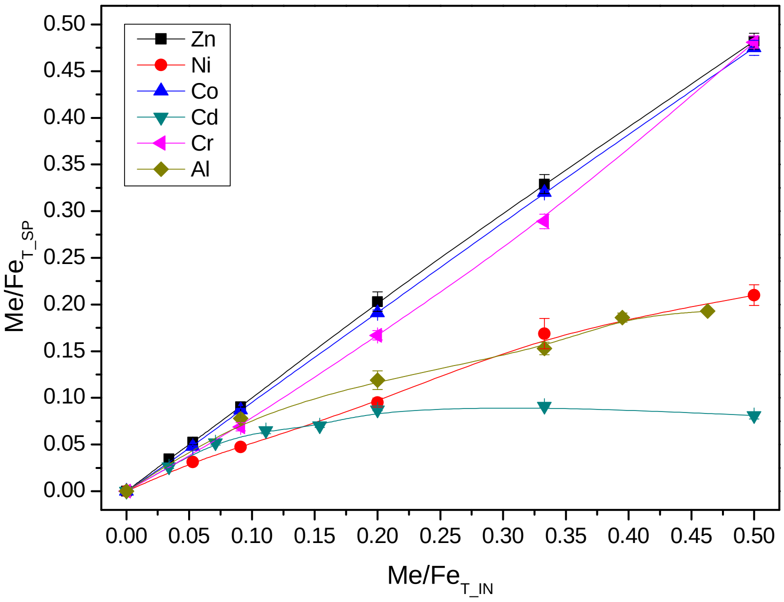

Figure 5.1: Me/Fe$_T$ ratio in the particles synthesised at 90°C as a function of Me/Fe$_{T\_IN}$.

Less than 100% Me incorporation observed for the other Me indicates that a proportion of these ions existed as a non-spinel phase, which was readily extracted during the rinsing procedure at pH 2. This phase was present either on the surface of the crystal ferrite or as a separate solid entity. Since the Me incorporation extents based on the chemical composition analysis still need to be confirmed by other analyses, the term incorporation extent, for the time being, is referred to as the association extent. Thus, the maximal association extent in terms of x in the formula $Me_xFe_{3\text{-}x}O_4$, was 2.0 for Cr^{3+}, 1.0 for Zn^{2+} and Co^{2+}, 0.52 for Ni^{2+}, 0.49 for Al^{3+}, and 0.25 for Cd^{2+}.

Further chemical analysis was conducted to determine the oxidation state of the ferrite. It is noted that the total divalent (M^{2+}) to total trivalent (M^{3+}) metal ratio of an ideal ferrite (termed stoichiometric ferrite) is 0.5, analogous to that of stoichiometric magnetite (Chapter 4). Figure 5.2 illustrates the divalent to trivalent metal ratio in the solid particles (M^{2+}/M^{3+}_{SP}) as a function of Me/Fe_{T_SP}. The plot for Cr^{3+} was omitted from this figure as Cr^{3+} is shown later to hardly enter the ferrite structure. The solid product of the Cr^{3+} incorporation experiments is hereafter named Cr-associated ferrite.

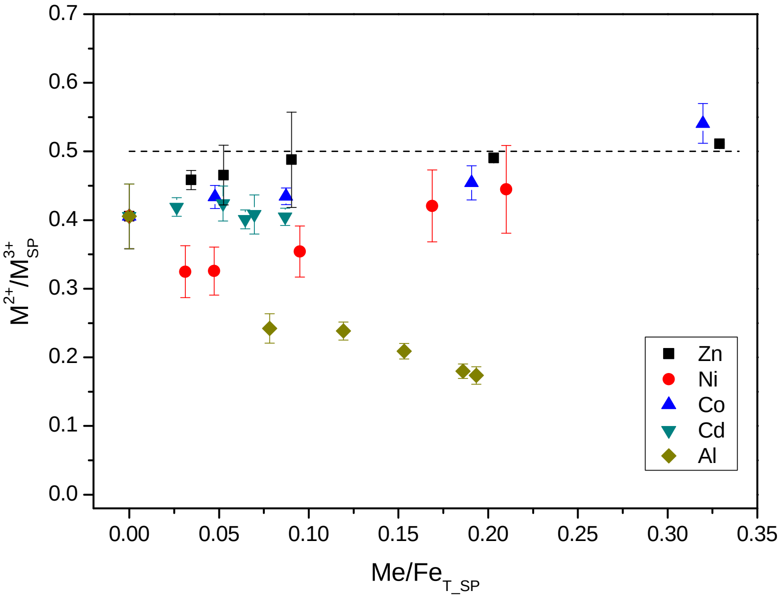

Figure 5.2: Ratio of divalent to trivalent metal ions in the particles synthesised at 90°C. *The dashed line represents the M^{2+}/M^{3+}_{SP} ratio of an ideal ferrite.*

It can be deduced from Figure 5.2 that all of the synthesised ferrites, except those comprising a high content of Zn^{2+} and Co^{2+} can be characterised as non-stoichiometric. In other words, they have a significant divalent cation deficiency. The non-stoichiometric character of Me-substituted ferrites was also reported by several authors to form under similar experimental conditions [94, 158, 167].

The high oxidation level of ferrite can be considered not high enough to explain the limited incorporation extent of several Me (due to electroneutrality consideration), except maybe for Al^{3+}. However, this oxidation level can influence to a certain extent the determination of Me content in the ferrite based on the change in the unit cell size. At identical Me content, ferrite with a high oxidation level can be expected to have a smaller unit cell size due to the lack of Fe^{2+} ions in its structure, as discussed further in the following section.

5.2.2 Crystalline phases and unit cell sizes

The X-ray diffraction patterns of all the solid particles indicated the presence of spinel-type compounds only. However, a small proportion of goethite could be identified in the XRD pattern of Ni ferrite, particularly the one produced at the Ni^{2+}/Fe_{T_IN} ratio of 0.5. The measured unit cell sizes of the spinel calculated based on the XRD patterns as a function of the Me content in the ferrite structure is depicted in Figure 5.3. The known unit cell size of the corresponding end-member, i.e. $MeFe_2O_4$ and $FeMe_2O_4$ for divalent and trivalent cation, respectively, based on the standard diffraction file is given in Table 5.2 as a reference.

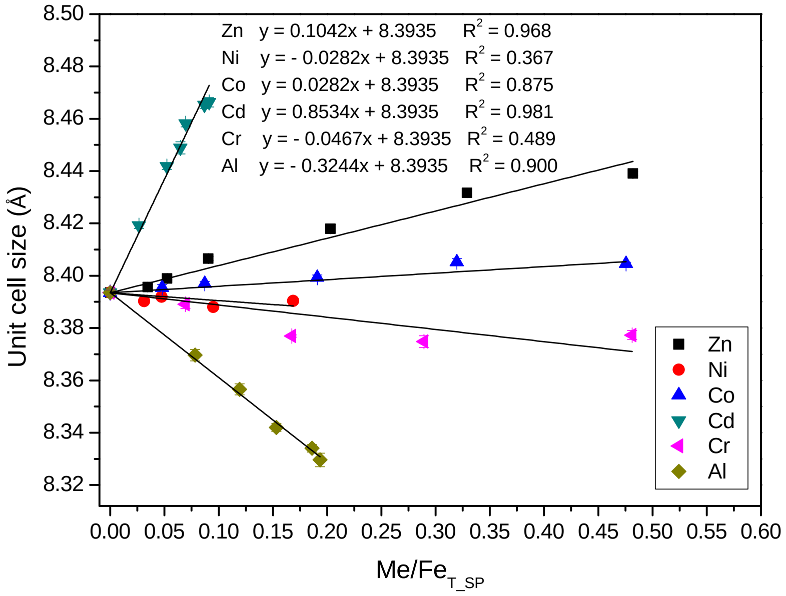

Figure 5.3: Unit cell size of the spinel phase synthesised at 90 °C *as a function of Me content in the product.*

As shown in Figure 5.3, the unit cell size (a) of Zn ferrite increases linearly with increasing Zn^{2+} content, indicating that the change in the a value of Zn ferrite follows the Vegard rule (i.e. a linear relationship between the metal content and the unit cell size). The a values of Zn ferrite obtained in this work are similar to those reported by Andrés-Vergés, et al. [148]. The unit cell enlargement of Zn ferrite is related to the strong tetrahedral site preference of Zn^{2+} [53, 168]. Since the ionic radius of Zn^{2+} (0.58 Å) is larger than that of Fe^{3+} (0.485 Å), the four oxygen atoms constituting tetrahedral sites have to move outward along the lattice diagonal to provide more space for Zn^{2+}, resulting in the increased unit cell size of the ferrite.

Data for Co ferrite revealed a slight increase in the a value of Co ferrite with Co^{2+} content (Figure 5.3). It was found that the measured a value for $CoFe_2O_4$ is about 8.4052 Å, which is slightly larger than the value reported in some previous works, i.e.

Table 5.2: Known unit cell size (a) of some ferrites [146].

Ferrite	JCPDS	Unit cell size (Å)
$FeFe_2O_4$	19-0629	8.396
$CdFe_2O_4$	22-1063	8.699
$ZnFe_2O_4$	22-1012	8.441
$CoFe_2O_4$	22-1086	8.391
$NiFe_2O_4$	10-0325	8.339
$FeCr_2O_4$	34-140	8.379
$FeAl_2O_4$	34-192	8.153

8.38 Å [149, 169] and 8.3849 Å [86]. The unit cell size given in the standard diffraction file also shows a different value, i.e. about 8.391 Å. Cobalt was identified to have octahedral site preference [170, 171]. In this case, it can be expected that the substitution process of Fe^{2+} by Co^{2+} in the ferrite structure does not change significantly the unit cell size of the spinel compound because the effective ionic radii of Co^{2+} and Fe^{2+} in octahedral coordination are relatively similar, i.e. 0.72 Å and 0.74 Å for Co^{2+} and Fe^{2+}, respectively (see Table 2.4).

The a value of Cd ferrite was found to increase significantly with the Cd^{2+} content. It has been suggested that Cd^{2+} ions prefer to occupy tetrahedral site [53]. Due to a considerable difference in the ionic radius of Cd^{2+} and Fe^{3+} in the tetrahedral coordination, i.e. 0.78 Å and 0.485 Å for Cd^{2+} and Fe^{3+}, respectively, the incorporation of Cd^{2+} in the ferrite structure causes a significant increase in the unit cell size. The unit cell size of the end member ($CdFe_2O_4$) estimated by extrapolation of the trend line in Figure 5.3 is close to that of Cd ferrite produced by the solid state reaction, i.e. 8.705 Å [49].

In contrast to Cd^{2+} incorporation, the incorporation of Al^{3+} into the ferrite structure decreased the unit cell size. Figure 5.3 shows the linear correlation between the a value and Al^{3+} content. A similar trend was also reported by Ito et al. [156]. The contraction of the unit cell size of Al ferrite can be related particularly to its smaller ionic radius compared to that of Fe (see Table 2.4).

The unit cell size of Ni ferrite barely changed with the increased Ni^{2+} content. This finding might indicate that either the incorporation of Ni^{2+} did not change the unit cell size or Ni^{2+} was not incorporated into the spinel structure. Due to the favourable fit of the charge distribution of this ion in the crystal field of the octahedral site, Ni^{2+} ions prefer to occupy the octahedral positions in the spinel lattice [151, 168, 172]. The unit cell of Ni ferrite is expected to decrease with increasing Ni^{2+} content as the ionic radius of Ni^{2+} (0.69 Å) is smaller than that of Fe^{2+} (0.74 Å). In accord with this conjecture, Huang and Matijević [74] reported that $NiFe_2O_4$ produced by calcination had a significantly lower unit cell size than that of magnetite. Interestingly, they found that the a value of Ni ferrite increased as x (in $Ni_xFe_{3\text{-}x}O_4$) increased from 0 to 0.1, while at a higher x value (0.3–1.0) it decreased.

Figure 5.3 indicates a decrease in the unit cell size of Cr-associated ferrite, leading to the a value of 8.377 Å for the Cr^{3+}/Fe_{T_SP} ratio of 0.48. Furthermore, it was found that between Cr^{3+}/Fe_{T_SP} of 0.7 and 2.0, the a value increased to a maximal value of about 8.388 Å (data not shown). This result implies that the change in unit cell parameter of Cr-associated ferrite deviates from Vegard's rule. This deviation was also reported by some researchers for Cr ferrites produced by solid-state reaction [51, 173]. The result of unit cell size for $Cr^{3+}/Fe_{T\_SP} \leq 0.48$ may thus support the previous result of chemical composition analysis. However, the M^{2+}/M^{3+}_{SP} ratio for Cr-associated ferrite in this range was very low ($\sim$0.25) indicating the oxidised nature of the ferrite, which could also contribute to the observed reduction in the unit cell size. It should be mentioned that the XRD patterns of Cr-associated ferrite showed a reduction in the peak intensity and an increase in the background intensity with increasing Cr^{3+}/Fe_{T_SP}. This result may suggest an increase content of amorphous phase with increasing Cr^{3+} content.

In conclusion, the XRD analyses support the incorporation trend of Zn^{2+}, Co^{2+}, Cd^{2+}, and Al^{3+} obtained previously from the chemical composition analysis. However, they could not satisfactorily explain the incorporation behaviour of Ni^{2+} and Cr^{3+}.

5.2.3 Metal spatial distribution

Analysis of sequential solution extracts during the dissolution of iron oxide can provide information regarding the distribution of Me and Fe within crystals of iron oxide. This method was employed in several studies not only for ferrite [92] but also for other iron oxides such as hematite and goethite [138, 174–177]. The congruency dissolution of Me and Fe is indicated by a line of unity slope for plots of fraction of Me vs. fraction of Fe dissolved. If Me and Fe dissolve at a similar rate, Me is distributed uniformly throughout the crystal. On the contrary, if Me dissolves faster (above the unity line) or slower (below the unity line) than Fe, Me is concentrated at the crystal periphery or toward the core, respectively. Heterogeneous dissolution may also indicate the presence of another separate phase [28].

Representative results of the dissolution congruency tests of the solid particles in 12.8% HCl solution are presented in Figure 5.4. All dissolution data indicate that Me and Fe in the Co, Cd, and Al ferrite dissolved congruently, suggesting that Co^{2+}, Cd^{2+}, and Al^{3+} are uniformly distributed in the particles. The Zn ferrites also dissolved congruently at the Zn^{2+}/Fe_{T_SP} ratios of 0.034, 0.052, and 0.48. However, the slopes of the dissolution curves at the Zn^{2+}/Fe_{T_SP} ratios of 0.09, 0.2 and 0.033 were below unity, indicating that at these ratios zinc was located closer to the particle core relative to iron.

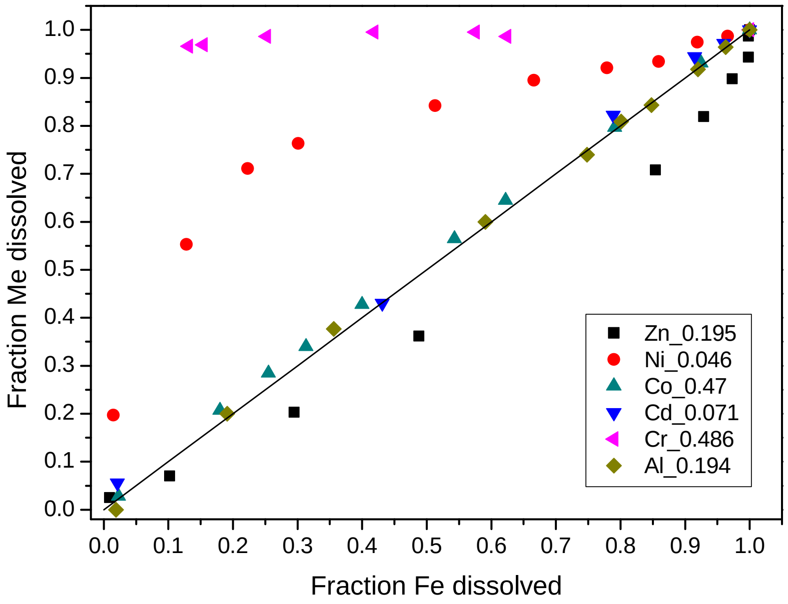

Figure 5.4: Plots of the fraction of Me versus Fe dissolved in 12.8% HCl solution for some representative solid particles produced at 90 °C*. The legend indicates the Me/*Fe_{T_SP} *ratio determined after washing with acidic solution (pH 2).*

The plots of the fraction of Ni^{2+} vs. Fe released for all Ni ferrites were above the unity line, suggesting that nickel concentrated toward the particle surface. At higher Ni^{2+} content, an increased portion (up to 60%) of the final Ni concentration was released immediately after dissolution started, whereas Fe was dissolved gradually over 2 h. This suggests that at a high Ni^{2+}/Fe_{T_SP} ratio, a significant amount of Ni was present as a non-ferrite phase that was not removed during the rinsing procedure. Uneven distribution of Ni and Fe in the Ni ferrite, $Ni_{0.53}Fe_{2.47}O_4$, was also found by Regazzoni and Matijević [178], although a congruent dissolution was reported by Sidhu et al. [92] for magnetite containing trace amounts of Ni^{2+} (∼0.2%).

Considering the finding that approximately 60% of Ni content in the ferrite with Ni^{2+}/Fe_{T_SP} of 0.2 (i.e. the highest attainable ratio obtained based on the chemical composition analysis) existed as a non-spinel phase, the maximal actual extent of Ni^{2+} incorporation achieved in this work, in terms of Ni^{2+}/Fe_{T_SP}, was 0.08 or $x = 0.2$.

The low incorporation capacity of Ni^{2+} found in this work is, however, not in agreement with other studies [76, 153] in which a much higher incorporation extent was achieved even after rinsing the product with 1 M HNO_3 solution. This discrepancy can be attributed to the different synthesis procedure applied. In the current work, ferrite was synthesised by titration of the metal solution with OH^-, resulting in relatively low precipitation pH, thus leading to the formation of Fe(III)-based precursors such as ferrihydrite or GR. However, the higher Ni^{2+} incorporation extent was attained by coprecipitation of Fe(II) and Ni(II) hydroxide precursors [76]. The nature of the precursor(s) may have affected the crystallisation kinetic which eventually could have determined the characteristic of the end product. In light of this discrepancy, the maximal attainable incorporation extent for Ni^{2+} was adopted from another study [76].

The dissolution tests for all Cr-associated ferrite showed that almost all of the Cr^{3+} was released from the particles within 15 min from start, while Fe dissolved gradually over 3 h (except for a small portion which dissolved instantly). This observation suggest that Cr^{3+} did not enter the ferrite structure to any appreciable extent, and possibly formed a non-spinel solid phase which apparently endured the rinsing procedure. Only when the particles were dissolved under extreme acidic conditions (12.8% HCl solution), as applied in the dissolution test, the Cr-nonspinel phase can be released. So far, only the work of Matijević et al. [160] indicated a similar finding, probably because they rinsed the particles with 1 M HNO_3 (pH∼0.7) for 1 h (concluded from the other publication by the same authors [76]) creating a more aggressive rinsing condition than that applied by the other studies (see Table 5.1).

In order to confirm the accumulation of Cr on the particle's surface, a sample containing Cr^{3+}/Fe_{T_SP} of 0.48 was analysed further by X-ray photoelectron spectroscopy (XPS). Based on this analysis, the elemental composition within 7–8 nm outer particle layer was O = 68.3%, Cl = 12.5%, Cr = 8.1%, Fe = 8.1%, and S = 3.1% (neglecting trace amount of Na). Thus, the ratio between metals (Fe and Cr) and oxygen in this surface layer was estimated to be about 0.24, much lower than in an ideal ferrite (0.75), indicating an excess of OH^- and/or H_2O in the particle surface. Furthermore, it was also estimated from XPS analysis that around 90% of the total chromium existed in this surface layer, assuming an average particle size of 62 nm estimated from SEM micrograph (see Section 5.3). The XPS analysis clearly indicates the accumulation of chromium at the particle surface, as suggested by the results of the dissolution congruency tests. The presence of most or all of the Cr in a relatively uniform Cr-rich layer surrounding an iron-rich (spinel) core is thus likely. A similar observation was recently reported by Viart et al. [179]. The XPS result for Ni ferrite with the Ni^{2+}/Fe_{T_SP} ratio of 0.096 indicated a similar trend, which was in agreement with the observation discussed above.

5.2.4 Infrared spectra of the precipitates

To corroborate the previous results regarding the existence of Ni- and Cr-non-spinel phase in the ferrite samples, further solid characterisation by FTIR spectroscopy was carried out. This method was suggested to be more suitable for the analysis of non-crystalline solids due to its sensitivity to local bond energies rather than to long range structural order. The latter is best characterised by XRD method [180].

Before discussing the features of the FTIR spectra of the solid products from the Ni^{2+} and Cr^{3+} incorporation experiments, it is necessary to describe the FTIR spectra of the other Me-substituted ferrites. The representative FTIR spectra of Zn, Co, Cd, Al ferrite are presented in Figure 5.5. The higher frequency band (ν_1) was observed at around 560–590 cm^{-1} and lower frequency band (ν_2) at around 400–440 cm^{-1}, typical of spinel phase [181]. Bands ν_1 and ν_2 are assigned to the stretching vibration due to the interactions between oxygen atoms and cations in tetrahedral and octahedral positions, respectively [50, 72, 182]. In addition to these bands, a broad band with a maximum at about 3400 cm^{-1} and a weak band at around 1600 cm^{-1} were seen. These bands are typical for the vibration of coordinated or adsorbed water molecules [183, 184]. Another very weak band was observed at about 1380 cm^{-1} which corresponds to carbonate. The presence of carbonate in these samples was probably structural in nature, inasmuch as surface-adsorbed carbonate would have been completely removed by evacuation when KBr pellets were pressed [180]. At about 1100 cm^{-1}, the existence of other weak bands assigned to the sulphate anion could also be identified [17, 185].

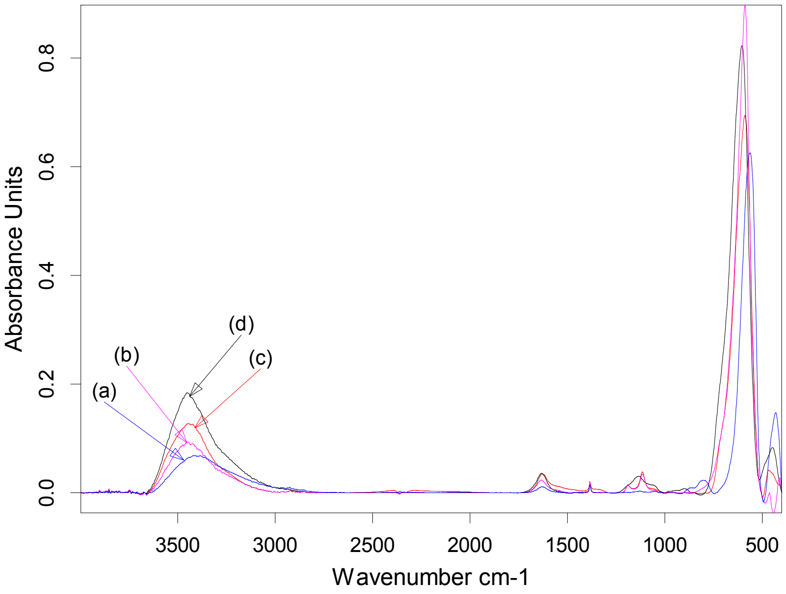

Figure 5.5: FTIR spectra of (a) Zn ferrite (Zn^{2+}/Fe_{T_SP} = 0.33),(b) Co ferrite (Co^{2+}/Fe_{T_SP} = 0.32), (c) Cd ferrite (Cd^{2+}/Fe_{T_SP} = 0.065), (d) Al ferrite (Al^{3+}/Fe_{T_SP} = 0.078) produced at 90°C.

Figure 5.6 illustrates two representative FTIR spectra of Ni ferrite. Besides the main bands assigned to the spinel phase, the FTIR spectra showed two bands at about 900 and 794 cm^{-1} which can be associated with the bending vibration of hydroxyl groups of goethite [177, 184], in agreement with the XRD analysis. The band intensities associated with water molecules (3400 cm^{-1} and 1600 cm^{-1}) appeared to increase with the $\mathrm{Ni}^{2+}/\mathrm{Fe}_{\mathrm{T\_SP}}$ ratio. A similar trend was also observed for the FTIR bands of anions, i.e. sulphate (at 1107 and 1180 cm^{-1}) and carbonate (1380 cm^{-1}). The prominent bands of molecular water and anions, particularly sulphate, may indicate the presence of a considerable amount of these compounds in the solid sample. These compounds were probably associated with the metals forming the Ni-non-spinel phase. This phase was reported by Kanzaki et al. [151] to have a composition similar to $Ni_{6.4}Fe_{6.4}SO_4[OH]_{16} \cdot 7\,H_2O$.

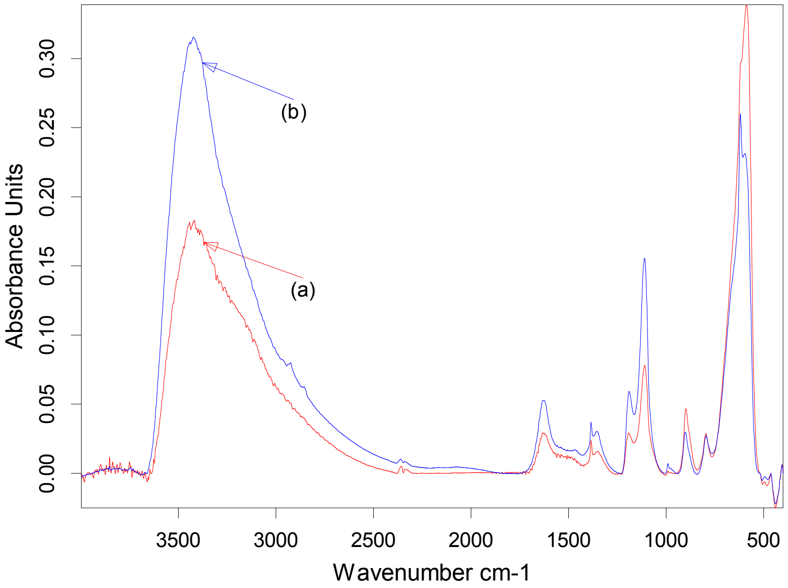

Figure 5.6: FTIR spectra of Ni ferrites produced at 90°C for Ni/Fe$_{T\_SP}$ ratio of (a) 0.095 and (b) 0.21.

The prominent feature of the water and anion bands could also be observed in the FTIR spectra of the Cr-associated ferrite. Some representative FTIR spectra are depicted in Figure 5.7 together with the spectrum of the solid precipitated from a $CrCl_3$ solution at pH 10.5, considered as non-crystalline (amorphous) chromium hydroxide or hydrous chromium oxide (HCO), $Cr(OH)_3 \cdot nH_2O$. The dominance of the water band in the FTIR spectrum of HCO clearly indicates the hydrous nature of the solid sample. In addition to the strong band of molecular water (at $3400\,cm^{-1}$), the spectrum of HCO contained several bands assigned to the carbonate anion, i.e. a carbonate doublet at about 1490 and $1380\,cm^{-1}$ due to the asymmetric stretching of the C–O bonds and a broad band at about $843\,cm^{-1}$ due to the out-of-plane bending vibrations of carbonate [180]. Another band assigned to the vibration of the Cr–O bonds was seen at a lower frequency ($510\,cm^{-1}$).

The significant increase in the water band intensities with increasing Cr^{3+}/Fe_{T_SP}, as observed in the FTIR spectra of the Cr-associated ferrite (Figure 5.7), can be attributed to the increase amount of Cr-non-spinel phase. This phase appears to exhibit a strong affinity for water molecules, leading to its hydrous nature. Considering this result and the previous XPS analysis, the Cr-non-spinel phase was hypothesised to consist of HCO and/or amorphous Cr(III)-Fe(III) hydroxides, $(Cr_xFe_{1\text{-}x})(OH)_3$. Although the former phase is considered amorphous by XRD, Charlet and Manceau [186] reported that it possesses a γ-CrOOH local structure, i.e. isostructural to lepidocrocite. It was reported that less than 1% of HCO precipitated on goethite surface was dissolved in 1 mM ammonium oxalate solution at pH 3.5 after 30 h [187]. The stability of the amorphous Cr(III)-Fe(III) phase was also reported by several authors [188, 189]. These findings may explain the persistence of the Cr-non-spinel phase during acidic rinsing employed in the current work. The association of this non-crystalline phase with anions also seems likely as indicated by the increase in the anion band intensities with the increased Cr^{3+} content.

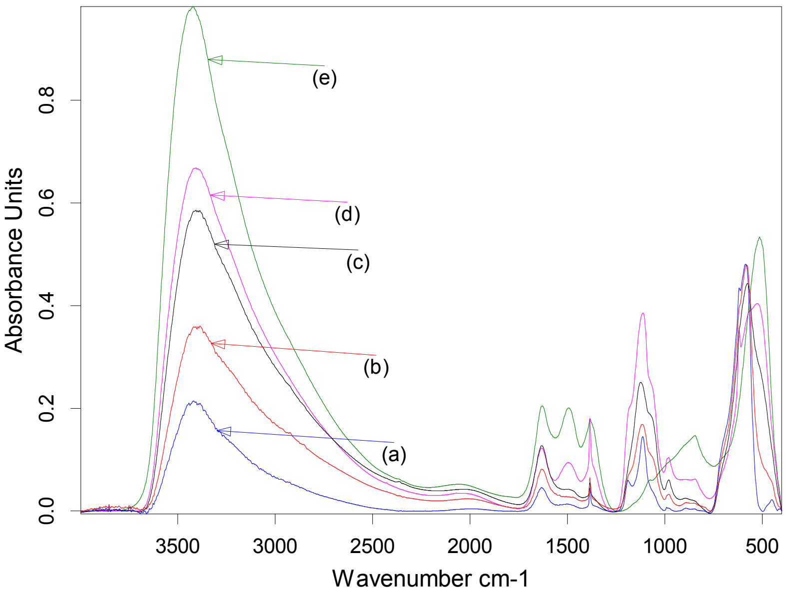

Figure 5.7: FTIR spectra of Cr-associated ferrites produced at 90 °C *for* Cr^{3+}/Fe_{T_SP} *ratio of (a) 0.07, (b) 0.17, (c) 0.48, (d) 2.0, and (e) amorphous Cr hydroxide.*

Based on the extensive investigation described above, the maximal attainable incorporation values (x) for the six investigated metals into ferrite by oxidative precipitation at 60–100 °C was concluded with a reasonable certainty to be: 1.0 for Zn^{2+}, 1.0 for Co^{2+}, 0.78 for Ni^{2+}, 0.49 for Al^{3+}, 0.35 for Cd^{2+}, and 0.0 for Cr^{3+}.

5.3 Morphological characterisation of the ferrites

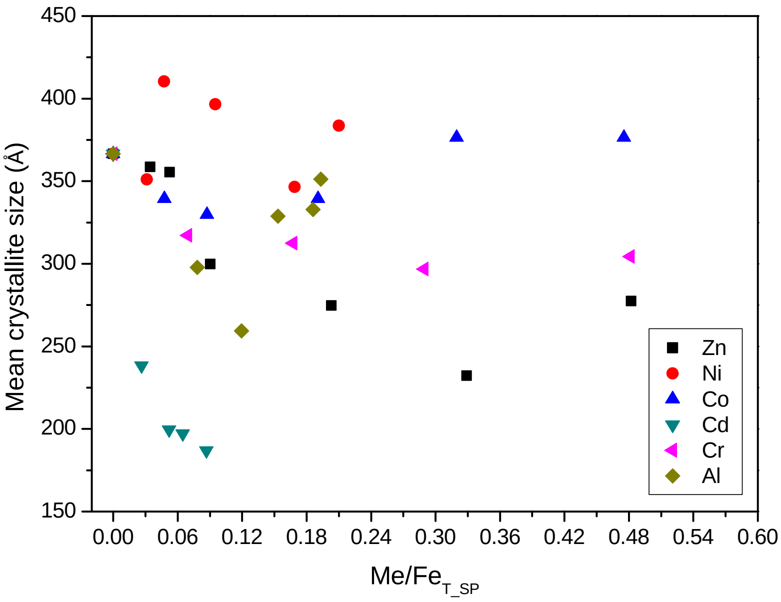

Figure 5.8: Changes in the crystallite size of ferrite produced at 90 °C *as a function of Me content.*

Morphological analyses were conducted in order further characterise the produced ferrites. The analyses include the determination of the crystallite size and the particle shape and size. The crystallite size (D_c) of the ferrite was calculated using Scherer formula based on the *hkl* 311 of the XRD pattern, as described in Chapter 3.4.2. The particle shape and size was investigated by visual observation using SEM.

The crystallite size of the ferrite particles as a function of Me/Fe$_{T\_SP}$ is presented in Figure 5.8. In general, it can be seen that the data obtained is rather scattered particularly for Ni ferrite. For Al and Co ferrites, it appears that the crystallite size was first decreased with increasing Me/Fe$_{T\_SP}$ and then it increased. The crystallite size of Zn ferrites and Cr-associated ferrites tended to decrease with increasing Me/Fe$_{T\_SP}$. For Cd ferrites, a sharp decrease of crystallite size could be observed.

Some SEM images of Zn ferrite particles with different Zn^{2+}/Fe$_{T\_SP}$ ratio are presented in Figure 5.9. It can be seen that Zn ferrites consisted of octahedral particles of about 50 to 200 nm.

In the case of Co ferrite, the SEM observation indicated the presence of octahedral particles of about 50 to 200 nm for the Co^{2+}/Fe$_{T\_SP}$ ratios of 0.05, 0.09, and 0.19. At higher Co^{2+}/Fe$_{T\_SP}$ ratios (i.e. 0.32 and 0.47), spherical particles with a fairly uniform size around 80–100 nm were obtained (Figure 5.10).

For Al ferrite, it was observed that spherical and octahedral crystals existed for all Al^{3+}/Fe$_{T\_SP}$ ratios. Two representative SEM images of Al ferrite are presented in Fig-

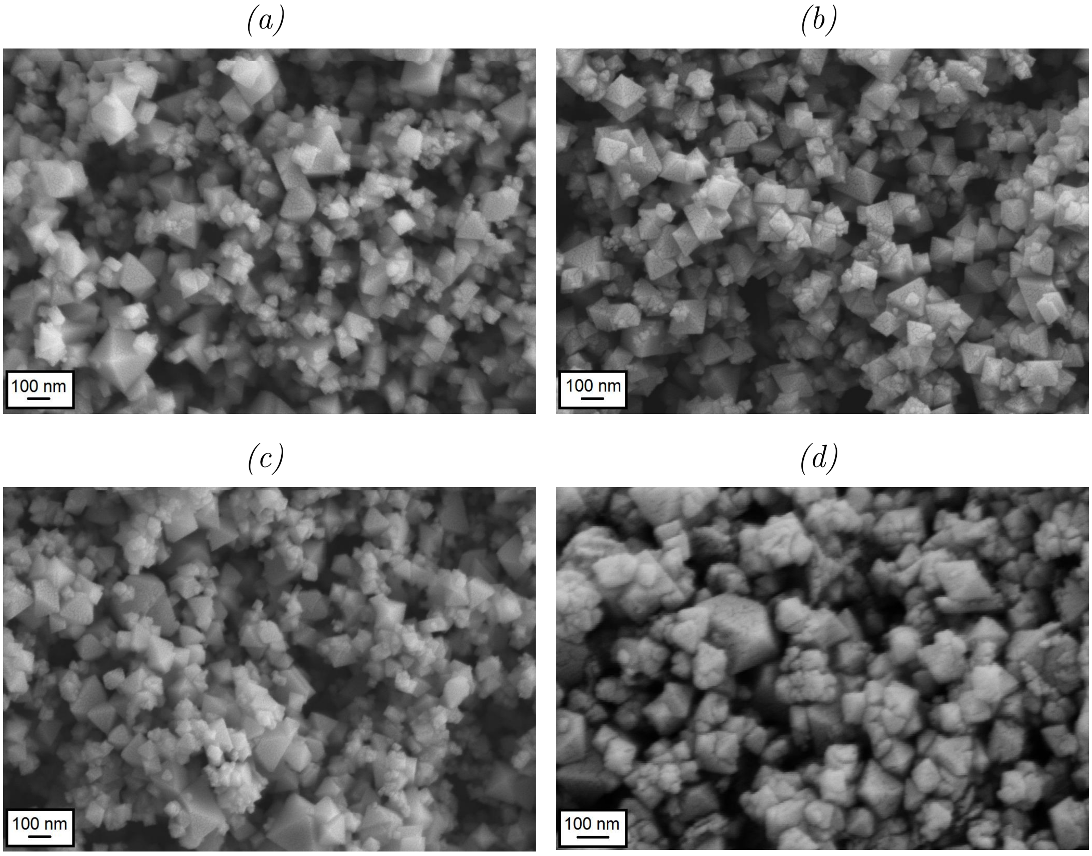

Figure 5.9: SEM images of Zn ferrites produced at 90°C for Zn^{2+}/Fe_{T_SP} ratio of (a) 0.090, (b) 0.196, (c) 0.322, (d) 0.476.

ure 5.11. No significant change in particle size was observed with increasing Al^{3+}/Fe_{T_SP} which was around 20–200 nm.

SEM observation for Cd ferrite with Cd^{2+}/Fe_{T_SP} of 0.03 showed that most of the particles were octahedral of around 50–200 nm across. When the Cd^{2+}/Fe_{T_SP} ratio increased to 0.07, the crystal form of Cd-particle changed to spherical with a more homogeneous size of about 50–100 nm. Interestingly, further increase in the Cd^{2+}/Fe_{T_SP} ratio to 0.087 resulted in larger particle size (70–200 nm) and the particle shape was transformed into octahedra (Figure 5.12). At the highest Cd^{2+}/Fe_{T_SP} ratio achieved in this work (0.91), spherical particles of about 60–100 nm were again observed.

The SEM images of Ni ferrite showed the presence of needle-shaped particles, a typical shape of goethite, together with octahedral shaped particles of ferrite (Figure 5.13). In the samples with a high Ni^{2+} content, the presence of undefined solid phases could also be observed.

The observation of Cr-associated ferrite by SEM showed that at a low Cr^{3+}/Fe_{T_SP} ratio (Figure 5.14a), octahedrally shaped particles existed together with some smaller particles. At the Cr^{3+}/Fe_{T_SP} ratio of 0.8, very small strongly agglomerated particles

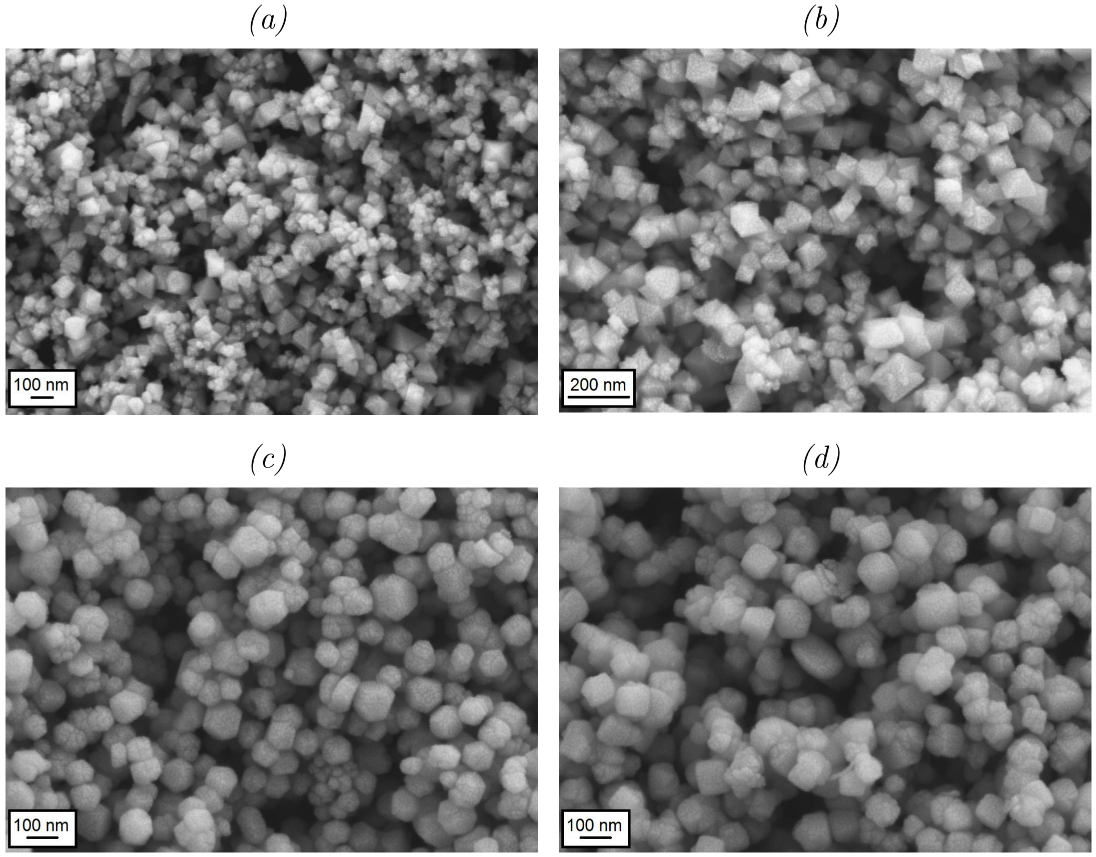

*Figure 5.10: SEM images of Co ferrites produced at 90°*C *ferrites for* Co^{2+}/Fe_{T_SP} *ratio of (a) 0.086, (b) 0.188, (c) 0.318, (d) 0.47.*

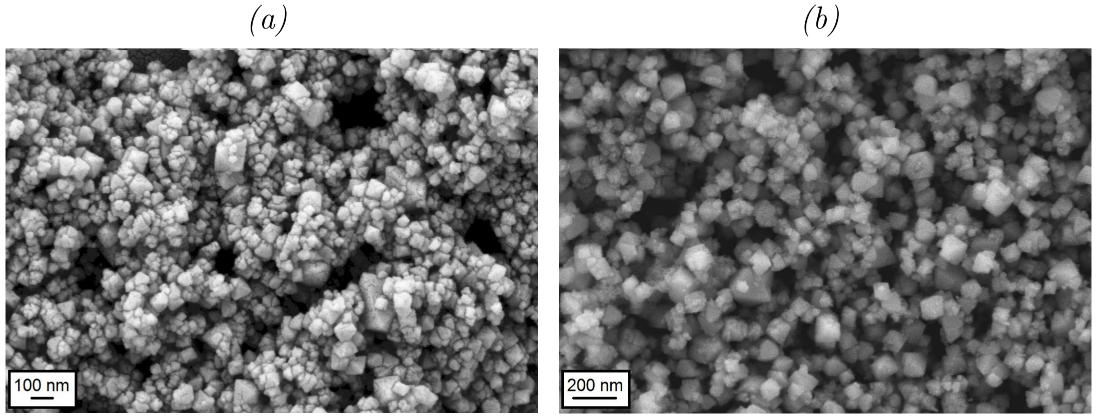

*Figure 5.11: SEM images of Al ferrites produced at 90°*C *for* Al^{3+}/Fe_{T_SP} *ratio of (a) 0.079 and (b) 0.189.*

started to form. As the $\mathrm{Cr}^{3+}/\mathrm{Fe}_{\mathrm{T\_SP}}$ ratio increased, small particles with no clear crystalline structure (amorphous) could be observed (Figure 5.14b). This observation supports the previous result regarding the presence of a non-crystalline phase in the solid samples.

The crystal of all investigated ferrites was found to have a polycrystalline nature

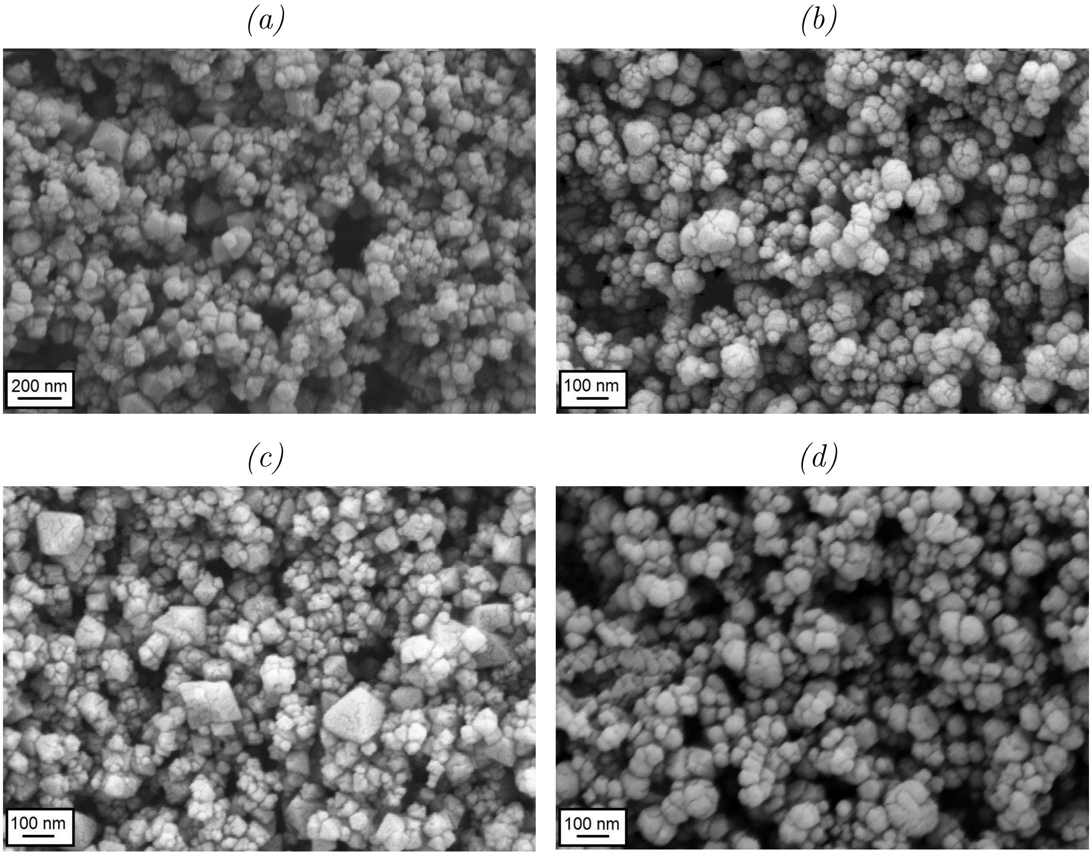

*Figure 5.12: SEM images of Cd ferrites produced at 90°*C *for* Cd^{2+}/Fe_{T_SP} *ratio of (a) 0.026, (b) 0.07, (c) 0.087, (d) 0.091.*

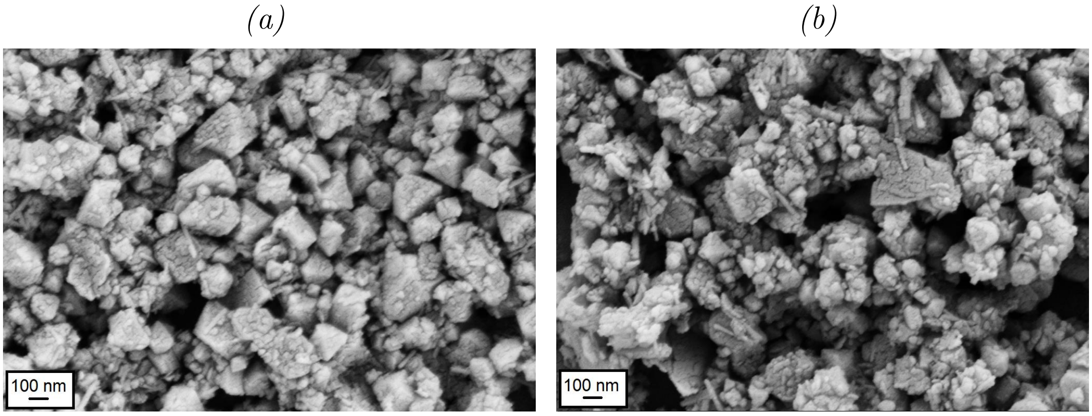

*Figure 5.13: SEM images of Ni ferrites produced at 90°*C *for* Ni^{2+}/Fe_{T_SP} *ratio of (a) 0.17 and (b) 0.21.*

(multi-domain crystallites) as the particle size observed by SEM was larger than the crystallite size measured by XRD. The polycrystalline character of the ferrite particles can be associated with the Ostwald ripening process, as suggested by Tang et al. [145]. This process would operate on the outer layer crystallite first, dissolving them, and transforming

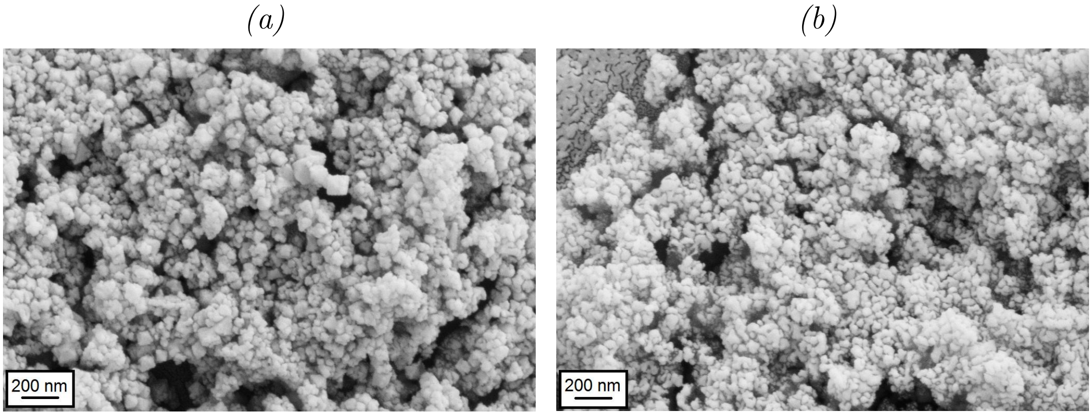

Figure 5.14: SEM images of Cr-associated ferrites produced at 90°C for Cr^{3+}/Fe_{T_SP} *ratio of (a) 0.486 and (b) 2.0.*

them to bigger ones, while the inner crystallites remain unaffected.

5.4 Predominant mechanisms determining the extent of metal ion incorporation into ferrites

As discussed in Section 5.1, different parameters related to the properties of metal ions or their corresponding ferrites were suggested to govern the incorporation of metal ions into the ferrite structure. These parameters can be roughly divided into three groups, i.e. driving force, structural, and kinetic parameters. To assess which of these groups is more significant in this respect, an initial correlation between the maximal incorporation extents obtained in the previous section and the related properties of metal ions or their corresponding ferrites (Table 5.3) was sought and evaluated.

Driving force parameters, such as ΔG_f^0, lattice energy (see Chapter 2.3.3), were considered generally to correlate poorly with the corresponding maximal incorporation extents. A certain correlation may be assumed to exist between the total structural energy (SE) and the maximal incorporations. However, the difference in the SE values appears to be too low to explain the empirical data, considering also the generalisations used for SE calculation (Chapter 2.3.3). Driving force parameters can also be considered in terms of the competition between phases with different thermodynamic energies. This approach may, however, lead to ambiguity, as it is known that the least stable phase is the first precipitated (Chapter 2.2.2). Furthermore, as mentioned in Section 5.1.2, other authors [74] already suggested that ΔG_f^0 does not take into account the surface energy of small particles, thus it cannot be directly used to explain the partial incorporation of certain Me.

Table 5.3: Some properties of the investigated metal ions and their corresponding ferrites.

Metal	Max. x[a]	SE[b] (eV)	ΔG_f^0[c] (kJ/mol)	r_{tet}[d] (Å)	r_{oct}[d] (Å)	EN[e]	log k_{sp}[f]	log $^*K_1$[g]	k_{-w}[h] (s^{-1})
Zn^{2+}	1.0	−775	−1066	0.58	(0.73)	1.65	−16.8	−8.96	7×10^7
Co^{2+}	1.0	−697	−980	(0.58)	0.72	1.88	−15.7	−9.2	2×10^6
Fe^{2+}	1.0	−684	−1015	(0.615)	0.74	1.83	−15.1	−9.5	4×10^6
Fe^{3+}				0.485	0.645	1.96	−38.8	−3.48	2×10^2
Ni^{2+}	0.78	−714	−973	(0.565)	0.69	1.91	−17.2	−9.86	3×10^4
Al^{3+}	0.49	−638	−1880	(0.39)	0.53	1.61	−33.5	−5.11	1
Cd^{2+}	0.35			0.78	(0.95)	1.69	−14.3	−10.08	3×10^8
Cr^{3+}	0.0	−662	−1356		0.615	1.66	−30	−5.62	5×10^{-7}

[a] Maximal attainable incorporation extent in terms of x in $Me_xFe_{3-x}O_4$.

[b] SE = total structural energy for $MeFe_2O_4$ based on known cation distribution in the spinel structure [54].

[c] ΔG_f^0 = free energy of formation of $Me^{2+}Fe_2O_4$ and $FeMe_2^{3+}O_4$ [190].

[d] r_{tet}, r_{oct} = effective ionic radii [65] according to the known cation distribution in $MeFe_2O_4$ [54, 144]. Parentheses represent the sites known to be unoccupied by the corresponding metal ion in the ferrite.

[e] EN = electronegativity [66].

[f] log k_{sp} = stability constants for solid hydroxides ($Me(OH)_2$ or $Me(OH)_3$) [24, 25].

[g] $^*K_1$ = stability constants of $MeOH^+$ (for divalent metals) or $Me(OH)_2^+$ (for trivalent metals) complex formation [31].

[h] k_{-w} = rate constants for water exchange [24].

Structural parameters, such as crystallite size and lattice strain, are probably a consequence of more fundamental sources such as the mismatch of ionic radii and the framework flexibility. The change of the crystallite size of the ferrites with increasing Me content, depicted in Figure 5.8, did not reveal notable trends which may indicate the development of structural strain, except for Cd ferrite. The crystallite size of this ferrite was significantly smaller than that of the others, probably due to the increase of structural strain with Cd^{2+} content.

Some parameters categorised in the kinetic group include ionic radii, electronegativities, stabilisation constant of metal complexes and hydroxides, and adsorption edges. Many studies, as summarised in Section 5.1.2, correlated the limited capability of the ferrite structure to incorporate metals with one or more of these parameters. A certain parameter may give one metal a kinetic advantage over the others in any of the sub-processes involved in the synthesis reaction. As a result, one of the metals is incorporated preferentially and is included at a higher proportion in the ferrite structure. When the reaction is carried out in the presence of only one Me, the competition is between that particular Me and the iron ion. However, this competition may not be straightforward because of some factors such as two oxidation states of iron and two available lattice sites exist in the spinel as well as the different lattice site preference for the metal ions.

By comparing two conventional parameters explaining the substitution extent of cation in mineral [92], i.e. ionic radius and electronegativity, with the maximal incorporation degree obtained in the current work, it is clear that these parameters cannot explain the incorporation trend of Ni^{2+}, Al^{3+}, and Cr^{3+}. The ionic radii of these metals are smaller than those of Fe with equal valency, but still their incorporation is considerably limited. This is most obvious with Cr^{3+} which also has a significantly lower electronegativity than Fe^{3+}. No clear correlation could also be established between the k_{sp} value and the maximal incorporation data. As mentioned before, in the current experimental work the most likely precursor is basically ferric in nature (i.e. GR, ferrihydrite, lepidocrocite). Under the precipitation pH (i.e. on formation of black magnetic precipitates) practiced in the current work (pH 7.0–8.0), a ferrous hydroxide precursor is unlikely due to the fast oxidation rate of Fe(II) [191]. Therefore, the k_{sp} value can be considered irrelevant in this respect.

The hydrolysis constants, $^{*}K_1$, presented in Table 5.3 indicate that Ni(II) and Cd(II) are slightly less hydrolysed than Fe(II), Zn(II), and Co(II) which could explain the lower incorporation degree of the former metals compared to the latter. However, the difference between the $^{*}K_1$ values is not significant enough to explain the big differences in the maximal attainable incorporation of these metals. Furthermore, it should be pointed out that under the above noted ferrite precipitation pH, all divalent metals are expected to be almost completely nonhydrolysed. In view of this fact, incorporation extent cannot be considered a function of $^{*}K_1$. Finally, this mechanism cannot provide a logical explanation for the fact that Cr(III) is hardly incorporated into the ferrite lattice, while hydrolysing easily.

Only very limited literatures are available regarding the adsorption edges (i.e. the pH range between 0 and 100% adsorption) of the investigated metals on iron oxides (Table 5.4). It appears that only a weak correlation can be established. The most noticeable exceptions are the trivalent metal ions, which seem to adsorb onto iron oxides at lower pH values than divalent ions, while their incorporation extents are generally lower.

Based on the above evaluation, it can be concluded that no strong correlation can be established with any of those suggested parameters. Therefore, another kinetic parameter was sought. The rate of water exchange (Section 2.1.3) seems to correlate with the incorporation behaviour of the metal ions and is suggested here.

The values of k_{-w} of the investigated metal ions with the maximal incorporation obtained for the corresponding metals are presented in Figure 5.15. It seems that a certain correlation exists between the water loss rate and the maximal incorporation of

Table 5.4: Adsorption edges (pH range) of the investigated metal ions on several iron oxides.

Metal	Magnetite	Lepidocrocite	Hematite	Goethite
Zn^{2+}		5–7.5[a]	4–9[a]	3.8–6.2[b]
Zn^{2+}			4.5–7[b]	
Co^{2+}	5–8[c]		4.5–7[b]	4.1–6.2[b]
Fe^{2+}		4.5–7[b]		
Ni^{2+}		5–7[b]		4.3–6.2[b]
Al^{3+}		3–5[b]		3–8.5[b]
Cd^{2+}		6–9[a]		
Cr^{3+}			2.5–7[a]	2.4–4[b]

[a] Ito et al. [94].
[b] Cornell and Schwertmann [28].
[c] Tewari et al. [192]

metal ions, i.e. metal ion with the higher k_{-w} is more likely to be incorporated into the ferrite structure. This correlation showed that the Cr^{3+} ion has a very low k_{-w}, thus, as established in the previous section, it was hardly incorporated the ferrite structure.

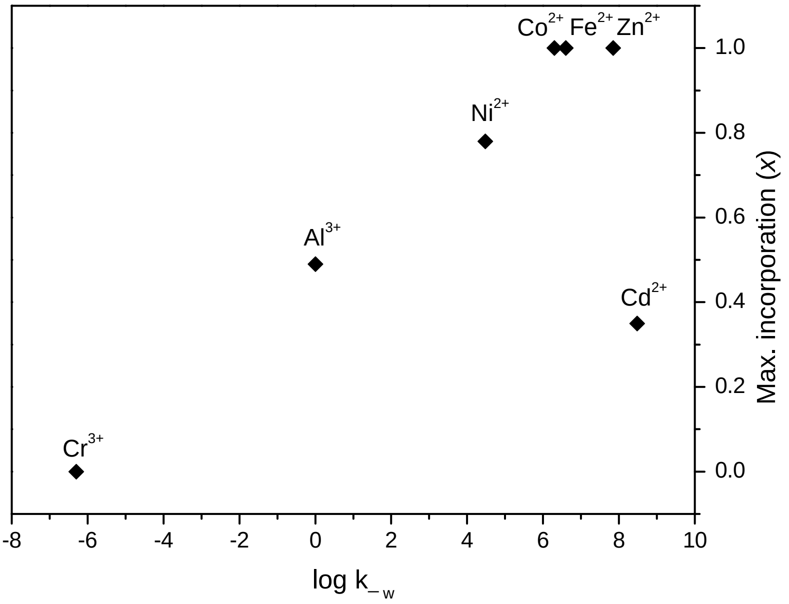

Figure 5.15: Maximal attainable incorporation values of six investigated metals versus their k_{-w} values.

The exception is Cd^{2+} which has the highest k_{-w} and yet entered the ferrite to a very limited extent. This behaviour might be related the large difference in the ionic radii of Cd^{2+} and iron ions. Cadmium(II) ion is about 60% larger than Fe^{3+} in the tetrahedral sites (see Table 5.3). The octahedral site occupation was, however, reported in the Cd ferrite produced by coprecipitation of Cd(II) and Fe(III) [144]. If it is the case, the ionic radius of Cd^{2+} is about 28.4% and 46% larger than that of Fe^{2+} and Fe^{3+}, respectively. In any event, the size difference between Cd^{2+} and iron is much higher than the difference between any of the other metals and iron. For example, Zn^{2+} is only about 19.6% larger than Fe^{3+} in the tetrahedral site. This significant large size difference may lead to the development of structural strain, thus hindering further incorporation.

The relation between the incorporation extents of metals and their k_{-w} values could be associated either with different release rates of the different metals from the precursor during its dissolution or with the simultaneous existence of different kinds of precursors which have different dissolution rates. This relation may also be associated with different adsorption or growth kinetics. Regardless of the precise kinetic process, metal ions having lower k_{-w} than that of iron will linger at intermediate, less stable phases, leading to their limited incorporation. Another outcome of such a mechanism is probably a non-homogeneous distribution of metals within the particles. Although this may not always be the case, it can explain the inhomogeneous distribution of Zn^{2+} and Ni^{2+} in the particles discussed above.

5.5 Chemical stability of the ferrites

Chemical stability of the produced ferrite was established by employing three different methods, i.e. dissolution test, TCLP, and BCR tests. The chemical stability based on the first method, referred to as dissolution stability, is correlated with the iron dissolution rate from the products in 12.8% HCl solution at $23 \pm 2\,^{\circ}\mathrm{C}$. On the other hand, the last two methods, often used to evaluate the environmental pollution potential of solid wastes, do not aim at completely dissolving the solid particles. Thus, these tests are used to quantify the extent of non-iron metal leaching.

5.5.1 Dissolution stability

Dissolution profile

The typical dissolved fraction profile ($f_{Me} = [Me]/[Me]_T$, with $[Me]_T$ is the expected concentration for total dissolution) as a function of time for iron in ferrite is shown in Figure 5.16 for Zn and Co ferrite. A similar dissolution profile was observed for the other metal ferrites with respect to iron and non-iron metals (data not shown). The main feature of this profile is a rapid initial dissolution rate for at least 60% of the dissolution process, falling off as the size of the particles decreases. The first dissolution reaction can be fitted by a simple cube rate law expressed in Equation 2.27. The plots of the left side of Equation 2.27 against t should give a linear correlation, implying that dissolution is surface controlled, three dimensional, and the crystal shape is maintained during the reaction [88].

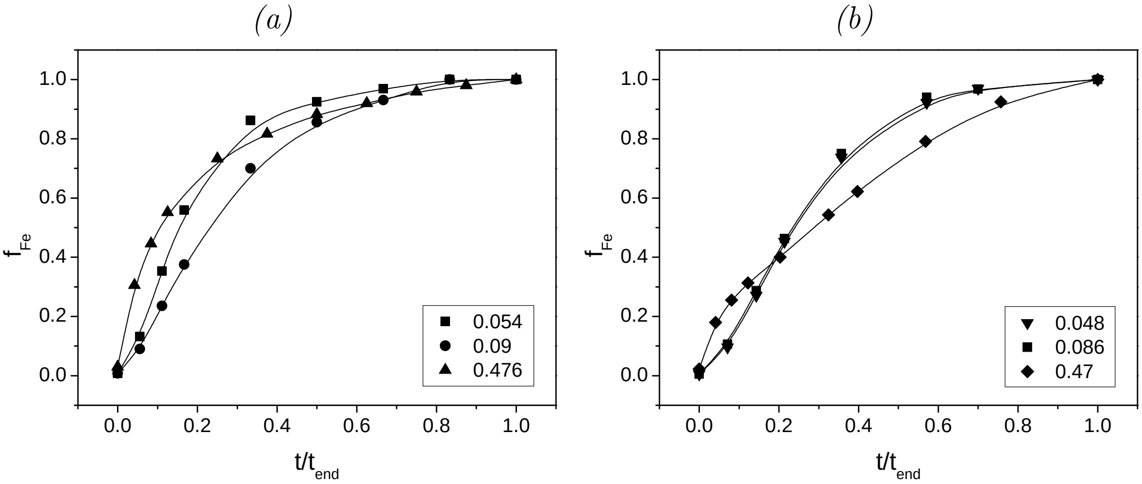

Figure 5.16: Dissolution profiles of (a) Zn ferrite and (b) Co ferrite for different Me/Fe_{T_SP} ratios.

As explained in Section 5.2.3, the dissolution of some metal ferrites, such as Zn ferrite with the Zn^{2+}/Fe_{T_SP} ratio of 0.195, was incongruent ($f_{Fe} \neq f_{Me}$) within the time span of the dissolution test. Thus, the dissolution profile based on the fraction of Fe was not similar to that based on the fraction of Me dissolved, as shown in Figure 5.17a. This resulted in the different slopes of the cube rate low plots for Fe and Me. When the dissolution was congruent, as is the case with Co ferrite (Figure 5.17b), the dissolution profiles for Fe and Me fell in the same curve and the linear cube rate law plots for these metals had an equal slope.

Influence of metal incorporation extent on the dissolution rate

To analyse the effect of metal incorporation on the dissolution stability, the initial iron dissolution rate of ferrite determined in the initial linear stage of the dissolution process were compared. The results are depicted in Figure 5.18. It was found that the Fe dissolution rate of all investigated ferrites decreased with increasing Me/Fe_{T_SP} ratio, except for Cd ferrite. This result suggests that the incorporation of Zn^{2+}, Co^{2+}, Ni^{2+}, and Al^{3+} increased the stability of the ferrite or, in other words, these metals stabilised the ferrite structure. The increase of ferrite stability with increasing Me incorporation extent (Co and Ni) was also reported by other authors [80, 86, 90, 91], as described in Chapter 2.5. The high stability of ferrite due to the substitution process of Fe ions with other metal ions, in this case Zn^{2+}, Co^{2+}, Ni^{2+}, and Al^{3+} may reflect the influence of bond strength on the stability of ferrite. The Me–O–Fe bonds can be considered to be stronger than the pure Fe–O bonds and thus more resistant to protonation [28]. Furthermore, the electron

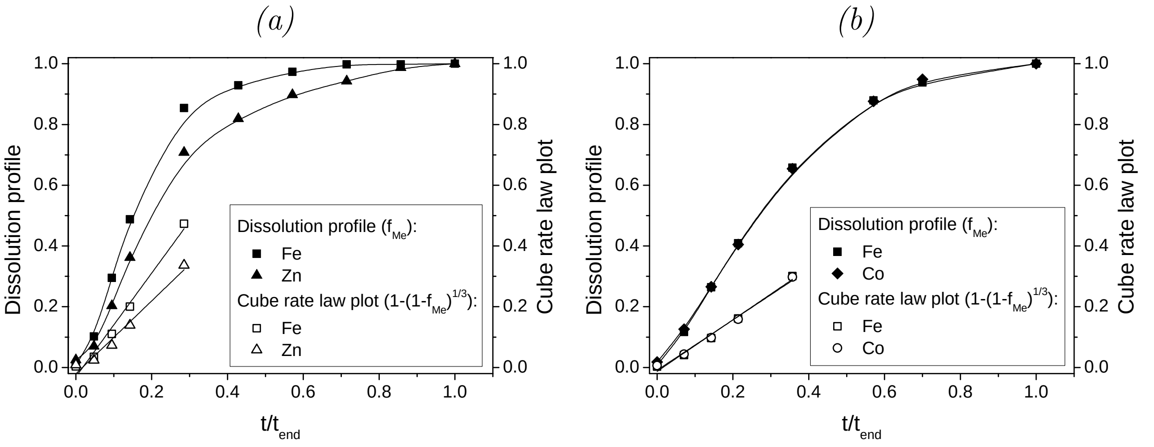

Figure 5.17: Dissolution profile and its cube rate law plot for (a) Zn ferrite at Zn^{2+}/Fe_{T_SP} *ratio of 0.195 and (b) Co ferrite at* Co^{2+}/Fe_{T_SP} *ratio of 0.188.*

mobility between Fe^{2+} and Fe^{3+} becomes less significant as the iron ions are substituted by other metal ions, leading to the deceleration of iron dissolution rate [80]. As opposed to the other metal ions, the incorporation of Cd^{2+} tends to labilise the ferrite structure. Apparently, the Cd–O–Fe bonds are weaker than the Fe–O bonds which may be correlated to the large ionic radius of Cd^{2+}. Furthermore, Cornell and Schwertmann [28] suggested that crystal defects created by substitution can accelerate dissolution. In this work, it has been shown that Cd ferrite has divalent cation deficiency (Section 5.2.1) with an appreciably small crystallite size (Section 5.3). The defect structure of Cd ferrite was also indicated in other works [193, 194]. This result may reflect the effect of the structural factors, such as crystal defect and strain, on the dissolution stability of solid. These factors were considered insignificant in the other ferrites as reflected by their increased stability. To be really meaningful and accurate, however, a detailed study of the solid morphology should be included. In the context of this study, the overall effect of the metal incorporation on the dissolution behaviour is much important than the detailed kinetic description.

In the case of Cr^{3+}, the stability of the ferrite particles also seemed to increase as the amount of Cr(III) associated with the ferrite particles increased (Figure 5.18). This finding may reflect the inhibition effect of Cr^{3+} toward ferrite dissolution. Similar inhibition effect on the acid-promoted dissolution of goethite has been reported by Bondietti et al. [195]. They suggested that Cr^{3+} ions prevent the approach of dissolution-promoting H^+, ligands, and reductants to the dissolution-active sites. As discussed earlier, because Cr^{3+} ions were not incorporated into the ferrite structure, the increased Cr^{3+}/Fe_{T_SP} ratio could be associated with increasing amount of the non-ferrite phase. During dissolution reaction, this phase must be first dissolved as it was located in the outer sphere of the solid particles. It is noted that this phase was observed to be resistible against acidic

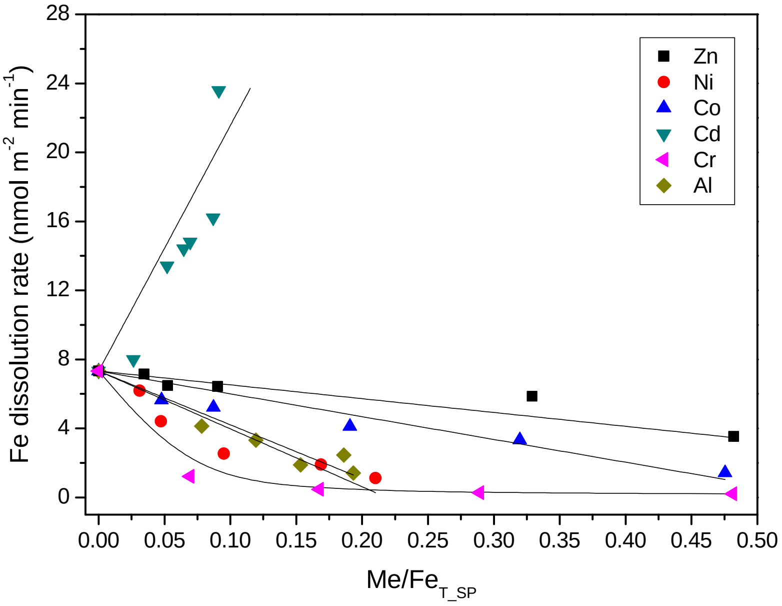

*Figure 5.18: Initial Fe dissolution rates (12.8% HCl solution, 23 ± 2°*C*) of the investigated ferrites synthesised at 90°*C*.*

conditions. These explanations seem to support the overall slow dissolution rate of Fe from the Cr-associated ferrites.

Mechanisms determining the stability trend of different metal ferrite

Based on the data in Figure 5.18, it can be deduced that the stability order of the ferrites is approximately according to the following order: $Al^{3+} \approx Ni^{2+} > Co^{2+} > Zn^{2+} > Fe^{2+} > Cd^{2+}$. The dissolution stability order obtained in this study is in line with the results of previous works described in Chapter 2.5, even though the dissolution reactions were done under different conditions.

Mechanisms of dissolution reactions have been extensively discussed in the literatures (e.g. [42, 43, 196]). It is not the aim of this work to establish the detailed mechanisms of the dissolution reaction. Emphasis is placed on the main mechanism affecting the stability trend of different ferrites.

The dissolution reaction of metal and mixed oxides implies that the coordination environment of the metal has changed [43]. In this sense, the metal ion in the crystal lattice exchanges its O^{2-} ligands for H_2O or another ligand such as H^+, OH^-, and complex-building ligands. The exchange rate of this reaction is controlled exclusively by short range forces between the metal, coordinated oxygens, and the incoming ligand [197]. Because the coordination numbers and metal-oxygen bond distances of metals in minerals are commonly similar to those in the hydrated ion, it is logical to start the examination of the main mechanism of dissolution reaction of different metal ferrites with a study of particularly simple ligand-exchange reactions, such as water exchange around dissolved metals.

The plot of the iron dissolution rate of different metal ferrites at $x = 0.24$ and the water exchange rate constant (k_{-w}) is depicted in Figure 5.19a. Although the dissolution rate of ferrite seemed to increase with k_{-w}, a clear linear correlation could not be established for all investigated ferrites. A strong correlation was found for Ni^{2+}, Co^{2+}, and Zn^{2+} ($R^2 = 0.972$), which is similar to the result reported by Rodenas et al. [78]. The Fe dissolution rate of Al ferrite appeared not to follow the trend line as its value was found to be high despite the lowest k_{-w} value of Al^{3+}. Another parameter suggested by Klas [198] to have a correlation with the stability of metal ferrite is the lattice energy. In Figure 5.19b, the dissolution rate of ferrite is plotted as a function of the total electrostatic energy (the main component of lattice energy, see Chapter 2.3.3). A correlation between the dissolution rate of Fe and electrostatic energy of different ferrites, except for Al ferrite, seemed to exist ($R^2 = 0.888$).

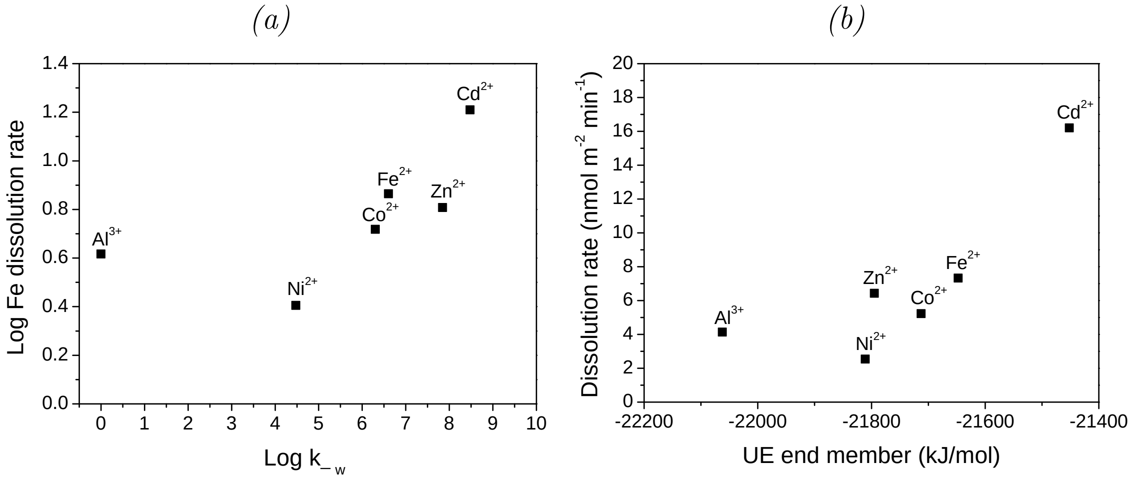

Figure 5.19: Correlation between the initial iron dissolution rates of different ferrites ($Me_xFe_{3-x}O_4$) at $x = 0.24$ (except for Fe^{2+} where $x = 1$) against (a) the water exchange rate and (b) the total electrostatic energy of the end member.

The results clearly show the difficulty in establishing a good correlation between the dissolution rates of all ferrites examined here with only one single parameter. For certain ferrites, such as Zn, Ni, and Co ferrite, the correlation between their dissolution rate and the corresponding k_{-w} value suggests that the dissolution proceeds along a similar pathway to solvent exchange around the divalent cations. A linear relationship between k_{-w} and dissolution rate was also reported for simple metal oxides (NiO, CoO, and ZnO) [78] and orthosilicate minerals [199]. In the case of Fe_3O_4, the role of Fe^{2+} released from the solid in accelerating the dissolution rate must also be considered. For Cd and Al ferrite, the structural changes such as changes in the lattice parameter and crystal defects might play significant roles to accelerate the dissolution rate as it is known that the ionic radius of Cd^{2+} and Al^{3+} is significantly larger and smaller than that of Fe, respectively.

5.5.2 Leaching

Due to the more extreme conditions employed in the BCR test (pH 1.5 and reducing condition) than in the TCLP test (pH 4.95), it can be expected that the Me leaching extent measured in the former is much higher compared to that obtained in the latter. This is consistent with the results depicted in Figure 5.20. In the TCLP test, Zn was barely leachable, while Co was leached to a similar extent in all Co^{2+}/Fe_{T_SP} ratios (i.e. about 1.2%). In the BCR test, the extent of Zn and Co leaching increased with Me/Fe_{T_SP}. A sharp increase in the leaching extent of Zn was observed at the highest Zn content. This is probably due to the existence of a less crystalline layer in the outer part of the ferrite which might only be formed at a very high Zn^{2+}/Fe_{T_SP} ratio.

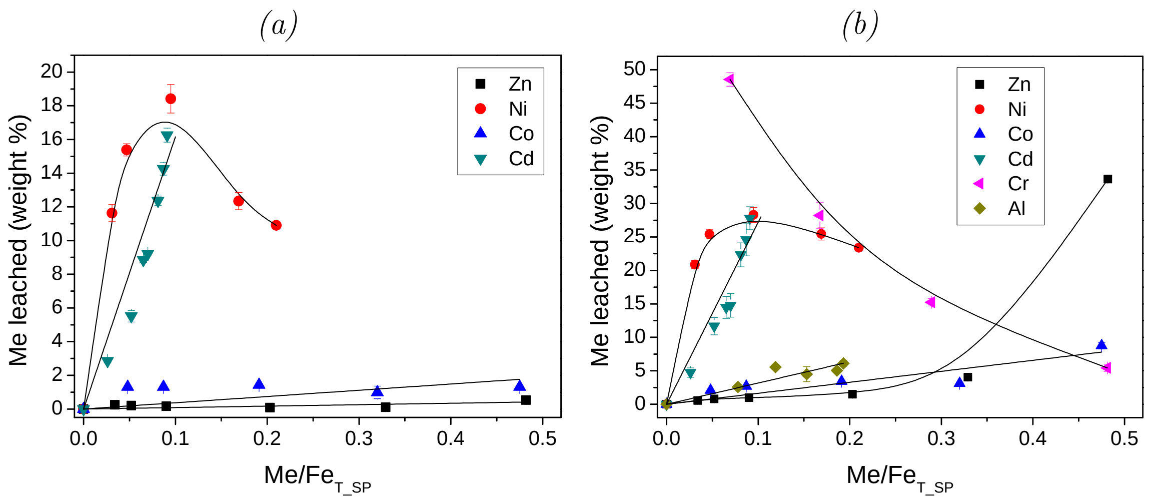

Figure 5.20: Weight percentages of non-iron metal leached from ferrites produced at 90 °C in the (a) TCLP test and (b) BCR test.

It can be seen in Figure 5.20 that the extent of Ni leaching was high in both procedures and tended to increase with Ni^{2+}/Fe_{T_SP}. This result is related to the fact that Ni was accumulated near the particle surface (Section 5.2.3). A high extent of Me leaching was also observed for Cd. It can be seen in Figure 5.20 that Cd leaching sharply increased with Cd^{2+}/Fe_{T_SP}. The low dissolution stability and small crystallite size of the Cd ferrite, as discussed earlier, are responsible for this observation.

The concentration of Al and Cr in the TCLP extraction fluid was below the detection limit. At relatively high pH employed in the TCLP test, it can be expected that these trivalent ions either precipitated as hydroxides or adsorbed onto the particle surface. It is noted that the adsorption of Al^{3+} and Cr^{3+} on different iron oxides starts at a relatively low pH value (Table 5.4). In the BCR test, the extent of Al leaching appeared to slightly increase with Al^{3+}/Fe_{T_SP}, but the value was relatively low ($<$ 6% weight) in all Al ferrite samples. Figure 5.20b indicates a decrease in the Cr leaching as the content of Cr^{3+} associated with the ferrite particles increases. This result is interpreted in terms of an increase formation of HCO, which was discussed earlier to have very low solubility even under acidic condition.

5.6 Conclusions

The maximal attainable incorporation extents for six investigated metals (in terms of x in the formula $Me_xFe_{3\text{-}x}O_4$, Me is a non-iron metal) into ferrite produced by oxidative precipitation at elevated temperatures (60–100 °C) were concluded to be 1.0, 1.0, 0.78, 0.49, 0.35, and 0.0 for Zn^{2+}, Co^{2+}, Ni^{2+}, Al^{3+}, Cd^{2+}, and Cr^{3+}, respectively.

The importance of using different techniques to characterise the produced ferrites was demonstrated. Chemical composition analysis alone can give misleading results because certain non-spinel phases can still exist even after rinsing the solid in acid solutions (pH 2). The proof of non-iron metal incorporation into the ferrite structure can be provided by X-ray diffraction analysis, but only on the condition that metal content linearly correlates with the unit cell size of the ferrite. However, this correlation can be inaccurate when the ferrite is non-stoichiometric and/or amorphous solid phases exist. The dissolution congruency test in 12.8% HCl solution was found to be an effective method to evaluate the incorporation extent of metal in the ferrite structure. The non-spinel phases were found to accumulate on the particle surface and were of hydrous nature.

The formation of ferrite addressed in this work involves direct precipitation from solution through a dissolution-reprecipitation mechanism. The metals must be associated with water molecules before being adsorbed and incorporated into the ferrite structure. One of the water molecules coordinated to the metal ion has to dissociate in order to form an inner sphere complex [25]. Thus, metals with higher water exchange rate (k_{-w}) are adsorbed and incorporated faster. Conversely, metals with very low k_{-w} tend to stay in the intermediate phase such as amorphous or hydroxides phase limiting their incorporation into the ferrite structure. When, however, a non-iron metal ion is significantly larger than iron (as is the case with Cd^{2+}), the main factor governing the incorporation extent is the ionic radius of the metal rather than k_{-w}.

The dissolution stability of ferrite produced under elevated temperature conditions is according to the following order: $Al^{3+} \approx Ni^{2+} > Co^{2+} > Zn^{2+} > Fe^{2+} > Cd^{2+}$. The incorporation of non-iron metal into the ferrite structure increased the stability of ferrite toward acidic dissolution, except for Cd^{2+}. The Fe dissolution rate of different ferrites seemed to correlate with the k_{-w} value as well as with the lattice energy. However, other factors such as small crystallite size and lattice defect could enhance the dissolution rate and reduce the stability of the ferrite. Leaching of Zn^{2+} and Co^{2+}, as well as the trivalent metals, in the TCLP test (pH ∼5) was very low. A significantly high leaching was observed for Ni^{2+} and Cd^{2+} ions. The tendency of Ni^{2+} to concentrate toward particle periphery was responsible for the observed high metal release. For Cd^{2+}, this was due to the low dissolution stability of the corresponding ferrite. Under more extreme conditions such as in the BCR test, the release of all metals from the ferrites was significantly increased.

Chapter 6

Incorporation of Metal Ions into Ferrites at Ambient Temperatures

Various conditions allowing the application of the ferrite process at ambient temperatures, such as seed addition [97, 127, 137], prolonged aging time [17, 97], high synthesis pH [126], high ferrous intermediate (FI) concentration [97, 127, 137], and slow Fe(II) oxidation rates [97, 200], have been proposed. Nonetheless, the incorporation extents of non-iron metals into the ferrite, as well as the product stability obtained under these conditions, have not been sufficiently quantified.

Accordingly, the current work thoroughly examines the formation of ferrite by the seeded ambient temperature ferrite process (ATFP). The incorporation extents of seven non-iron metals, Zn^{2+}, Ni^{2+}, Cd^{2+}, Co^{2+}, Cu^{2+}, Cr^{3+} and Al^{3+}, into the ferrite are quantified and the other product characteristics such as ferrite morphology and stability are assessed. Comparison of the overall performance of two methods of seeded ATFP, i.e. oxidation ferrite process (OxFP) and stoichiometric ferrite process (StFP) is also presented. The characteristics of the ferrite produced under ambient and elevated temperatures are then compared and the possible explanations for the differences are suggested. Simultaneous incorporation of several non-iron metals into the ferrite structure by the seeded ATFP is addressed as well. The formation of multi-metal-substituted ferrite under different conditions is studied to gain a comprehensive process understanding and derive the best operational conditions.

The experiments of seeded ATFP were carried out mainly in a batch mode and partly in a continuous mode. As explained in Chapter 3.2.2, the batch experiments with seed consisted of a sequence of repeated batch cycles. The main advantage of this approach is the replacement of the original magnetite seed with the newly formed ferrite allowing an accurate determination of the actual capacity of the ferrite structure to incorporate the metal ions. On the other hand, this approach is time intensive and required about one to two months until steady state (i.e. the Me/Fe_{T_SP} ratio remains constant for several cycle) was observed for each experimental condition. It should be mentioned that steady state condition can be achieved in a shorter time (around two weeks) by employing the continuous setup, but large amount of chemicals is required.

6.1 Previous works

This section summarises some published works on ATFP. The results of the recent works by Klas [198] and Klas et al. [201] are discussed in the next sections, together with the results obtained in the current work.

6.1.1 Ferrite precipitation by oxidation method

A complete incorporation of Zn^{2+} was reported by Perales-Perez et al. [202] in the ferrite produced at 25 °C and pH 11 under moderate oxidising conditions and 24 h of aging. The rinsing procedure included only washing with distilled water. Wang et al. [203] found that a maximal Co^{2+}/Fe ratio obtained in the ferrite synthesised at room temperature was approximately 0.18. It is noted that they washed the solid with HCl solution at pH 1.0 for 1 h prior to analysis. A significantly higher Co^{2+} incorporation was reported by Nishimura et al. [204], i.e. 0.38 (in terms of Co^{2+}/Fe ratio in the product). However, no information about the rinsing procedure for the produced ferrite was provided. The feasibility of the OxFP has been proven by Petrick et al. [97]. They demonstrated that Co ferrite could be easily formed at ambient temperatures with less than 1% cobalt leaching at pH 5.0. The rate limiting step in this method appeared to be the oxidation rate which has to be low enough to minimise the formation of Fe(III) oxide. This was reflected by the high FI concentration required to overcome the inhibitory effects of Co^{2+} on the ferrite formation ($\geq$ 1500 mg Fe^{2+}/l).

Under ambient condition, ferrite is also considered to form through a series of transformation reactions. Wang et al. [203] identified two different mechanisms of ferrite formation based on different mixing procedures of metal and alkaline solution (pH 11–11.5). In the first procedure, the alkaline solution was dropped into the mixture solution containing Fe^{2+} and Co^{2+}. It was suggested that green rust (GR) was formed before the ferrite. In the second procedure, the mixture solution of Fe^{2+} and Co^{2+} was added drop-wise into alkaline solution. In this procedure, Fe(II) hydroxide was considered to be rapidly oxidised to Fe(III) hydroxide, which coprecipitated as ferrite with Co(II) and Fe(II) hydroxide, without involving green-rust intermediation. The smaller particles formed in procedure 1 was associated with the higher degree of supersaturation for nucleation resulting from the high concentration of reactants during mixing. It was also found that the presence of Fe^{3+} in the starting solution of procedure 1 led to the formation of amorphous phase only. It was thus suggested that a large amount of Fe^{2+} in the starting solution was essential for the formation of GR. In procedure 2, with the increase of Fe^{3+} in the initial solution, ferrite was still formed together with the amorphous phase.

6.1.2 Ferrite precipitation by stoichiometric method

The use of magnetite seed to increase the amount of ferrite phase in the precipitates produced by coprecipitation of Fe(II)-Fe(III) solution was examined by McKinnon et al. [9]. The magnetite seed was introduced to the initial solution containing Me^{2+}, Fe^{2+}, and Fe^{3+} at a ratio corresponding to the stoichiometric ferrite (i.e. divalent to trivalent ratio of 0.5). This approach seemed to increase the yield of magnetic solids and the scavenging of non-iron metal ions. The available seed surface area was considered the rate limiting parameter in this approach. However, uncertainty may arise due to the fact that the experiments consisted only one cycle, i.e. the magnetite seeds were analysed together with the precipitated ferrites without reaching steady state conditions.

6.2 Incorporation of single metal ions

The incorporation of Zn^{2+}, Ni^{2+}, Cd^{2+}, Al^{3+}, Cu^{2+}, and Cr^{3+} into the ferrite precipitated by the ATFP was investigated at 30 °C and pH 10.5. Several aspects with regard to the incorporation process of each non-iron metal, i.e. chemical composition, crystalline phases and unit cell sizes, metal distribution, infrared spectra of the precipitates, particle morphology, and product stability, are presented.

6.2.1 Chemical composition

The attainable incorporation extents based on chemical composition analysis for each non-iron metal are discussed in the following sections.

6.2.1.1 Zinc

The incorporation of Zn^{2+} into the ferrite produced by the StFP and the OxFP was carried out in the batch system at different Zn^{2+}/Fe_{T_IN} ratios. The Zn^{2+}/Fe_T ratio in the ferrite (Zn^{2+}/Fe_{T_SP}) as a function of cycle number is presented in Figure 6.1a. For the experiments at Zn^{2+}/Fe_{T_IN} ratio of 0.1, the Zn^{2+}/Fe_{T_SP} ratio achieved by the StFP at steady state was slightly higher than that obtained by the OxFP, i.e. 0.097 vs. 0.093, corresponding to about 97% and 93% Zn incorporation efficiency, respectively. Another experiment using the OxFP at Zn^{2+}/Fe_{T_IN} ratio of 0.05 showed that at steady state the attainable Zn^{2+}/Fe_{T_SP} ratio was 0.046, while it was 0.194 for the experiment using the StTP at Zn^{2+}/Fe_{T_IN} ratio of 0.2 (Figure 6.1a). The Zn incorporation efficiencies obtained in these two experiments were thus similar to those attained at Zn^{2+}/Fe_{T_IN} ratio of 0.1.

In order to establish the maximal incorporation level of Zn^{2+} at 30 °C, the experiment was carried out at a higher Zn^{2+}/Fe_{T_IN} ratio (i.e. 0.33) in a continuous mode. The Zn^{2+}/Fe_T ratio in the product as a function of time is presented in Figure 6.1b. As can be seen, the Zn^{2+}/Fe_{T_SP} ratio at steady state was 0.32, indicating about 96% Zn incorporation efficiency. As the attempt to incorporate Zn^{2+} at Zn^{2+}/Fe_{T_IN} ratio of 0.5 under the current experimental conditions was failed, it can be concluded that the maximal Zn^{2+}/Fe_{T_SP} ratio achieved at ambient temperature was 0.32 or $x = 0.73$ (as in $Me_xFe_{3\text{-}x}O_4$).

To find out the degree of ferrite oxidation, the ratio of total divalent (M^{2+}) to total metals (M_T) in the product was plotted as a function of Zn^{2+}/Fe_{T_SP} (Figure 6.2). As the M^{2+}/M_T ratio in the product (M^{2+}/M_{T_SP}) was less than that of an ideal ferrite (0.33), all the Zn ferrites produced under the current experimental conditions were considered non-stoichiometric. Furthermore, it can also be observed that the M^{2+}/M_{T_SP} ratio tended to increase with Zn^{2+}/Fe_{T_SP}.

The M^{2+}/M_T ratio in the Zn ferrite produced at Zn^{2+}/Fe_{T_IN} ratio of 0.1 by the StFP was about 0.27, while the ferrite synthesised by the OxFP had a ratio of approximately 0.29. This result suggests that the Zn ferrite produced by the StFP is more oxidised than the product of the OxFP. It should be noted that at the highest Zn^{2+}/Fe_{T_SP} ratio achieved by the StFP, the M^{2+}/M_{T_SP} ratio was relatively close to an ideal ferrite (Figure 6.2).

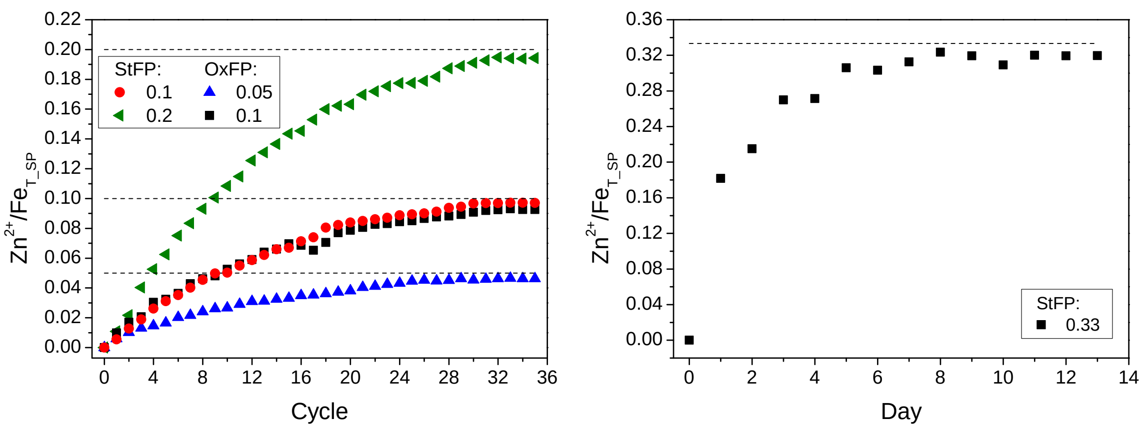
(a) (b)

Figure 6.1: Zn^{2+}/Fe_T ratios in the ferrite produced at 30°C in the (a) batch and (b) continuous system. The values in the legend indicate the Zn^{2+}/Fe_{T_IN} ratio and the dashed lines represent the theoretical maximal Zn^{2+}/Fe_{T_SP} ratio.

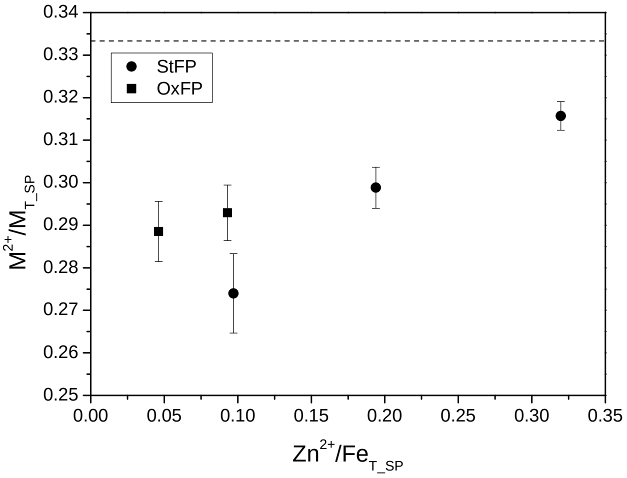

Figure 6.2: Divalent metal to total metal ratio in Zn ferrite produced at 30 °C *as a function of* Zn^{2+}/Fe_{T_SP}*. The dashed line represents the* M^{2+}/M_{T_SP} *ratio of an ideal ferrite.*

6.2.1.2 Nickel

The incorporation of Ni^{2+} into the ferrite structure was investigated at a Ni^{2+}/Fe_{T_IN} ratio of 0.05 in the batch system employing the StFP and the OxFP. The Ni^{2+}/Fe_T ratio in the ferrite (Ni^{2+}/Fe_{T_SP}) produced by the StFP at steady state was slightly higher than that formed by the OxFP (Figure 6.3a). The Ni incorporation efficiency achieved by the former and the latter was 88% and 85%, respectively.

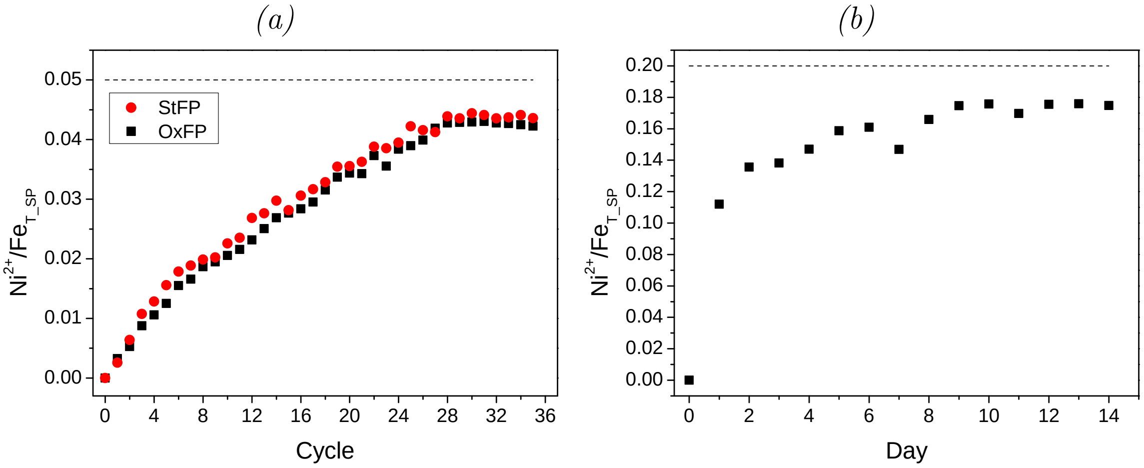

Figure 6.3: Ni^{2+}/Fe_T *ratios in the ferrite produced at 30* °C *and* Ni^{2+}/Fe_{T_IN} *ratio of (a) 0.05 in the batch system and (b) 0.2 in the continuous system. The dashed lines represent the theoretical maximal* Ni^{2+}/Fe_{T_SP} *ratio.*

To investigate the maximal incorporation of Ni^{2+} at 30 °C, the StFP experiment was carried out at a Ni^{2+}/Fe_{T_IN} ratio of 0.2 in a continuous mode (Figure 6.3b). It was found that the Ni^{2+}/Fe_{T_SP} ratio obtained at steady state was around 0.18. The effort to incorporate Ni^{2+} at a Ni^{2+}/Fe_{T_IN} ratio > 0.2 was unsuccessful. Under this high ratio, much amorphous precipitate was formed; thus, the experiment was not continued. Under the current experimental work, the maximal Ni^{2+}/Fe_{T_SP} ratio attained was 0.18 or $x = 0.46$.

It was also observed that the Ni ferrite produced by the StFP had a lower M^{2+}/M_T ratio than that formed by the OxFP (i.e. 0.24 and 0.29 for the former and the latter, respectively), similar to the trend observed in Zn ferrite. Furthermore, the Ni ferrite obtained by the StFP seemed to have a higher M^{2+}/M_T ratio with increasing Ni^{2+}/Fe_{T_SP}, i.e. 0.28 for the Ni^{2+}/Fe_{T_SP} ratio of 0.18.

6.2.1.3 Cadmium

The incorporation experiments with Cd^{2+} were conducted at a Cd^{2+}/Fe_{T_IN} ratio of 0.071 applying the StFP and the OxFP. The results in terms of the Cd^{2+}/Fe_T ratio in the solid product (Cd^{2+}/Fe_{T_SP}) are presented in Figure 6.4. As can be seen, the Cd^{2+}/Fe_{T_SP} ratio achieved by the StFP was significantly lower than that obtained by the OxFP, i.e. 0.050 vs. 0.036, corresponding to about 71% and 50% Cd incorporation efficiency, respectively. It was also found that the M^{2+}/M_T ratio in the Cd ferrite produced by the StFP was lower than that precipitated by the OxFP (i.e. 0.23 vs. 0.3).

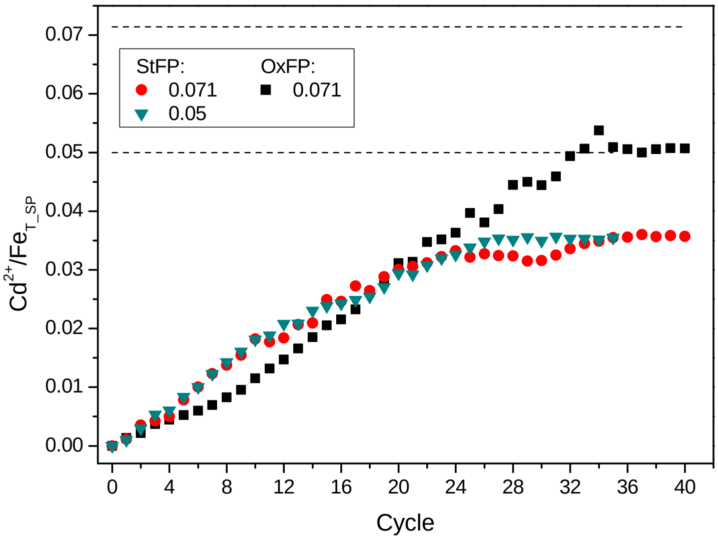

Figure 6.4: Cd^{2+}/Fe_T ratios in the ferrite produced at 30°C. The values in the legend indicate the Cd^{2+}/Fe_{T_IN} ratio and the dashed lines represent the theoretical maximal Cd^{2+}/Fe_{T_SP} ratio.

As it was found that the incorporation efficiency of Cd^{2+} achieved by the StFP at Cd^{2+}/Fe_{T_IN} ratio of 0.07 was relatively low, another experiment at a lower Cd^{2+}/Fe_{T_IN} ratio (i.e. 0.05) was conducted (Figure 6.4). It was observed that the

Cd^{2+}/Fe_{T_SP} ratio at steady state was about 0.0354, similar to that obtained in the experiment at Cd^{2+}/Fe_{T_IN} ratio of 0.07 (i.e. 0.036). The degree of Cd ferrite oxidation was also equal, as indicated by the similar M^{2+}/M_{T_SP} ratio achieved in these two experiments. Based on these results, it can be concluded that the maximal Cd^{2+}/Fe_{T_SP} ratio achieved by the StFP was approximately 0.036. The maximal incorporation extent under the current experimental conditions is, however, taken from the extent achieved by the OxFP, i.e. $Cd^{2+}/Fe_{T\_SP} = 0.05$ or $x = 0.14$.

6.2.1.4 Aluminium

The incorporation of Al^{3+} was conducted at a Al^{3+}/Fe_{T_IN} ratio of 0.1 using the StFP in the batch system. The ratio of Al^{3+}/Fe_T in the solid particles (Al^{3+}/Fe_{T_SP}) at steady state was 0.085 or $x = 0.24$. No further experiment was done for this metal. The maximal incorporation extent of Al^{3+} under ambient temperature conditions was deduced by comparing the current result to that reported by other authors. Schwertmann and Murad [157] found that the highest possible extent of Al^{3+} incorporation into the ferrite produced by slow oxidation of mixed $FeCl_2$-$AlCl_3$ solutions at room temperature with a reaction time of up to 155 days was about 0.36 (in terms of x in $Me_xFe_{3-x}O_4$). However, the end-products consisted of a 70% ferrite-30% goethite mixture. When the product composed almost exclusively of ferrite, the highest value of x was only about 0.25 [157], close to the result obtained in this study. As shown later (Section 6.2.2), ferrite was also the only solid product found in the current experiment. It should be noted that in this work the maximal incorporation extent of Me is only considered in the condition of ferrite-only end product. As stated previously, the attempts to incorporate Me at a higher incorporation level were discontinued when the settling, colour, and magnetic properties of the solid was deteriorated (i.e. much amorphous solid phase was formed). Although ferrite was the only solid phase formed during the incorporation of Al^{3+}, it had a significantly higher oxidation degree than the other ferrites (Zn, Ni, and Cd ferrite) ($M^{2+}/M_{T\_SP} = 0.16$).

6.2.1.5 Copper

Preliminary experiments of Cu^{2+} incorporation at elevated temperature (90 °C) indicated that Cu^{2+} could only be incorporated to a very low extent. Thus, the experiments of Cu^{2+} incorporation at 30 °C were conducted at a low Cu^{2+}/Fe_{T_IN} ratio, i.e. 0.033 in a batch mode. The Cu^{2+}/Fe_T ratios in the solid particles (Cu^{2+}/Fe_{T_SP}) produced by the StFP and the OxFP are illustrated in Figure 6.5. The Cu^{2+}/Fe_{T_SP} ratio at steady state was indeed very low, i.e. around 0.0018 and 0.0021 for the OxFP and the StFP sample, respectively. Thus, the efficiency of Cu^{2+} incorporation into the ferrite produced by the OxFP and the StFP was only about 5.4 and 6.3%, respectively. Although copper was not structurally incorporated into the ferrite structure, it could be completely removed from the aqueous solution. A high amount of copper seemed to exist as an adsorbed metal species on the particle surface or as a separate solid phase, which was readily removed during the rinsing procedure.

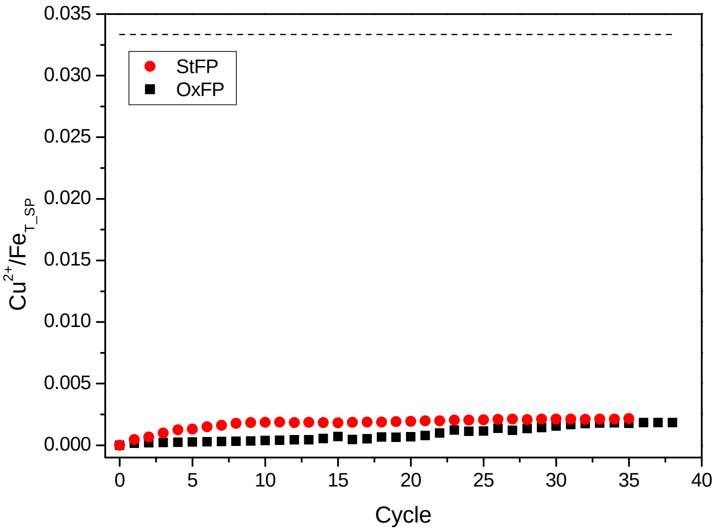

Figure 6.5: Cu^{2+}/Fe_T ratios in the solid particles produced at 30°C and Cu^{2+}/Fe_{T_IN} ratio of 0.033. The dashed lines represent the theoretical maximal Cu^{2+}/Fe_{T_SP} ratio.

The M^{2+}/M_T ratio in the solid particles was also relatively low, i.e. about 0.24 and 0.15 for the solid produced by the OxFP and the StFP, respectively. This result can be related both to the high oxidation degree of the spinel phase and to the formation of Fe(III) oxide. The former was not measured directly because no phase separation (between ferrite and Fe(III) oxide) was carried out prior to the chemical analysis. Unit cell size of the ferrite discussed later in Section 6.2.2 can provide an indication of ferrite oxidation degree.

Based on the above results, it can be deduced that copper hardly entered the ferrite structure. As similar findings were observed at ambient and elevated temperatures, it seems that temperature did not have much influence on the incorporation process of copper. The limited incorporation extent of Cu^{2+} can be related to the reduction process of Cu^{2+} by Fe^{2+}. In the presence of oxygen, it is known that Cu^{2+} can act as a catalyst in the oxidation of dissolved Fe^{2+} [205] or even structural Fe^{2+} [206]. In a recent work, Matocha et al. [207] reported that under anoxic conditions the Fe^{2+} ions can reduce Cu^{2+} resulting in the consumption of one mole Fe^{2+} and production of one mole Cu^{+}, as shown in Equation 6.1.

$$Cu^{2+}(aq) + Fe^{2+}(aq) \longrightarrow Cu^{+}(aq) + Fe^{3+}(aq) \tag{6.1}$$

If Cu exist in the solution as monovalent ions, it cannot enter the ferrite structure. Upon increasing the pH, it probably precipitates as cuprite (Cu_2O). The other important fact that should be considered is the tetragonally distorted octahedral geometry of Cu^{2+} due to the Jahn-Teller effect [92, 208], which may inhibit the incorporation of Cu^{2+} into the ferrite structure.

6.2.1.6 Chromium

To verify the results of the elevated temperature experiments showing that Cr^{3+} was not incorporated into the ferrite structure, the batch experiments of Cr^{3+} incorporation were conducted at 30 °C. The investigations can be divided into two parts based on the preparation of the Cr(III) solution. In the first part, the Cr(III) solution was prepared by dissolving Cr(III) salt ($CrCl_3$), while in the second part, the Cr(III) solution was prepared by reducing Cr(VI) solution with ferrous sulphate under acidic conditions (pH 2). The first investigation is termed “one-step Cr^{3+} incorporation”, whereas the second one is denoted “two-step Cr^{3+} incorporation”.

The one-step Cr^{3+} incorporation experiments were conducted using the OxFP and the StFP at a Cr^{3+}/Fe_{T_IN} ratio of 0.1. The ratios Cr^{3+}/Fe_T in the solid particles (Cr^{3+}/Fe_{T_IN}) obtained under these experimental conditions are presented in Figure 6.6a. On the other hand, the two-step Cr^{3+} incorporation experiments were carried out using the StFP at two different Cr^{3+}/Fe_{T_IN} ratios, i.e. 0.05 and 0.2. The results in terms of Cr^{3+}/Fe_{T_SP} are illustrated in Figure 6.6b. In the one-step Cr^{3+} incorporation experiments, it was observed that the Cr^{3+}/Fe_T ratio in the solid particle produced by the the OxFP and the StFP achieved a constant value of about 0.06 and 0.07, respectively (Figure 6.6a). In the two-step Cr^{3+} incorporation experiments (Figure 6.6b), the Cr^{3+}/Fe_{T_SP} ratio was about 0.035 and 0.1 at Cr^{3+}/Fe_{T_IN} ratio of 0.05 and 0.2, respectively. The results of the chemical composition analysis are later validated by the dissolution test discussed in Section 6.2.6.

The one-step Cr^{3+} incorporation experiments showed that the M^{2+}/M_T ratio in the solid particles (M^{2+}/M_{T_SP}) produced by the the OxFP and the StFP was 0.25 and 0.05, respectively. The low ratio of M^{2+}/M_T found in the latter solid can be attributed to the relatively low initial M^{2+}/M^{3+} (i.e. $Fe^{2+}/(Fe^{3+} + Cr^{3+})$) ratio applied in this experiment (about 0.48). This was conducted as an attempt to maintain the initial Fe^{2+}/Fe^{3+} ratio similar to that applied in the other Me incorporation experiments. In the OxFP, where Fe^{2+} was presented in excess, the M^{2+}/M_{T_SP} ratio was indeed higher.

The M^{2+}/M_T ratio in the solid particles obtained in the two-step Cr^{3+} incorporation experiments using the StFP was 0.21 and 0.11 for the experiment at Cr^{3+}/Fe_{T_IN} ratio of 0.05 and 0.2, respectively. These ratios were higher than that attained in the one-step Cr^{3+} incorporation using the same method mentioned before. The results could be related to a higher initial M^{2+}/M^{3+} ratio applied in the two-step Cr^{3+} incorporation experiments. It is noted that in these experiments the initial M^{2+}/M^{3+} ratio employed was 0.61 and 1.13

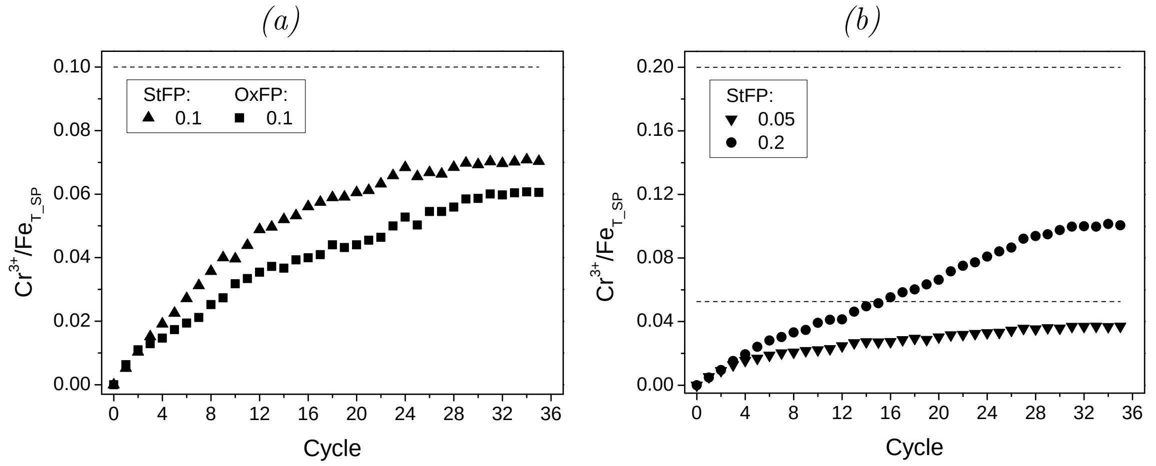

Figure 6.6: Cr^{3+}/Fe_T ratios in the solid particles produced at 30 °C in the (a) one-step Cr^{3+} incorporation and (b) two-step Cr^{3+} incorporation experiments. The values in the legend indicate the Cr^{3+}/Fe_{T_IN} ratio and the dashed lines represent the theoretical maximal value of Cr^{3+}/Fe_{T_SP}.

at Cr^{3+}/Fe_{T_IN} ratio of 0.05 and 0.2, respectively. The low M^{2+}/M_{T_SP} ratio obtained in all Cr^{3+} experiments indicates a high oxidation degree of the spinel phase as well as the presence of Fe(III) oxide.

6.2.2 Crystalline phases and unit cell sizes

The XRD patterns of Zn, Ni, and Al ferrite showed spinel compounds only with a high degree of crystallinity. In the case of Cd ferrite, however, the peak intensities of the product obtained by the StFP were significantly lower than those of the OxFP product, indicating its lower crystallinity degree (Figure 6.7). The presence of a significant amount of goethite (up to 30%) as admixture to the spinel particles could be observed in the XRD patterns of the solid particles obtained in the experiments with Cu^{2+} and Cr^{3+} by the StFP. Clearly less goethite was observed in the solid samples produced by the OxFP, probably less than 5% of the product.

Based on the XRD patterns, the unit cell size (a) of the spinel phase was calculated and shown in Figure 6.8. The a value of Zn ferrite was linearly increased with Zn^{2+} content, similar to the trend observed for Zn ferrites precipitated at 90 °C. The unit cell size variations with Zn^{2+} content observed for Zn ferrites produced by the OxFP appeared to be similar to those found for the StFP samples. More data points with respect to the former are, however, required to confirm this finding.

The a value of Ni ferrite appeared to be smaller than that of magnetite (Figure 6.8). It was also observed that the unit cell size of Ni ferrite with the Ni^{2+}/Fe_{T_SP} ratio of 0.044 was similar to that of 0.18. In view of the fact that the former ferrite had a higher

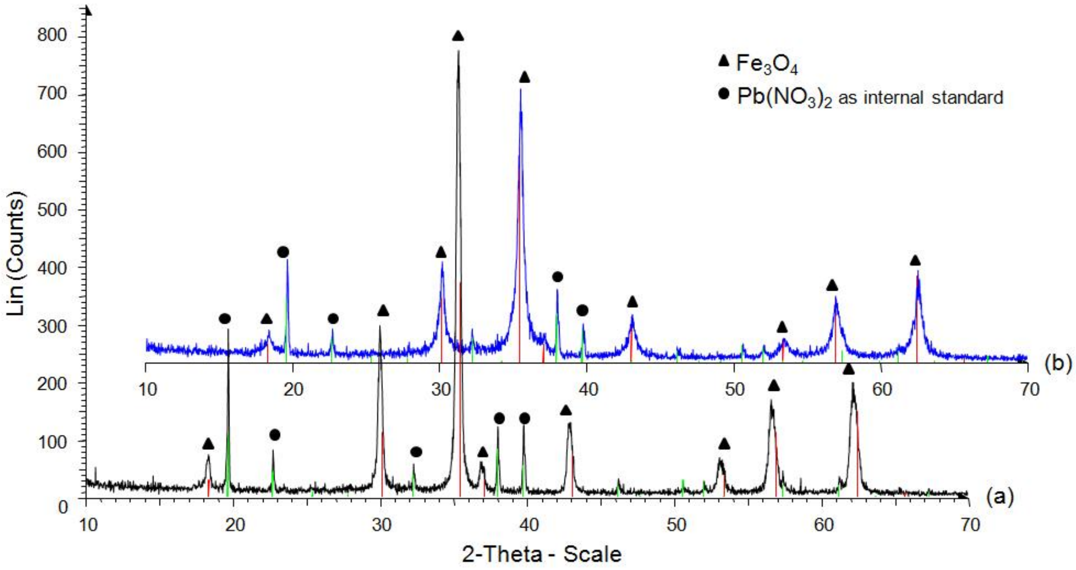

Figure 6.7: XRD patterns of Cd ferrites produced at 30 °C by (a) OxFP and (b) StFP.

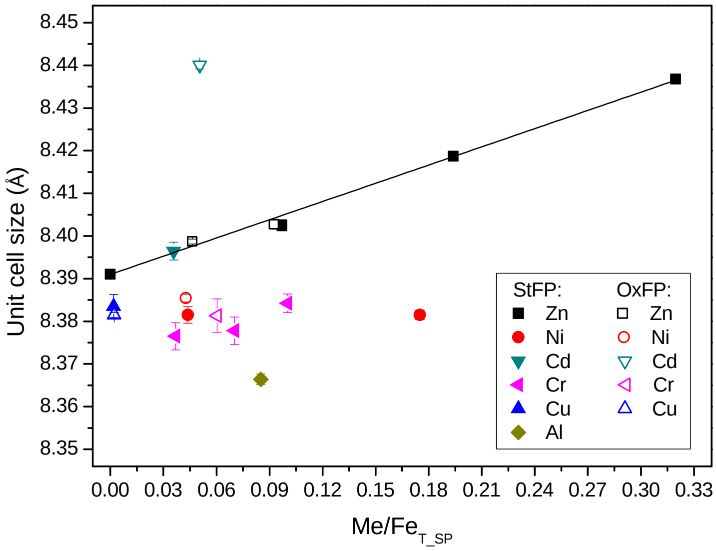

Figure 6.8: Unit cell size of the spinel phase produced at 30 °C as a function of Me content in the product. Only data points related to the Zn ferrites are connected by a solid line.

oxidation degree than the latter (Section 6.2.1.2), it is suggested that the oxidation degree of Ni ferrite affects its unit cell size, particularly the one with a low Ni^{2+} content.

The degree of oxidation was also considered to have a significant effect on the unit cell size of Cd ferrite produced by the StFP. As shown in Figure 6.8, the unit cell size of this ferrite was only slightly larger than that of magnetite, deviating from the expectation that Cd^{2+} incorporation considerably increases the unit cell size. The enlargement of the unit cell size due to Cd^{2+} incorporation was apparently counteracted by the effect of Fe^{2+} deficiency (higher oxidation degree). However, this opposite effect was not observed for

Cd ferrite synthesised by the OxFP as it had a M^{2+}/M_T ratio close to the stoichiometric value

The *a* value of the only Al ferrite synthesised at ambient temperature was found to be smaller than that of magnetite (Figure 6.8). Due to the limitation of data, no correlation between the unit cell size and the Al^{3+} content could be established. It is noted that a non linear relationship was reported by Schwertmann and Murad [157] due to the variation of *a* with both the degree of oxidation and Al^{3+} incorporation.

As shown in Figure 6.8, the unit cell size of the spinel phase formed in the incorporation of Cu^{2+} and Cr^{3+} was smaller than that of magnetite. As Cu^{2+} and also Cr^{3+} (shown later) were not incorporated into the ferrite structure, the contraction of the unit cell size of the spinel phase reflected the high oxidation degree of the corresponding phase.

Based on the above results, it can be concluded that the unit cell sizes of most ferrites produced at ambient temperatures are largely affected by the oxidation degree of the corresponding ferrites. Thus, the changes in the unit cell size cannot directly indicate whether Me incorporation has occurred.

6.2.3 Metal spatial distribution

Similar to the experiments at elevated temperatures, the distribution of metals within the ferrite particle is evaluated by the dissolution of the solid particles in 12.8% HCl solution at $23 \pm 2\,^{\circ}$C. Dissolution data for Zn and Fe for all Zn ferrite samples were well described by a line of slope ∼1 (results not shown graphically), that is, the ratio Zn/Fe remained almost unaffected during the dissolution test, strongly suggesting that Zn and Fe were uniformly distributed within the crystal structure of ferrite, resulting in a nearly congruent dissolution of the Zn ferrites. A similar result was also observed for Al ferrite.

Representative dissolution data for the particles produced in the incorporation of Ni^{2+}, Cd^{2+}, and Cr^{3+} are shown in Figure 6.9. The data for Cu^{2+} are not depicted in this figure as the Cu^{2+} content in the solid particles can be considered insignificant. It is noted that the trace amount of Cu^{2+} measured in the solid particles was found to be concentrated close to the particle surface.

The dissolution data of Ni ferrite particles indicated a congruent distribution of Ni^{2+} (Figure 6.9). This finding is different from the result obtained for Ni ferrite produced at 90 °C discussed in Chapter 5.2.3, where Ni^{2+} was found to dissolve incongruently. The homogeneous distribution of Ni^{2+} obtained in the experiments at ambient temperature might be associated with the presence of seed, which was suggested to reduce the activation energy for ferrite formation [9]. Furthermore, a higher pH applied in the Ni ferrite synthesis at ambient temperature (10.5) compared to the value practiced at 90 °C (∼7) may also result in the homogeneity of the Ni^{2+} distribution in the former Ni ferrite.

It was also found that the distribution of Cd^{2+} in the Cd ferrite was not completely

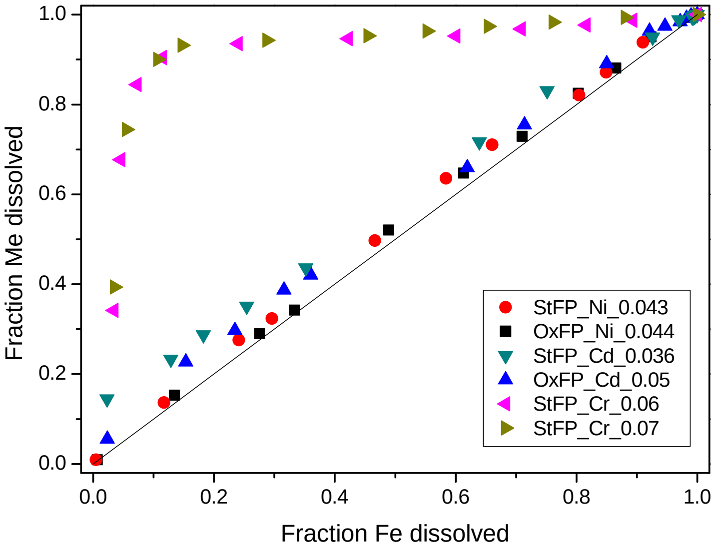

*Figure 6.9: Plots of the fraction of Me versus Fe dissolved in 12.8% HCl solution for some representative solid particles produced at 30 °*C*. The legend indicates the Me/*Fe_{T_SP} *ratio determined after washing with acidic solution (pH 2).*

homogeneous. As can be seen in Figure 6.9, Cd^{2+} was dissolved faster than Fe particularly in the earlier stage of the dissolution, indicating that cadmium tended to concentrate in the outer layers of the ferrite particles. This behaviour could lead to a higher Me leaching extent, as discussed later.

Similar to the results obtained at elevated temperatures, the dissolution tests of all solid particles produced in the incorporation of Cr^{3+} at 30 °C showed that Cr^{3+} was released significantly faster than Fe (Figure 6.9). Dissolved Cr^{3+} reached its final concentration in about 20 min, while iron was dissolved slowly in about 6 h, suggesting the enrichment of the amorphous chromium phase on the particle surface. As goethite existed together with the ferrite particles, the incorporation of Cr^{3+} into the goethite structure also seems possible, as observed by several authors [177, 209, 210] in the goethite formed by coprecipitation of Cr(III) and Fe(III) at elevated temperatures. No specific analysis was conducted to investigate this issue. A congruent distribution of Cr^{3+} in the goethite structure reported by Kaur et al. [177] may lead to the deduction that Cr^{3+} was not incorporated neither into the ferrite nor goethite structure under the current experimental conditions.

6.2.4 Infrared spectra of the precipitates

The FTIR spectra of Zn, Ni, Cd, and Al ferrites contained a main band (ν_1) at about 560–590 cm^{-1}, corresponding to the metal-oxygen vibration in tetrahedral site [182]. Another band also attributed to the spinel ferrite (ν_2) appeared in the range of 400–440 cm^{-1}. The existence of molecular water in the spinel structure was also indicated by two bands at around 3400 and 1600 cm^{-1}. The intensities of these bands seemed to increase with Me/Fe$_{T\_IN}$, as represented in Figure 6.10 for Zn ferrite. This result indicates the increased amount of water molecules remained in the spinel lattice with increasing Me content in the initial solution.

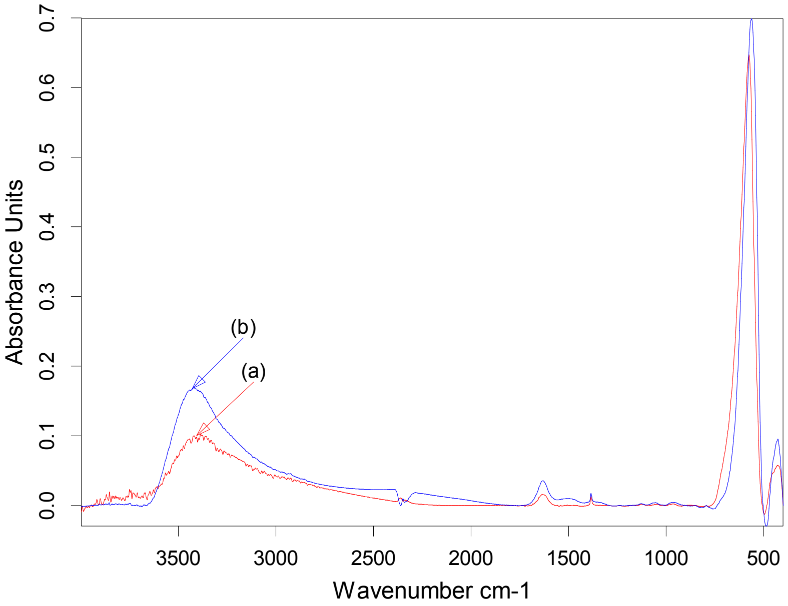

Figure 6.10: FTIR spectra of Zn ferrites produced by StFP at 30°C*, pH 10.5,* Zn^{2+}/Fe_{T_IN} *ratio of (a) 0.2 and (b) 0.33.*

The water and anion band intensities for Zn, Ni, and Cd ferrite produced by the StFP and the OxFP at a low Me/Fe$_{T\_IN}$ ratio was found to be relatively similar. However, at a high Me/Fe$_{T\_IN}$ ratio (≥ 0.2) the water band intensities for the StFP samples were observed to be higher than those found for the OxFP samples. This is demonstrated in Figure 6.11 in the case of Ni ferrite.

With regard to the StFP, it seemed that the ratio of Fe^{2+}/Fe^{3+} in the initial solution affected the amount of water molecule retained in the ferrite lattice. As shown in Figure 6.11b and c, the water band intensity at 3400 cm^{-1} for the StFP sample synthesised at the initial Fe^{2+}/Fe^{3+} ratio of 0.5 was higher than that of 0.57. Thus, it seems that the presence of Fe^{2+} promotes the removal of water molecules from the ferrite structure, improving the crystallinity of the ferrite. This postulation can also explain the difference in the water band intensities between the OxFP and the StFP samples explained before as the OxFP was known to be carried out in the presence of excess Fe(II).

In the FTIR spectra of the solid particles produced in the incorporation of Cr^{3+} and also Cu^{2+} (Figure 6.12), the features due to the vibration of hydroxyl groups associated with goethite were seen along with the bands corresponding to spinel lattice vibration. The bands assigned to the bending vibration of hydroxyl groups of goethite were observed

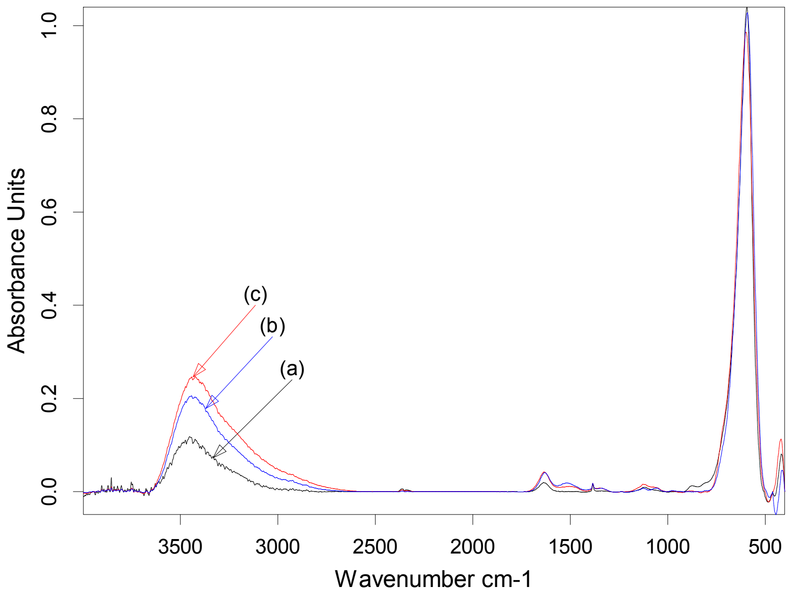

*Figure 6.11: FTIR spectra of Ni ferrites produced at 30°*C*, Ni^{2+}/Fe_{T_IN} ratio of 0.2, by (a) OxFP and StFP produced at the initial Fe^{2+}/Fe^{3+} ratio of (b) 0.57, (c) 0.5. Sample (a) and (c) were prepared by Klas [198].*

at about 797–802 cm^{-1} (γOH) and 893–900 cm^{-1} (δOH), while the band ν_1 and ν_2 of the spinel phase was found in the range of 580–610 cm^{-1} and 400–460 cm^{-1}, respectively.

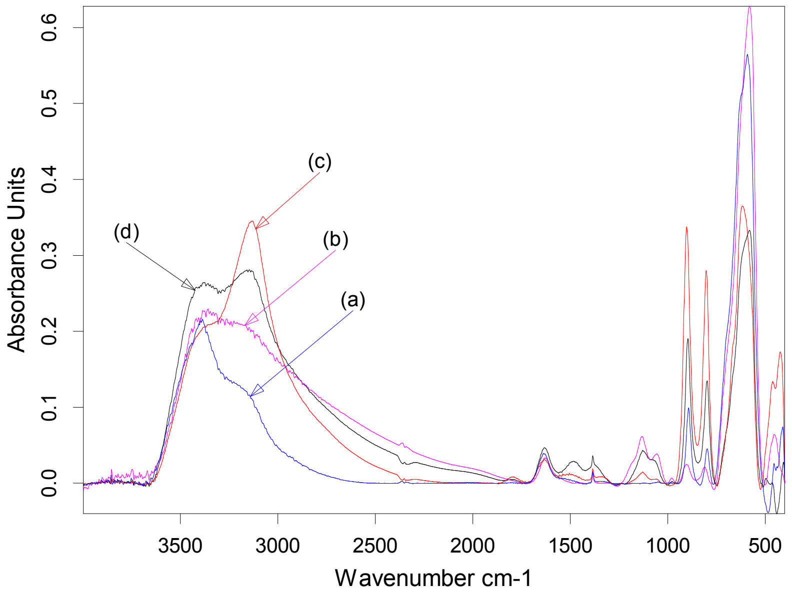

*Figure 6.12: FTIR spectra of the solid particles obtained in the incorporation experiments at 30°*C *with Cu^{2+} by (a) StFP and Cr^{3+} by (b) OxFP and StFP at Cr^{3+}/Fe_{T_IN} ratio of (c) 0.1, (d) 0.2.*

For the solid particles containing a significant amount of goethite, such as those produced by StFP, another band associated with the bulk OH stretching of goethite could also be observed at about 3100 cm^{-1} [47]. In accordance to the results at elevated temperatures, the FTIR spectra of the solid particles obtained in the incorporation of Cr^{3+} were characterised by the prominent feature of the molecular water band (at 3400 cm^{-1}) which tended to increase with Cr^{3+}/Fe_{T_IN}. The existence of the hydrous precipitates is thus likely.

6.2.5 Morphological characterisation

Morphological analysis of solid particles, except those produced in the experiments with Cu^{2+} and Cr^{3+}, indicated that they mostly consisted of almost spherical particles, which were strongly adhered to form larger aggregates. Due to the aggregation of the particles, the measurement of the particle size (single particle not aggregate) based on the visual observation by SEM could only give a rather rough estimation. The particles produced by the StFP were generally smaller and had less sharp boundaries than those synthesised by the OxFP. The particle size of Zn and Ni ferrites containing low Me levels produced by the StFP under batch condition was estimated to be approximately 30–80 nm, while those produced by the OxFP were about 50–120 nm. The particles produced by the StFP under continuous condition with high Me contents ($Zn^{2+}/Fe_{T\_SP} = 0.32$ and $Ni^{2+}/Fe_{T\_SP} = 0.18$) seemed to have a more homogeneous and smaller size, roughly about 45 nm. Some representative SEM images of Zn and Ni ferrites are presented in Figure 6.13. Surface area measurement (BET method) confirmed this analysis showing a higher surface area in the particles produced by the StFP compared to those synthesised by the OxFP and an increase in the surface area with increasing Me content (Figure 6.14).

Cd ferrite produced by the OxFP composed of particles over a relatively wide size range, about 30–140 nm. Some cubic particles about 170 nm was also observed (Figure 6.15a). Conversely, the Cd ferrite produced by the StFP consisted of smaller particles with relatively homogeneous size of about 30–40 nm (Figure 6.15b). Some small goethite particles were also observed, although this mineral fraction was below the detection limit of XRD. This observation was supported by surface area measurement showing a surface area of about 18 and 41 m^2/g in the Cd ferrite produced by the OxFP and the StFP, respectively. It should be noted that a change in colour from black to dark brown was observed in the latter Cd ferrite during sample drying at 40 °C. A similar change also occurred when samples were dried at room temperature. Since no measure had been taken to remove oxygen from air during sample drying, it can be assumed that the sample was oxidised to some extent during the drying process. This observation also means that the oxidation degree of the Cd ferrite obtained by the StFP was enhanced during the drying process. This resulted in a reduced crystallinity, additional formation of Fe(III) oxides such as goethite, and also a decrease in unit cell size as indicated earlier. The sensitivity of Cd ferrite produced by the StFP towards oxidation process can be associated with its

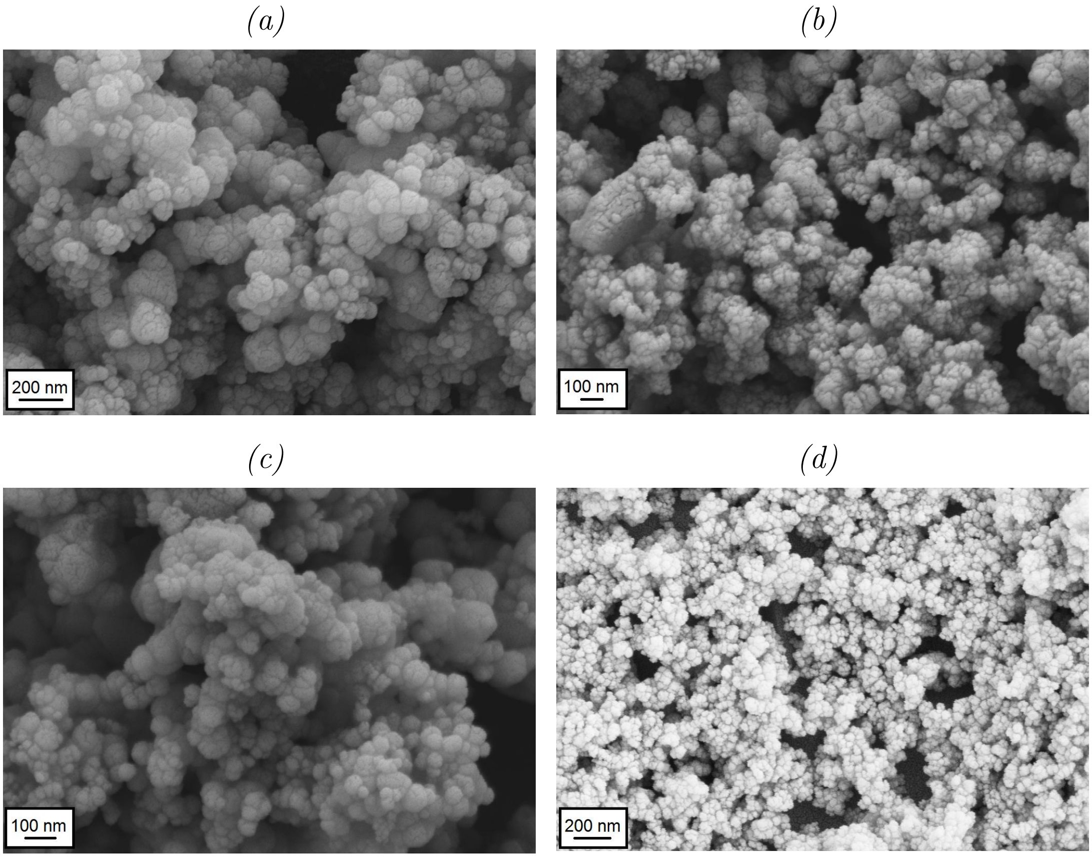

Figure 6.13: SEM images of Zn ferrites for Zn^{2+}/Fe_{T_SP} *ratio of (a) 0.093 produced at 30°C by OxFP, (b) 0.097 by StFP and Ni ferrites for* Ni^{2+}/Fe_{T_SP} *ratio of (c) 0.043 by OxFP, (c) 0.18 by StFP.*

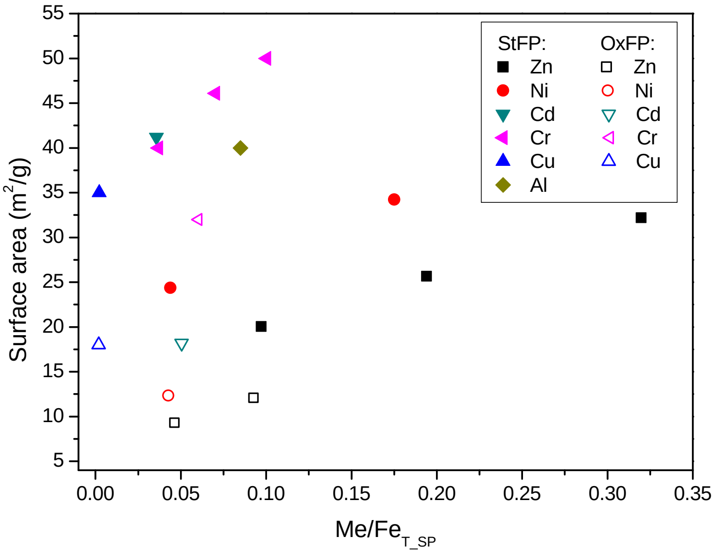

Figure 6.14: Specific surface area of the solid particles obtained in the Me incorporation at 30°C as a function of Me/Fe_{T_SP}.

significantly smaller particle size.

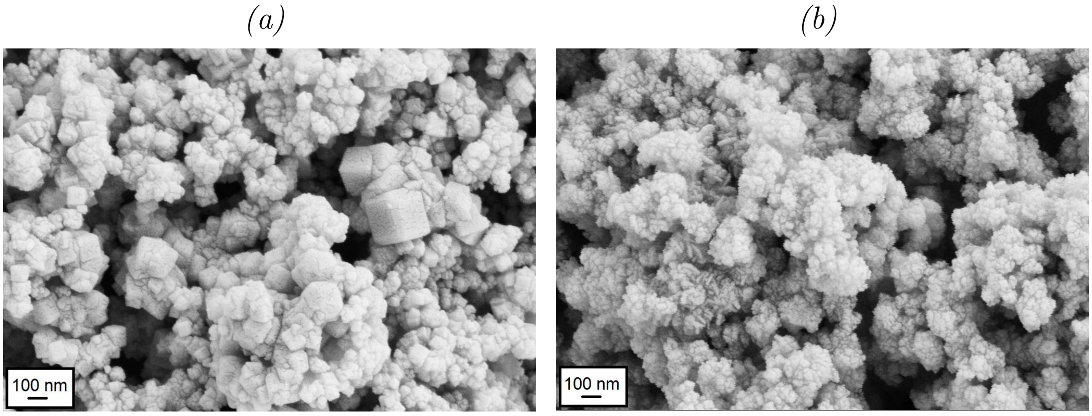

*Figure 6.15: SEM images of Cd ferrites produced at 30°*C *by (a) OxFP and (b) StFP.*

In the case of Al ferrite produced by the StFP, the size of the particles varied in a relatively narrow range of about 40–50 nm with a surface area of 40 m^2/g. It is noted that Schwertmann and Murad [157] found that the crystals had less well-defined shapes with increasing Al^{3+} substitution.

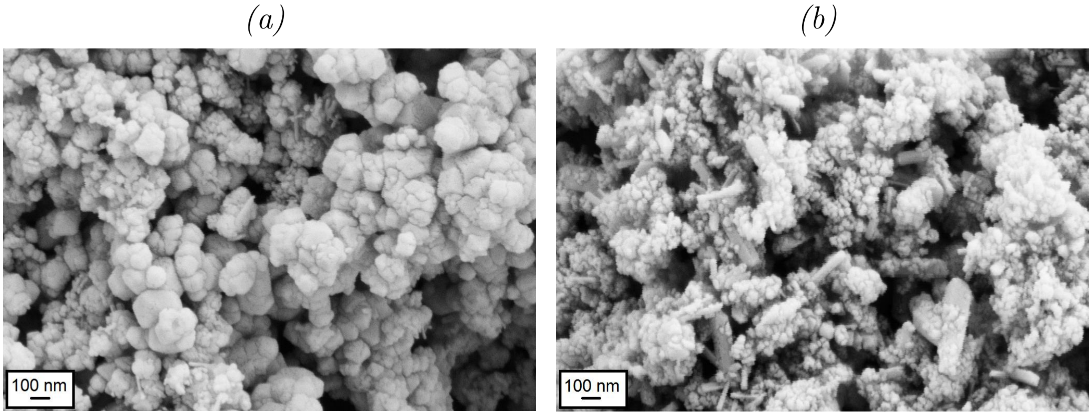

*Figure 6.16: SEM images of the solid particles obtained in the incorporation of Cu^{2+} at 30°*C *by (a) OxFP and (b) StFP.*

In addition to the nearly spherical ferrite particles, solid products synthesised in the experiments with Cu^{2+} and Cr^{3+} also consisted of acicular goethite particles (Figure 6.16 and 6.17). Clearly less goethite particles were observed in the solid samples produced by the OxFP compared to those synthesised by the StFP. The Fe(II) excess in the initial solution seemed to suppress the formation of goethite, in accordance to the previous results found in the magnetite formation discussed in Chapter 4. The ferrite particles produced in the experiment with Cu^{2+} by the OxFP were generally larger with a wider particle size distribution than those produced by the StFP, i.e. about 30–120 nm vs. 30–40 nm for the OxFP and the StFP sample, respectively (Figure 6.16).

The ferrite particle size produced in the experiment with Cr^{3+} by the OxFP and the StFP was found to be relatively similar, i.e. approximately 35–45 nm (Figure 6.17a and 6.17b). A better developed goethite crystals was clearly observed in the sample produced at a high Cr^{3+}/Fe_{T_IN} ratio (Figure 6.17d), suggesting a very rapid growth of goethite under this condition.

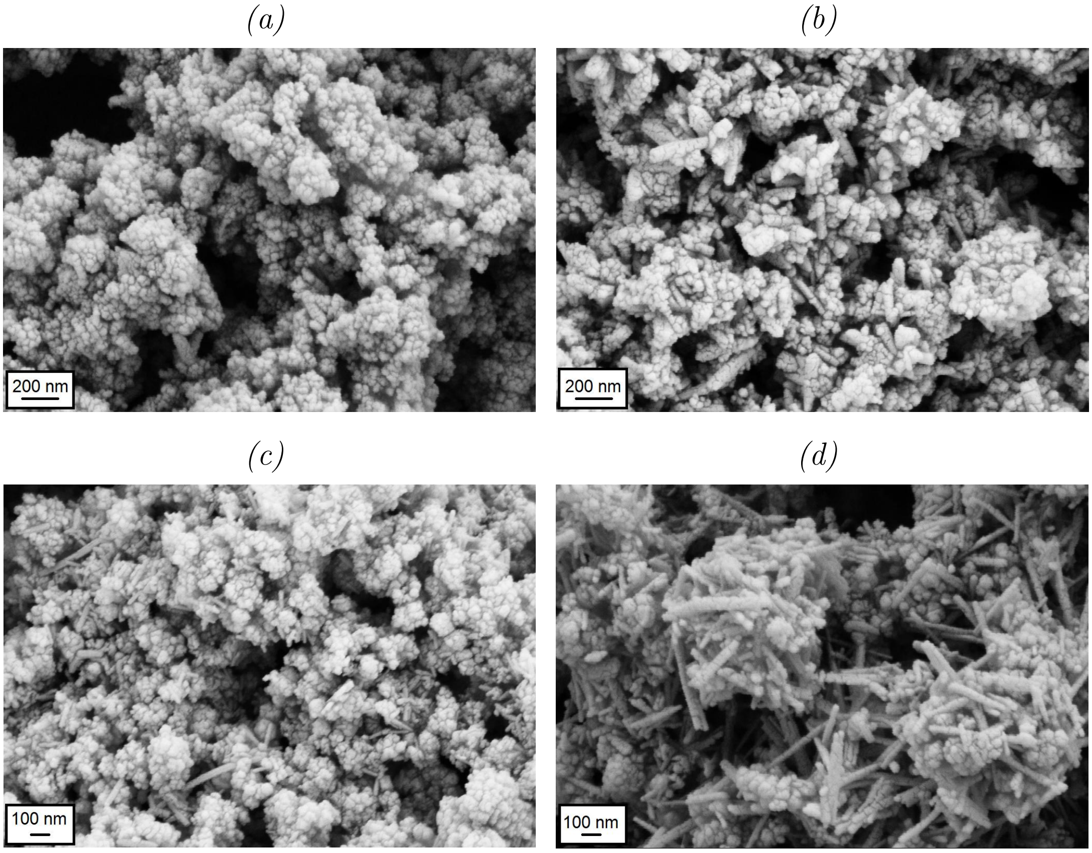

Figure 6.17: SEM images of the solid particles obtained at 30 °C *in the one-step* Cr^{3+} *incorporation by (a) OxFP, (b) StFP and in the two-step* Cr^{3+} *incorporation at* Cr^{3+}/Fe_{T_IN} *ratio of (c) 0.05, (d) 0.2.*

The crystallite sizes of the ferrite particles produced by the OxFP, as depicted in Figure 6.18, were larger than those synthesised by the StFP. The decrease in the crystallite size with increasing Me/Fe_{T_SP} was also observed, suggesting that the solid became less crystalline as the Me content increased. Furthermore, it was noticed that the Cd ferrite produced by the StFP had a significantly small crystallite size, which may indicate structural strain.

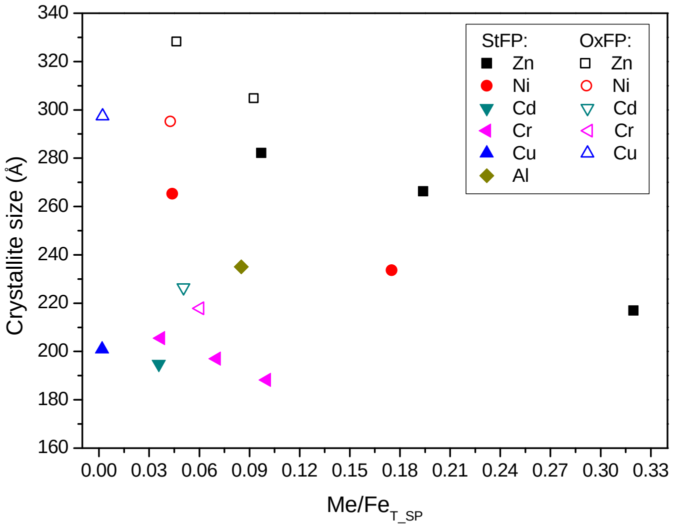

Figure 6.18: Crystallite size of the spinel phase produced at 30°C *as a function of Me/Fe$_{T\_SP}$.*

6.2.6 Chemical stability

The dissolution stability of the ferrite synthesised at ambient temperatures was assessed based on the results of solid dissolution in 12.8% HCl solution at 23 ± 2 °C. The initial linear dissolution rates of Fe obtained from the dissolution profile data of the products are plotted in Figure 6.19.

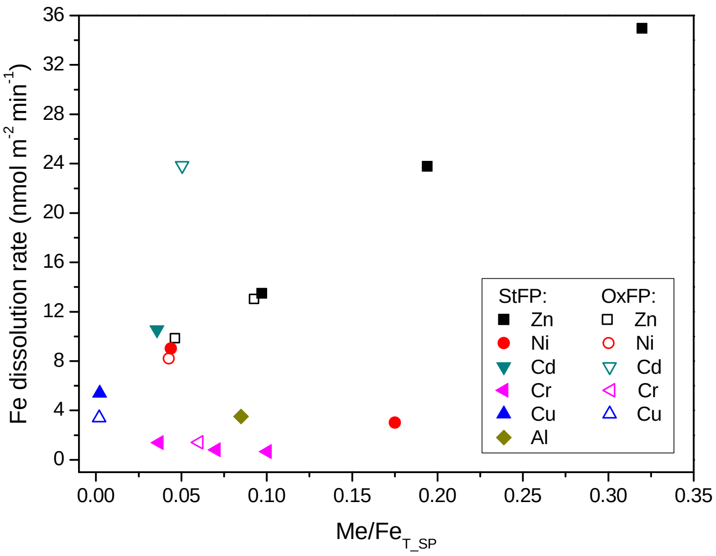

Figure 6.19: Initial Fe dissolution rates (12.8% HCl solution, 23 ± 2 °C *of the products synthesised at 30*°C.

The results showed that the Fe dissolution rate of Zn ferrite increased with Zn^{2+}/Fe_{T_SP}, suggesting that Zn ferrite was less stable with increasing Zn^{2+} content. A similar behaviour was also observed for Cd ferrite. In contrast to the other ferrites, it appeared that the Fe dissolution rate of Ni ferrite diminished with increasing Ni^{2+} substitution as a lower rate was observed at a high Ni^{2+}/Fe$_{T\_SP}$ ratio. Due to limitation of the data, it is rather difficult to deduce the stability tendency of Al ferrite at different Al^{3+} contents. However, the data showed in Figure 6.19 presumably indicate that the stability trend of Al ferrite is similar to that of Ni ferrite. In this case, the stability order of the ferrite synthesised at ambient temperatures is Al^{3+} $\approx$ Ni^{2+}$>$ Zn^{2+} $>$ Cd^{2+}.

Although Cr^{3+} was not incorporated into the ferrite structure, this ion was an effective dissolution inhibitor, as demonstrated in Chapter 5.5.1. This behaviour could explain the apparent low dissolution of the Cr-associated ferrite synthesised at ambient temperatures, as depicted in Figure 6.19.

The dissolution of the solid particles produced in the Cu^{2+} incorporation basically involved the Cu-free ferrite (i.e. magnetite) and goethite particles because the dissolution test was conducted on the washed solid samples. It is noted that goethite was reported to dissolve slower than magnetite [44, 157]. Several authors [48, 176] found that the dissolution curve of the solid samples containing two different phases of iron oxides (i.e. goethite and hematite) gave two lines with different slopes. This was not observed in this work, reflecting that the current dissolution test conditions could not effectively separate ferrite and goethite particles.

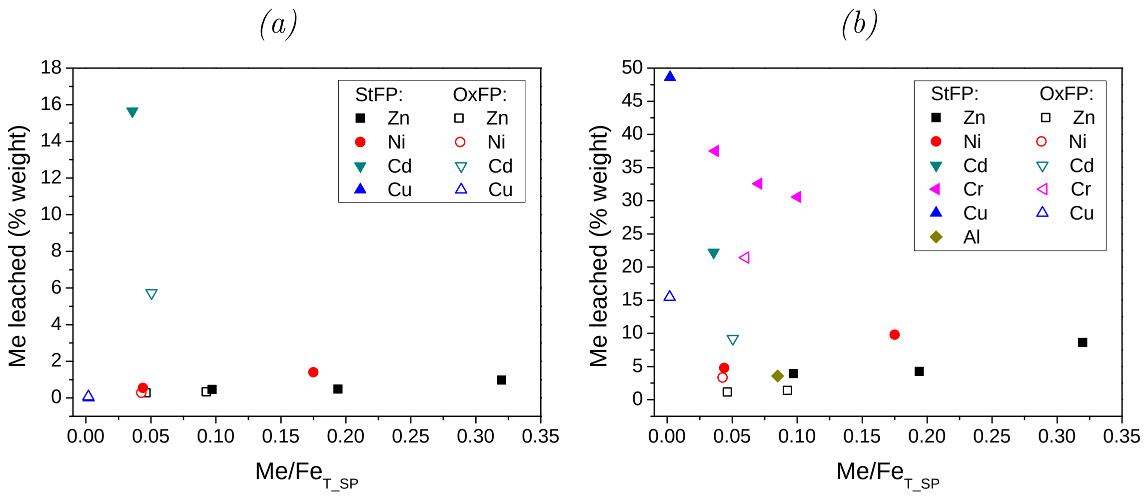

Figure 6.20: Weight percentages of non-iron metal leached from the products synthesised at 30°C in (a) TCLP test and (b) BCR test.

The extents of Me leaching based on the TCLP and BCR procedures are depicted in Figure 6.20. The leaching extents of Al and Cr from the solid product in the TCLP test are not shown in Figure 6.20a as they were very close to zero, in agreement with the results obtained at elevated temperatures. The leaching of Zn and Ni in the TCLP and BCR test seemed to increase with Me/Fe$_{T\_SP}$. Cd leaching was high in both test due to the existence of some fraction of Cd^{2+} close to the particle surface as revealed by the dissolution congruency test (Section 6.2.3) and also due to the low dissolution stability of Cd ferrite. The results in Figure 6.20 also suggest that Me was leached to a lower extent in the samples produced by the OxFP. This result can be associated with the larger particle size (lower surface area) of the solid particles obtained by this method.

The incongruent distribution of the trace amount of Cu^{2+} found in the solid particles led to the observed high Cu leaching extent in the BCR test. A similar reasoning can be used to explain the high leaching extent of Cr.

Based on the above discussion, it is clear that only Zn^{2+}, Ni^{2+}, Cd^{2+}, and Al^{3+} could be incorporated into the ferrite structure at ambient temperatures. On the contrary, the incorporation degree of Cu^{2+} and Cr^{3+} was close to zero. Thus, they are not further discussed in the following sections. Their presence in the aqueous solution is again considered in the last section of this chapter (Section 6.6).

6.3 Comparison of two ambient temperature ferrite synthesis methods

Based on the results of Me incorporation into the ferrite produced by the StFP and the OxFP presented in the previous sections, the StFP seemed to have an advantage over the OxFP with respect to the higher incorporation extent of Zn^{2+} and Ni^{2+}. A similar trend was also observed for Co^{2+} in the multi-metal system, as shown later in Section 6.5. The difference between the incorporation extent attained by the StFP and the OxFP was found to be relatively small. A comparable result was reported by Klas [198] for Co^{2+} in the single-metal system at a Co^{2+}/Fe_{T_IN} ratio of up to 0.33. A more distinct difference was, however, observed for the incorporation of Ni^{2+} at a Ni^{2+}/Fe_{T_IN} ratio of 0.2 [198]. The maximal incorporation extent of Cd^{2+} reported by Klas [198] was higher than that found in the current work, i.e. 0.06 vs. 0.05 (in terms of Cd^{2+}/Fe_{T_SP}). It must be noted that these values were obtained by different methods. Klas [198] synthesised Cd ferrite using the StFP, while the OxFP was employed in the current work. Based on this comparison, it can be deduced that a higher incorporation extent of Cd^{2+} was also obtained by the StFP.

The lower incorporation extent of Cd^{2+} achieved by the StFP in this work as compared to the value reported by Klas [198] can be associated with the difference in the initial Fe^{2+}/Fe^{3+} ratio employed during the synthesis procedure, i.e. 0.5 vs. 0.67 in the former and latter work, respectively. Thus, it is suggested that the initial Fe^{2+}/Fe^{3+} ratio influences the Me incorporation degree. The importance of maintaining the initial Fe^{2+}/Fe^{3+} ratio at a certain level to achieve the highest possible extent of Me incorporation is highlighted. Based on the results of this work, it is proposed that the initial Fe^{2+}/Fe^{3+} ratio employed in the StFP should be maintained around or above 0.5 (i.e. 0.33 in terms of Fe^{2+}/Fe_{T_IN}).

However, it is assumed that, until a certain level, increasing the initial Fe^{2+}/Fe^{3+} ratio will not much affect the incorporation extent as the larger amount of Fe^{2+} will be preferentially incorporated into the spinel structure relative to the Me ion. This could probably result in an even lower Me incorporation.

The ferrites produced by the OxFP were found to be more crystalline than those synthesised by the StFP, which can be associated with the lesser amount of water molecules retained in the crystal structure. This difference was particularly noticed at a high Me/Fe_{T_IN} ratio ($\geq$0.2). As shown earlier, the dehydration process seemed to be promoted by the Fe(II) excess in the initial solution.

Due to its larger particle size (lower surface area), the ferrite obtained by the OxFP had a lower oxidation degree (higher M^{2+}/M_T ratio) and a lower metal leaching potential. However, the difference did not seem to be very large, except for Cd^{2+}. The larger particle size obtained by the OxFP indicates that the nucleation number in the OxFP is less than that in the StFP. The supersaturation degree for nucleation is lower because oxidation of Fe(II) to Fe(III) in the solution, which is necessary to occur for the formation of ferrite, is supposed to require time to occur.

The precipitates produced by these two methods were characterised by charcoal black colour and excellent settling properties. They also responded strongly to magnetic fields. The metal concentrations in the effluents were normally below the detection limit. The base consumption was comparable to the theoretical value of about 2 and 2.67 mol NaOH per total initial metal added according to the OxFP and the StFP reaction shown in Equation 6.2 and 6.3, respectively. Thus, it can be deduced that the StFP requires about 25% more base than the OxFP. From an operational point of view, the StFP has the advantage of operational simplicity as no aeration control is needed.

$$\mathrm{Fe^{2+} + 2\,Fe^{3+} + 8\,OH^- \longrightarrow Fe_3O_4 + 4\,H_2O} \tag{6.2}$$

$$\mathrm{3\,Fe^{2+} + 0.5O_2 + 6\,OH^- \longrightarrow Fe_3O_4 + 3\,H_2O} \tag{6.3}$$

It is clear that each method has its advantages and limitations. Based on the results obtained so far, no clear preference between these methods can be suggested. However, due to its convenient operation, the StFP seems to be a more attractive option.

6.4 Comparison of ambient- and elevated-temperature ferrites

To have a better understanding about the influence of a large synthesis temperature difference on the characteristics of the forming ferrites, the results obtained at ambient temperatures are compared to the elevated temperature results. The comparison includes three different aspects, i.e. metal incorporation extent, morphology, and chemical stability.

6.4.1 Metal incorporation extent

The maximal incorporation extents of different non-iron metals (Me) attained at ambient and elevated temperatures are summarised in Table 6.1 together with those reported by Klas [198]. It can be deduced that the maximal incorporation extent of Me at ambient temperatures was about 49–73% of the corresponding value attained at elevated temperatures. It was also found that the preferential order of Me incorporation at ambient temperature was similar to that observed at elevated temperature. Thus, it can be assumed that the fundamental processes responsible for metal ion incorporation under both ambient and elevated temperature ferrite syntheses are similar.

Table 6.1: Maximal incorporation extents of five metal ions into ferrites produced at ambient and elevated temperatures.

Metal	Method	T(°C)	pH	Initial[a] Fe^{2+}/Fe^{3+}	Initial Me/Fe_T	Max. Me/Fe_{T_SP}	Max. x[b]	Max. x[b] at 90 °C
Zn^{2+}	StFP	30	10.5	0.57	0.33	0.32	0.73	1.0
Co^{2+}	StFP	30	10.5	0.25[c]	0.33[c]	0.29[c]	0.67[c]	1.0
	OxFP	30	10.5	-	0.33[c]	0.28[c]	0.66[c]	
Ni^{2+}	StFP	30	10.5	0.57	0.20	0.18	0.46	0.78
	StFP	20	10.5	0.57[c]	0.20[c]	0.15[c]	0.39	
	OxFP	30	10.5	-	0.20[c]	0.12[c]	0.32	
Al^{3+}	StFP	30	10.5	0.5	0.1	0.085	0.24	0.49
Cd^{2+}	StFP	30	10.5	0.67[c]	0.07[c]	0.060[c]	0.17[c]	0.35
	OxFP	30	10.5	-	0.07	0.05	0.14	

[a] Initial Fe^{2+}/Fe^{3+} ratio in the StFP

[b] x in $Me_xFe_{3\text{-}x}O_4$

[c] Klas [198]

It is generally accepted that the precipitation of ferrite at elevated temperatures (60–100 °C) proceeds mainly through a dissolution-reprecipitation mechanism (Chapter 5). Considering two competitive mechanisms of ferrite formation proposed by Jolivet et al. [33, 131, 132] (see Chapter 4.1.2), Klas et al. [201] recently suggested that lowering the synthesis temperature increases the importance of the Fe^{2+}-Fe^{3+} interaction (process (i)) over the dissolution-reprecipitation mechanism (process (ii)). As Fe^{2+} is the only divalent metal that gives rise to electron transfer with Fe^{3+} at ambient temperatures, the presence of high Me in the initial solution (a high Me/Fe_{T_IN}) reduces the Fe^{2+}-Fe^{3+} electron transfer in the precursor. Consequently, dehydration reaction is impeded, which results in an interference with the overall ferrite cystallisation process. This postulation was supported by FTIR analysis of ferrite samples produced under different temperatures. As shown in Figure 6.21a, b, and c, the molecular water band intensities for Co ferrites produced at 30 °C were significantly higher than those for the sample prepared at 90 °C. This result clearly indicates that a larger amount of molecular water was retained in the structure of the former ferrite. The same trend was also observed for Zn ferrite (Figure 6.21d and e). It should be noted that the high water band intensities in the FTIR spectrum of Co ferrite produced by the StFP (Figure 6.21c) is also correlated with a very low initial Fe^{2+}/Fe^{3+} ratio (i.e. 0.25) employed during its synthesis [198].

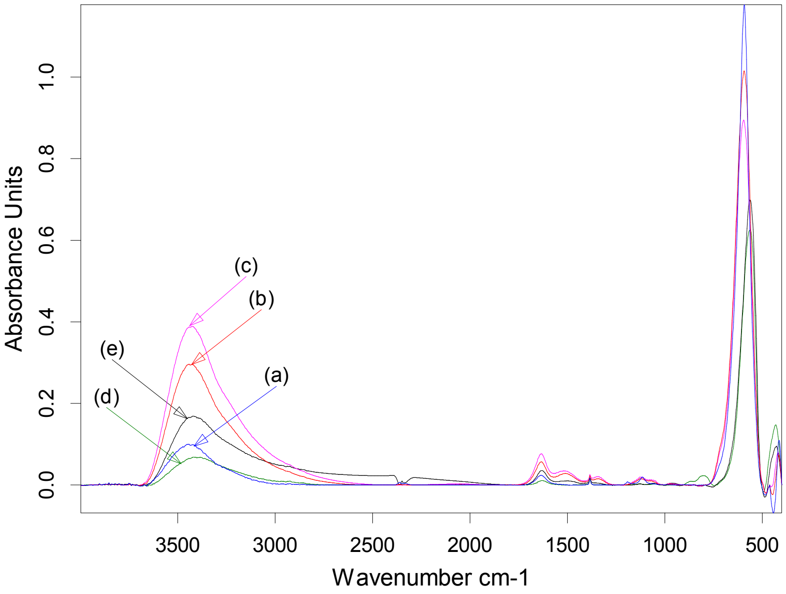

Figure 6.21: FTIR spectra of Co ferrites produced at (a) 90 °C *($x = 0.74$) and 30* °C *by (b) OxFP ($x = 0.66$) and (c) StFP ($x = 0.67$); Zn ferrites at (d) 90* °C *($x = 0.75$) and (e) 30* °C *by StFP ($x = 0.73$). Sample (b) and (c) were prepared by Klas [198].*

As the interaction between Fe^{2+} and Fe^{3+} becomes less intense, it can be expected that the incorporation of iron is preferred [201], leading to the reduced non-iron metal incorporation extent, in comparison to the extent attained at elevated temperature. According to this postulation, an excess of Fe(II) in the initial solution (high initial Fe^{2+}/Fe^{3+} ratio) can improve ferrite crystallisation under ambient temperature conditions to some extent, as previously demonstrated.

6.4.2 Morphology

Morphological analysis by SEM presented in Section 6.2.5 and in Chapter 5.3 suggests that the ferrites produced at ambient temperatures were less well crystalline than those synthesised at elevated temperatures. Small spherical particles were dominant in the former, while large octahedral crystals were often observed in the latter. Thus, it seems that ferrite was precipitated under a higher supersaturation degree at ambient temperatures. As described in Chapter 4.2.3, nucleation rate is high under a high supersaturation condition, producing large number of smaller particles, while under a lower supersaturation the opposite occurs.

As the overall ferrite growth is temperature dependent [37], it is affected more adversely by the temperature decrease in comparison with the dissolution process of the precursor. This resulted in a higher supersaturation level with respect to ferrite at ambient temperature, as the growth units, supplied by the dissolution of the precursor, were accumulated in the system. The slower growth rate may also be associated with the dehydration difficulty according to the above suggested mechanism.

6.4.3 Chemical stability

The chemical stability of the ferrite produced by the ATFP is compared to the stability of the ferrite produced at 90 °C in terms of the initial linear Fe dissolution rate obtained from the dissolution studies in 12.8% HCl solution at 23 ± 2 °C. As illustrated in Figure 6.22, the Fe dissolution rates of the ferrites produced at 30 °C were higher than those of ferrites formed at 90 °C, suggesting a reduced stability degree with decreasing synthesis temperature. This result is associated with the less crystalline nature and smaller particle size of the former ferrites, as described previously. It can also be deduced from Figure 6.22 that the chemical stability order of ferrites produced at 30 °C is similar to that found for the elevated-temperature ferrites.

The Fe dissolution rates of the ferrite produced at 30 °C appeared to vary over a wider range. While the Fe dissolution rate of Zn ferrite produced at 90 °C decreased with increasing Zn^{2+} content, the opposite trend seemed to characterise the Zn ferrite synthesised at 30 °C. A similar observation was also reported by Klas et al. [201] for Co ferrite. As the incorporation of Zn^{2+} and Co^{2+} at 90 °C was found to decrease the Fe dissolution rate of the respective ferrites, the reduced stability of Zn and Co ferrite produced at 30 °C with increasing Me content could not be directly associated with Me incorporation. According to the previous proposed mechanism, it seemed that the high molecular water content in the ferrite structure brought about the faster dissolution of Zn and Co ferrite.

The similar trend in the effect of Ni^{2+} incorporation on the dissolution rate for the ambient- and elevated-temperature Ni ferrites may, however, suggest that the molecular water content did not affect appreciably the dissolution rates of the former. Thus, the content of Ni^{2+} in the structure is the main factor that affects the dissolution stability of Ni ferrite. Similarly, the reduced stability observed in the Cd ferrites produced at 30 °C

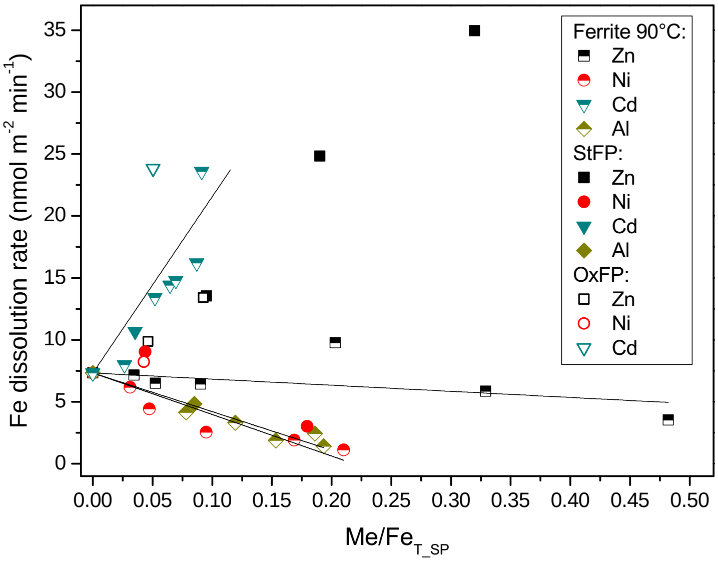

Figure 6.22: Initial Fe dissolution of ferrites produced at 30°C *and 90*°C *as a function of Me/Fe*$_{T\_SP}$ *ratio. The lines represent the stability trend observed in the ferrites produced at 90*°C.

and 90 °C upon increased Cd^{2+} content could also be associated with Cd^{2+} incorporation.

The results also suggest that the dissolution behaviour of ferrite must be viewed with caution because several factors such as the extent of Me incorporation, sample surface area, crystallinity are interrelated. The effect of the molecular water content in the ferrite structure cannot also be ruled out in accelerating the dissolution process particularly for the ferrites produced at low temperatures.

6.5 Simultaneous incorporation of metal ions

The results discussed in the previous sections refer to the experiments in which the Me ions was incorporated alone (i.e. in the presence of iron ions only). This section presents the simultaneous incorporations of several Me ions by the ATFP under various experimental conditions. The batch experiments were carried out in the presence of different number of Me combination.

The first experimental series focused on the di-metal incorporation of Zn^{2+} and Ni^{2+} into the ferrite produced under different initial Me/Fe_T ratios, pH values, temperatures (T), and reaction times (t). The second series dealed with the tri-metal incorporation of Zn^{2+}, Ni^{2+}, and Co^{2+} into the ferrite synthesised at two different initial Me/Fe_T ratios and temperatures. Additionally, one experiment of penta-metal incorporation of Zn^{2+}, Ni^{2+}, Co^{2+}, Cd^{2+}, Al^{3+} was also carried out. Due to the extensive experimental method, relatively low number of combination of synthesis conditions was tested, as presented in Table 6.2.

Table 6.2: Operational conditions applied in multi-metal incorporation experiments.

Exp.	Method	Me/Fe_{T_IN}[a]	Me_T/Fe_{T_IN}[b]	T (°C)	pH	t (min)
Di-metal system: Zn^{2+}, Ni^{2+}						
1	StFP	0.1	0.2	30	10.5	150
2	StFP	0.1	0.2	30	10.5	60
3	StFP	0.1	0.2	25	10.5	150
4	StFP	0.1	0.2	30	9.5	150
5	StFP	0.2	0.4	30	10.5	150
6	StFP	0.2	0.4	30	9	150
Tri-metal system: Zn^{2+}, Ni^{2+}, Co^{2+}						
7	StFP	0.083	0.25	30	10.5	150
8	StFP	0.083	0.25	20	10.5	150
9	StFP	0.1	0.3	30	10.5	150
10	OxFP	0.083	0.25	30	10.5	150
Penta-metal system: Zn^{2+}, Ni^{2+}, Co^{2+}, Cd^{2+}, Al^{3+}						
11	StFP	0.071	0.36	30	10.5	150

[a] Non-iron metal to total iron ratio in the initial solution

[b] Total non-iron metals to total iron ratio in the initial solution

6.5.1 Chemical composition

Figure 6.23 shows the Me/Fe_T ratio in the solid particles (Me/Fe_{T_SP}) as a function of cycle number for some simultaneous Me incorporation experiments. The corresponding ratios at steady state and the Me incorporation efficiency achieved in all multi-metal incorporation experiments are summarised in Table 6.3. The removal efficiency of each Me from the solution was over 99.9% in all experiments suggesting that different non-iron metals can be completely and simultaneously precipitated. This finding is of importance to the application of the ATFP, which is discussed further in the next chapter.

To examine the effect of the presence of co-metals on the Me incorporation, the Me/Fe_{T_SP} ratios obtained under similar experimental conditions (T = 30 °C, pH = 10.5, t = 150 min using the StFP) in the multi-metal and in the single-metal system are plotted as a function of Me/Fe_{T_IN} in Figure 6.24. Only Zn^{2+} was almost completely incorporated into the ferrite structure without and with the presence of co-metals. Thus, it can be deduced that the incorporation of Zn^{2+} was not affected by the presence of other non-iron metals. On the other hand, Co^{2+} appeared to be incorporated to a lower extent than Zn^{2+} in the tri-metal system. A slight decrease in the incorporation efficiency of Co^{2+} was observed in the penta-metal system in comparison to that attained in the tri-metal

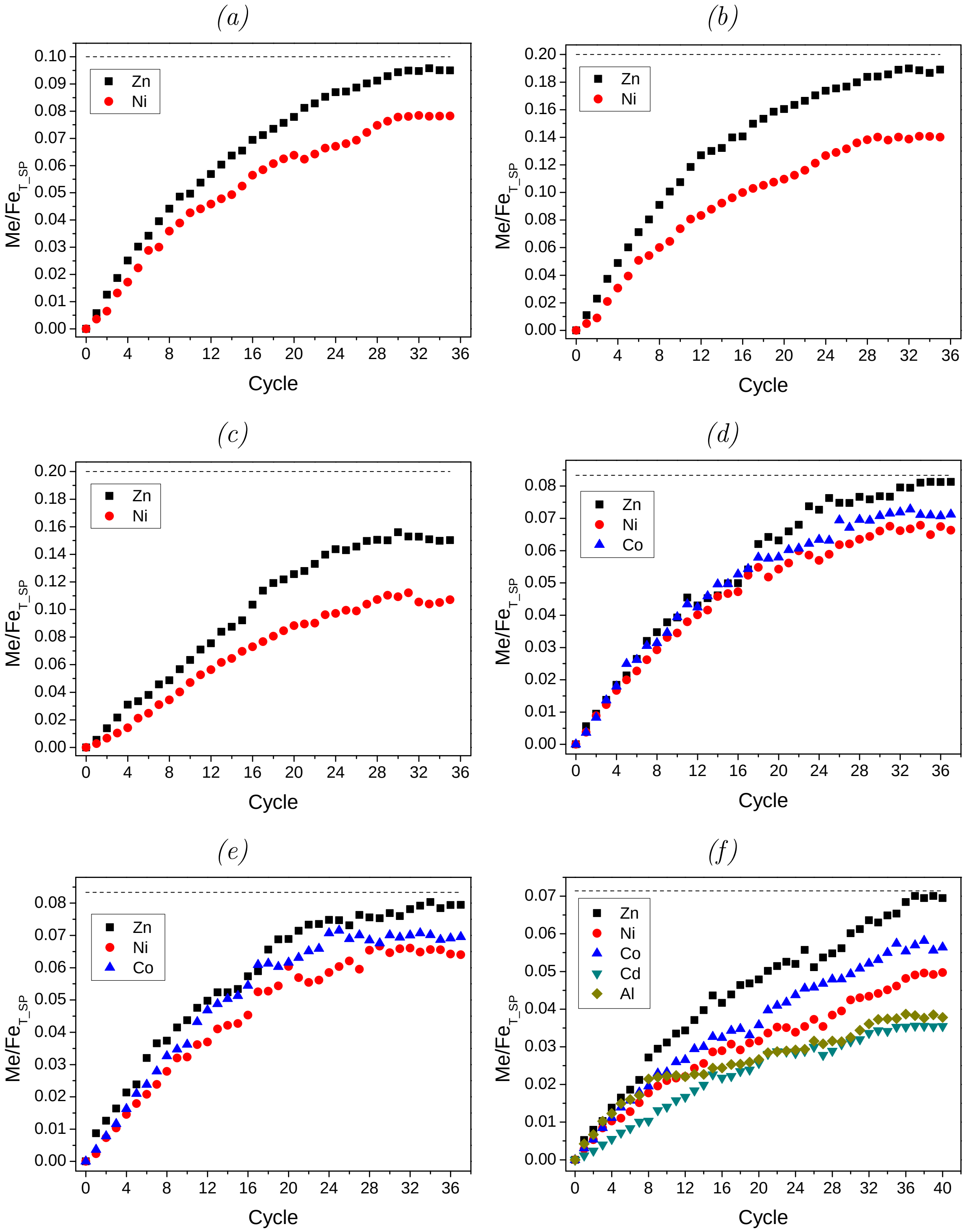
(a) *(b)* *(c)* *(d)* *(e)* *(f)*

Figure 6.23: Me/Fe$_T$ ratios in the ferrite produced from a solution containing several Me ions under different experimental conditions listed in Table 6.2: (a) Exp. 1, (b) Exp. 5, (c) Exp. 6, (d) Exp. 7, (e) Exp. 10, and (f) Exp. 11. The dashed lines represent the theoretical maximal Me/Fe$_{T\_SP}$ ratio.

system (Table 6.3). However, the effect of co-metals on the incorporation of Co^{2+} can be considered insubstantial.

Table 6.3: Me/Fe_{T_SP} ratios at steady state and Me incorporation efficiency obtained in the simultaneous Me incorporation experiments.

Exp. No.	Me/Fe_{T_SP}					Incorporation (%)				
	Zn^{2+}	Ni^{2+}	Co^{2+}	Cd^{2+}	Al^{3+}	Zn^{2+}	Ni^{2+}	Co^{2+}	Cd^{2+}	Al^{3+}
Di-metal: Zn^{2+}, Ni^{2+}										
1	0.095	0.078	-	-	-	95	78	-	-	-
2	0.093	0.071	-	-	-	93	71	-	-	-
3	0.090	0.074	-	-	-	90	74	-	-	-
4	0.092	0.076	-	-	-	92	76	-	-	-
5	0.189	0.140	-	-	-	94	70	-	-	-
6	0.151	0.107	-	-	-	76	53	-	-	-
Tri-metal: Zn^{2+}, Ni^{2+}, Co^{2+}										
7	0.081	0.067	0.071	-	-	97	80	86	-	-
8	0.078	0.060	0.068	-	-	93	72	81	-	-
9	0.095	0.073	0.083	-	-	95	73	83	-	-
10	0.079	0.065	0.070	-	-	95	78	84	-	-
Penta-metal: Zn^{2+}, Ni^{2+}, Co^{2+}, Cd^{2+}, Al^{3+}										
11	0.069	0.049	0.057	0.035	0.038	97	69	80	50	53

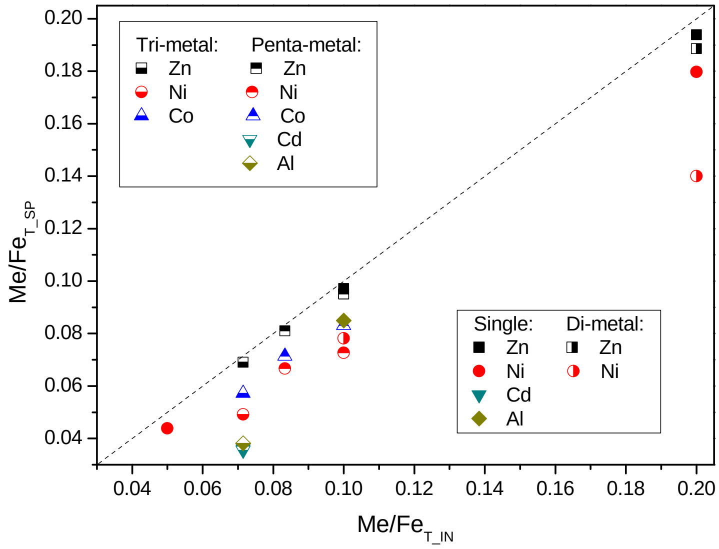

Figure 6.24: Me/Fe_T ratios in the ferrite produced at $T = 30°C$, $pH = 10.5$, $t = 150$ min using StFP in the multi-metal and single-metal system a function of Me/Fe_{T_IN}. The dashed line represents the theoretical correlation assuming 100% incorporation.

A more substantial effect of co-metals was noticed in the incorporation of Ni^{2+}. As shown in Figure 6.24, the Ni^{2+}/Fe_{T_SP} ratio obtained at Ni^{2+}/Fe_{T_IN} ratio of 0.2 in the di-metal system was 0.14 (Exp. 5 in Table 6.3), while it was about 0.18 in the single-metal system. This result reflected the negative influence of the presence of Zn^{2+} on Ni^{2+} incorporation. The effect of co-metal seemed to reduce at a lower Ni^{2+}/Fe_{T_IN} ratio. This was supported by the fact that the incorporation efficiency of Ni^{2+} increased from 70% to 78% as the Ni^{2+}/Fe_{T_IN} ratio decreased from 0.2 to 0.1 (Exp. 5 and 1 in Table 6.3). At the latter initial Ni^{2+}/Fe_T ratio, the incorporation efficiency of Ni^{2+} was slightly lower in the tri-metal system compared to that in the di-metal system (Exp. 1 and 9 in Table 6.3). The effect of co-metals was more influential in the penta-metal system as a further decrease in the Ni^{2+} incorporation efficiency was observed even at a lower Ni^{2+}/Fe_{T_IN} ratio (Exp. 11 in Table 6.3).

A significant negative effect of the presence of co-metals was clearly demonstrated in the incorporation of Al^{3+}. Comparison between the Al^{3+}/Fe_T ratio in the solid particles and in the initial solution indicated that about 85% Al incorporation effiency was attained in the single-metal system, while it was only about 53% in the penta-metal system (Figure 6.24). Conversely, no significant effect of co-metals could be observed in the incorporation of Cd^{2+} as a similar Cd^{2+}/Fe_{T_SP} ratio was attained in both the single- and penta-metal system (i.e. about 0.035).

Due to the substantial negative influence of the presence of co-metals, Al^{3+} was incorporated to an almost equal extent as Cd^{2+}. Thus, the preferential order of Me incorporation in the multi-metal system was $Zn^{2+} > Co^{2+} > Ni^{2+} > Al^{3+} \approx Cd^{2+}$. This order is generally similar to that observed in the single-metal system. Nonetheless, the results from single-metal subsituted ferrites are not necessarily applicable to the multi-metal system.

The influence of the different experimental conditions on the incorporation of Me in the multi-metal system could be appreciated from Table 6.3. A slightly lower Me/Fe_{T_SP} ratio obtained at a reaction time of 60 min (Exp. 2) compared to that attained at 150 min (Exp. 1) suggests that a longer reaction time is favourable for the Me incorporation, allowing a more complete transformation of the metal intermediates into the crystalline solids. The ratio of Me/Fe_T in the ferrite produced at pH 9.5 was found to be relatively similar to that in the ferrite synthesised at pH 10.5 (Exp. 1 and 4). A distinct negative effect of pH reduction on the incorporation of Me was, however, observed when the ferrite was synthesised at a higher Me/Fe_{T_IN} ratio (i.e. 0.2), as shown in Exp. 5 and 6. At this ratio, the incorporation efficiency of Zn^{2+} decreased from 94% to 76% with pH changing from 10.5 to 9.0, respectively. A similar effect was also observed for Ni^{2+} (see Table 6.3). This result clearly demonstrates that a high pH condition (more alkaline condition) is more favourable for the Me incorporation into the ferrite, particularly at a high Me/Fe_{T_IN} ratio (high Me content in the initial solution). A slight increase in the synthesis temperature was also found to have a positive effect on the extent of Me incorporation, as demonstrated in the di-metal (Exp. 1 vs. 3) and tri-metal (Exp. 7 vs. 8) system. It is noted that in the latter system the initial Fe^{2+}/Fe^{3+} ratio in the last ten cycles was increased from 0.5 to

0.57 because a rapid decrease in the seed concentration was measured in the reactor and the colour of the precipitates started changing from black to dark brown. This measure effectively solved the problem, supporting the previous finding regarding the important role of excess Fe(II) in compensating the adverse effect of a low synthesis temperature on the crystallisation of ferrite. With regard to the OxFP, it was found that the Me incorporation extent was slightly lower than that obtained by the StFP, in agreement with the result of the single-metal incorporation experiment. Nevertheless, the preferential order of Me incorporation into the ferrite produced by these two methods was similar.

Figure 6.25 presents the plot of the M^{2+}/M_{T_SP} ratio as a function of total non-iron metals (Me_T) to total Fe (Fe_T) ratio in the solid particles (Me_T/Fe_{T_SP}) obtained in the multi-metal experiments. The M^{2+}/M_{T_SP} ratio obtained in the di-metal system at a Me/Fe_{T_IN} ratio of 0.1 and different reaction times, temperatures, and pH values (Exp. 1 to 4) was found to be relatively similar, suggesting that the ferrites produced under the investigated conditions had a comparable oxidation degree.

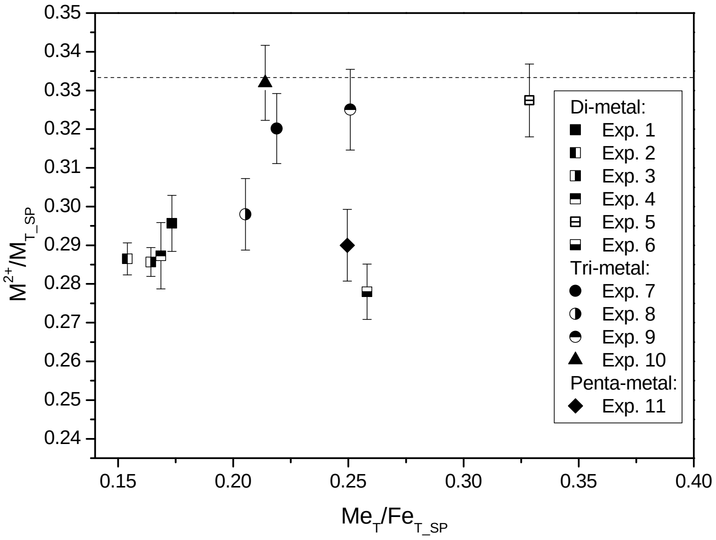

Figure 6.25: Divalent metal to total metal ratios in the multi-metal-subtituted ferrites (M^{2+}/M_{T_SP}). The dashed line represents the M^{2+}/M_{T_SP} ratio of an ideal ferrite.

An increased M^{2+}/M_{T_SP} ratio with increasing Me content was observed for ferrites produced at pH 10.5 (di- and tri-metal system). The ferrite produced at pH 9 (Exp. 6) had a relatively lower M^{2+}/M_{T_SP} ratio (higher oxidation degree) than the other ferrites, despite its high Me content. This outcome suggests that a decrease in the synthesis pH leads to the production of a more oxidised ferrite, similar to the finding of Kanzaki et al. [147]. It was also noticed that the ferrites produced by the StFP (Exp. 7) had a higher oxidation degree than those synthesised by the OxFP (Exp. 10), in accordance with the findings of the single-metal incorporation experiments. The M^{2+}/M_T ratio in the ferrite produced in the penta-metal system was lower than that of the other ferrites (Exp. 11).

This result could be related to the presence of Cd^{2+} and Al^{3+} in the structure. As shown in the single-metal system, the incorporation of these ions resulted in the formation of ferrite with a relatively high oxidation degree.

6.5.2 Crystalline phases and unit cell sizes

The XRD patterns of all solids produced in the multi-metal incorporation experiments consisted only of peaks typical of spinel-type compounds. The peaks of the ferrite synthesised in the di-metal system at pH 9 (Exp. 6) were found to be lower and broader than those of the other preparations, indicating a lower crystallinity. It is also noted that the XRD patterns of the ferrite produced in the tri-metal system at 20 °C (Exp. 7) were not much different from the patterns of other tri-metal ferrite samples; only slightly lower peaks intensities were observed. A higher initial Fe^{2+}/Fe^{3+} ratio applied in this experiment, as mentioned before, played a significant role to improve the crystallinity degree of the solid.

The unit cell size of ferrite produced in the multi-metal system depends on the identity and the extents of incorporation of individual metals. In the investigated di-metal system, the effect of the incorporation of Zn^{2+} and Ni^{2+} on the unit cell size of the ferrite, called hereafter Zn-Ni ferrite, should be considered. As described earlier, the incorporation of Zn^{2+} caused a linear increase in the unit cell size of Zn ferrite. Contrary, the incorporation of Ni^{2+} tended to decrease the size of the unit cell. In the tri-metal system, the incorporation of Co^{2+} into the ferrite (i.e. Zn-Ni-Co ferrite) could also affect the unit cell size to a certain extent, as discussed in Chapter 5.2.2.

Figure 6.26 presents the calculated unit cell size of the multi-metal-substituted ferrite as a function of the extent of total Me incorporation (Me_T/Fe_{T_SP}). As may be seen, the unit cell size (a) was linearly increased with the extent of total Me incorporation in the Zn-Ni ferrite($R^2 = 0.95$) and the Zn-Ni-Co ferrite ($R^2 = 0.99$), which could be attributed to the presence of Zn^{2+} in the crystal structure. The flatter slope for the linear regression of a vs. total Me content of the Zn-Ni ferrite compared to that of the Zn ferrite may reflect the opposite effect of Ni^{2+} incorporation on the unit cell size of ferrite. It is also noted that the linear regression slope obtained for Zn-Ni-Co ferrite was slightly larger than that for Zn-Ni ferrite (0.075 vs. 0.056 for the former and the latter, respectively), indicating the influence of Co^{2+} incorporation on the size of the unit cell.

In the penta-metal system, the effect of the incorporation of five different Me ions on the unit cell size of ferrite (named hereafter Zn-Ni-Co-Cd-Al ferrite) is probably much more complex than in the other multi-metal systems described before. The larger size of the unit cell can be related not only to the presence of Zn^{2+} but also Cd^{2+}. The opposite effect of Ni^{2+} and also Al^{3+} on the unit cell size, as previously shown, could not be ruled out.

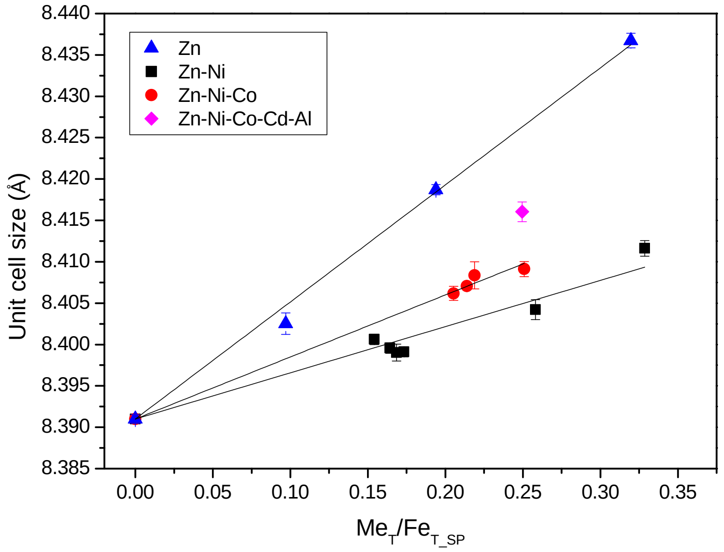

Figure 6.26: Unit cell sizes of Zn ferrites and multi-metal-substituted ferrites as a function of total Me content in the product.

6.5.3 Metal spatial distribution

The dissolution congruency test conducted on the Zn-Ni and Zn-Ni-Co ferrite showed that the fraction of Fe released was proportional to the fraction of Me released suggesting a uniform distribution of all metal ions in the ferrite particles. The exception was Zn-Ni ferrite produced at pH 9 (Exp. 6). It was observed that the fraction of released Ni^{2+} was relatively higher than Fe, while Zn^{2+} showed the opposite trend (Figure 6.27a).

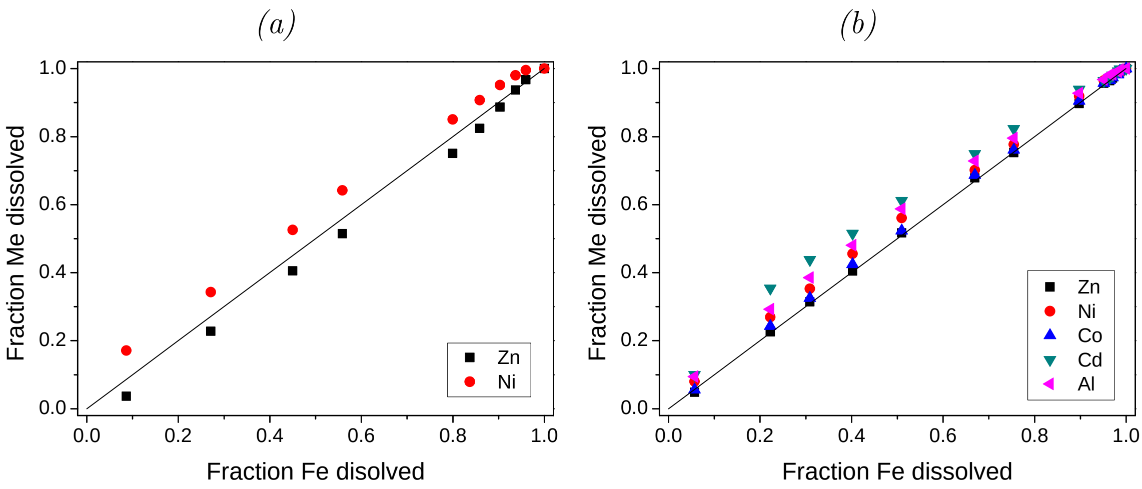

Figure 6.27: Plots of fraction of Me versus Fe dissolved in 12.8% HCl solution for (a) Zn-Ni ferrite (Exp. 6) and (b) Zn-Ni-Co-Cd-Al ferrite (Exp. 11).

The above result indicates that the distribution of Zn^{2+} and Ni^{2+} in the ferrite was not entirely homogeneous. The former was found close to the particle core, while the latter was near to the particle surface.

The dissolution study of the Zn-Ni-Co-Cd-Al ferrite indicated that all metal ions, except Al^{3+} and Cd^{2+}, were homogeneously distributed within the ferrite (Figure 6.27b). As Al^{3+} and Cd^{2+} were enriched in the near-surface region, these ions can be easily leached to the solution, as shown later.

6.5.4 Infrared spectra of the precipitates

Some representative FTIR spectra of the ferrites produced in the multi-metal system are shown in Figure 6.28. The spectra contained two main bands (ν_1 and ν_2) typical of spinel structure at about 580 and 400–460 cm^{-1} and two bands assigned to the molecular water at around 1600 and 3400 cm^{-1}. These features were similar to those observed in the FTIR spectra of single-metal substituted ferrites.

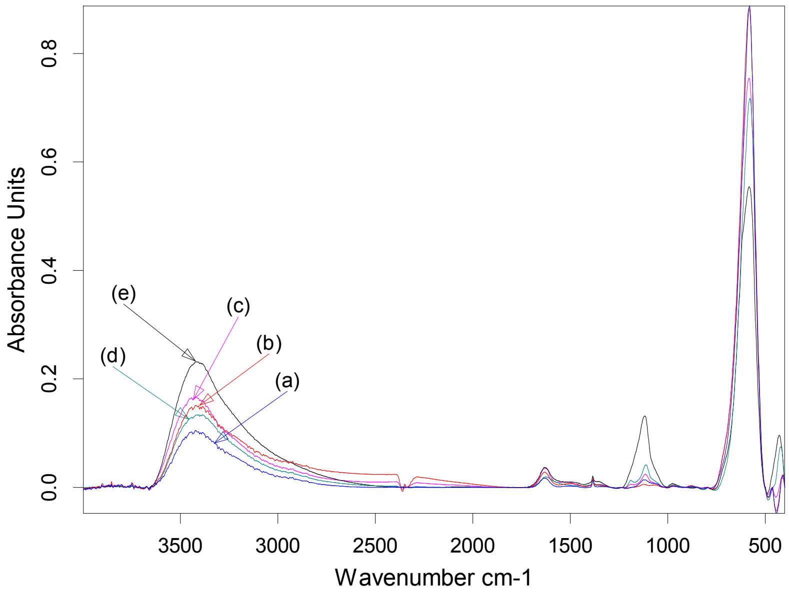

Figure 6.28: FTIR spectra of multi-metal-substituted ferrites:(a) Zn-Ni-Co ferrite (Exp. 10), (b) Zn-Ni-Co ferrite (Exp. 7), (c) Zn-Ni-Co-Cd-Al ferrite (Exp. 11), (d) Zn-Ni ferrite (Exp. 5), (e) Zn-Ni ferrite (Exp. 6).

The water band intensities for the ferrites produced by the StFP at pH 10.5 increased slightly as the number of Me in the system increased (Figure 6.28a, b, c). The effect of synthesis pH on the dehydration process of ferrite was more noticeable. As depicted in Figure 6.28d, the highest water and sulphate band (at about 1100 cm^{-1}) intensities were detected in the Zn-Ni ferrite produced at pH 9 (Exp. 6). A low synthesis pH inhibited the removal of water molecules and sulphate anions during ferrite precipitation process and consequently ferrite with lower crystallinity was produced. The water band intensities for the ferrite produced by the OxFP (Figure 6.28e) were also noticed to be the lowest, in agreement with the previous observation in the single-metal system.

6.5.5 Morphological characterisation

Similar to the ferrite particles produced in the single-metal system, the particles produced in the multi-metal system composed of almost spherical particles forming aggregates. The particle size appeared to vary in the similar range, i.e. 30–100 nm, except for the particles of Zn-Ni ferrite produced at pH 9 (Exp. 6), which was approximately 20–25 nm (see Figure 6.29a). It is noted that the decrease in the synthesis pH did not affect the particle size of Zn-Ni ferrite precipitated at a lower $\mathrm{Me_T/Fe_{T\_IN}}$ ratio (Exp. 4), as shown in Figure 6.29b. SEM observation also showed that although the particle size of the ferrite produced by the OxFP (Exp. 10) and the StFP (Exp. 7) varied in a similar range, the particles obtained by the StFP consisted of larger number of particles with a smaller size (Figure 6.29c and 6.29d).

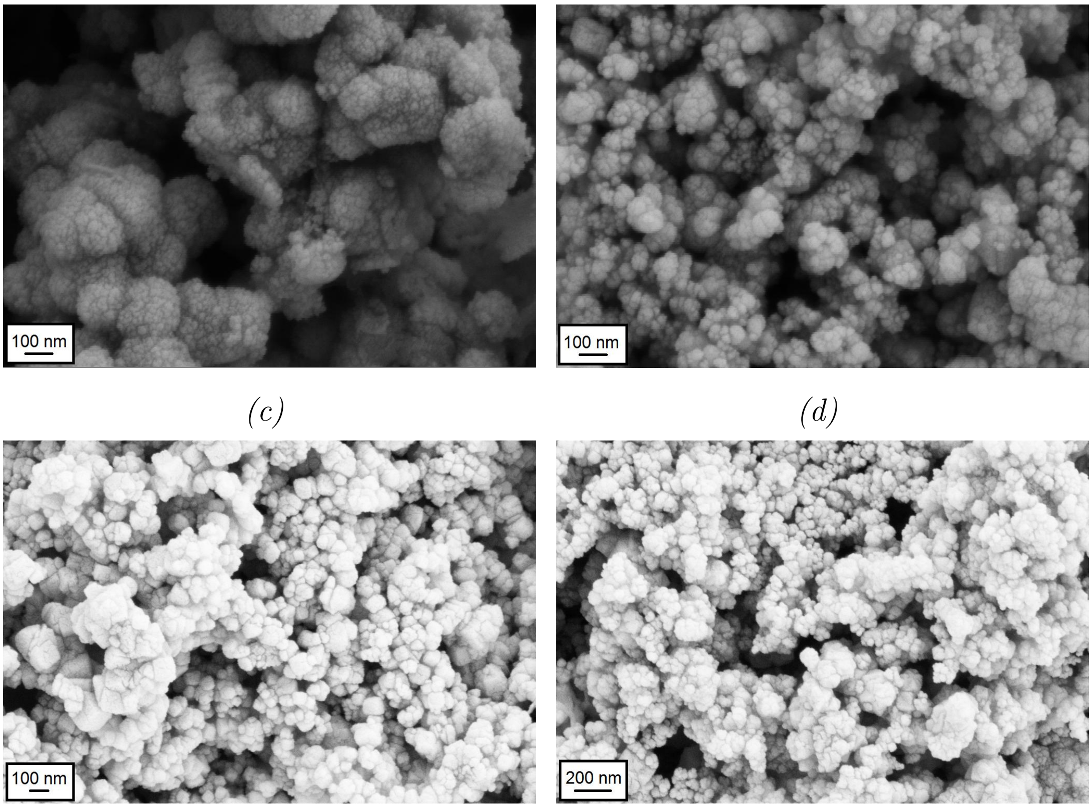
(a) *(b)* *(c)* *(d)*

Figure 6.29: SEM images of Zn-Ni ferrites obtained at Me_T/Fe_{T_IN} ratio of (a) 0.4 and pH 9 (Exp. 6), (b) 0.2 and pH 9.5 (Exp. 4) and Zn-Ni-Co ferrites produced by (c) OxFP (Exp. 10), (d) StFP (Exp. 7).

In general, the surface area of the ferrite increased with Me content, as shown in Figure 6.30. In accordance with SEM observation, the ferrite produced at pH 9 (Exp. 6) and that synthesised by the OxFP (Exp. 10) had a significantly higher and lower surface area, respectively than the other ferrite samples. A decrease in the synthesis temperature was observed to slightly increase the surface area, i.e. 27 and 31 m^2/g for the Zn-Ni-Co ferrite produced at 20 (Exp. 8) and 30 °C (Exp. 7), respectively. It was also noticed that the surface area of the Zn-Ni-Co-Cd-Al ferrite (Exp. 11) appeared to be slightly larger than that of the Zn-Ni-Co ferrite (Exp. 9), i.e. 29 and 33 m^2/g for the former and the latter, respectively. Nevertheless, decreasing synthesis temperature (slight decrease), as well as increasing Me number, did not seem to have a significant effect on the ferrite surface area.

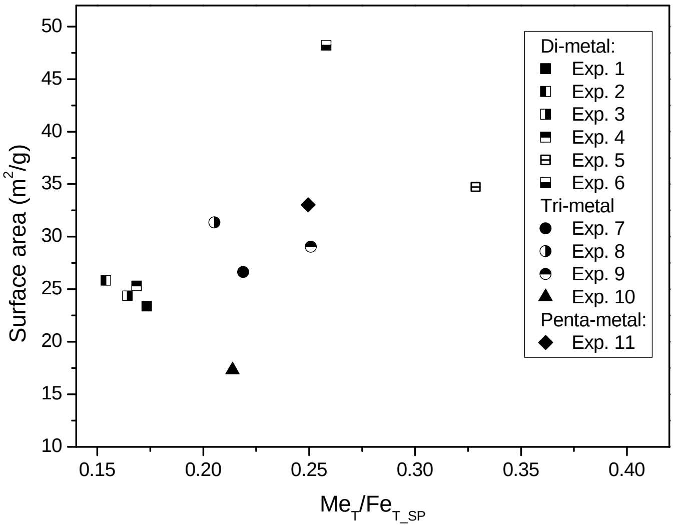

Figure 6.30: Specific surface area of the solid particles obtained in the simultaneous Me incorporation as a function of Me_T/Fe_{T_SP}.

Figure 6.31 shows the crystallite size of the ferrite produced in the multi-metal system as a function of the total Me content. In general, the crystallite size of the ferrite produced by the StFP under similar experimental conditions appeared to decrease (less crystalline) with increasing Me content. A considerably small crystallite size (low crystallinity) was observed in Zn-Ni ferrite synthesised at pH 9 (Exp. 6).

It was also noticed that the Zn-Ni-Co ferrite precipitated by the OxFP (Exp. 10) had a larger crystallite size than the StFP samples, in accordance with the results obtained in the single-metal system. It should be noted that the relatively small crystallite size of Zn-Ni-Co-Cd-Al ferrite (Exp. 11) may indicate structural strain, probably induced by the incorporation of Cd^{2+}. This issue needs to be further investigated as the development of structural strain might inhibit the incorporation of other Me in the system. Based on the crystallite size presented in Figure 6.31 and the particle size discussed before, it can be deduced that the multi-metal-substituted ferrites were polycrystalline, except for Zn-Ni ferrite synthesised at pH 9, which composed of mostly monocrystallite.

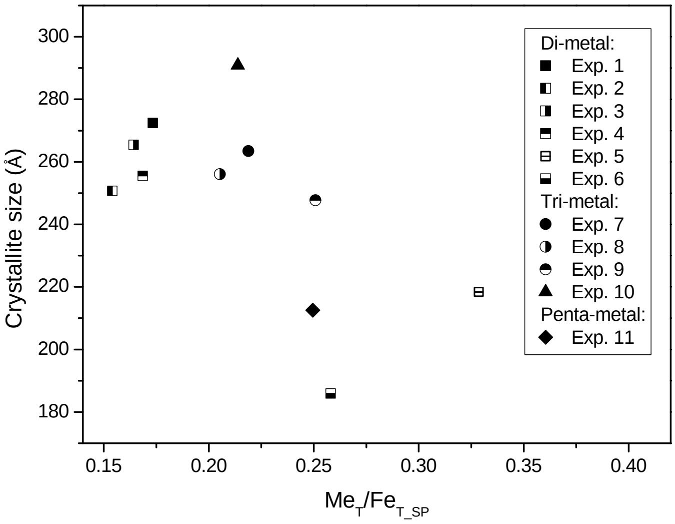

Figure 6.31: Crystallite size of ferrite obtained in the simultaneous Me incorporation as a function of Me_T/Fe_{T_SP}.

6.5.6 Chemical stability

The initial linear Fe dissolution rate of multi-metal-substituted ferrite particles in 12.8% HCl solution normalised for the surface area is given in Figure 6.32a. The dissolution rate of ferrite produced in the di-metal system appeared to reduce with the increased Me content in the ferrite. This result is particularly attributed to the increased Ni^{2+} content in the crystal structure as this ion tended to stabilise the corresponding ferrite (Section 6.4.3). The low dissolution rate of ferrite produced at pH 9 (Exp. 6) could also be ascribed to its high surface area (Figure 6.30). The normalised dissolution rate accounting for solid concentration of this ferrite sample, presented in Figure 6.32b, was in fact higher than that of the other ferrite samples produced in the di-metal system. Furthermore, the high Fe dissolution rate observed in the ferrite produced at reaction time of 60 min (Exp. 2) may suggest that a short reaction time is less favourable for the formation of stable ferrite. It is also apparent in Zn-Ni ferrites produced at 25 °C (Exp. 3) and 30 °C (Exp. 1) and Zn-Ni-Co ferrites at 20 °C (Exp. 8) and 30 °C (Exp. 7) that a slight increase in the synthesis temperature could stabilise the solid products.

The dissolution rates of ferrites produced by the StFP in the tri-metal system was generally higher than those of the di-metal-substituted ferrites. In the tri-metal system, the dissolution rate of the OxFP sample was lower than that of the StFP sample due to the larger particle size of the former. The significantly higher dissolution rate of ferrite produced in the penta-metal system in comparison to the other ferrites was particularly related to the incorporation of Cd^{2+}. As previously found, this metal strongly labilised the corresponding ferrite.

The leaching of Me in the TCLP and the BCR tests is depicted in Figure 6.33 and

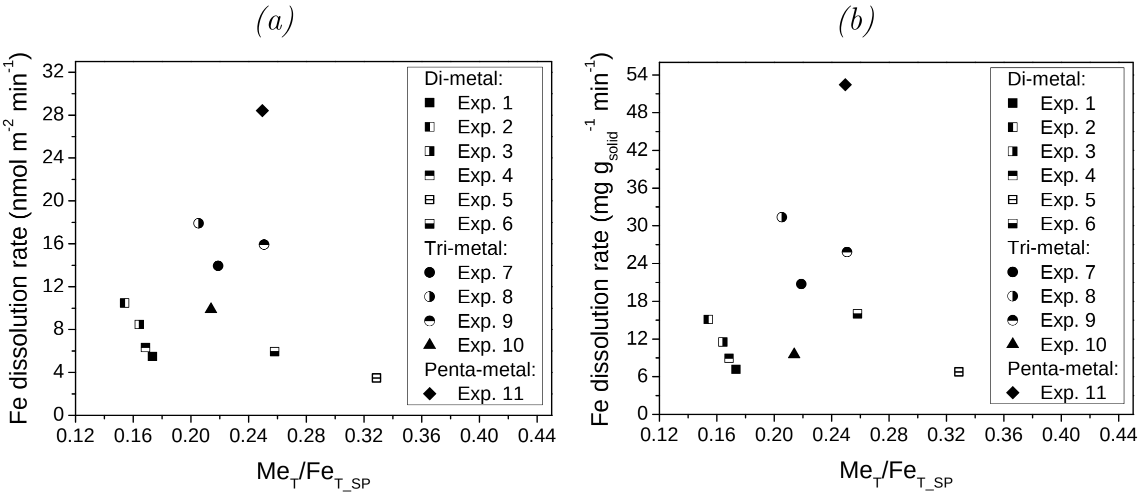

Figure 6.32: Initial Fe dissolution rates (12.8% HCl solution, $23 \pm 2\,^{\circ}\mathrm{C}$) of multi-metal-substituted ferrites normalised by (a) surface area and (b) solid concentration.

6.34. It was found that the Ni leaching extent for the Zn-Ni ferrite produced at pH 9 (Exp. 6) was significantly higher than that for the other ferrites. This outcome was the result of the enrichment of Ni in the near-surface region, as discussed earlier. A similar reasoning, as well as a low dissolution stability, can also be used to explain the high leaching extent of Cd from the Zn-Ni-Co-Cd-Al ferrite.

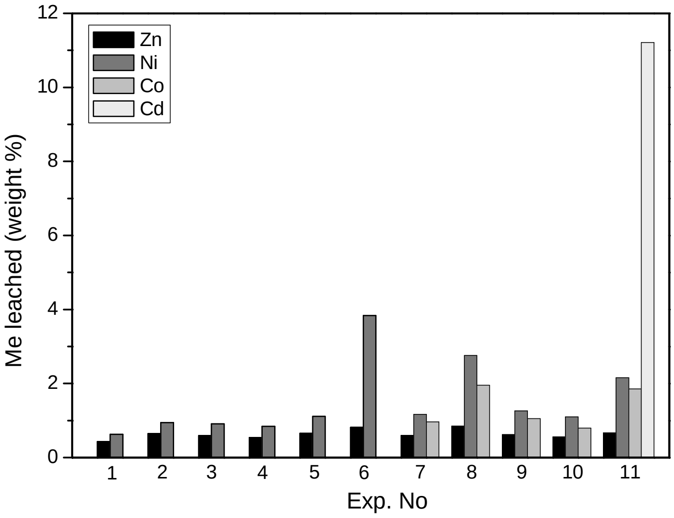

Figure 6.33: Weight percentages non-iron metal leached from the multi-metal-substituted ferrites in the TCLP test.

Aluminium was also leached to a significantly high extent in the BCR test, although its leaching was nearly zero in the TCLP test. It is also noted that the higher Me leaching extent observed for the Zn-Ni-Co ferrite synthesised at 20 °C (Exp. 8) could be correlated with its lower dissolution stability, while the opposite was true for the ferrite synthesised by the OxFP (Exp. 10).

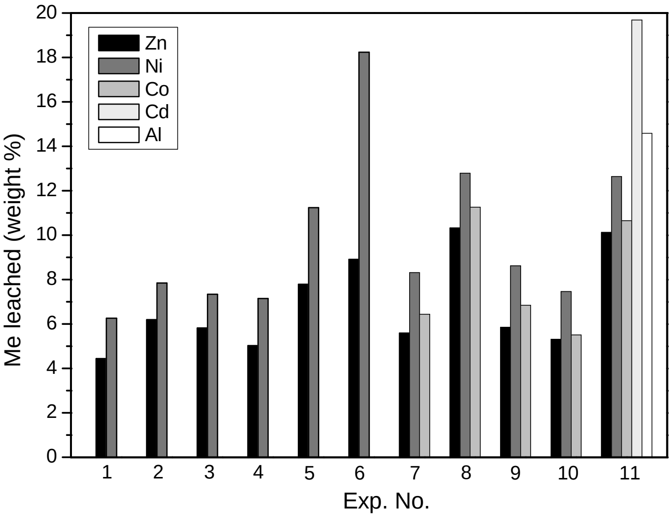

Figure 6.34: Weight percentages non-iron metal leached from the multi-metal-substituted ferrites in the BCR test.

6.6 Incorporation of metal ions in the presence of Cr^{3+} ions

In the industrial wastewater, such as galvanic wastewater, Cr^{3+} ions were commonly found together with other metal ions. As the first trial to simulate the treatment of galvanic wastewater by the ATFP, this section presents the removal and incorporation of Zn^{2+} and also Ni^{2+} together with Cu^{2+} in the presence of Cr^{3+} using the StFP in a continuous system at 30 °C and pH 10.5. In the first experiment, named Zn,Cr-experiment, the Zn^{2+}/Fe_{T_IN} and Cr^{3+}/Fe_{T_IN} ratio employed was 0.05, while in the second experiment (Ni,Cu,Cr-experiment) the Me/Fe_{T_IN} ratio for Ni^{2+}, Cu^{2+}, and Cr^{3+} was 0.025, 0.017, and 0.05, respectively.

The removal efficiency of all metals from solution was above 99.9% in both the Zn,Cr- and Ni,Cu,Cr-experiment. The Me/Fe_T ratio in the solid particles (Me/Fe_{T_SP}) as a function of time attained in the Zn,Cr-experiment is presented in Figure 6.35a. As can be seen, the Me/Fe_{T_SP} ratio approached a constant value of about 0.049 and 0.031 for Zn^{2+} and Cr^{3+}, respectively. In the Ni,Cu,Cr-experiment, the Me/Fe_{T_SP} ratio attained a value of approximately 0.018, 0.0, 0.023 for Ni^{2+}, Cu^{2+}, and Cr^{3+}, respectively, as shown in Figure 6.35b.

The Me^{2+}/Me_{T_SP} ratio in the Zn,Cr-experiment was low, i.e. 0.148, while it was only about 0.044 in the Ni,Cu,Cr-experiment. The explanations for this finding are the existence of a significant amount of goethite together with ferrite particles, as established by XRD analysis, and probably also the high oxidation level of the ferrite particles. SEM images of the solid particles obtained in these experiments are depicted in Figure 6.36. The

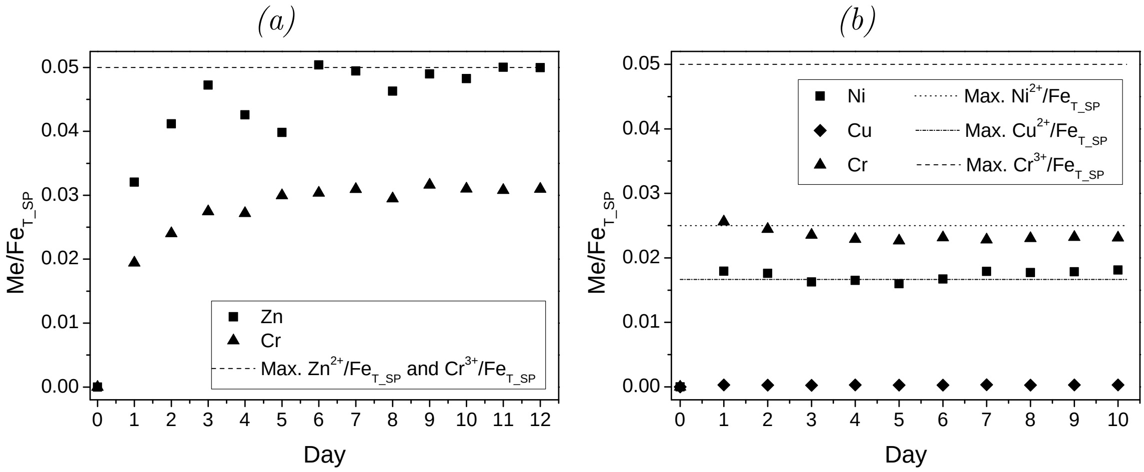

Figure 6.35: Me/Fe_T ratios in the solid particles obtained in the (a) Zn,Cr-experiment and (b) Ni,Cu,Cr-experiment. The lines represent the theoretical maximal Me/Fe_{T_SP} ratio.

goethite particles formed in the Ni,Cu,Cr-experiment appeared to be wider and thicker than those produced in the Zn,Cr-experiment, suggesting that the formation of goethite was probably more enhanced in the former experiment.

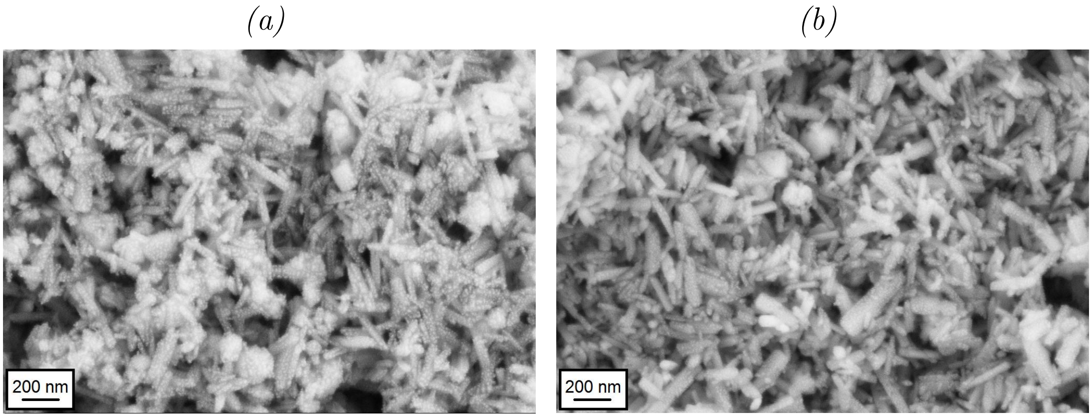

Figure 6.36: SEM images of the solid particles obtained in the (a) Zn,Cr-experiment and (b) Ni,Cu,Cr-experiment.

Dissolution studies of the solid particles obtained in the Zn,Cr- and Ni,Cu,Cr-experiment indicated that Cr^{3+} was dissolved completely in about 15 min after the dissolution commenced, while Fe was gradually dissolved in 6 h (Figure 6.37). Thus, it can be confirmed that Cr^{3+} was not structurally incorporated into the crystal structure, similar to the conclusion derived in Section 6.2 (where Cr^{3+} was singly incorporated). On the other hand, Zn^{2+} appeared to be homogeneously distributed in the solid particles obtained in the Zn,Cr-experiment (Figure 6.37a). The incorporation of Zn^{2+} into the crystal structure was thus likely. Nevertheless, it cannot be confirmed whether Zn^{2+} was incorporated into ferrite, goethite, or into both ferrite and goethite. More importantly, the incorporation of Zn^{2+} was not affected by the presence of Cr^{3+} as about 97% Zn incorporation efficiency was achieved.

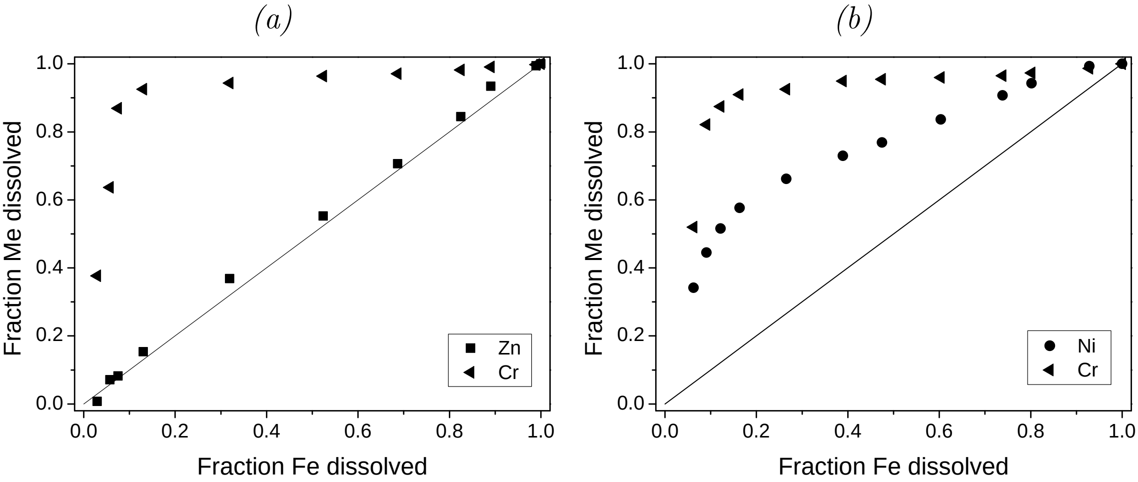

Figure 6.37: Plots of fraction of Me versus Fe dissolved in 12.8% HCl solution for the solid particles obtained in the (a) Zn,Cr-experiment and (b) Ni,Cu,Cr-experiment.

The distribution of Ni^{2+} in the solid particles produced in the Ni,Cu,Cr-experiment was found to be incongruent, as shown in Figure 6.37b. The dissolution data for Cu^{2+} is not displayed in this figure as the solid particles did not contain any Cu^{2+}. It was found that about 30% of the final Ni concentration was released immediately after the dissolution started. This result suggests that only about 70% of the total amount of Ni (after rinsing process) was present in a crystalline phase. Thus, the incorporation efficiency of Ni^{2+} was approximately 50%, indicating the inhibition effect of Cr^{3+} on the Ni^{2+} incorporation.

The initial linear Fe dissolution rate of the solid samples obtained in the Zn,Cr- and Ni,Cu,Cr-experiment was relatively similar to that found in the incorporation of Cr^{3+} alone (Section 6.2.6). Thus, the dissolution stability of the ferrite seemed to be governed mainly by the presence of Cr^{3+} ions. The effect of other Me ions is probably more noticeable when they exist in a significantly larger amount than Cr^{3+} ions.

All non-iron metals were leached to a relatively low extent in the TCLP test (1–2%), while in the BCR test the extent was enhanced, as expected. It is noted that the leaching extent of Ni was higher than that of other Me due to its concentration toward the particles surface (incongruent distribution).

6.7 Conclusions

The feasibility of the ambient temperature ferrite process (ATFP) for treating synthetic wastewater was demonstrated. The process permitted the elimination of all toxic metals from initial solutions to very low concentration resulting in above 99% purification efficiency.

Two methods of seeded ATFP, i.e. stoichiometric and oxidation ferrite process (StFP and OxFP, respectively) were successfully applied to produce crystalline ferrite directly from aqueous solutions, as long as the initial Me/Fe_T ratio was not excessively high. Higher metal incorporation extent was achieved by the StFP, while higher crystallinity (larger particle and crystallite size) and chemical stability was demonstrated by the OxFP. The main advantage of the former is its convenient operation (no aeration control required). Yet, its base consumption was higher than the latter. In general, the performance of ferrite synthesis by the StFP and the OxFP did not seem significantly different.

The maximal incorporation extents of Zn^{2+}, Co^{2+}, Ni^{2+}, Al^{3+}, and Cd^{2+} into the ferrite produced by the ATFP were concluded to be (in terms of x in the formula $Me_xFe_{3\text{-}x}O_4$) 0.73, 0.67, 0.46, 0.24 and 0.17, respectively. These values are approximately 49% to 73% of the corresponding values obtained by precipitation at 90 °C. The preferential order of metal incorporation at ambient temperature was found to be comparable to that observed at elevated temperature. Thus, the mechanisms governing the metal ion incorporation under both ambient and elevated temperature ferrite syntheses are also analogous.

The crystallinity and chemical stability of ferrites synthesised by the ATFP were generally lower than those of ferrites precipitated at 90 °C. This trend seemed to increase with Me content. The ferrites produced at ambient temperature were smaller and had less well-defined shapes than those formed at elevated temperature, leading to a higher degree of ferrite oxidation. Although the former was less stable than the latter, the stability order for these ferrites was similar.

Under ambient temperature and high initial Me content (i.e. a high Me/Fe_T in the initial solution), electron mobility between Fe^{2+} and Fe^{3+} in the ferrite precursor is reduced, resulting in a dehydration difficulty. It was evident that increasing the initial Fe^{2+}/Fe^{3+} ratio facilitated the dehydration process and eventually enhance the Me incorporation extent and crystallinity of the product.

Simultaneous incorporation of different metal ions into ferrite at ambient temperatures is possible. Multi-metal-substituted ferrites with Me_T/Fe_{T_SP} ratios of up to 0.33 could be produced by applying the StFP. Under a high content of total non-iron metals ($Me_T/Fe_{T\_IN} = 0.4$) and a low synthesis pH (pH 9), the formation of ferrite with low incorporation capacity and poor crystallinity was promoted. The optimised combination of parameters for simultaneous metal ion incorporation is thus suggested to be: T = 30 °C, pH = 10.5, t = 150 min, initial $Fe^{2+}/Fe^{3+} \geq 0.5$, $Me_T/Fe_{T\_IN} = 0.2$–0.4. The sequence of metal entry into multi-metal-substituted ferrites was $Zn^{2+} > Co^{2+} > Ni^{2+} > Al^{3+} \approx Cd^{2+}$. The incorporation of Zn^{2+}, Co^{2+}, and Cd^{2+} was not substantially affected by the presence of other non-iron metals, whereas the incorporation of Ni^{2+} and Al^{3+} was reduced. The changes in multi-metal-substituted ferrite (e.g. unit cell size and dissolution stability) appeared to be the complex combination of that of the individually incorporated metals.

The incorporation extent of Cu^{2+} into the ferrite structure was close to zero due to the reduction of Cu^{2+} by Fe^{2+} as well as the Jahn-Teller effect. Similar to the result obtained at elevated temperature, Cr^{3+} could also not be incorporated into the ferrite structure at ambient temperature, confirmed by the dissolution congruency test. Both Cu^{2+} and Cr^{3+} were observed to have a goehite-promoting effect. The presence of Cr^{3+} appeared to inhibit the incorporation of Ni^{2+}, while it did not affect Zn^{2+} incorporation.

Chapter 7

Treatment of Galvanic Wastewater by Ferrite Process

The investigations conducted so far can give an overview regarding the extent and mechanism of metal incorporation into the ferrite structure. This issue is very important for assessing the application of ferrite process in industrial wastewater treatment. As shown in the experiments with synthetic wastewater, the concentration of metals in the effluent was very low; in most cases it was below the detection limit. Thus, it can be expected that this process is able to remove metal ions from the wastewater completely.

The feasibility of the ATFP for treating galvanic wastewater is then assessed. The metal removal efficiency achieved in each experiment is presented and characteristics of the product are discussed. Some suggestions for the process improvement and a short overview of the treatment cost are also given.

7.1 Characteristics of galvanic wastewater

The industrial galvanic wastewater examined in this study was obtained from WAFA Kunststofftechnik GmbH in Augsburg, Germany and could be divided into two types. The first type mainly contained Ni^{2+}, Cu^{2+}, and chelating agents. The exact type and concentration of the chelating agents in this wastewater was not known. Considering the most common chelating agents in the metal finishing wastewater and their relative metal binding capacities, ethylenediaminetetraacetic acid (EDTA), nitrilotriacetic acid (NTA) and some organic acids were assumed to be present [211]. The second type did not contained chelating agents, but chromium also existed as Cr(VI). The concentration of each type of metal in the investigated galvanic wastewater is presented in Table 7.1. In additions to these metal ions, galvanic wastewater may also contain different types of non-ionic and anionic surfactants.

Table 7.1: Metal concentrations in the investigated galvanic wastewater.

Wastewater	pH	Concentration (mg/l)			
		Ni^{2+}	Cu^{2+}	Cr^{3+}	Cr(VI)
With chelating agents	2.5	406	137	35	-
Without chelating agents	1.7	477	240	337	137

Table 7.2 presents the maximum effluent discharge standards in different countries. Accordingly, the metal concentrations in the effluent of the treatment process should be below these standards.

Table 7.2: Maximum effluent discharge standards of Ni, Cu, and Cr in surface water.

Metal	Maximum effluent standards (mg/l)	
	Germany [212]	USA [12]
Ni^{2+}	0.5	0.2
Cu^{2+}	0.5	0.25
Cr(VI)	0.1	0.05
Cr^{3+}	-	0.1
Cr_{total}	0.5	-

7.2 Experiments performed on galvanic wastewater

The experiments of metal removal from both types of wastewater were conducted by applying the StFP. The results are discussed in the following sections.

7.2.1 Treatment of galvanic wastewater with chelating agents

The experiment was carried out at Me_T/Fe_{T_IN} ratio of 0.1, total metal concentration of 100 mM and total metal flux of 35.5 mg $l^{-1}min^{-1}$ in a continuous mode. Temperature and pH of the experiment was kept at 30 °C and 10.5, respectively. However, the experiment could only be run properly for 2 days. On the third day, it was observed that the produced solids did not settle well in the sedimentation reactor and they escaped to the effluent. The experiment was thus terminated. Apparently, the formation of dense solids from the wastewater solution failed.

A further experiment without seed, operated in a single-cycle batch mode, was then conducted in order to validate the result obtained in the continuous system. In this experiment, about 1000 ml of wastewater was poured into the reactor and then a similar volume of solution containing Fe^{3+} and Fe^{2+} ions was added by a peristaltic pump over

150 min. The other experimental conditions (i.e. Me_T/Fe_{T_IN}, pH, and temperature) were similar to those of the continuous experiment.

The result obtained in the experiment without seed clearly supported the result in the continuous system. The solids formed consisted of a mixture of dark and light brown precipitates. Most of them were found to be nonmagnetic. The XRD pattern of the solid showed a few weak magnetite peaks and high background indicating the formation of mostly non-crystalline phases with traces of magnetite particles (see Figure 7.2). Thus, it can be concluded that ferrite was not formed in this experiment. The metal concentrations in the clear supernatant taken after all the solids had settled was, however, very low indicating almost complete removal. The removal efficiencies obtained are presented in Table 7.3.

Table 7.3: Metal ion removal from galvanic wastewater with chelating agents.

Metal	Concentration (mg/l)		Removal (%)
	Initial	Final	
Ni^{2+}	406	0.09	∼100
Cu^{2+}	137	0.1	∼100
Cr^{3+}	35	0.25	99.3

The above results clearly suggest that most metals were coprecipitated with iron, forming amorphous mixed-metal hydroxides. The chelating agents did not seem to prevent the formation of this precipitate. The coprecipitation of metal ions onto the solid substrate such as hydrated iron oxide was reported by Crawford et al. [213] to have a higher metal removal efficiency than by simple chemical precipitation which sometimes failed to produce an effluent complying with the effluent standard [12].

7.2.2 Treatment of galvanic wastewater without chelating agents

As the wastewater without chelating agents contained Cr(VI), it first had to be reduced before introducing it into the process. This was done during the input solution preparation by adding ferrous sulphate salt at a stoichiometric ratio followed by mixing the solution. Completion of the reduction process was checked by the 1,5-diphenyl carbazide method. The experiment was firstly conducted in the continuous system at Me_T/Fe_{T_IN} ratio of 0.2, total metal concentration of 120 mM, and total metal flux of 44.2 mg $l^{-1}min^{-1}$. The initial Fe^{2+}/Fe^{3+} ratio was adjusted to 0.59. Temperature of the experiment was kept at 30 °C and pH 10.5. The settling property of the solid in this experiment was slightly better than that in the previous experiment with chelating agents. However, the solid density was not sufficient for an efficient solid-liquid separation. After 10 days of operation, the experiment was terminated as solid particles escaped to the effluent.

Figure 7.1 shows the XRD patterns of the solids precipitated from the galvanic wastewater without and with chelating agents. In general, it can be seen that both XRD patterns have high backgrounds suggesting the presence of high amounts of amorphous precipitates. However, the peak intensities of precipitates produced without chelating agents were higher, particularly at reflections with *hkl* 200, 311, 400, 511, 440 indicating that the spinel was of a higher structural order than precipitates formed in the presence of chelating agents. Nevertheless, the formation of solids with a high crystallinity degree in a continuous system did not seem to be successful. It should be noted that the peak with *hkl* 311 in the XRD pattern of the solids produced in the experiment with chelating agents was probably the footprint of the pure magnetite seed used in the experiment as this experiment was only run for 2 days (Section 7.2.1).

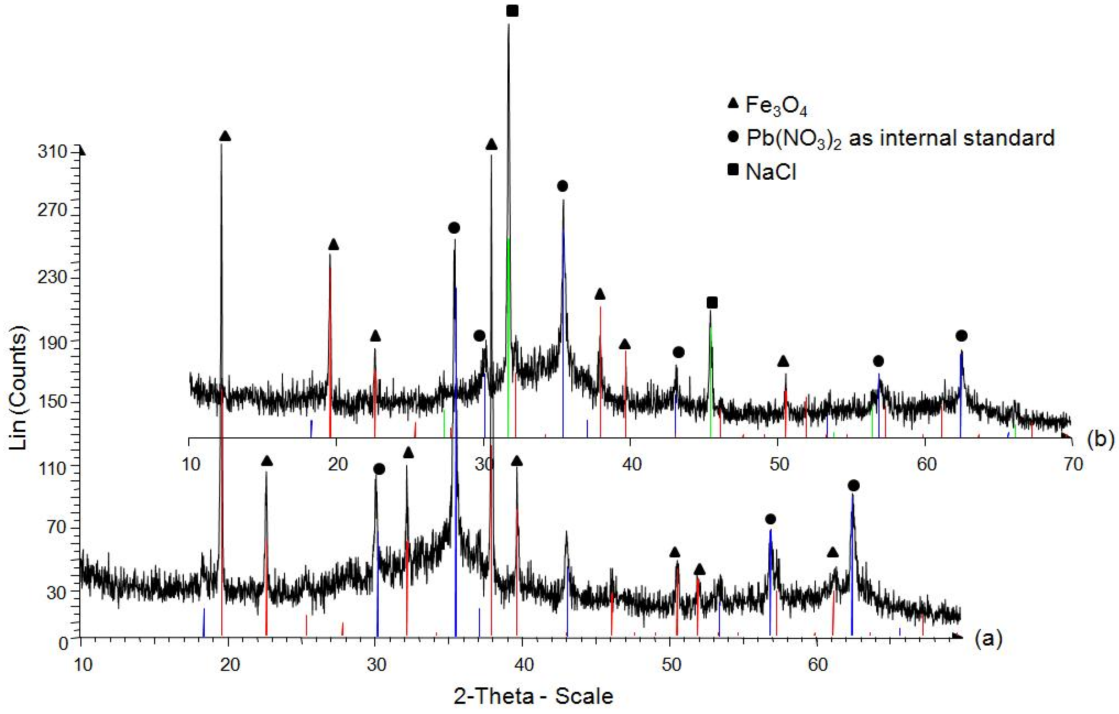

Figure 7.1: XRD patterns of the solids precipitated from galvanic wastewater (a) without chelating and (b) with chelating agents in a continuous mode.

Similar to the experiment with chelating agents, it was found that all metals can be completely removed from the wastewater without chelating agents (Table 7.4). About 30% of the Ni^{2+} was incorporated into the spinel structure, but Cr^{3+} and Cu^{2+} were not incorporated. On the basis of the earlier findings, this result was actually as expected. As most of the metals were not incorporated into the crystal, they were present in a non-spinel phase either on the particle surface or possibly as separate phases, as extensively discussed in the previous chapters.

As the continuous experiment indicated that to some extent ferrite could be formed

Table 7.4: Metal ion and COD removal from galvanic wastewater without chelating agents in the continuous experiment.

Parameter	Concentration (mg/l)		Removal (%)
	Initial	Final[a]	
Ni^{2+}	477	0.14	~100
Cu^{2+}	240	0.05	~100
Cr_{total}	474	0.15	~100
COD	1152	430	62.7

[a] Average concentration for 10 days operation.

in the wastewater without chelating agents, experiments without seed (single-cycle batch mode) were then carried out under different experimental conditions to further improve the process. The experimental conditions tested are listed in Table 7.5. Each experiment was repeated twice and temperature was maintained at 30 °C. During input solution preparation, it was found that that almost all Cr(VI) in the wastewater had been reduced to Cr^{3+}. This process is assumed to have occurred during storage due to the presence of organic substances in the galvanic wastewater. Like Fe^{2+}, these compounds are capable of reducing Cr(VI) [214].

Under all experimental conditions given in Table 7.5, the metal ions were removed completely from the wastewater, as shown in Table 7.6. The effluent concentrations complied with the standards (Table 7.2). The solids formed had black colour; only those produced at the Me_T/Fe_{T_IN} ratio of 0.2 were dark brown. Furthermore, it was found that all solids responded more strongly to magnetic fields compared to those produced in the continuous system.

Table 7.5: Operational conditions of batch experiments applied for treating galvanic wastewater without chelating agents.

Exp.	Me_T/Fe_{T_IN}	Fe^{2+}/Fe^{3+}	t (min)	pH	Anion	
					Fe^{2+}	Fe^{3+}
1	0.1	0.75	10.5	150	SO_4^{2-}	Cl^-
2	0.1	0.75	9.5	150	SO_4^{2-}	Cl^-
3	0.1	1	10.5	150	SO_4^{2-}	Cl^-
4	0.143	0.75	10.5	150	SO_4^{2-}	Cl^-
5	0.143	0.75	10.5	240	SO_4^{2-}	Cl^-
6	0.143	0.75	10.5	60	Cl^-	Cl^-
7	0.143	0.75	10.5	150	SO_4^{2-}	SO_4^{2-}

Continued on next page . . .

Exp.	Me_T/Fe_{T_IN}	Fe^{2+}/Fe^{3+}	t (min)	pH	Anion	
					Fe^{2+}	Fe^{3+}
8	0.143	0.75	10.5	150	Cl^-	Cl^-
9	0.2	0.75	10.5	150	SO_4^{2-}	Cl^-

Table 7.6: Metal ion removal from galvanic wastewater without chelating agents in the batch experiments.

Exp.	Initial concentration (mg/l)			Final concentration (mg/l)			Removal (%)		
	Ni^{2+}	Cu^{2+}	Cr^{3+}	Ni^{2+}	Cu^{2+}	Cr^{3+}	Ni^{2+}	Cu^{2+}	Cr^{3+}
1	477	240	474	0.05	0.02	0.06	~100	~100	~100
2	477	240	474	0.05	0.02	0.05	~100	~100	~100
3	477	240	474	0.06	0.03	0.05	~100	~100	~100
4	477	240	474	0.1	0.05	0.08	~100	~100	~100
5	477	240	474	0.12	0.05	0.06	~100	~100	~100
6	477	240	474	0.13	0.06	0.11	~100	~100	~100
7	477	240	474	0.14	0.07	0.06	~100	~100	~100
8	477	240	474	0.15	0.06	0.05	~100	~100	~100
9	477	240	474	0.11	0.09	0.12	~100	~100	~100

The XRD pattern of all solids showed the presence of spinel compounds. It was observed that the peak intensities of the XRD patterns decreased as the ratio of Me_T/Fe_{T_IN} increased, indicating a decrease in the crystallinity degree of the solids with increasing Me content in the initial solution (Figure 7.2). For the solids produced at the same Me_T/Fe_{T_IN} ratio, the peak intensities were found to be relatively similar. The ferrites formed in these experiments were, however, highly oxidised (non-stoichiometric). It should be noted that the presence of goethite was not detected neither by XRD nor SEM.

The incorporation extents of Ni^{2+} into ferrite precipitated from wastewater without chelating agents in terms of the Ni^{2+}/Fe_T ratio in the solid particles (Ni^{2+}/Fe_{T_SP}) and incorporation efficiencies are presented in Figure 7.3. The results for Cu^{2+} and Cr^{3+} are not presented as they were not incorporated into the spinel structure. The experiments conducted at different Me_T/Fe_{T_IN} ratios (Exp. 1, 4, and 9) showed that the Ni^{2+}/Fe_{T_SP} ratio increased with the Ni^{2+}/Fe_{T_IN} ratio. However, the incorporation efficiency was found to be significantly reduced (Figure 7.3b), suggesting the inhibition of Ni^{2+} incorporation under high Me content in the initial solution. An increase in the initial Fe^{2+}/Fe^{3+} ratio from 0.75 (Exp. 1) to 1 (Exp. 3) did not result in the increased Ni^{2+}/Fe_{T_SP} ratio. An opposite effect was even observed, supporting the previous hypothesis discussed in

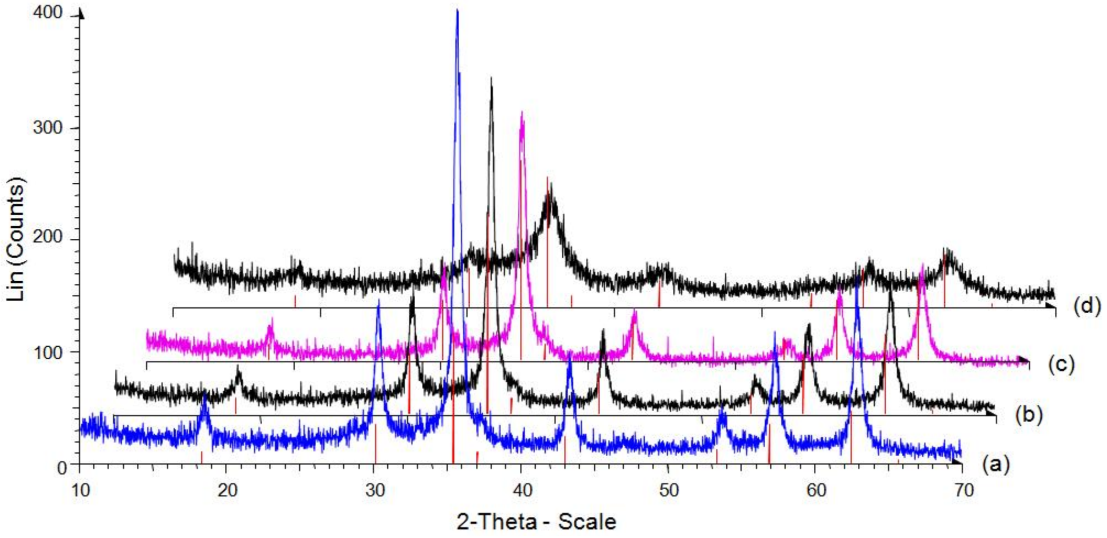

Figure 7.2: XRD patterns of the solids precipitated from galvanic wastewater without chelating agents at Me_T/Fe_{T_IN} ratio of (a) 0.1, (b) 0.143, (c) 0.2 and with chelating agents at Me_T/Fe_{T_IN} ratio of (d) 0.1 in a single-cycle batch mode. The vertical lines are from the JCPDS diffraction data card of magnetite.

Chapter 6.3 regarding the maximal Fe^{2+}/Fe^{3+} ratio employed in the StFP.

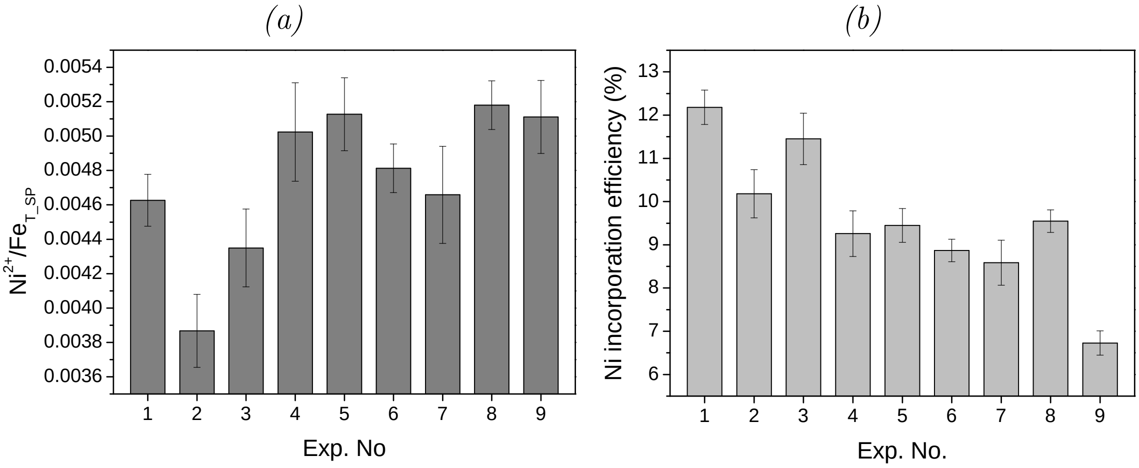

Figure 7.3: The extents of Ni incorporation into ferrite precipitated from galvanic wastewater without chelating agents under different operational conditions listed in Table 7.5 in terms of (a) Ni^{2+}/Fe_{T_SP} and (b) incorporation efficiency.

In line with the synthetic wastewater experiments, a decrease in the synthesis pH from 10.5 (Exp. 1) to 9.5 (Exp. 2) resulted in the reduced Ni^{2+} incorporation. The prolongation of reaction time from 150 min (Exp. 1) to 240 min (Exp. 5) seemed to increase the Ni^{2+} content. The opposite effect was observed, when reaction time was shortened to 60 min (Exp. 6). Among three combinations of anions used in the experiments, the lowest Ni^{2+}/Fe_{T_SP} ratio was obtained for chlorides (Exp. 7), though the other combinations (Exp. 8 and 9) did not seem to significantly affect the content of Ni^{2+} in the solid particles. Further detailed experiments regarding the influence of anions are, however, required. Although the content of Ni^{2+} in the ferrite did not vary significantly under the experimental conditions tested, probably related to the relatively low incorporation degree of Ni^{2+}, the results can describe the conditions under which Ni^{2+} in the galvanic wastewater can still be partially incorporated into the ferrite structure.

The pollution potential of the formed solids was determined mainly by the TCLP test. This procedure was applied to solids washed with distilled water only to better represent the extent of metal leaching as most of the metals were not incorporated into the crystal structure. With regard to chromium, no leaching could be detected, in accordance with the previous results of the synthetic wastewater experiments. The extents of Ni and Cu leaching in the TCLP test are presented in Figure 7.4. As can be seen, Cu was hardly leached, except in the experiment at pH 9.5 (Exp. 2). The leaching extent of Ni was found to be higher than that of Cu. Nickel was leached to the highest extent in the experiment at pH 9.5 (Exp. 2), suggesting the negative effect of a low synthesis pH on ferrite quality, as indicated in the experiments with synthetic wastewater. The reaction time of 60 min could also be considered unsuitable, as more Ni was found to leach from the ferrite synthesised for 60 min (Exp. 6) than from the solid produced for 240 min (Exp. 5). The extent of Ni leaching in the other experiments was found to be relatively low.

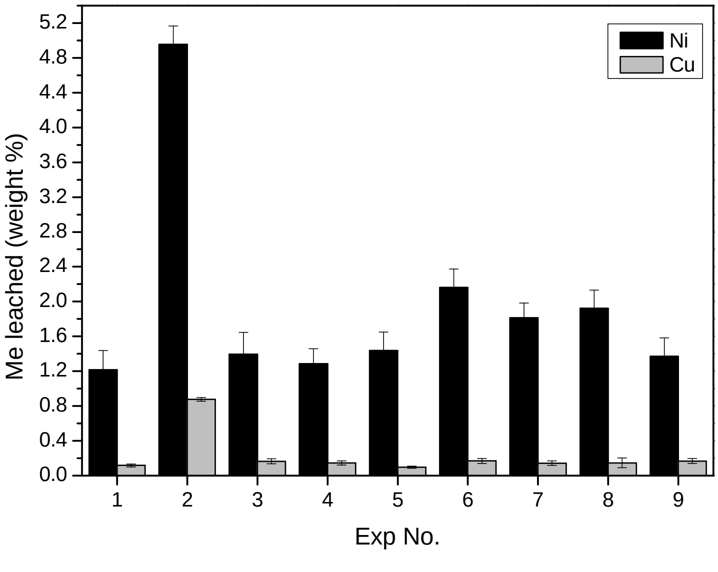

Figure 7.4: Weight percentage of Ni and Cu leached at pH 5 (TCLP test) from the solid particles produced in the experiment without chelating agents.

The above findings clearly demonstrate that ferrite with a better crystallinity was more likely to form in the batch system. The optimum temperature, pH, and reaction time was similar to those obtained in the synthetic wastewater. However, the optimum range of Me_T/Fe_{T_IN} ratio appeared to be lower (0.1–0.2). The initial Fe^{2+}/Fe^{3+} ratio of 0.75 could be considered as the maximal value. Considering the previous results of the synthetic wastewater experiments, the suggested initial Fe^{2+}/Fe^{3+} ratio in the StFP ranges between 0.5 and 0.75.

7.3 Assessment of galvanic wastewater treatment by ATFP

Based on the above results, it can be deduced that the formation of ferrite in the galvanic wastewater seems to be limited. When chelating agents are present in the wastewater, it is hardly possible to form ferrite unless perhaps other metal ions are added to the wastewater, thus displacing the metal ions from their complexes so they can form ferrite. Tünay et al. [211] proposed the usage of Ca^{2+} as a ligand-binding agent to effectively precipitate metal hydroxides in the presence of a chelating agent. In case of ferrite process, the addition of Ca^{2+} does not seem feasible as this ion was identified to hinder to formation of ferrite [215]. More appropriate alternatives without significant interferences to the ferrite formation should be further investigated. On the other hand, it is possible to synthesis ferrite in the wastewater without chelating agents. However, the ferrite formed in this wastewater was considered to be less crystalline compared to the product of the synthetic wastewater treatment described in the previous chapters. This result could be correlated with the presence of other organic compounds such as surfactants in the wastewater.

In general, organic compounds in the system can be assumed to influence the process in two different ways [28]:

- The organic compounds might have a high affinity for the surface of the ferrite precursor. Therefore, they can be retained by the precursor via adsorption. The access of the metal-hydroxo complexes towards the nucleation sites of the precursor can be blocked by these compounds leading to a lower incorporation extent of the metal. They can also suppress the reactivity of ferrite precursor towards internal ordering and/or dissolution resulting in the formation of crystals with less defined structure.

- The organic compounds can also act solely in solution and retard the nucleation or growth of ferrite by competing with soluble metal-hydroxo complexes for the sites on the nucleus or on the growing crystals.

The presence of organic compounds in the wastewater without chelating agents was supported by chemical oxygen demand (COD) measurement. The COD removal of about 63% (see Table 7.4) indicated that the adsorption of organic compounds indeed happened during ferrite precipitation.

It can be concluded that another auxiliary process is required to improve the performance of the ATFP. Figure 7.5 illustrates a scheme of an integrated treatment system based on the StFP. A pre-treatment method is included in this system to remove the interfering compounds such as the chelating agents and other organic substances. For wastewater containing Cr(VI), a reduction step is done by adding ferrous salt. As the pH of galvanic wastewater is relatively low, no pH adjustment is required for this treatment step. In the following step, the pre-treated wastewater is combined with seed in a contact stabilisation reactor. In this reactor, the ratio of non-iron metals to iron is adjusted (0.1–0.2) by adding ferrous and/or ferric sulphate (or chloride) and the pH is raised to 10.5 by the addition of NaOH. As pH increases, metals are coprecipitated to form ferrite. The mixture suspension will flow to a gravity settler or possibly a magnetic separation reactor for a solid phase separation. To complete the transformation process of the metal intermediates into the crystalline phase, an aging tank is used. A fraction of the aged solids will be recirculated to the reactor to maintain the seed concentration at a certain level (about 20 g Fe/l). The influence of an aging step in the whole treatment process should be further studied as in the current experimental work no aging tank was employed. To further improve the quality of the formed ferrite, a secondary solid treatment can be applied, for example by exhaustive oxidation, as proposed by Morgan et al. [137].

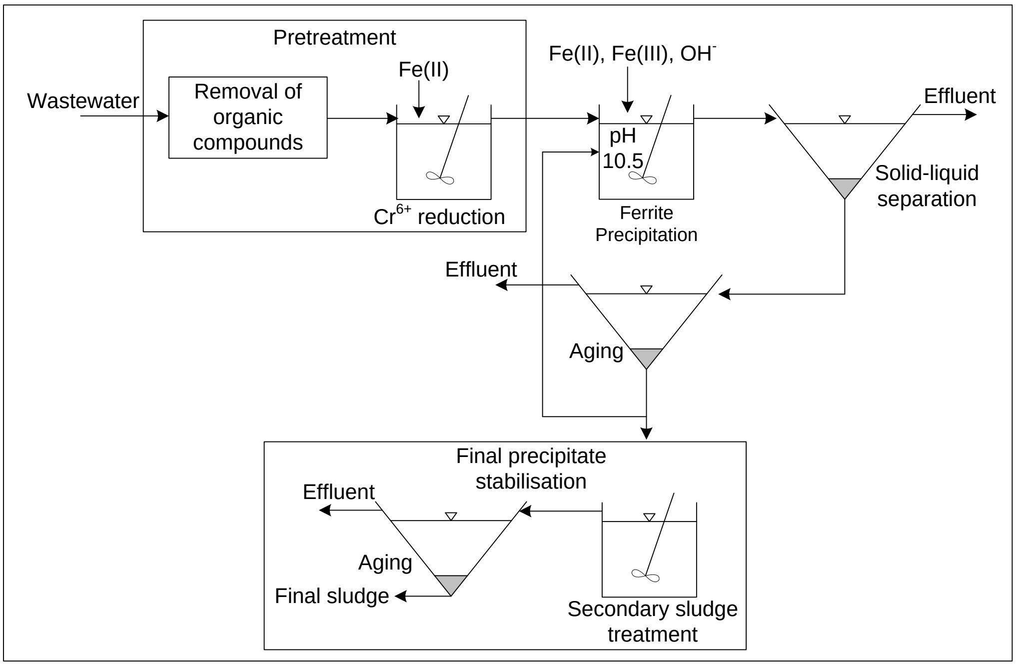

Figure 7.5: Scheme of an integrated ATFP for wastewater laden with metal ions.

7.4 Cost comparison of treatment technologies for galvanic wastewater

In general, the overall treatment costs of a wastewater treatment plant include the construction costs and the operational and maintenance costs (O&M). The required effluent quality and the installation capacity normally determine the construction costs, while manpower, energy, chemicals and maintenance are the most important components of the O&M costs [12].

A reliable estimation of treatment cost for metal-contaminated wastewater is difficult due to the many cost components involved such as pumping equipment and treatment facility. Furthermore, changes in the quality and quantity of the wastewater also contribute to the variations of its treatment cost, as reflected in the reported operational costs of different treatment techniques presented in Table 7.7. Thus, information on the treatment cost of galvanic wastewater is rarely reported.

Based on the results presented in the previous chapters, it is clear that the elevated temperature ferrite process has advantages with regard to a higher metal incorporation extent and chemical stability. The proposed ATFP can produce ferrite with similar crystallinity and stability degree to the one produced at high temperature, but only at a relatively low initial non-iron metal to iron ratio. The additional chemical costs for the process at ambient temperature are probably similar to the heating costs for the high temperature process. The deciding factor is apparently the composition of the wastewater. If the wastewater contains high concentrations of Fe and non-iron metals without organic compounds, like in acid mine drainage, the ferrite process at ambient temperature seems to be a better option. The application of the ATFP for acid mine drainage has been investigated by several authors [137, 215]. For the wastewater containing metal ions together with organic compounds (e.g. galvanic wastewater), the elevated temperature ferrite process should be considered because the retardation effects of other compounds can be minimised [28].

It is noted that the primary sludge/solid treatment in the ferrite process is basically only aging (Figure 7.5) which is a relatively simple and cheap process. This inherent sludge treatment is the advantage of the ferrite process over the other treatment techniques which normally require relatively high costs for sludge treatment and disposal, up to 60% of the total operational costs (Table 7.7).

Table 7.7: Operational costs of different treatment techniques for metal containing wastewater.

Type of wastewater	Initial concentration (mg/l)	Operational costs (€/m^3)							Ref.
		Chemical			Energy	Sludge treatment		Total	
		CP	EC^{a}	IE^{b}	EC^{a}	CP	EC^{a}		
Electroplating	Cr = 3860		0.73		1.38		3.09	5.2	[216]
Electroplating	Cr = 500	1.03^{c}				4.66^{c}		5.69^{c}	[216]
Electroplating	Cr = 406			5.27				5.27	[216]
Industrial effluent	Cu = 932; Cr=494; Ni=468							3.76	[217]
Sewage sludge leachate	Cu = 29; Zn = 7	7.44^{d} 37.38^{e}				6.61^{d} 7.08^{e}		14.05^{d} 44.46^{e}	[218]
Sewage sludge leachate	Cu = 29; Zn = 7		3.05				6.39	9.44	[218]
Acidic soil leachate	Cu = 3; Pb = 30; Zn = 18	8.59^{d} 27.00^{e}				0.97^{d} 0.43^{e}		9.56^{d} 27.43^{e}	[219]
Acidic soil leachate	Cu = 3; Pb = 30; Zn = 18				1.73		5.34	7.07	[219]
Acidic soil leachate	Cd = 107; Cr = 96; Cu = 106; Ni = 110; Pb = 100; Zn = 94	14.7^{d} 47.49^{e}				2.93^{d} 2.19^{e}		17.66^{d} 49.68^{e}	[219]

Continued on next page ...

Type of wastewater	Initial concentration (mg/l)	Operational costs (€/m^3)							Ref.
		Chemical			Energy	Sludge treatment		Total	
		CP	EC[a]	IE[b]	EC[a]	CP	EC[a]		
Acidic soil leachate	Cd = 107; Cr = 96; Cu = 106; Ni = 110; Pb = 100; Zn = 94				1.59		6.77	8.36	[219]

[a] EC: Electrocoagulation

[b] IE: Ion exchange

[c] CP: Chemical precipitation by $Na_2S_2O_5$ reduction and NaOH precipitation

[d] CP: Chemical precipitation by $Ca(OH)_2$ precipitation

[e] CP: Chemical precipitation by NaOH precipitation

7.5 Conclusions

All metal ions could be completely and concurrently removed from the galvanic wastewater by the ATFP. However, the formation of crystalline ferrite in the wastewater with chelating agents was strongly retarded. In the wastewater without chelating agents, ferrite with a better crystalline structure could be formed. The overall metal incorporation extent was, however, low as the galvanic wastewater tested in this study mainly contained Cu^{2+} and Cr^{3+} which are reluctantly incorporated into the ferrite structure. The incorporation tendency of Ni^{2+} was lowered to a significant extent due to the antagonistic effect of the other metal ions. The optimum conditions for ferrite formation in this wastewater were similar to those obtained in the synthetic wastewater, except that the initial non-iron metals to iron ratio was approximately two times lower.

The formation of high crystalline ferrite in galvanic wastewater was limited due to the presence of organic compounds, suggesting that the performance of the ferrite process is rather sensitive to the presence of interfering compounds. To overcome this problem, another pre-treatment step is needed. Alternatively, the ferrite process at elevated temperature can also be considered with additional incentives of lower chemical demand and higher product stability. The presence of metal ions having low incorporation tendency such as Cr^{3+} and Cu^{2+} can be problematic when ferrite with high metal incorporation extent and crystallinity should be synthesised from the industrial wastewater. As long as metal removal efficiency is concerned, the performance of the ATFP is comparable with other treatment techniques.

Chapter 8

Concluding Summary and Outlook

The removal of toxic metals by their incorporation into ferrites is a novel technique for the treatment of industrial wastewater. The present work critically demonstrates the possibility of turning an environmental hazard into a source material, magnetic ferrites. The experimental results showed that all non-iron metals could be completely removed from the synthetic wastewater. However, less than 100% incorporation efficiency was attained for some or all of the investigated metals at elevated and ambient temperature, respectively. This result indicates that a proportion of these guest ions existed as a non-spinel phase on the particle surface or as a separate solid entity that were removed prior to analysis in the acidic rinsing prosess (pH 2). Because a certain non-spinel phase, particularly the one containing Cr^{3+}, was persistent toward this rinsing step, the dissolution test was found to be of importance in the determination of metal incorporation.

At elevated temperature (60–100 °C), a complete metal incorporation was achieved by Zn^{2+} and Co^{2+}, while Cr^{3+} was hardly incorporated into the ferrite structure. The rate of water exchange between the inner and outer sphere around a metal ion in aqueous solution (k_{-w}) seemed to be correlated with the metal incorporation extent. An exception to this correlation is Cd^{2+} which can be attributed to its large ionic radius. The incorporation of metal ions also affected the dissolution stability of the ferrite. Al^{3+} and Ni^{2+} had the largest stabilisation effect, followed by Co^{2+}, Zn^{2+}, and Cd^{2+}. However, the dissolution stability of the ferrites could not be explained satisfactorily by one parameter only. The leaching extent of non-iron metal at pH $\sim$5 (TCLP test) was generally low and under the more extreme conditions (BCR test) the release was enhanced as expected.

At ambient temperature, electron transfer between Fe^{2+} and Fe^{3+} plays a fundamental role in the crystallisation of spinel. In the presence of high non-iron metal to iron ratio in the initial solution, the Fe^{2+}-Fe^{3+} interaction is less intense, impeding dehydration and spinel ordering [201]. This leads to a reduced non-iron incorporation level, crystallinity, and stability (for some ferrites). Although the maximal incorporation extents attained by the seeded ambient temperature ferrite process (ATFP) are approximately 49% to 73% of the corresponding values obtained under elevated temperature precipitation, the preferential order of metal incorporation found in both processes is similar. This result suggests that the main mechanisms responsible for metal ion incorporation at ambient and elevated temperature are also analogous.

The differences in the performances of the stoichiometric ferrite process (StFP) and oxidation ferrite process (OxFP) were not found to be large. Both methods were able to completely remove all toxic metals from aqueous solution and to produce ferrites with good settling and magnetic properties. A higher metal incorporation extent and simpler operation were the main advantages of the former method, while a more crystalline ferrite was produced by the latter method. Simultaneous incorporation of different non-iron metals by the seeded ATFP was shown to be possible. In general, the sequence of non-iron metal entry into ferrite in the multi- and single-metal system is similar. However, the incorporation extent of certain non-iron metals, such as Ni^{2+} and Al^{3+} might be reduced due to the negative effect of co-metals. The investigated operational parameters of the StFP affected to some extent the formation of multi-metal-substituted ferrites. Under a high non-iron metal content in the initial solution (high Me_T/Fe_{T_IN} ratio), high synthesis pH and long reaction time are favourable for ferrite formation. A slight increase in the synthesis temperature can also improve the ferrite quality.

The ATFP was capable of removing all metal ions from the galvanic wastewater. However, the overall metal incorporation extent was low because the wastewater mainly contained Cu^{2+} and Cr^{3+} which could not be incorporated into the ferrite structure. Furthermore, the formation of high crystalline ferrite appeared to be limited due to the presence of organic compounds.

At present time, further optimisation and improvement of the ATFP are still necessary. Comparison of the OxFP and StFP should be further studied with respect to the other operational parameters such as reaction time and pH. The critical role of the initial Fe^{2+}/Fe^{3+} ratio in the StFP has been clearly indicated, but this parameter needs to be further optimised. The simultaneous incorporation of different metal ions has been investigated in a relatively limited combination. Thus, the investigation other metal combinations can be very useful to gain a further knowledge regarding the synergetic and antagonistic effects of the presence of co-metal ions.

The investigation of the application of ATFP for galvanic wastewater treatment highlights the need of combining the ATFP with a pre-treatment step to improve the overall treatment performance. What kinds of technique could be applied as a pre-treatment step after considering several factors such as the type of compounds existed in the wastewater, treatment efficiency, and costs? How is the performance of these combined processes? Does the pre-treatment step improve the crystallisation of the ferrite? These are some of the open questions that can be further explored in upcoming studies. Finally, investigation of the performance of ATFP for the treatment of industrial wastewater containing different metal compositions is recommended.

References

[1] Liu, J.; Goyer, R.A.; Waalkes, M.P. Toxic effects of metals. In *Casarett and Doull's toxicology*; Casarett, L.J.; Doull, J.; Klaassen, C.D., Eds.; McGraw-Hill: New York, 2008.

[2] Nordberg, G.F.; Fowler, B.A.; Nordberg, M.; Friberg, L.T. Introduction-General considerations and international perspective. In *Handbook on the toxicology of metals*; Nordberg, G.F.; Fowler, B.A.; Nordberg, M.; Friberg, L.T., Eds.; Elsevier: Amsterdam, 2007.

[3] Sharma, Y.C.; Srivastava, V.; Singh, V.K.; Kaul, S.N.; Weng, C.H. Nano-adsorbents for the removal of metallic pollutants from water and wastewater. *Environmental Technology* **2009**, *30(6)*, 583–609.

[4] Förstner, U.; Wittmann, G.T.W. *Metal pollution in the aquatic environment*, 2. rev ed.; Springer Verlag: Berlin, 1981.

[5] Beliles, R.P. The metals. In *Patty's industrial hygiene and toxicology*; Clayton, G.D.; Clayton, F.E., Eds.; Wiley: New York, 1994; Vol. Pt. C, *Toxicology*.

[6] Landesumweltamt NRW. Galvanikschlämme. 2005. Available online: `http://www.lanuv.nrw.de/abfall/bewertung/galvanikschl_sich060518.pdf`, accessed on 10.05.2010.

[7] Magalhães, J.M.; Silva, J.E.; Castro, F.P.; Labrincha, J.A. Physical and chemical characterisation of metal finishing industrial wastes. *Journal of Environmental Management* **2005**, *75*, 157–166.

[8] Förster, H.; Moran, R.; Hartinger, L.; Karigl, B.; Waginger, H.; Huger, P. Branchenkonzept Oberflächentechnik. 2003. Available online: `www.harald-förster.at/media/studien/BK_OFT_2003.pdf`, accessed on 10.05.2011.

[9] McKinnon, W.; Choung, J.W.; Xu, Z.; Finch, J.A. Magnetic seed in ambient temperature ferrite process applied to acid mine drainage treatment. *Environmental Science and Technology* **2000**, *34(12)*, 2576–2581.

[10] Egiebor, N.O.; Oni, B. Acid rock drainage formation and treatment; a review. *Asia-Pasific Journal of Chemical Engineering* **2007**, *2*, 47–62.

[11] Barrado, E.; Vega, M.; Pardo, R.; Ruipérez, M.; Medina, J. Application of the Taguchi experimental design to the removal of toxic metals from waste waters by precipitation as magnetic ferrites. *Analytical Letters* **1996**, *29(4)*, 613–633.

[12] Kurniawan, T.A.; Chan, G.Y.S.; Lo, W.H.; Babel, S. Physico-chemical treatment techniques for wastewater laden with heavy metals. *Chemical Engineering Journal* **2006**, *118*, 83–98.

[13] Tamaura, Y.; Tu, P.Q.; Rojarayanont, S.; Abe, H. Stabilization of hazardous materials into ferrite. *Water Science and Technology* **1991**, *23*, 399–404.

[14] Tamaura, Y.; Katsura, T.; Rojarayanont, S.; Yoshida, T.; Abe, H. Ferrite process; heavy metal ions treatment system. *Water Science and Technology* **1991**, *23*, 1893–1900.

[15] Yang, K.; Misra, M.; Mehta, R.K. Ambient temperature treatment of Noranda Tailing and Barkeley Pit acid mine water by modified ferrite coprecipitation and magnetic separation. EPD Congress; Warren, G.W., Ed. The Minerals, Metals & Materials Society, 1994.

[16] Wang, W.; Xu, Z.; Finch, J. Fundamental study of an ambient temperature ferrite process in the treatment of acid mine drainage. *Environmental Science and Technology* **1996**, *30(8)*, 2604–2608.

[17] Perales-Perez, O.; Tohji, K.; Umetsu, Y. Ambient-temperature synthesis of metal-bearing ferrites: how and why? *Journal of Alloys and Compounds* **1999**, *290*, 129–136.

[18] Morgan, B.E.; Loewenthal, R.E.; Lahav, O. Fundamental study of a one-step ambient temperature ferrite process for treatment of acid mine drainage waters. *Water SA* **2001**, *27(2)*, 277–282.

[19] Sarig, S. Fundamentals of aqueous solution growth. In *Handbook of crystal growth, Vol. 2: Bulk crystal growth*; Hurle, D.T.J., Ed.; North-Holland: Amsterdam, 1994; pp. 1217–1269.

[20] Steefel, C.I.; van Cappellen, P. A new kinetic approach to modeling water-rock interaction: The role of nucleation, precursors, and Ostwald ripening. *Geochimica et Cosmochimica Acta* **1990**, *54*, 2657–2677.

[21] Nielsen, A.E. *Kinetics of precipitation*; Vol. 18, *International series of monographs on analytical chemistry*, Pergamon Press: London, 1964.

[22] Jolivet, J.P.; Henry, M.; Livage, J. *Metal oxide chemistry and synthesis: From solution to solid state*; Wiley: Chichester, 2000.

[23] Jensen, J.N. *A problem-solving approach to aquatic chemistry*; Wiley: New York, 2003.

[24] Morel, F.M.M.; Hering, J.G. *Principles and applications of aquatic chemistry*; John Wiley & Sons, Inc.: New York, 1993.

[25] Stumm, W.; Morgan, J.J. *Aquatic chemistry: Chemical equilibria and rates in natural waters*, 3rd ed.; A Wiley-Interscience publication, Wiley: New York, 1996.

[26] Helm, L.; Merbach, A.E. Water exchange on metal ions: experiments and simulations. *Coordination Chemistry Reviews* **1999**, *187*, 151–181.

[27] Burgess, J.A. *Metal ions in solution*; Ellis Horwood Limited: Chichester, 1978.

[28] Cornell, R.M.; Schwertmann, U. *The iron oxides: Structure, properties, reactions, occurences and uses*, 2nd ed.; Wiley-VCH: Weinheim, 2003.

[29] Brown, T.L.; LeMay, H.E.; Bursten, B.E.; Gardner, T. *Chemistry: The central science*, 8th ed.; Prentice-Hall: New Jersey, 2000.

[30] Richens, D.T. *The chemistry of aqua ions: Synthesis, structure and reactivity; a tour through the periodic table of the elements*; Wiley: Chichester, 1997.

[31] Benjamin, M.M. *Water chemistry*, 1st ed.; McGraw-Hill Series in water resources and environmental engineering, McGraw-Hill: Boston, 2002.

[32] Schwertmann, U. Solubility and dissolution of iron oxides. *Plant and Soil* **1991**, *130*, 1–25.

[33] Jolivet, J.P.; Tronc, E.; Chanéac, C. Iron oxides: From molecular clusters to solid. A nice example of chemical versatility. *Comptes Rendus Geoscience* **2006**, *338*, 488–497.

[34] Jolivet, J.P.; Chanéac, C.; Chiche, D.; Cassaignon, S.; Durupthy, O.; Hernandez, J. Basic concepts of the crystallization from aqueous solution: The example of aluminium oxy(hydroxi)des and aluminosilicates. *Comptes Rendus Geoscience* **2011**, *343*, 113–122.

[35] Boistelle, R.; Astier, J.P. Crystallization mechanism in solution. *Journal of Crystal Growth* **1988**, *90*, 14–30.

[36] Botsaris, G.D.; Denk, E.G. Growth rates of aluminum potassium sulfate crystals in aqueous solutions. *Industrial and Engineering Chemistry Fundamentals* **1970**, *9(2)*, 276–282.

[37] Mullin, J.W. *Crystallization*, 3rd ed.; Butterworth-Heinemann: Oxford, 1993.

[38] van der Heijden, A.E.D.M.; van Rosmalen, G.M. Industrial mass crystallisation. In *Handbook of crystal growth, Vol. 2: Bulk crystal growth*; Hurle, D.T.J., Ed.; North-Holland: Amsterdam, 1994; pp. 315–415.

[39] Sugimoto, T. Preparation of monodispersed colloidal particles. *Advances in Colloid and Interface Science* **1987**, *28*, 65–108.

[40] Blesa, M.A.; Matijević, E. Phase transformations of iron oxides, oxohydroxides, and hydrous oxides in aqueous media. *Advances in Colloid and Interface Science* **1989**, *29*, 173–221.

[41] Stumm, W. *Chemistry of the solid water interface: Processes at the mineral-water and particle-water interface in natural systems*; Wiley: New York, 1992.

[42] Blesa, M.A.; Morando, P.J.; Regazzoni, A.E. *Chemical dissolution of metal oxides*; CRC Press: Boca Raton, 1994.

[43] Stumm, W.; Furrer, G. The dissolution of oxides and aluminum silicates; examples of surface-coordination-controlled kinetics. In *Aquatic surface chemistry*; Stumm, W., Ed.; Wiley: New York, 1987; pp. 197–219.

[44] Sidhu, P.S.; Gilkes, R.J.; Cornell, R.M. Dissolution of iron oxides and oxyhydroxides in hydrochloric and perchloric acids. *Clays and Clay Minerals* **1981**, *29(4)*, 269–276.

[45] Cornell, R.M.; Giovanoli, R. Acid dissolution of akaganéite and lepidocrocite: The effect on crystal morphology. *Clays and Clay Minerals* **1988**, *36(5)*, 385–390.

[46] Chiarizia, R.; Horwitz, E.P. New formulations for iron oxides dissolution. *Hydrometallurgy* **1991**, *27*, 339–360.

[47] Schwertmann, U.; Cambier, P.; Murad, E. Properties of goethites of varying crystallinity. *Clays and Clay Minerals* **1985**, *33(5)*, 369–378.

[48] Schwertmann, U.; Latham, M. Properties of iron oxides in some New Caledonian oxisols. *Geoderma* **1986**, *39*, 105–123.

[49] Hill, R.J.; Craig, J.R.; Gibbs, G.V. Systematics of the spinel structure type. *Physics and Chemistry of Minerals* **1979**, *4*, 317–339.

[50] Gözüak, F.; Köseoglu, Y.; Baykal, A.; Kavas, H. Synthesis and characterization of $Co_xZn_{1-x}Fe_2O_4$ magnetic nanoparticles via a PEG-assisted rout. *Journal of Magnetism and Magnetic Materials* **2009**, *321*, 2170–2177.

[51] O'Neill, H.C.; Navrotsky, A. Cation distributions and thermodynamic properties of binary spinel solid solutions. *American Mineralogist* **1984**, *69*, 733–753.

[52] Urusov, V.S. Interaction of cations on octahedral and tetrahedral sites in simple spinels. *Physics and Chemistry of Minerals* **1983**, *9*, 9–15.

[53] Goldman, A. *Modern ferrite technology*, 2nd ed.; Springer: Boston, MA, 2006.

[54] Grimes, R.W.; Anderson, A.B.; Heuer, A.H. Predictions of cation distributions in AB_2O_4 spinels from normalized ion energies. *Journal of the American Chemical Society* **1989**, *111(1)*, 1–7.

[55] Della Giusta, A.; Carbonin, S.; Ottonello, G. Temperature-dependent disorder in a natural Mg-Al-Fe^{2+}-Fe^{3+}-spinel. *Mineralogical Magazine* **1996**, *60*, 603–616.

[56] Lavina, B.; Salviulo, G.; Della Giusta, A. Cation distribution and structure modelling of spinel solid solutions. *Physics and Chemistry of Minerals* **2002**, *29*, 10–18.

[57] Andreozzi, G.B.; Princivalle, F.; Skogby, H.; Della Giusta, A. Cation ordering and structural variations with temperature in $MgAl_2O_4$ spinel: An X-ray single-crystal study. *American Mineralogist* **2000**, *85*, 1164–1171.

[58] Sickafus, K.E.; Wills, J.M.; Grimes, N.W. Structure of spinel. *Journal of American Ceramic Society* **1999**, *82(12)*, 3279–3292.

[59] O'Neill, H.S.C.; Annersten, H.; Virgo, D. The temperature dependence of the cation distribution in magnesioferrite ($MgFe_2O_4$) from powder XRD structural refinements and Mössbauer spectroscopy. *American Mineralogist* **1992**, *77*, 725–740.

[60] Verwey, E.J.W.; Heilmann, E.L. Physical properties and cation arrangement of oxides with spinel structures: I. Cation arrangement in spinels. *The Journal of Chemical Physics* **1947**, *15(4)*, 174–180.

[61] West, A.R. *Solid state chemistry and its applications*; Wiley: Chichester, 1984.

[62] Rodgers, G.E. *Introduction to coordination, solid state, and descriptive inorganic chemistry*; McGraw-Hill: New York, 1994.

[63] Shannon, R.D.; Prewitt, C.T. Effective ionic radii in oxides and fluorides. *Acta Crystallographica* **1969**, *B25*, 925–946.

[64] Shannon, R.D. Revised effective ionic radii and systematic studies of interatomic distances in halides and chalcogenides. *Acta Crystallographica* **1976**, *A32(5)*, 751–767.

[65] O'Neill, H.C.; Navrotsky, A. Simple spinels: crystallographic parameters, cation radii, lattice energies, and cation distribution. *American Mineralogist* **1983**, *68*, 181–194.

[66] Barsoum, M.W. *Fundamentals of ceramics*, 2nd ed.; IOP: Bristol, 2003.

[67] Ottonello, G. Energetics of multiple oxides with spinel structure. *Physics and Chemistry of Minerals* **1986**, *13*, 79–90.

[68] Thompson, P.; Grimes, R.W. Madelung calculations for the spinel structure. *Philosophical Magazine* **1977**, *36(3)*, 501–505.

[69] Nath, M.; Sharma, C.L.; Bharti, N. Rare earth - Iron mixed oxides: A review. *Reviews in Inorganic Chemistry* **2000**, *20(2)*, 137–186.

[70] Mallapur, M.M.; Shaikh, P.A.; Kambale, R.C.; Jamadar, H.V.; Mahamuni, P.U.; Chougule, B.K. Structural and electrical properties of nanocrystalline cobalt substituted nickel zinc ferrite. *Journal of Alloys and Compounds* **2009**, *479*, 797–808.

[71] Shahane, G.S.; Kumar, A.; Arora, M.; Pant, R.P.; Lal, K. Synthesis and characterization of Ni-Zn ferrite nanoparticles. *Journal of Magnetism and Magnetic Materials* **2010**, *322*, 1015–1019.

[72] Hankare, P.P.; Vader, V.T.; Patil, N.M.; Jadhav, S.D.; Sankpal, U.B.; Kadam, M.R.; Chougule, B.K.; Gajbhiye, N.S. Synthesis, characterization and studies on magnetic and electrical properties of Mg ferrite with Cr substitution. *Materials Chemistry and Physics* **2009**, *113*, 233–238.

[73] Gnanaprakash, G.; Philip, J.; Raj, B. Effect of divalent metal hydroxide solubility product on the size of ferrite nanoparticles. *Materials Letters* **2007**, *61*, 4545–4548.

[74] Huang, C.L.; Matijević, E. Preparation and characterization of ultrafine iron-rich nickel ferrites. *Solid State Ionics* **1996**, *84*, 249–258.

[75] Sugimoto, T.; Matijević, E. Formation of uniform spherical magnetite particles by crystallization from ferrous hydroxide gels. *Journal of Colloid and Interface Science* **1980**, *74(1)*, 227–243.

[76] Regazzoni, A.E.; Matijević, E. Formation of spherical colloidal nickel ferrite particles as model corrosion products. *Corrosion-Nace* **1982**, *38*, 212–218.

[77] Regazzoni, A.E.; Matijević, E. Formation of colloidal mixed cobalt-nickel ferrite particles. *Colloids and Surfaces* **1983**, *6*, 189–201.

[78] Rodenas, L.G.; Blesa, M.A.; Morando, P.J. Reactivity of metal oxides: Thermal and photochemical dissolution of MO and $M\mathrm{Fe_2O_4}$ (M = Ni, Co, Zn). *Journal of Solid State Chemistry* **2008**, *181*, 2350–2358.

[79] Blesa, M.A.; Maroto, A.J.G.; Morando, P.J. Dissolution of cobalt ferrites by thioglycolic acid. *Journal of the Chemical Society, Faraday Transactions 1* **1986**, *82(8)*, 2345–2352.

[80] Blesa, M.A.; Maroto, A.J.G. Dissolution of metal oxides. *Journal de chimie physique* **1986**, *83(11/12)*, 757–764.

[81] Bruyere, V.I.E.; Blesa, M.A. Acidic and reductive dissolution of magnetite in aqueous sulfuric acid: Site binding model and experimental results. *Journal of Electroanalytical Chemistry* **1985**, *182*, 141–156.

[82] Baumgartner, E.C.; Blesa, M.A.; Maroto, A.J.G. Kinetics of the dissolution of magnetite in thioglycolic acid solutions. *Journal of the Chemical Society, Dalton Transactions* **1982**, pp. 1649–1654.

[83] Borghi, E.B.; Regazzoni, A.E.; Maroto, A.J.G.; Blesa, M.A. Reductive dissolution of magnetite by solutions containing EDTA and $\mathrm{Fe^{II}}$. *Journal of Colloid and Interface Science* **1989**, *130(2)*, 299–310.

[84] Baumgartner, E.C.; Blesa, M.A.; Marinovich, H.A.; Maroto, A.J.G. Heterogeneous electron transfer as a pathway in the dissolution of magnetite in oxalic acid solution. *Inorganic Chemistry* **1983**, *22(16)*, 2224–2226.

[85] Blesa, M.A.; Marinovich, H.A.; Baumgartner, E.C.; Maroto, A.J.G. Mechanism of dissolution of magnetite by oxalic acid-ferrous ion solutions. *Inorganic Chemistry* **1987**, *26*, 3713–3717.

[86] Sileo, E.E.; Rodenas, L.G.; Paiva-Santos, C.O.; Stephens, P.W.; Morando, P.J.; Blesa, M.A. Correlation of reactivity with structural factors in a series of Fe(II) substituted cobalt ferrites. *Journal of Solid State Chemistry* **2006**, *179*, 2237–2244.

[87] Sellers, R.M.; Williams, W.J. High-temperature dissolution of nickel chromium ferrites by oxalic acid and nitrilotriacetic acid. *Faraday Discussions of the Chemical Society* **1984**, *77*, 265–274.

[88] Segal, M.G.; Sellers, R.M. Kinetics of metal oxide dissolution: Reductive dissolution of nickel ferrite by Tris(picolinato)vanadium(II). *Journal of the Chemical Society, Faraday Transactions 1* **1982**, *78*, 1149–1164.

[89] Lu, Z.Y.; Muir, D.M. Dissolution of metal ferrites and iron oxides by HCl under oxidising and reducing conditions. *Hydrometallurgy* **1988**, *21*, 9–21.

[90] Kishi, T.; Nagai, T. Cathodic dissolution of nickel ferrous ferrites in acid solutions. *Surface Technology* **1983**, *19*, 9–15.

[91] Kishi, T.; Miki, T.; Nagai, T. Anodic behaviour of cobalt ferrous ferrites in acid solutions. *Surface Technology* **1983**, *20*, 279–286.

[92] Sidhu, P.S.; Gilkes, R.J.; Posner, A.M. The synthesis and some properties of Co, Ni, Zn, Cu, Mn, and Cd substituted magnetites. *Journal Inorganic Nuclear Chemistry* **1978**, *40*, 429–435.

[93] Regazzoni, A.E.; Urrutia, G.A.; Blesa, M.A.; Maroto, A.J.G. Some observations on the composition and morphology of synthetic magnetites obtained by different routes. *Journal Inorganic Nuclear Chemistry* **1981**, *43*, 1489–1493.

[94] Ito, K.; Tamaura, Y.; Katsura, T. Cadmium(II)-, Magnesium(II)-, and Zinc(II)-bearing ferrites formed from γ-FeOOH at various reaction pH's. *Bulletin of the Chemical Society of Japan* **1984**, *57*, 2820–2823.

[95] Music, S.; Ristic, M. Adsorption of trace elements or radionuclides on hydrous iron oxides. *Journal of Radioanalytical and Nuclear Chemistry* **1988**, *120(2)*, 289–304.

[96] Katsumata, H.; Kaneco, S.; Inomata, K.; Itoh, K.; Funasaka, K.; Masuyama, K.; Suzuki, T.; Ohta, K. Removal of heavy metals in rinsing wastewater from plating factory by adsorption with economical viable materials. *Journal of Enviromental Management* **2003**, *69*, 187–191.

[97] Petrick, L.; Dubowski, Y.; Klas, S.; Lahav, O. Stable incorporation of Co^{2+} into ferrite structure at ambient temperature: effect of operational parameters. *Water Air Soil Pollution* **2008**, *190*, 245–257.

[98] Herrera, L.; Ruiz, P.; Aguillon, J.C.; Fehrmann, A. A new spectrophotometric method for the determination of ferrous iron in the presence of ferric iron. *Journal Chemical Technology Biotechnology* **1989**, *44*, 171–181.

[99] Connell, D.W. *Basic concepts of environmental chemistry*, 2nd ed.; CRC/Taylor & Francis: Boca Raton, 2005.

[100] Karamanev, D.G.; Nikolov, L.N.; Mamatarkova, V. Rapid simultaneous quantitative determination of ferric and ferrous ions in drainage waters and similar solutions. *Minerals Engineering* **2002**, *15*, 341–346.

[101] Gendel, Y.; Lahav, O. Accurate determination of Fe(II) concentrations in the presence of a very high soluble Fe(III) background. *Applied Geochemistry* **2008**, *23*, 2123–2129.

[102] Foley, R.T.; Anderson, R.C. Spectrophotometric studies on complex formation with sulfosalicyclic acid. I. With Iron III. *Journal of the American Chemical Society* **1948**, *70(3)*, 1195–1197.

[103] Zolotov, Y.A. *Fundamental of Analytical Chemistry: Practical Guide*; Visshaya Shkola: Moscow, 2001.

[104] Sawyer, C.N.; McCarty, P.L.; Parkin, G.F. *Chemistry for environmental engineering*, 4th ed.; McGraw-Hill: New York, 1994.

[105] West, A.R. *Basic solid state chemistry*, 2nd ed.; Wiley: Chichester, 1999.

[106] Pecharsky, V.K.; Zavalij, P.Y. *Fundamentals of powder diffraction and structural characterization of materials*, 2nd ed.; Springer: New York, 2009.

[107] Cockcroft, J.K.; Fitch, A.N. Experimental setups. In *Powder diffraction*; Dinnebier, R.E.; Billinge, S.J.L., Eds.; Royal Society of Chemistry: Cambridge, 2008.

[108] Dinnebier, R.E.; Billinge, S.J.L. Principles of powder diffraction. In *Powder diffraction*; Dinnebier, R.E.; Billinge, S.J.L., Eds.; Royal Society of Chemistry: Cambridge, 2008.

[109] Goldstein, J.; Newbury, D.E.; Echlin, P.; Joy, D.C.; Lyman, C.E.; Lifshin, E.; Sawyer, L.; Michael, J.R. *Scanning electron microscopy and X-ray microanalysis*, 3rd ed.; Springer: New York, 2003.

[110] Brunauer, S.; Emmett, P.H.; Teller, E. Adsorption of gases in multimolecular layers. *Journal of American Chemical Society* **1938**, *60*, 309–319.

[111] Barrett, E.P.; Joyner, L.G.; Halenda, P.P. The determination of pore volume and area distribution in porous substances. I. Computations from nitrogen isotherms. *Journal of the American Chemical Society* **1951**, *73(1)*, 373–380.

[112] Lowell, S.; Shields, J.E. *Powder surface area and porosity*, 3rd ed.; Chapman & Hall: London, 1991.

[113] U.S. Environmental Protection Agency. Toxicity Characteristic Leaching Procedure: Method 1311. 1992. Available online: `http://www.ene.gov.on.ca/stdprodconsume/groups/lr/@ene/@subject/@hazardwaste/documents/nativedocs/stdprod_080476.pdf`, accessed on 10.07.2008.

[114] Rauret, G.; López-Sánchez, J.F.; Sahuquillo, A.; Rubio, R.; Davidson, C.; Ure, A.; Quevauviller, P. Improvement of the BCR three step sequential extraction procedure prior to the certification of new sediment and soil reference material. *Journal of Environmental Monitoring* **1999**, *1*, 57–61.

[115] Rauret, G.; López-Sánchez, J.F.; Sahuquillo, A.; Barahona, E.; Lachica, M.; Ure, A.M.; Davidson, C.M.; Gomez, A.; Lück, D.; Bacon, J.; Yli-Halla, M.; Muntau, H.; Quevauviller, P. Application of a modified BCR sequential extraction (three step) procedure for the determination of extractable trace metal contents in a sewage sludge amended soil reference material (CRM 483), complemented by a three-year stability study of acetic acid. *Journal of Environmental Monitoring* **2000**, *2*, 228–233.

[116] Mossop, K.F.; Davidson, C.M. Comparison of original and modified BCR sequential extraction procedures for the fractionation of copper, iron, lead, manganese, and zinc in soils and sediments. *Analytica Chimica Acta* **2003**, *478*, 111–118.

[117] Gržeta, B.; Ristić, M.; Nowik, I.; Musić, S. Formation of nanocrystalline magnetite by thermal decomposition of iron choline citrate. *Journal of Alloys and Compounds* **2002**, *334*, 304–312.

[118] Feitknecht, W. Über die Oxydation von festen Hydroxyverbindungen des Eisens in wäßrigen Lösungen. *Zeitschrift für Elektrochemie* **1959**, *63*, 34–43.

[119] Misawa, T.; Hashimoto, K.; Shimodaira, S. The mechanism of formation of iron oxide and oxyhydroxides in aqueous solutions at room temperature. *Corrosion Science* **1974**, *14*, 131–149.

[120] Kiyama, M. Conditions for the formation of Fe_3O_4 by the air oxidation of $Fe(OH)_2$ suspensions. *Bulletin of the Chemical Society of Japan* **1974**, *47(7)*, 1646–1650.

[121] Tamaura, Y.; Yoshida, T.; Katsura, T. The synthesis of green rust II($Fe^{III}{}_1$-$Fe^{II}{}_2$) and its spontaneous transformation into Fe_3O_4. *Bulletin of the Chemical Society of Japan* **1984**, *57*, 2411–2416.

[122] Tamaura, Y.; Ito, K.; Katsura, T. Transformation of γ-FeO(OH) to Fe_3O_4 by adsorption of iron(II) ion on γ-FeO(OH). *Journal of the Chemical Society, Dalton Transactions* **1983**, *2*, 189–194.

[123] Perales-Perez, O.; Umetsu, Y.; Sasaki, H. Precipitation and densification of magnetic iron compounds from aqueous solutions at room temperature. *Hydrometallurgy* **1998**, *50*, 223–242.

[124] Perales-Perez, O.; Umetsu, Y. ORP-monitored magnetite formation from aqueous solutions at low temperatures. *Hydrometallurgy* **2000**, *55*, 35–56.

[125] Lahav, O.; Morgan, B.E.; Hearne, G.; Loewenthal, R.E. One-step ambient temperature ferrite process for treatment of acid mine drainage waters. *Journal of Environmental Engineering* **2003**, *129(2)*, 155–161.

[126] Wang, J.; Deng, T.; Dai, Y. Study on the processes and mechanism of the formation of Fe_3O_4 at low temperature. *Journal of Alloys and Compounds* **2005**, *390*, 127–132.

[127] Morgan, B.E.; Lahav, O.; Hearne, G.E.; Loewenthal, R.E. A seeded ambient temperature ferrite process for treatment of AMD waters: Magnetite formation in the presence and absence of calcium ions under steady state operation. *Water SA* **2003**, *29(2)*, 117–124.

[128] Jolivet, J.P.; Tronc, E. Interfacial electron transfer in colloidal spinel iron oxide. Conversion of Fe_2O_3 in aqueous medium. *Journal of Colloid and Interface Science* **1988**, *125(2)*, 688–701.

[129] Welo, L.A.; Baudisch, O. The two-stage transformation of magnetite into hematite. *The London, Edinburgh, and Dublin Philosophical Magazine and Journal of Science* **1925**, *50*, 399–408.

[130] Mann, S.; Sparks, N.H.C.; Couling, S.B.; Larcombe, M.C.; Frankel, R.B. Crystallochemical characterization of magnetic spinels prepared from aqueous solution. *Journal of the Chemical Society, Faraday Transactions 1* **1989**, *85(9)*, 3033–3044.

[131] Jolivet, J.P.; Chanéac, C.; Prené, P.; Vayssiéres, L.; Tronc, E. Wet chemistry of spinel iron oxide particles. *Journal de Physique* **1997**, *7(C1)*, 573–576.

[132] Jolivet, J.P.; Tronc, E.; Chanéac, C. Synthesis of iron oxide-based magnetic nanomaterials and composites. *Comptes Rendus Chimie* **2002**, *5*, 659–664.

[133] Géhin, A.; Ruby, C.; Abdelmoula, M.; Benali, O.; Ghanbaja, J.; Refait, P.; Génin, J.M.R. Synthesis of Fe(II-III) hydroxysulphate green rust by coprecipitation. *Solid State Sciences* **2002**, *4*, 61–66.

[134] Ruby, C.; Géhin, A.; Abdelmoula, M.; Génin, J.M.R.; Jolivet, J.P. Coprecipitation of Fe(II) and Fe(III) cations in sulphated aqueous medium and formation of hydroxysulphate green rust. *Solid State Sciences* **2003**, *5*, 1055–1062.

[135] Domingo, C.; Rodríguez-Clemente, R.; Blesa, M.A. Nature and reactivity of intermediates in the auto-oxidation of iron (II) in aqueous acid media. *Solid State Ionics* **1993**, *59*, 187–195.

[136] Barrado, E.; Prieto, F.; Vega, M.; Fernandez-Polanco, F. Optimization of the operational variables of a medium-scale reactor for metal-containing wastewater purification by ferrite formation. *Water Research* **1998**, *32(10)*, 3055–3061.

[137] Morgan, B.E.; Lahav, O.; Loewenthal, R.E. Advances in seeded ambient temperature ferrite formation for treatment of acid mine drainage. *Environmental Science and Technology* **2005**, *39(19)*, 7678–7683.

[138] Giovanoli, R.; Cornell, R.M. Crystallization of metal substituted ferrihydrites. *Zeitschrift für Pflanzenernährung und Bodenkunde* **1992**, *155*, 455–460.

[139] He, Y.T.; Traina, S.J. Transformation of magnetite to goethite under alkaline pH conditions. *Clay Minerals* **2007**, *42*, 13–19.

[140] Tronc, E.; Belleville, P.; Jolivet, J.P.; Livage, J. Transformation of ferric hydroxide into spinel by Fe^{II} adsorption. *Langmuir* **1992**, *8*, 313–319.

[141] Hirano, M.; Okumura, S.; Hasegawa, Y.; Inakagi, M. Direct precipitation of spinel-type $Zn(Fe, Ga)_2O_4$ solid solutions from aqueous solutions at 90 °C: Influence of iron valence of starting salt on their crystallite growth. *Journal of Solid State Chemistry* **2002**, *168(1)*, 5–10.

[142] Vayssières, L.; Chanéac, C.; Tronc, E.; Jolivet, J.P. Size tailoring magnetite particles formed by aqueous precipitation: An example of thermodynamic stability of nanometric oxide particles. *Journal of Colloid and Interface Science* **1998**, *205*, 205–212.

[143] Jolivet, J.P.; Chanéac, C.; Tronc, E. Iron oxide chemistry. From molecular clusters to extended solid networks. *Chemical Communications* **2004**, pp. 481–487.

[144] Yokoyama, M.; Sato, T.; Ohta, E. Magnetization of cadmium ferrite prepared by coprecipitation. *Journal of Applied Physics* **1996**, *80(2)*, 1015–1019.

[145] Tang, Z.X.; Sorensen, C.M.; Klabunde, K.J.; Hadjipanayis, G.C. Preparation of manganese ferrite fine particles from aqueous solution. *Journal of Colloid and Interface Science* **1991**, *146*, 38–52.

[146] Klas, S.; Dubowski, Y.; Pritosiwi, G.; Gerth, J.; Calmano, W.; Lahav, O. Extent and mechanism of metal ion incorporation into precipitated ferrites. *Journal of Colloid and Interface Science* **2011**, *358*, 129–135.

[147] Kanzaki, T.; Nakajima, J.; Tamaura, Y.; Katsura, T. Formation of Zn-bearing ferrite by air oxidation of aqueous suspension. *Bulletin of the Chemical Society of Japan* **1981**, *54*, 135–137.

[148] Andrés-Vergés, M.; de Julián, C.; González, J.M.; Serna, C.J. Preparation and magnetic properties of monodispersed Zn ferrites of submicrometric size. *Journal of Materials Science* **1993**, *28*, 2962–2966.

[149] Kiyama, M. The formation of manganese and cobalt ferrite by the air oxidation of aqueous suspensions and their properties. *Bulletin of the Chemical Society of Japan* **1978**, *51(1)*, 134–138.

[150] Tamura, H.; Matijević, E. Precipitation of cobalt ferrites. *Journal of Colloid and Interface Science* **1982**, *90(1)*, 100–109.

[151] Kanzaki, T.; Tajima, K.; Doi, K.; Nakayama, S.; Itagaki, R.; Waragai, M.; Sato, S.; Suzuki, S.; Wada, S.; Kitayama, K. Formation of nickel and nickel, zinc-bearing ferrite in aqueous suspension by air oxidation. *Journal of Electron Spectroscopy and Related Phenomena* **1998**, *97*, 225–234.

[152] Barrado, E.; Prieto, F.; Garay, F.J.; Medina, J.; Vega, M. Characterization of nickel-bearing ferrites obtained as by-products of hydrochemical wastewater purification processes. *Electrochimica Acta* **2002**, *47*, 1959–1965.

[153] Shailaja, M.; Narasimhan, S.V. Dissolution kinetics of nickel ferrite in chelating and reducing agents. *Journal of Nuclear Science and Technology* **1991**, *28(8)*, 748–756.

[154] Mathur, B.S.; Venkataramani, B. Surface charge and surface chemical characteristics of magnetites substituted with nickel, cobalt and chromium. *Colloids and Surfaces* **1998**, *140*, 403–416.

[155] Yang, J.; Peng, J.; Liu, K.; Guo, R.; Xu, D.; Jia, J. Synthesis of ferrites obtained from heavy metal solutions using wet method. *Journal of Hazardous Materials* **2007**, *143*, 379–385.

[156] Ito, K.; Kanzaki, T.; Tamaura, Y.; Katsura, T. Formation of aluminium-bearing ferrite in aqueous suspension by air oxidation. *Journal of the Chemical Society, Dalton Transactions* **1981**, *11*, 2217–2219.

[157] Schwertmann, U.; Murad, E. The influence of aluminum on iron oxides: XIV. Al-substituted magnetite synthesized at ambient temperatures. *Clays and Clay Minerals* **1990**, *38(2)*, 196–202.

[158] Kaneko, K.; Takei, K.; Tamaura, Y.; Kanzaki, T.; Katsura, T. The formation of the Cd-bearing ferrite by the air oxidation of an aqueous suspension. *Bulletin of the Chemical Society of Japan* **1979**, *52(4)*, 1080–1085.

[159] Tamaura, Y.; Rasyid, U.; Katsura, T. Formation of a chromium-bearing ferrite, $Cr_{0.42}Fe_{2.56}O_{4.00}$ in aqueous suspension by nitrate oxidation. *Journal of the Chemical Society, Dalton Transactions* **1980**, *11*, 2125–2128.

[160] Matijević, E.; Simpson, C.M.; Amin, N.; Arajs, S. Preparation and magnetic properties of well-defined colloidal chromium ferrites. *Colloids and Surfaces* **1986**, *21*, 101–108.

[161] Erdem, M.; Tumen, F. Chromium removal from aqueous solution by the ferrite process. *Journal of Hazardous Materials* **2004**, *B109(1)*, 71–77.

[162] Barrado, E.; Prieto, F.; Medina, J.; López, F.A. Characterisation of solid residues obtained on removal of Cr from waste water. *Journal of Alloys and Compounds* **2002**, *335*, 203–209.

[163] Tamaura, Y. Ni(II)-bearing green rust II and its spontaneous transformation into Ni(II)-bearing ferrites. *Bulletin of the Chemical Society of Japan* **1986**, *59*, 1829–1832.

[164] Tamaura, Y. Ferrite formation from the intermediate, green rust II, in the transformation reaction of γ-FeO(OH) in aqueous suspension. *Inorganic Chemistry* **1985**, *24(25)*, 4363–4366.

[165] Cornell, R.M.; Giovanoli, R. Effect of cobalt on the formation of crystalline iron oxides from ferrihydrite in alkaline media. *Clays and Clay Minerals* **1989**, *37(1)*, 65–70.

[166] Tamaura, Y.; Abe, M. Metal ion adsorption - incorporation mechanism in the Zn(II)-bearing ferrite formation reaction in aqueous solution. *Journal of Colloid and Interface Science* **1989**, *129(2)*, 327–334.

[167] Kaneko, K.; Katsura, T. The formation of Mg-bearing ferrite by the air oxidation of aqueous suspension. *Bulletin of the Chemical Society of Japan* **1979**, *52(3)*, 747–752.

[168] Daniels, J.M.; Rosencwaig, A. Mössbauer study of the Ni-Zn ferrite system. *Canadian Journal of Physics* **1970**, *48(4)*, 381–396.

[169] Hasegawa, K.; Sato, T. Particle-size distribution of $CoFe_2O_4$, formed by the coprecipitation method. *Journal of Applied Physics* **1967**, *38(12)*, 4707–4713.

[170] Pandya, P.B.; Joshi, H.H.; Kulkarni, R.G. Bulk magnetic properties of Co-Zn ferrites prepared by the co-precipitation method. *Journal of Materials Science* **1991**, *26*, 5509–5512.

[171] Suwalka, O.; Sharma, R.K.; Sebastian, V.; Lakshmi, N.; Venugo, K. A study of nanosized Ni substituted Co-Zn ferrite prepared by coprecipitation. *Journal of Magnetism and Magnetic Materials* **2007**, *313*, 198–203.

[172] Bid, S.; Pradhan, S.K. Characterization of crystalline structure of ball-milled nano-Ni-Zn-ferrite by Rietveld method. *Materials Chemistry and Physics* **2004**, *84*, 291–301.

[173] Kurepin, V.A. A thermodynamic model of Fe-Cr spinel. *Contributions to Mineralogy and Petrology* **2005**, *149*, 591–599.

[174] Ford, R.G.; Kemner, K.M.; Bertsch, P.M. Influence of sorbate-sorbent interactions on the crystallization kinetics of nickel- and lead-ferrihydrite coprecipitates. *Geochimica et Cosmochimica Acta* **1999**, *63(1)*, 39–48.

[175] Alvarez, M.; Sileo, E.E.; Rueda, E.H. Structure and reactivity of synthetic Co-substituted goethites. *American Mineralogist* **2008**, *93(4)*, 584–590.

[176] Alvarez, M.; Rueda, E.H.; Sileo, E.E. Simultaneous incorporation of Mn and Al in the goethite structure. *Geochimica et Cosmochimica Acta* **2007**, *71*, 1009–1020.

[177] Kaur, N.; Singh, B.; Kennedy, B.J. Dissolution of Cr, Zn, Cd, and Pb single- and multi-metal-substituted goethite: relationship to structural, morphological, and dehydroxylation properties. *Clays and Clay Minerals* **2010**, *58(3)*, 415–430.

[178] Regazzoni, A.E.; Matijević, E. Interactions of metal hydrous oxides with chelating agents. VI. Dissolution of a nickel ferrite in EDTA solutions. *Corrosion-Nace* **1984**, *40(5)*, 257–261.

[179] Viart, N.; Pourroy, G.; Grenèche, J.M.; Niznansky, D.; Hommet, J. Microstructural and magnetic properties of Fe/Cr-substituted ferrite composites. *The European Physical Journal Applied Physics* **2000**, *12*, 37–46.

[180] Amonette, J.E.; Rai, D. Identification of noncrystalline $(Fe,Cr)(OH)_3$ by infrared spectroscopy. *Clays and Clay Minerals* **1990**, *38(2)*, 129–136.

[181] Ladgaonkar, B.P.; Kolekar, C.B.; Vaingankar, A.S. Infrared absorption spectroscopic study of Nd^{3+} substituted Zn-Mg ferrites. *Bulletin of Materials Science* **2002**, *25(4)*, 351–354.

[182] Waldron, R.D. Infrared spectra of ferrites. *Physical Review* **1955**, *99(6)*, 1727–1735.

[183] Musat Bujoreanu, V.; Segal, E. On the dehydration of mixed oxides powders coprecipitated from aqueous solutions. *Solid State Ionics* **2001**, *3*, 407–415.

[184] Gotić, M.; Jurkin, T.; Musić, S. Factors that may influence the micro-emulsion synthesis of nanosize magnetite particles. *Colloid Polymer Science* **2007**, *285*, 793–800.

[185] Hug, S.J. In situ Fourier transform infrared measurements of sulfate adsorption on hematite in aqueous solutions. *Journal of Colloid and Interface Science* **1997**, *188*, 415–422.

[186] Charlet, L.; Manceau, A.A. X-ray absorption spectroscopic study of the sorption of Cr(III) at the oxide-water interface: II. Adsorption, coprecipitation, and surface precipitation on hydrous ferric oxide. *Journal of Colloid and Interface Science* **1992**, *148(2)*, 443–458.

[187] Fendorf, S.E.; Li, G.; Gunter, M.E. Micromorphologies and stabilities of chromium(III) surface precipitated elucidated by scanning force microscopy. *Soil Science Society of America Journal* **1996**, *60*, 99–106.

[188] Sass, B.M.; Rai, D. Solubility of amorphous chromium(III)-iron(III) hydroxide solid solutions. *Inorganic Chemistry* **1987**, pp. 2228–2232.

[189] Skovbjerg, L.L.; Stipp, S.L.S.; Utsonomiya, S.; Ewing, R.C. The mechanisms of reduction of hexavalent chromium by green rust sodium sulphate: Formation of Cr-goethite. *Geochimica et Cosmochimica Acta* **2006**, *70*, 3582–3592.

[190] Barin, I. *Thermochemical data of pure substances*; VCH: New York, 1995.

[191] Morgan, B.E.; Lahav, O. The effect of pH on the kinetics of spontaneous Fe(II) oxidation by O_2 in aqueous solution - basic principles and a simple heuristic description. *Chemosphere* **2007**, *68*, 2080–2084.

[192] Tewari, P.H.; Campbell, A.B.; Lee, W. Adsorption of Co^{2+} by oxides from aqueous solution. *Canadian Journal of Chemistry* **1972**, *50(11)*, 1642–1648.

[193] Wolski, W.; Wolska, E.; Kaczmarek, J.; Politanska, U. Nonstoichiometric solid solutions during formation of Cd/Ni ferrites. *Solid State Ionics* **1993**, *63-65*, 628–632.

[194] Gillot, B.; Thiebaut, D.; Laarj, M. Synthesis of stoichiometric cadmium substituted magnetites and formation by oxidation of solid solutions of cadmium ferrite and γ-iron oxide. *Thermochimica Acta* **1999**, *342*, 167–174.

[195] Bondietti, G.; Sinniger, J.; Stumm, W. The reactivity of Fe(III) (hydr)oxides: effects of ligands in inhibiting the dissolution. *Colloids and Surfaces A: Physicochemical Engineering Aspects* **1983**, *79*, 157–167.

[196] Furrer, G.; Stumm, W. The coordination chemistry of weathering: I. Dissolution kinetics of δ-Al_2O_3 and BeO. *Geochimica et Cosmochimica Acta* **1986**, *50*, 1847–1860.

[197] Casey, W.H. Surface chemistry during the dissolution of oxide and silicate minerals. In *Mineral surfaces*; Vaughan, D.J.; Pattrick, R.A.D., Eds.; Chapman & Hall: London, 1994; pp. 187–217.

[198] Klas, S. Removal of toxic metals from industrial wastewater by their stable incorporation into ferrites at ambient temperature: Process development and modelling. PhD thesis, Technion, Haifa, Israel, 2010.

[199] Casey, W.H.; Westrich, H.R. Control of dissolution rates of orthosilicate minerals by divalent metal-oxygen bonds. *Nature* **1992**, *355*, 157–159.

[200] Perales-Perez, O.; Umetsu, Y. Ambient-temperature precipitation of Zn ions from aqueous solutions as ferrite-type compounds. *Hydrometallurgy* **2002**, *63*, 235–248.

[201] Klas, S.; Dubowski, Y.; Lahav, O. Chemical stability and extent of isomorphous substitution in ferrites precipitated under ambient temperatures. *Journal of Hazardous Materials* **2011**, *193*, 59–64.

[202] Perales-Perez, O.; Tohji, K.; Umetsu, Y. Theory and practice of the removal of heavy metal ions by their precipitation as ferrite-type compounds from aqueous solution at ambient temperature. *Metallurgical Review of The Mining and Materials Processing Institute of Japan (MMIJ)* **2001**, *17(2)*, 137–180.

[203] Wang, J.; Deng, T.; Dai, Y. Comparative study on the preparation procedures of cobalt ferrites by aqueous processing at ambient temperatures. *Journal of Alloys and Compounds* **2006**, *419*, 155–161.

[204] Nishimura, K.; Abe, M.; Inoue, M. Wide variety of ferrite fine particles synthesized from aqueous solution at room temperature. *IEEE Transactions on Magnetics* **2002**, *38*, 3222–3224.

[205] Stumm, W.; Lee, G.F. Oxygenation of ferrous iron. *Industrial and Engineering Chemistry* **1961**, *53(2)*, 143–146.

[206] Sayin, M. Catalytic action of copper on the oxidation of structural iron in vermiculitized biotite. *Clays and Clay Minerals* **1982**, *30(4)*, 287–290.

[207] Matocha, C.J.; Karathanasis, A.D.; Rakshit, S.; Wagner, K.M. Reduction of copper(II) by iron(II). *Journal of Environmental Quality* **2005**, *34*, 1539–1546.

[208] Singh, B.; Sherman, D.M.; Gilkes, R.J.; Wells, M.; Mosselmans, J.F.W. Structural chemistry of Fe, Mn, and Ni in synthetic hematites as determined by extended X-ray absorption fine structure spectroscopy. *Clays and Clay Minerals* **2000**, *48*, 521–527.

[209] Schwertmann, U.; Gasser, U.; Sticher, H. Chromium-for-iron substitution in synthetic goethite. *Geochimica et Cosmochimica Acta* **1989**, *53(6)*, 1293–1297.

[210] Krehula, S.; Music, S. The influence of Cr-dopant on the properties of α-FeOOH particles precipitated in highly alkaline media. *Journal of Alloys and Compounds* **2009**, *469*, 336–342.

[211] Tünay, O.; Kabdasli, N.I. Hydroxide precipitation of complexed metals. *Water Research* **1994**, *28(10)*, 2117–2124.

[212] Bundesministerium der Justiz. Verordnung über Anforderungen an das Einleiten von Abwasser in Gewässer (Abwasserverordnung - AbwV). 1997. Available online: `http://bundesrecht.juris.de/bundesrecht/abwv/gesamt.pdf`, accessed on 12.04.2011.

[213] Crawford, R.J.; Harding, I.H.; Mainwaring, D.E. Adsorption and coprecipitation of multiple heavy metal ions onto the hydrated oxides of iron and chromium. *Langmuir* **1993**, *9*, 3057–3062.

[214] Fendorf, S.E.; Li, G. Kinetics of chromate reduction by ferrous iron. *Environmental Science and Technology* **1996**, *30*, 1614–1617.

[215] Choung, J.W.; Xu, Z.; Finch, J.A. Advances in the ambient temperature ferrite process applied to acid mine drainage treatment. *Environmental Science and Technology* **2000**, *21*, 201–207.

[216] Kongsricharoern, N.; Polprasert, C. Electrochemical precipitation of chromium (Cr^{6+}) from an electroplating wastewater. *Water Science and Technology* **1995**, *31(9)*, 109–117.

[217] Hunsom, M.; Pruksathorn, K.; Damronglerd, S.; Vergnes, H.; Duverneuil, P. Electrochemical treatment of heavy metals (Cu^{2+}, Cr^{6+}, Ni^{2+}) from industrial effluent and modeling of copper reduction. *Water Research* **2005**, *39*, 610–616.

[218] Meunier, N.; Drogui, P.; Gourvenec, C.; Mercier, G.; Hausler, R.; Blais, J.F. Removal of metals in leachate from sewage sludge using electrochemical technology. *Environmental Technology* **2004**, *25*, 235–245.

[219] Meunier, N.; Drogui, P.; Montane, C.; Hausler, R.; Mercier, G.; Blais, J.F. Comparison between electrocoagulation and chemical precipitation for metals removal from acidic soil leachate. *Journal of Hazardous Materials* **2006**, *B137*, 581–590.